MECHANICS OF CALCITE-POLYMER MICROCOMPOSITES USING NANOINDENTATION AND MICRO-COMPRESSION

A thesis submitted to The University of Manchester for the degree of Doctor of Philosophy in the Faculty of Engineering and Physical Science

2012

LUIS RIBEIRO

SCHOOL OF MATERIALS

TABLE OF CONTENTS

Word count: 52,432

Index of Tables

Index of Figures

ABSTRACT

The University of Manchester
Luis Ribeiro
Doctor of Philosophy
Mechanics of synthetic calcite-polymer microcomposites using Nanoindentation and Micro-compression
October 2012

The aim of this project is to investigate the suitability of specific polymers inclusions in improving some important mechanical properties of single crystals of calcite. The mechanical properties of synthetic and mineral single crystals of pure calcite are reported and compared with synthetic and biogenic crystals incorporating polystyrene particles or di-block co-polymer micelles and organic molecules respectively. The mechanical properties of these crystals are measured using nanoindentation and micro-compression techniques. It is shown that the crystals'mechanical properties obtained by the nanoindentation Oliver-Pharr method are influenced by the compliance of the resin substrate into which the crystal samples are embedded. The embedding of the crystals is shown to be necessary in order to achieve a flat surface onto which reliable indentation can be made. An estimate of the elastic moduli of the samples was obtained by using the Song-Pharr model, which takes into account substrate compliance. The hardness of all the tested samples was also recalculated by using conventional methods.

By analyzing the obtained substrate independent data it was found that although the occlusion of co-polymer micelles reduced the modulus of pure calcite its hardness was not affected. This behaviour was not observed in the composites occluded with 200 nm polystyrene particles which showed a significant hardness reduction. The 20 nm co-polymer micelles also increased the specific hardness of the crystals whereas the 200 nm polystyrene particles showed no such behaviour. The micro-compression data showed that the 200 nm polystyrene particles could potentially be used to reduce the brittleness of calcite. Images of cracks, post-fracture of the crystals, indicated deformation of the polymer. This is evidence of the occurrence of a crack bridging mechanism. It was thought that this could lead to an enhancement of the strain at fracture and work of fracture of these composites when compared with pure calcite. Mechanical data from these tests showed however that the polystyrene particles' occlusion was inadequate to increase the strain to fracture and the work of fracture of calcite. In addition to this the specific compressive strength, specific compressive modulus and specific compressive work of fracture of calcite also decreased with the addition of PS particles.

Declaration

No portion of work referred to within this thesis has been submitted in support of an application for another degree or qualification of this or any other university, or other institution of learning.

Copyright Statement

Acknowledgements

The author would like to thanks both Professor Steve Eichhorn and Professor Fiona Meldrum for their supervision and support. Thanks are also due to the EPSRC for their funding, and to Dr Yi-Yeoun who kindly made the samples used in this work.

The author would also like to thanks all members of the Raman Group who have provided a great deal of help and support. Thanks also to staff and colleagues within the Materials Science Center, particularly to Andy Forrest and Chris Wilkins for their help and support over the pasts years.

The author also wishes to thanks all of his family, friends and house mates for their encouragement and friendship.

1. INTRODUCTION

1.1 Background

Calcite is a ceramic material made of calcium carbonate ($CaCO_3$), and is the cheapest commercially available inorganic mineral (Sheng *et al*., 2006). When used as a construction material calcite displays a major drawback, characteristic of all ceramic materials: it is very brittle. Since the greatest disadvantage of ceramics such as calcite, compared with metals and polymers, is a low fracture toughness, improving the toughness of ceramic materials is therefore a major goal (Carter, 2007). The requirements for the mechanical properties of a material are obviously dependent on its specific application. In general, for applications in polishing ceramic abrasives, structural crashworthiness, light protective armour and construction industries, an increase in hardness, strength, toughness and specific mechanical properties are desirable (Carter, B. and Norton, 2007; Sun, L. *et al.*, 2009; Saint-Gobain, 2012). Organisms such as echinoderms have been using calcite as a construction material during millions of years of evolution. Echinoderm calcite, when compared with inorganic calcite, however shows a different mechanical behaviour by behaving as a composite, with a reduced elastic modulus, increased hardness and strength compared to inorganic calcite (Weber *et al.*, 1969; Emlet, 1982; Ma *et al.*, 2008; Moureaux *et al.*, 2010).

Studies have shown that textural differences between sea urchin spine calcite and pure inorganic calcite are due to the occlusion inside the biogenic echinoderm crystal of macromolecules that constitute only about 0.1% by weight of the spicule (Weiner *et al*., 2000). Experiments with calcite crystals grown in the presence of echinoderm intracrystalline proteins showed that these macromolecules remain occluded inside the crystal on specific planes, and their presence alters the mechanical properties of the crystal host (Addadi *et al*., 1994). Incorporation of these proteins into pure calcite crystals produced a calcite crystal composite with a 50% reduction in coherence length in the *a,b*-plane, perpendicular to the *c* direction (Aizenberg, 2006).

Indentation tests performed on these synthetic crystals with occluded proteins showed additionally that they behave plastically compared to the brittle behaviour of control crystals without macromolecules (Weiner *et al*., 2000). Since organic molecules occluded in biogenic crystals have common attributes such as carboxylate groups, phosphate and sulfate groups, many polymers functionalized by surface groups have been used in crystal growth studies (Weiner and Addadi, 1997). Based on these previous studies, and through biomimetics (the science of imitating nature), a new composite, made of a calcite matrix reinforced with polystyrene inclusions, has been produced by Prof Fiona Meldrum and Dr Yi-Yeoun Kim (Chemistry, University of Leeds) in a joint project funded by the EPSRC. Prior to this project, the integration of synthetic polymers into the calcite crystal was mainly limited to the crystal's outer surface. The use of a particular high acid functionalized polystyrene polymer overcame issues over partial integration and permitted a uniform distribution of the polymer throughout the crystal. In another study performed by the same authors, smaller di-block co-polymer micelles were also successfully integrated throughout the entire calcite crystal.

Before this project, the mechanical properties of these new composites were unknown. The particular problem was how to evaluate the polymer inclusions' influence on the mechanical properties and deformation behaviour of these micron-scale crystal composites. Nanoindentation and micro-compression techniques have recently become very frequently used techniques in order to determine the mechanical response of various materials at the small scale. Nanoindentation has already successfully been used to measure the hardness and modulus of single crystal needles and plates (1-2 μm diameter) from fresh sea urchin teeth (Ma *et al.*, 2008) and 100 μm inorganic calcite crystals (Zügner, 2002; Zügner *et al.*, 2006).

The micro-compression technique, in which a conventional nanoindentation instrument is fitted with a flat-punch tip, has also been used to characterise the strength and fracture of wood cell walls (Xinan *et al.*, 2010), glass (Koopman *et al.*, 2004) and biomaterials (Ziskind *et al.*, 2010). The emergence of commercial focused ion beam (FIB) instruments provided the opportunity to fabricate micron-sized specimens. The micro-compression

technique has been used in conjunction with FIB to investigate specimen geometry and size effects on the mechanical properties of micron-scale single crystals of metals and alloys (Uchic *et al.*, 2004; Greer and Nix, 2005; Uchic and Dimiduk, 2005; Choi *et al.*, 2007; Kiener *et al.*, 2009; Yang *et al.*, 2009). The nanoindentation technique and the micro-compression technique in conjunction with the FIB were therefore utilised in the present study to investigate the effect of synthetic polystyrene inclusions on the mechanical properties of calcite single crystals. Due to the late availability of the composite occluded with di-block co-polymer micelles, only a nanoindentation technique was used on this composite.

1.2 Objectives

The work presented in this thesis is part of a larger project which principal goal is to produce a macroscopically tougher and possibly harder lightweight component from a brittle material. Taking sea urchin spine calcite as a hard and crack resistant calcite-polymer model, the objective will be therefore to improve the mechanical behaviour of calcite by the occlusion of different kinds of synthetic polymers. Improving the mechanical properties of calcite will not only increase its application in industries already using it but will also expand its application on other industries requiring tougher lightweight materials (see Section 2.7.1). According to this major goal, the subject of this thesis will be to investigate the suitability of specific polymers inclusions in creating calcite composites with improved mechanical properties when compared to pure calcite: higher toughness or energy absorption capacity, higher strength, higher strain, lower density, higher hardness etc. Taking into consideration the micron-size scale and specific shapes of the samples under study, the capacity of the utilised methodology in obtaining reliable results will also be investigated. This work will therefore try to answer the following questions:

i. Can the polymer inclusions increase the energy absorption capacity of calcite and prevent the occurrence of catastrophic failure?

ii. Since for some engineering applications weight is an important factor, will the polymer inclusions increase the specific mechanical properties of calcite?
iii. How do the co-polymer micelles and different amounts of polystyrene inclusions affect the modulus, hardness and deformation behaviour of calcite?
iv. How do the different amounts of polystyrene inclusions affect the bulk deformation and compressive mechanical properties of pure calcite?
v. Is the methodology employed adequate to obtain reliable results?

In order to answer these questions the following activities will be undertaken:

i. Investigation of the influence of different amounts of polystyrene inclusions on the bulk deformation behaviour and compressive mechanical properties of pure calcite.
ii. Study and compare the compressive properties of FIB machined and non-machined crystal specimens using micro-compression.
iii. Compare the modulus, hardness and the deformation behaviour under load of biogenic calcite (sea urchin spine calcite) and nonbiogenic calcite (Iceland spar calcite) using nanoindentation.
iv. Investigate the influence of different amounts of polystyrene inclusions on the modulus, hardness and surface deformation behaviour of calcite using nanoindentation.
v. Investigate the influence of co-polymer micelles inclusions on the modulus, hardness and surface deformation behaviour of calcite using nanoindentation.
vi. Investigate the reliability of the obtained results by finding the sources and resolutions of possible problems affecting the performed measurements.
vii. Investigate and compare the obtained data using appropriate statistical methodology.

2. LITERATURE REVIEW

2.1 The principle of biomimetics

Biomimetics, sometimes called biomimicry or bionics, is the science of imitating nature, in which ideas taken from nature are applied in another field such as engineering, design or material science (Sarikaya, 1994; Rao, 2003; Vincent *et al.*, 2006). Biomimetics is therefore a large area of research which requires a close collaboration between physical sciences (physics, chemistry, engineering and materials sciences) and biological fields (zoology, microbiology, biochemistry and genetics) (Sarikaya, 1994). In biomimetics, the physical functions and structures of biological composites of engineering interest are investigated in order to produce new and improved materials (Sarikaya, 1994). The total transfer of these natural materials features for technological applications may not be advantageous, not only because not every single microstructural feature observed in these materials serves a structural purpose, but also because in fields such as engineering there is less restrictions on material selection than in nature (biocompatibility, limited availability, etc.). It is therefore very important in biomimetics to identify which features control the performance of these materials in order to use them in artificial bio-inspired synthetic materials (Barthelat, 2007).

2.2 Calcium carbonate

Calcium carbonate is a mineral compound with the chemical formula $CaCO_3$ and is the cheapest commercially available inorganic material (Sheng *et al.,* 2006). It is a common substance found as rock (chalk, limestone and marble) in all parts of the world, and is the main component of shells of marine organisms, snails, and eggshells (Tegethoff, 2002). Calcium carbonate can exist in five crystallographic forms: three anhydrous crystalline polymorphs (calcite, aragonite and vaterite), two hydrated crystalline polymorphs (calcium carbonate hexahydrate and calcium carbonate monohydrate) and an amorphous form of calcium carbonate. Calcite and aragonite are the most stable forms at ambient temperatures and pressures, while calcium carbonate mono- and hexa-hydrate and amorphous calcium

carbonate are very unstable and hence rare in non-biological environments (Lippmann, 1973).

2.3 Calcite

Calcite, which gets its name from the Latin *calx*, (burnt lime) is formed in many different geological environments and is one of the most common minerals in the Earth's crust (Tegethoff, 2002; Downs, 2006). The calcite structure (Figure 2.1 (a)) consists of alternating layers of calcium ions and carbonate ions oriented perpendicular to the *c*-axis with interionic bonding between layers. Carbonate ions within a layer are all coplanar and have identical orientations. Alternate layers are rotated 180º degrees with respect to the layers above and below (Rachlin *et al.*, 1992).

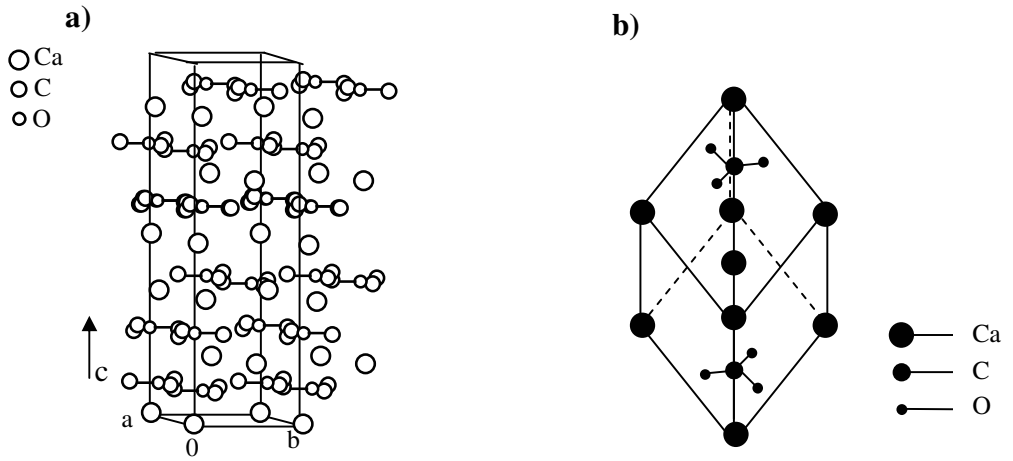

Figure 2.1 (a) Crystal structure of calcite (reproduced from Lippman, 1973); (b) Elementary unit cell of the calcite crystal lattice (Reproduced from Lu *et al.*, 2007).

Calcite crystallises in the rhombohedral system, where the elementary unit cell of the crystal lattice is a rhombohedral prism (Figure 2.1 (b)). The rhombohedral cell of calcite contains two $CaCO_3$ formula units and belongs to space group D^6_{3d} (R3m, n.167; the homomorphism is D_{3d}) (Lu *et al.*, 2007). Crystals belonging to this system have six independent elastic constants, the full set of elastic constants of calcite measured by ultrasonic methods are C_{11} = 137, C_{33} = 81.1, C_{44} = 35.0, C_{12} = 48.2, C_{13} = 56.8, and C_{14} =

20.0 GPa (Bhimasenachar, 1945). Calcite has rhombohedral cleavage planes, called {104} planes, which intersect the alternating layers of calcium and carbonate ions at 44º37' (Rachlin *et al*., 1992). The calcite rhombohedral structure is delimited by a set of equivalent oblique faces which are thermodynamically very stable. A high stability energy layer that holds the ions together within a layer is always accompanied by a proportionally low attachment energy layer that holds parallel layers together (Hartman and Perdok, 1955). If the sum of the layer energy and attachment energy is constant then the higher the energy layer the lower will be the attachment energy. This explains why calcite crystals cleave easily along their 104 planes, where a crack can propagate along a minimum energy pathway (Lawn, 1993).

2.4 Polystyrene (PS)

Polystyrene is an aromatic polymer made by polymerization from the aromatic monomer styrene (Figure 2.2), it is composed of the repeat unit –(CHX–CH2*)*–, where –X is the benzene ring styrene. Polystyrene can be either amorphous (atactic) or semicrystalline (isotactic and syndiotactic), and has a glass transition temperature (T_g) of 100 ^oC (ASM, 2003).

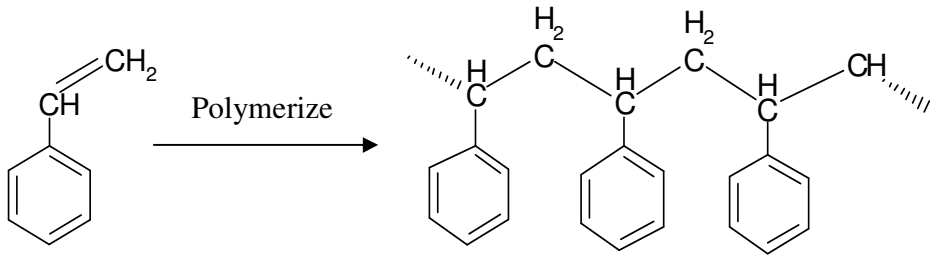

Figure 2.2 Schematic reaction mechanism for polystyrene (PS) (Reproduced from Pine, 2007).

The elastic modulus and hardness of a polystyrene film measured by nanoindentation gave values of 3.8 GPa (Miyake *et al*., 2006) and 0.26 GPa, respectively (Briscoe, 1998; Li, M. *et al*., 2001).

2.5 Composite materials

The term composite is usually applied for those materials in which properties such as the hardness are significantly changed in comparison with those of a homogeneous material, and in which the distinct phases are separated on a larger scale than the atomic (Park and Lakes, 1992). Composites may be classified in many ways: by bulk form characteristics, such as matrix composites or laminated composites; distribution of constituents, such as continuous or discontinuous; or function, like electrical or structural composites (Mitchell, 2004). Classifying by the geometry of the strengthening particles there are particulate, fibrous or platelet reinforced composites. Classifying by the materials used in the matrix, composites can be classified as (Chawla, 2003):

1. Polymer Matrix Composites (PMCs)
2. Metal Matrix Composites (MMCs)
3. Ceramic Matrix Composites (CMCs)

The matrix phase is the continuous phase, whilst the distributed phase, the reinforcement phase, can be in the form of particles, short fibres, continuous fibres, whiskers or sheets. The reinforcing material in a matrix can be metallic, polymeric or ceramic. In a composite the matrix can have several functions: to deform and distribute the stress under load to the reinforcing phase, to hold the fibrous phase in place, to protect the surface of the reinforcement from oxidation, corrosion, scratching or abrasion (Mitchell, 2004).

2.6 Mechanical properties of biogenic and synthetic calcite composites

Ceramic materials such as calcite or aragonite have been used by organisms as a construction material for millions of years of evolution. When used as a construction material calcite behaves in a brittle manner. This is due to the existence of specific planes of preferred cleavage inside its crystal structure where cracks can propagate easily (Addadi *et al.*, 1994). Organisms have evolved strategies to avoid this ceramic brittleness problem by creating two kinds of composite materials. One of these composite materials is widely used in nature and produced synthetically by man; it is composed of a pliant organic matrix reinforced by stiffer particles. The other kind of composite material uses the same basic

concept of combining a stiff component with a pliant one, but the roles are reversed. In this composite, the matrix is a single crystal and the reinforcement particles are polymeric macromolecules occluded into the single crystal (Aizenberg, 2006). One example of such a composite is biogenic echinoderm calcite, whose mechanical properties can be compared with inorganic calcite (Table 2.1).

Table 2.1 Elastic modulus and hardness of inorganic and echinoderm single crystal calcite (Zugner *et al*., 2006; Moureaux *et al*., 2010)

	Elastic modulus (GPa)	Hardness (GPa)
Inorganic calcite	83 - 88	2.8 - 3.4
Echinoderm calcite	58.6 ± 3.8	3.84 ± 0.25

The mechanical properties of single crystal echinoderm calcite (Table 2.1) were measured at a maximum load of 50 mN using a nanoindenter with a Berkovich tip (Moureaux *et al.*, 2010). The mechanical properties of inorganic calcite were measured using a conventional AFM base adapted with a Berkovich tip and on 500 μm calcite crystals . The same author (Zügner, 2002) observed an increase in the modulus from 83 to 88 GPa as the indentation depth was increased from 50 nm to 300 nm respectively. The hardness also varied from 3.4 to 2.8 GPa as the indentation depth was increased from 50 nm to 300 nm respectively. These results showed a dependence of the mechanical properties according to indentation depth, confirming therefore the presence of an indentation size effect (ISE) (see Section 2.16). The same author also observed a 8.3 % hardness increase, from 2.89 ± 0.34 GPa to 3.13 ± 0.38 GPa as the crystal size was reduced from 500 μm to 100 μm. This crystal size effect was not observed in relation to the modulus. The modulus was only reduced by -0.47 %, from 84.7 ± 7.0 GPa to 84.3 ± 7.1 GPa as the crystal size was reduced from 500 μm to 100 μm. The Knoop hardness anisotropy of calcite has also been studied by Carter *et al*., (1993). They found that the Knoop hardness varied between 1.73 GPa and 1.92 GPa upon rotating the crystal from 0 to 180° (Figure 2.3).

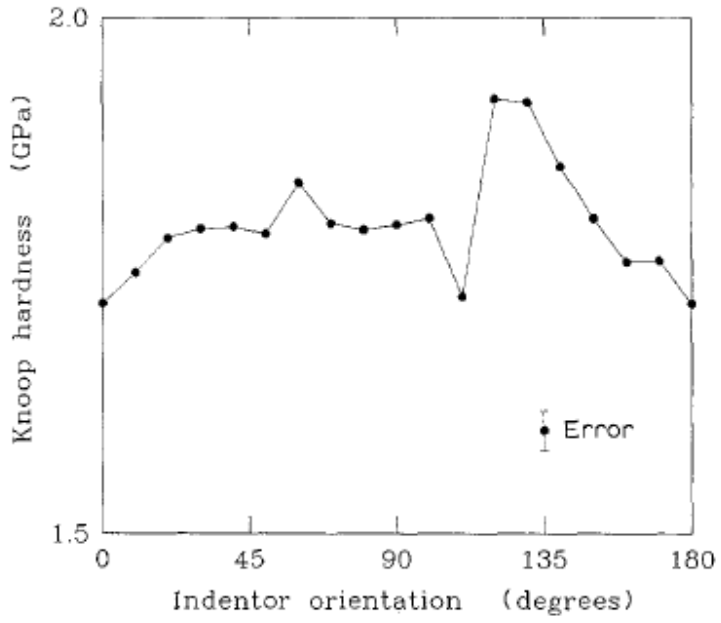

Figure 2.3 Variation in Knoop hardness (10 g load) with indenter orientation of the (001) cleavage plane of calcite. 0° is parallel to the [0 10] direction (Carter, G. M. *et al.*, 1993).

By using a Berkovich tip, Zugner (2002), also studied the anisotropy of calcite crystals by measuring at 300 nm depth the elastic modulus and hardness of different surfaces of two crystals. A change in the modulus from 89 ± 7.4 GPa to 88 ± 7.1 GPa was observed between different surfaces of the first crystal and a change in the modulus from 99 ± 6.5 GPa to 100 ± 7.8 GPa between different surfaces of the second crystal. In relation to hardness the change was from 2.7 ± 0.2 GPa to 2.8 ± 0.2 GPa between different surfaces of the first crystal and a change in the hardness from 2.5 ± 0.2 GPa to 2.6 ± 0.2 GPa between different surfaces of the second crystal. These data showed therefore a larger difference in the measured hardness and modulus between different crystals than between different surfaces of the same crystal. Although some details on this experiment were absent (axis orientation, crystal size etc), this study suggested that anisotropy doesn't appear to have a very large influence on the hardness and modulus of pure calcite. Although calcite crystals are anisotropic, the lower elastic modulus of echinoderm calcite cannot be attributed to a varying *c*-axis orientation (Emlet, 1982).

The compressive strength of echinoderm spines (72 MPa) was also found to be of the same order as calcite limestone of high bulk density, and much larger than that of calcite limestone of the same bulk density (Weber *et al.*, 1969). The strength of echinoderm spines is however not only due to the nanometer scale of the single calcite crystals but also the micron scale of the porous structure of the spine itself (Presser *et al.*, 2009). At the nanometer scale the crystal of a sea urchin spine is made up of coherent blocks with dimensions (coherence lengths) of ~210 nm and they are misaligned (angular spread) by around 130 millidegrees from the 104 direction. The 104 coherence lengths of a geological calcite crystal are often more than 800 nm, and have angular spreads as small as 3 millidegrees (Aizenberg *et al.*, 1997). The crystal structure of sea urchin spine calcite is therefore less ordered than pure calcite.

An important and not fully resolved question is how the organic molecules are arranged within the calcite mineral lattice. The discovery of anisotropic lattice distortions in aragonitic and calcitic shells led some authors to suggest that biomolecules are accommodated within the calcite lattice. According to these authors, the carbonate groups of the biomolecule glutamic and aspartic residues would replace those of the calcium carbonate (Pokroy *et al.*, 2006). By using X-ray diffraction with synchrotron radiation on sea urchin spines, Berman, *et al*., (1990) proposed however that the bulky proteins could not be accommodated inside perfect lattice domains and therefore must be concentrated at the boundaries of coherently scattered crystal blocks.

By using transmission electron microscopy on sea urchin tooth plates Robach *et al*., (2005) found that the biogenic calcite occluded macromolecules resided in 10-225 nm spherical cavities inside the crystal. These authors did not find any evidence of lattice distortion from macromolecules incorporated directly into the crystalline lattice. Seto *et al*., (2012) also found biogenic sea urchin spine calcite to be a mesocrystal structure composed of coherent domains, with lengths of 100–300 nm and widths of approximately 50 nm, coated by a 2 nm layer of amorphous calcium carbonate and 1.4 ± 0.3 nm biomolecules. These authors observed that the macromolecules were not only concentrated at the boundary regions between different domains but also occluded within spherical cavities (10 to 100 nm) within each domain. By generating discontinuities in this mesocrystal structure, the

biomolecules located at these boundaries and inside the domains would interfere with the propagation of fracture along the cleavage planes of calcite. Nanoindentation on the outer part of the sea urchin spine (septa), which is characterised by smaller coherent blocks, also revealed a higher hardness and modulus than the centre of the spine (stereom), made up of larger coherent blocks (Moureaux *et al.*, 2010). This study shows therefore a relation between the domain size and the mechanical properties of the sea urchin spine.

Experiments with calcite crystals grown in the presence of echinoderm intracrystalline proteins showed that these macromolecules remain occluded inside the crystal on specific planes, and their presence alters the mechanical properties of the crystal host (Addadi *et al.*, 1994). Incorporation of these proteins into pure calcite crystals produced a calcite crystal composite with a 50 % reduction in coherence length in the *ab*-plane, perpendicular to the *c* direction (Figure 2.4 and 2.5) (Aizenberg, 2006).

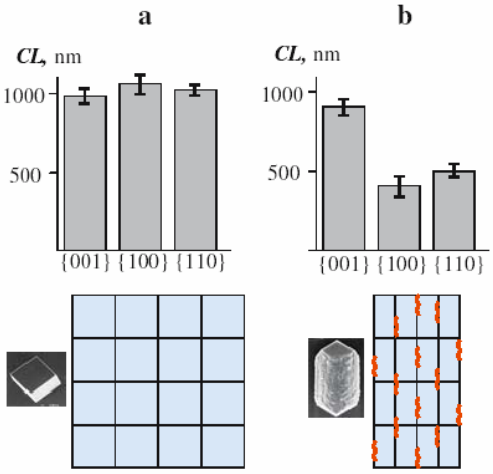

Figure 2.4 Textural parameters of synthetic calcite crystals. Top: Coherence lengths (Xu, Z.-H. and Rowcliffe) measured in 3 perpendicular directions: [001], [100] and [110]. Bottom: Schematic presentation of the crystal viewed as a combination of corresponding perfect domains. Macromolecules are indicated by red lines. a) Pure calcite crystal; b) Elongated crystal grown in the presence of macromolecules extracted from sea urchin spines (Aizenberg, 2006).

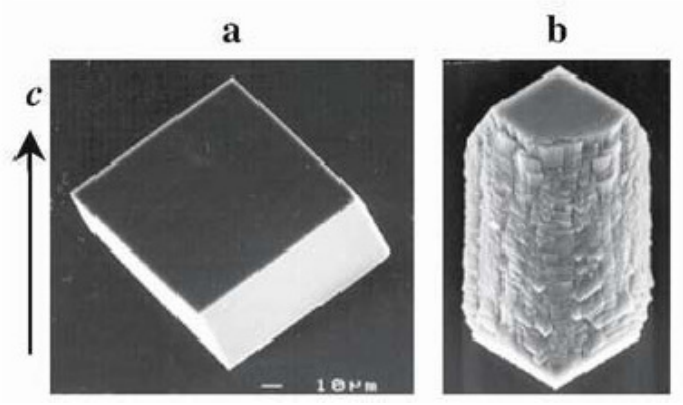

Figure 2.5 Synthetic calcite crystals. The orientation of the *c* crystallographic axis is indicated. a) Pure calcite crystal; b) Elongated crystal grown in the presence of macromolecules extracted from sea urchin spines (Aizenberg, 2006).

Indentation tests performed on these synthetic crystals with occluded proteins showed that they behave plastically compared to the brittle behaviour of control crystals without macromolecules (Weiner *et al*., 2000) (Figure 2.6).

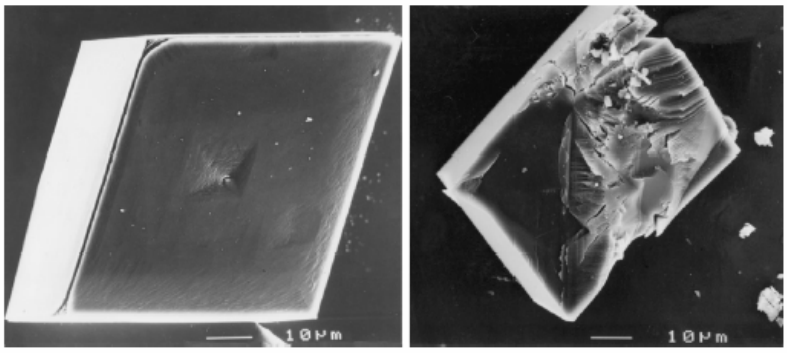

Figure 2.6 Indentations performed with the same load (10 $N\mu m^{-1}$) on single calcite crystals with occluded proteins (left) and without occluded sea urchin test proteins (Weiner *et al*., 2000).

Mechanical tests performed in these synthetic crystals by microindentation also produced stress-strain curves indicative of increasing plasticity and reduced brittleness (Figure 2.7).

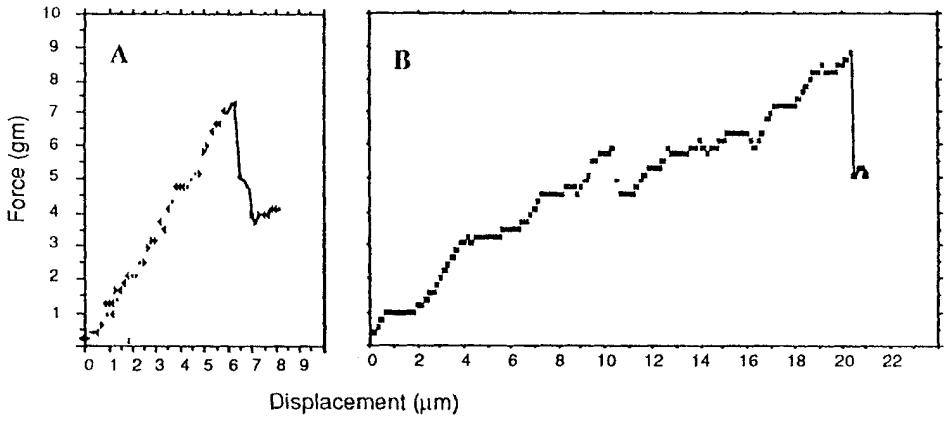

Figure 2.7 Force-displacement curves; (A) a pure synthetic calcite crystal. (B) a synthetic calcite crystal containing proteins extracted from sea urchin spines (Addadi *et al.*, 1994).

Figure 2.7 shows that the penetration depth of the indenter before the final crystal fracture occurs is larger for the crystal with occluded proteins (curve B) than for the crystal without proteins (curve A). The area under the curve is proportional to the energy absorbed by the crystal before fracture, therefore it can be concluded that the crystal with occluded proteins has a higher energy absorption capacity (work of fracture) than the crystal without occluded proteins (Addadi *et al.*, 1994; Motz *et al.*, 2002; Mitchell, 2004; Liu *et al.*, 2010). It should be noted that these authors did not give further details on their conducted experiments. In Figure 2.6, for example, it is observed that the tested crystals do not have the same dimensions. This may lead to a different mechanical response of the crystals under load which reduces the results accuracy. Many mechanisms can explain the different mechanical behaviour displayed by the synthetic composite crystals: plastic yield of the material remote from the crack tip, plastic deformation at the crack tip, increase in the area of the fracture surface or dissipation of energy by deformation of the polymer (Lippmann, 1973). The deviation of cracks by the proteins introduced along planes oblique to the cleavage planes of calcite has also been proposed by Aizenberg (2006) as a crystal toughening mechanism (Figure 2.8).

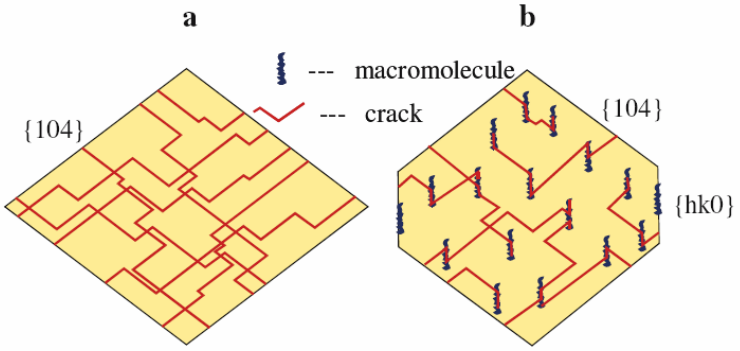

Figure 2.8 Schematic of crack propagation in pure calcite (a) and the crack arresting function of specific intracrystalline macromolecules positioned oblique to the cleavage planes (b) during microindentation experiments (Aizenberg, 2006).

The concept of occluding polymers into a crystal in order to improve mechanical properties is not yet fully developed in the production of synthetic composite crystals. Further studies are therefore needed to elucidate the mechanisms by which these new composites obtain these mechanical properties.

2.7 Ceramic matrix composites (CMCs) and their applications

Ceramic can be defined as chemically very stable, crystalline, inorganic, non-metallic compounds or mixtures of such compounds. Its chemical bonding is mostly ionic with some covalent bonding. Several mechanical characteristics such as high strength or high hardness result from such bonding (Warren, 1992; Rösler *et al.*, 2007). Ceramic can be categorised as traditional ceramic (bricks, pottery or tiles) or advanced ceramic (oxides, nitrides and carbides of silicon, aluminium, titanium etc.). It can also be classified as functional ceramic or structural ceramic. Functional ceramic is used primarily for non-mechanical properties such as thermal insulation, electrical resistance/conductivity, etc. Structural ceramic is used in applications requiring capacity to bear various forms of mechanical load, high temperature strength or wear and erosion resistance.

The low atomic and dislocation mobility in ceramic microstructures leads to high creep resistance and hardness, but also to low fracture toughness (Chawla, 2003). Since the

greatest disadvantage of ceramics compared with polymers and metals is their extremely low fracture toughness, improving the toughness of ceramic materials is therefore a major objective. This important goal can be attained via ceramic matrix composites. In ceramic matrix composites, the ceramic material is used as a matrix to which second phase in the form of particles, fibres or platelets are added in. Among the reinforcements for ceramic matrices are carbides, borides, nitrides and oxides which have a high strength, low density, high modulus and high melting point. Common ceramic matrix materials include various glasses, glass-ceramic, and ceramics such as carbon, silicon carbide, silicon nitride, aluminides and oxides.

The general applications of CMCs can be divided into aerospace and non-aerospace applications. Aerospace applications demand high thrust to weight ratio, faster speeds and increased altitudes. These goals translate into material requirements involving increased strength to density and stiffness to density ratios, higher temperature resistance and improved damage tolerance. In non-aerospace applications CMCs can be used in several areas; namely automotive, energy, cutting tools, wear resistant parts or medicine. The requirements for CMCs in the automotive area for example are good heat insulation, high strength, low abrasion and corrosion, high toughness, low density, high thermal resistance and low cost (Chawla, 2003). In medicine CMCs can be used as biocompatible ceramic (bioceramic) in the repair and reconstruction of human body parts such as bone.

2.7.1 Potential applications of new calcite-polymer composites

As CMCs are being developed to offer an alternative to single-phase ceramics because of the possibility of designing with higher toughness, the new biomimetic CMCs occluded with polymers can potentially lead to an enormous subset of tougher and less brittle ceramics. The new calcite-polymer composites could therefore replace calcium carbonate as a reinforcing filler in the polymer composite industry. Calcium carbonate has been used as a mineral filler in paper, rubber, plastic, architectural materials, coatings and light chemicals. In the plastic industry, which represents 26% of the total 74 Mt consumption of calcium carbonate in 2011 (Roskill, 2012), materials such as polypropylene, polyvinyl

chloride (PVC), polyethylene, and unsaturated polyesters are used in automotive components, home appliances, construction and industrial applications.

Within these materials, grounded (GCC) or precipitated (PCC) calcium carbonate can have several functions: reducing formulation costs, as a rheology control agent, reducing brittleness, increasing opacity, surface gloss, toughness, impact strength, tensile strength, stiffness, etc. Specific gravity is also an important factor to take into consideration since mineral fillers with high specific gravity will increase significantly the weight of the finished product. In the construction industry calcium carbonate is also used as a filler in the production of concrete structures, bricks and masonry products such as plasters, mortars or asphalt roofing shingles (Wiebking, 1998; Bryant and Wiebking, 2002; Wiebking, 2005; Hanim *et al.*, 2008; Specialty-Minerals, 2012).

The new calcite-polymer composite crystals could also be used in applications such as: polishing ceramic abrasives (Carter, B. and Norton, 2007), structural crashworthiness, impact-resistant protective armor and lightweighting. For crashworthy applications, the composite under load requires to be designed in such a way that it absorbs energy in a controlled manner. The energy absorbed in this way, as in progressive crushing, would be larger than the energy absorbed in a catastrophic mode. This is essential in the design of specific automobiles, rail cars and aircraft components, where in the event of a crash, the crashworthy structure can absorb the impact energy in a controlled manner before the energy gets transmitted into the passenger compartment. Although metals have traditionally been used for crashworthy structural applications, due to their plastic deformation characteristics, other materials are now been used. By increasing the plastic deformation capacity of brittle polymers for example, some polymer composite materials with higher energy absorption capacity than metals are also used in crashworthy applications (Ramakrishna and Hamada, 1998).

Calcite-polymer composites could also be used in the development of light impact-resistant materials for military or special forces applications (protective clothing, shields, helmets, etc) where hardness, strength and weight are of critical importance (Saint-Gobain, 2012).

For lightweight applications, such as in the automotive or aerospace industries, some of the components would be replaced by composites with higher specific mechanical properties (strength, hardness, modulus and energy absorption capacity) (Sun, L. *et al.*, 2009).

2.8 Mechanical properties and reinforcement of ceramic matrix composites

The mechanical properties of a ceramic composite material depend on many geometrical parameters such as the volume fraction, shape, dimensions and orientation of the second phase (particulate, platelet or fibre). In addition to these geometrical factors, others are also important in determining the fracture mechanisms of composites (Kelly and Zweben, 2000):

- Relative magnitudes of thermal expansion coefficients between matrix and reinforcement
- Mechanical properties of constituents (elasticity, hardness, toughness etc)
- Interface properties
- Phase continuity

Adding whiskers, fibres, or particles to a ceramic matrix can lead to tougher ceramic materials. This happens because the introduction of reinforcement materials (whiskers, fibres, or particles) introduces energy-dissipating mechanisms such as debonding at the fibre or particle/matrix interface, crack deflection, crack bridging, etc (Barry, 2007, Warren, 1992 and Chawla, 2003).

2.8.1 Crack deflection

If the crack is deflected from its straight path, the crack surface area becomes larger for the same advanced distance. The propagation of the crack will require thus additional energy and will increase the fracture toughness. One possible way to achieve deflection is by adding particles. The stress available to propagate the crack can be reduced if the particles have a larger Young's modulus than the matrix. With such particles the matrix will be

partly unloaded at the proximity of the particles and the crack will be deflected from the particle (Rösler *et al.*, 2007) (Figure 2.9).

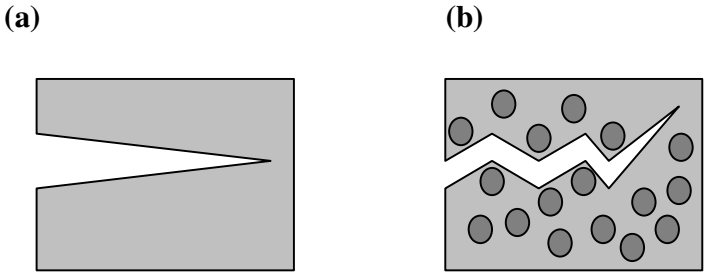

Figure 2.9 (a) Crack not deflected; (b) Deflection of a crack by appropriate particles in a ceramic matrix (adapted from Rösler, 2007).

The crack can also be deflected toward the particle if the Young's modulus of the particles is smaller than that of the matrix. If the crack cannot penetrate the particle, the crack will advance along its boundary thereby increasing its path (Rösler *et al.*, 2007).

2.8.2 Crack bridging

Adding ductile fibres or particles to a ceramic matrix can create another energy-dissipating mechanism called crack bridging. This occurs when a crack penetrating a ductile particle has to do additional work to deform it (Figure 2.10). It is therefore reasonable to utilise particles that deflect the crack toward them by using particles with a smaller Young's modulus (Rösler *et al.*, 2007).

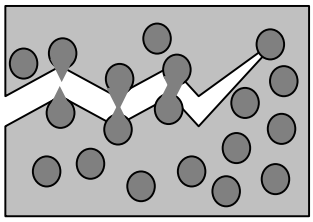

Figure 2.10 Hampering crack propagation by ductile particles (adapted from Rösler, 2007).

This toughening mechanism has the main disadvantage that the ceramic cannot be used at high temperatures: the particulate phase may lose its properties at high temperatures.

2.8.3 Material models

In this thesis, two material models that estimate the elastic modulus and hardness of particulate filled composites will be used for comparison purposes. In order to predict the mechanical properties of spherical particulate filled composites several models have been proposed in the scientific literature. The Mori-Tanaka model (Mori and Tanaka, 1973; Larson and Palazotto, 2009) can be used to predict the elastic modulus of composites occluded with spherical particles, based on the volume fractions and individual properties of the constituents. According to this model, the effective bulk modulus K_f and the effective shear modulus G_f of the composite can be expressed by

$$\frac{K_f - K_p}{K_m - K_p} = \frac{V_m \psi_1}{(1 - V_m) + V_m \psi_1} \tag{2.1}$$

$$\frac{G_f - G_p}{G_m - G_p} = \frac{V_m \psi_2}{(1 - V_m) + V_m \psi_2} \tag{2.2}$$

where K_p and G_p are the bulk and shear modulus of the particulate phase and K_m, G_m the bulk and shear modulus of the matrix respectively. V_m is the volume fraction of the matrix and the parameters ψ_1 and ψ_2 are expressed by

$$\psi_1 = \frac{K_p + \frac{4G_p}{3}}{K_m + \frac{4G_p}{3}} \tag{2.3}$$

$$\psi_2 = \frac{G_p + f_1}{G_m + f_1} \tag{2.4}$$

where f_1 is expressed by

$$f_1 = \frac{G_p(9K_p + 8G_p)}{6(K_p + 2G_p)} \tag{2.5}$$

From Equations 2.1 and 2.2, the effective elastic modulus of the composite, E_f, can be expressed by

$$E_f = \frac{9K_f G_f}{3K_f + G_f} \tag{2.6}$$

The indentation hardness of a composite occluded with spherical particles was also successfully modelled by Miyata and Jinno (Miyata and Jinno, 1982). By assuming a particle size much smaller than the scale of deformation produced by the indentation, these authors predicted the hardness of a two-phase lead-borate glass system. For soft spherical particles occluded in a hard matrix the hardness can be modelled according to

$$\frac{H}{H_m} = 1 + V_p\left[\frac{G_m}{G_p - G_m} + \frac{6(K_m + 2G_m)(1 - V_p)}{5(3K_m + 4G_m)}\right]^{-1} \tag{2.7}$$

where K_m and G_m are the bulk and shear modulus of the matrix and G_p the shear modulus of the particulate phase. H_m is the hardness of the matrix and V_p is the volume fraction of the particulate phase.

2.9 Influence of microstructural parameters on the mechanical properties of CMCs

The mechanical properties of CMCs are not always consistent with material models, variations in the microstructure due to the composite fabrication process can also have a significant effect on the measured mechanical properties. The most important parameters to consider are the reinforcement particle size, shape and orientation, matrix-filler interface, porosity, matrix grain morphology, matrix grain size and properties of grain boundaries (Warren, 1992). Some experiments, for example, showed a linear increase in hardness with increasing particle size for silica glass matrix reinforced with harder alumina particles (Stryjak and McMillan, 1978). These particular reports were however not clear in differentiating the particle size effect from the rule of mixtures. Particle size effects are not always observed to have a major influence on the measured mechanical properties. Experiments with glass matrices reinforced with softer glass spherical particles showed that the hardness and elastic properties varied with the volume fraction of the dispersed phase and not with the particle size and spacing (Miyata and Jinno, 1982).

For CMCs, toughness generally increases as the dimensions of the occluded filler increase. For the strength, the opposite effect is generally observed. Due to greater crack deflection/bridging capacity of larger particles, these can contribute more to toughening than small particles. Strengths are typically determined by smaller flaws that provide fewer opportunities for such toughening effects as crack bridging with larger cracks. Ceramic matrix composites will therefore generally show increased toughness with larger particles, while such larger particles are often the origin of fracture that control normal strength behavior (Rice, 2000).

When a single crystal fractures, a particular plane of separation is preferred. In a disoriented aggregate of many crystals the preferred fracture plane must change its direction at most grain boundaries. As the area of the fracture surface is increased by all these changes in the direction of the crack, more surface energy is required to fracture the materials compared to a single crystal. More than often, since a change in direction is required, the larger will be the resistance to fracture under a given stress. Hence, the smaller the grain size the larger should be the compressive strength of the material. Porosity can also have a marked effect

on the mechanical properties of CMCs. Pores produce stress concentrations which cause a strength reduction. For Vuggy Oolitic limestones Moh'd (2009) found that the reduction in compressive strength according to pore fraction could be expressed according to the equation

$$\sigma = 225.4e^{-0.0834V} \quad (2.8)$$

where σ is the compressive strength and V is the total porosity (%) of the tested specimen. Experiments showed that the addition of a plastic filler (PMMA) to a 12 % porous concrete increased its compressive strength from 36 MPa to 155 MPa and its modulus from 24 GPa to 43 GPa. It was suggested that apart from filling up the voids, the PMMA also improved the bonding between the interfaces (Auskern and Horn, 1971; Wainwright, 1976).

2.10 Introduction to Nanoindentation

The choice of a testing method to measure the mechanical properties of a material must take into account a few factors such as size, shape or weight of the test sample. The characteristics of some typical testing machines may prevent the testing of very large or very small samples. The determination of mechanical properties such as hardness or elastic modulus of small volumes is most frequently carried out using nanoindentation. Nanoindentation as a technique has its origins at the end of the nineteenth century, when a device which allowed the simultaneous measurement of indentation force and depth was presented by Martens (Martens, 1898; Lucca *et al.,* 2010). In the second half of the twentieth century instruments which measured load and indentation depth started to be utilised in several countries (Tabor, 1948; Grodzinski, 1952; Ternovskij *et al.*; 1973, Kinosita *et al*., 1972; Frohlich *et al*., 1975; Lucca, 2010).

In the 1990s improvements in the methods and instrumentation for extracting mechanical properties from the test allowed significant progress towards establishing nanoindentation as very important tool (Oliver and Pharr, 1992; Field and Swain, 1993). Since that time, nanoindentation has been successfully implemented in experimental work to investigate the

mechanical behaviour of a wide range of materials; namely polymers (Kermouche *et al.*, 2008), metallic films (Beegan *et al.*, 2005), ceramics (Zügner *et al.*, 2006), biological materials (Li, X. and Nardi, 2004; Bruet *et al.*, 2005) and organic-inorganic composite materials (Koch *et al.*, 2007).

Nanoindentation, also known as depth sensing indentation or instrumented indentation testing (IIT), has been developed to overcome some limitations of traditional indentation testing. In a traditional indentation testing an indenter of a given geometry and material type, such as a sphere (Brinell and Rockwell test), a cone (Rockwell test), or a pyramid (Vicker and Knoop tests) made of steel or diamond, is pushed into a material. Upon unloading, the residual indent impression left in the surface of the tested material is measured with an optical microscope. The hardness value is usually defined as the ratio of the indentation load and the projected area of residual indents (Fischer-Cripps, 2002).

An advantage of nanoindentation over the conventional indentation or hardness testing is that the contact area of the residual indent impression can be directly obtained from the load-penetration depth curve without measuring the indent. This feature makes nanoindentation particularly suitable for measuring the mechanical properties of materials indented at the nanoscale where precise determination of the contact area would be very difficult using standard optical techniques. Another advantage of nanoindentation over conventional indentation testing is the ability to measure the elastic, as well as the plastic properties of the test sample (Bhushan and Marti, 2007).

The Berkovich indenter is generally used in small-scale indentation studies and has the advantage that the edges of the pyramid are more easily constructed to meet at a single point. The Berkovich tip has a radius on the order of 50-100 nm and its face angle of 65.3º gives the same surface area to depth ratio as the Vickers indenter (which is a four-sided pyramid). The Berkovich indenter also produces plasticity at very low loads and is less affected by friction (Fischer-Cripps, 2002).

2.11 Continuous Stiffness Measurements

Important improvements to nanoindentation testing have also been facilitated by the introduction of specific techniques and calibration procedures. One of the most important of these is the continuous stiffness measurement (CSM) technique (Oliver and Pharr, 2004). CSM allows stiffness to be measured continuously during the loading of the indenter by imposing a small dynamic oscillation on the force (or displacement) signal and measuring the corresponding displacement (or force) signal with a frequency-specific amplifier (Oliver and Pharr, 1992; Lucas *et al.*, 1998; Oliver and Pharr, 2004). The amplitude of the force oscillation is kept sufficiently small that the deformation process is not significantly affected by its addition.

The phase difference between the force signal and the displacement signal can also be monitored (Oliver and Pharr, 1992). The stiffness of the contact between the indenter and the test material can be described by a dynamic model (Figure 2.11), which considers the response of the entire system.

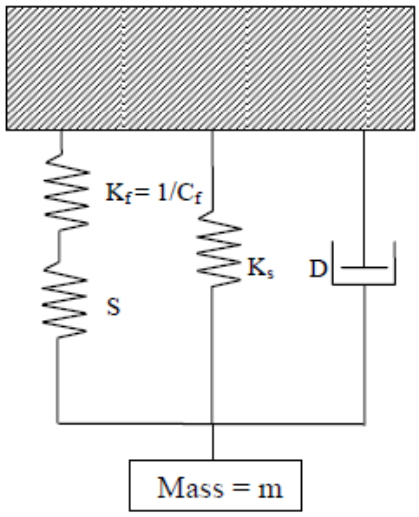

Figure 2.11 Schematic of the dynamic model for a nanoindentation measurement using CSM (Continual Stiffness Measurement). Adapted from Oliver and Pharr (1992)

Analysing of the model reveals that the stiffness of the contact can be determined by calculating the amplitude of the displacement signal using the equation

$$\left|\frac{P_{os}}{h(\omega)}\right| = \sqrt{\left[\left\{\left(S^{-1} + C_f\right)^{-1} + K_s - m\omega^2\right\}^2 + \omega^2 D^2\right]} \qquad (2.9)$$

The contact stiffness can also be determined from the phase difference between the force and the displacement signals according to the equation (Oliver and Pharr, 1992)

$$\tan(\phi) = \frac{\omega D}{\left(S^{-1} + C_f\right)^{-1} + K_s - m\omega^2} \qquad (2.10)$$

where

C_f = the compliance of the load frame (~1.13 m/MN)

K_s = the stiffness of the column support springs (~ 60 N/m)

D = the damping coefficient (~ 54 N s/m)

P_{os} = the magnitude of the force of oscillation

$h(\omega)$ = the magnitude of the resulting displacement oscillation

ω = frequency of the oscillation (69.3 Hz)

Φ = the phase angle between the force and displacement signals

m = mass

The constants K_s and D can be determined experimentally by examining the motion of the nanoindentation system according to the model in Figure 2.11 when the indenter is not touching the material surface. The dynamic model can be simplified to the one shown in Figure 2.12 by defining a reduced spring constant according to the equation

$$K = \left(S^{-1} + C_f\right)^{-1} + K_s \qquad (2.11)$$

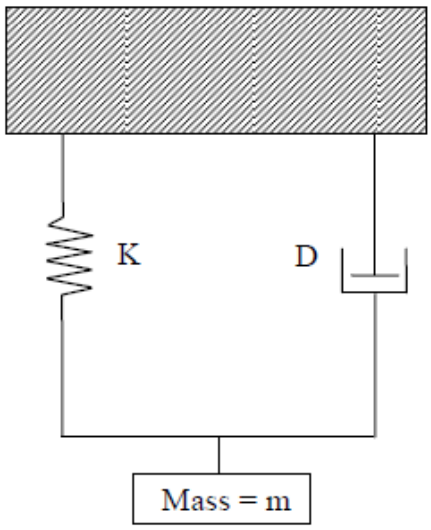

Figure 2.12 A simplified dynamic model used for Continual Stiffness measurements (CSM). Adapted from Oliver and Pharr (1992)

The CSM technique reduces reliance on unloading curves and offers several advantages over testing where stiffness measurements are taken solely from the unloading curve:

1. The CSM technique provides continuous results as a function of depth.
2. The time required for calibration and testing procedures with the CSM method is considerably reduced because there is no need for multiple indentations or unloadings.
3. At high frequencies, the CSM technique avoids some negative effects of time-dependent plasticity and thermal drift.
4. By monitoring the change in stiffness, the CSM technique allows the point of initial contact between the indenter and the sample to be precisely identified.

The CSM technique has also been used to calibrate the nanoindenter machine compliance and indenter area function (Oliver and Pharr, 2004) without the need to image the indentations. The calibration procedure is based on the indentation of fused silica. Among the most important reasons for the choice of this material are: it does not pile-up, it is elastically isotropic, its modulus is known and independent of indentation depth. During continuous stiffness measurement several parameters can be controlled and measured. These include the harmonic load (the amplitude of the oscillation in the load signal), the harmonic displacement (the amplitude of the oscillation in the displacement signal), the harmonic frequency (the frequency of the oscillation) and the harmonic stiffness (which is derived from the other quantities).

2.12 The Oliver-Pharr Method

The two mechanical properties measured most frequently using load and depth sensing indentation techniques are the elastic modulus, *E,* and the hardness, *H.* In the Oliver-Pharr method (Oliver and Pharr, 1992), data are obtained from one complete cycle of loading and unloading. This method assumes that deformation of the material during loading is both elastic and plastic. During unloading it is assumed that only the elastic displacement is recovered. Since the method is based on the elastic nature of the unloading curve it is not considered suitable for materials in which plasticity reverses (i.e. non-elastic recovery).

Since the method was first introduced, finite element simulations have shown, however, that in many materials reversible plastic deformation is negligible (Pharr and Bolshakov, 2002). Four important parameters are measured from the load-displacement curves (Figure 2.13); namely the maximum load, P_{max}, the maximum displacement, h_{max}, the final depth, h_f, and the elastic unloading stiffness, S = dP/dh, which is defined as the slope of the upper portion of the unloading curve. These four parameters are then used to determine the hardness and elastic modulus.

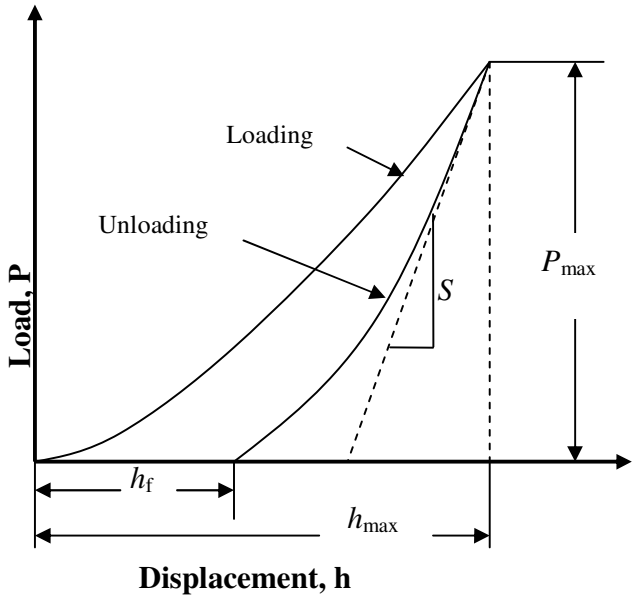

Figure 2.13 Schematic representation of load versus indenter displacement data for a typical nanoindentation experiment. The quantities shown are P_{max}: the peak indentation load, h_{max}: the indenter displacement at peak load, hf: the final depth of the contact impression after unloading and S, the initial unloading stiffness (Reproduced from Oliver, W. C. and Pharr, G. M. 2004).

To determine the hardness, H, and elastic modulus, E, the Oliver-Pharr method uses the same model utilised by Doerner and Nix (1986), but introduces some correction to determine the stiffness from the unloading curve. The Doerner and Nix model is based on the observation that during the initial stages of unloading the elastic behaviour of the indentation contact can be approximated to that of a flat punch. In the flat punch approximation the contact area remains constant as the indenter is withdrawn from the material, and the resulting unloading curve is linear. Oliver and Pharr (1992) used the Doerner and Nix model in some experiments and observed that by using a Berkovich tip the unloading curves are indeed curved and cannot be accounted for by the flat punch approximation. Oliver and Pharr found that unloading curves can be better described by the following power law equation

$$P = A\left(h - h_f\right)^m \tag{2.12}$$

where A is a power law fitting constant (contains geometric constants, the sample elastic modulus, the sample Poisson's ratio, the indenter elastic modulus, and the indenter

Poisson's ratio), h_f is the final unloading depth, and m is a power law exponent that is related to the geometry of the indenter (Oliver and Pharr, 1992, 2004; VanLandingham, 2003). The elastic unloading stiffness can therefore be established by evaluating the derivative of Equation 2.12 at peak load-displacement using the following relation

$$S = A_m \left(h_{\max} - h_f\right)^{m-1} \tag{2.13}$$

Once the unloading stiffness is known, the elastic modulus can be calculated from the reduced elastic modulus, E_r, to take into account the fact that at this size scale, the elastic response of the probe tip, E_i, as well as the elastic modulus of the test material, E, must be considered (Oliver and Pharr, 1992) (Equation 2.14):

$$S = 2\beta E_r \sqrt{\left(\frac{A}{\pi}\right)} \tag{2.14}$$

where β is a constant that depends on the geometry of the indenter; for a Berkovich type indenter, $\beta = 1.034$. E_r is the reduced elastic modulus and is defined by the equation

$$\frac{1}{E_r} = \frac{\left(1 - v^2\right)}{E} + \frac{\left(1 - v_i^2\right)}{E_i} \tag{2.15}$$

where ν and ν_i are Poisson's ratios for the test material and the indenter material respectively. For diamond, which is typically the Berkovich tip indenter material, $E_i = 1141$ GPa and $\nu_i = 0.07$. The Oliver-Pharr (1992) procedure is based on the assumption that the behavior of a conical indenter gives a better description of the elastic unloading of an indentation made with a Berkovich indenter than the flat punch approximation. Like the Berkovich indenter, the conical indenter cross-sectional area varies as the square of the depth of contact and its geometry is singular at the tip. For both geometries, the load-displacement relationships are nonlinear and the contact area changes continuously during unloading. An important assumption in the Oliver-Pharr (2004) procedure is that the indented area sinks in a manner that can be described by models for indentation of a flat

elastic halfspace by rigid punches of simple geometry. This assumption limits the applicability of the method because it does not take into account the pile-up of material at the periphery of the indenter that occurs in some elastic–plastic materials. Figure 2.14 illustrates the unloading process schematically showing the parameters that characterise the contact geometry.

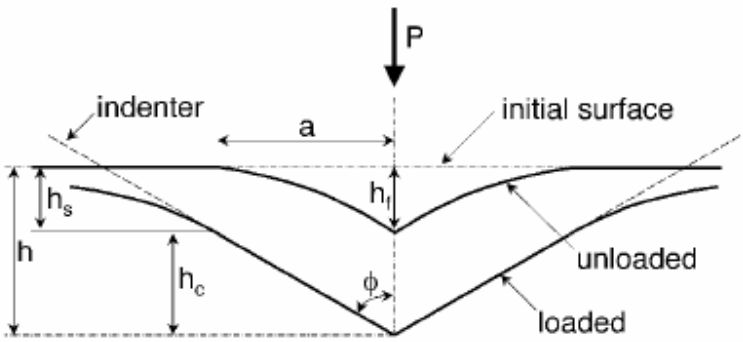

Figure 2.14 Schematic diagram of unloading process (Oliver and Pharr, 2004)

Assuming that pile-up is negligible, the amount of sink-in, h_s, is given by equation (Oliver and Pharr, 1992; Mann, 2005)

$$h_s = \varepsilon\left(\frac{P_{\max}}{S}\right) \tag{2.16}$$

where ε is a constant that depends on the geometry of the indenter (ε = 0.75 is standard value). Referring to Figure 2.14, the depth along which contact is made between the indenter and the specimen, $h_c = h_{max} - h_{s,}$ is given by equation

$$h_c = h_{\max} - \varepsilon\left(\frac{P_{\max}}{S}\right) \tag{2.17}$$

where h_c = contact depth. F (d), the indenter shape function or area function is then used to describe the projected (or cross-sectional) area of the indenter at a distance d back from its tip. The contact area, A, is then expressed as

$$A = F(h_c) \tag{2.18}$$

The indenter shape function must be carefully calibrated by independent measurements so that any deviations from nonideal indenter geometry are taken into consideration. These deviations can be very large near the tip of the Berkovich indenter, where some rounding occurs due to the grinding during the tests. Once the contact area has been determined from the load–displacement curve, the hardness can be determined by the equation

$$H = \frac{P_{\max}}{A} \tag{2.19}$$

where $P_{\max}$ is the peak load and A is the projected contact area at peak load. By using large indents in aluminium, Oliver and Pharr (1992) determined that the area function for a perfect Berkovich indenter can be given by Equation 2.20:

$$A(h_c) = 24.5h_c^2 \tag{2.20}$$

Thus, for a perfect Berkovich indenter, the hardness can be estimated by Equation 2.21:

$$H = \frac{P_{\max}}{24.5h_c^2} \tag{2.21}$$

This definition of hardness is based on the contact area under load and may be different from the more conventional hardness, in which the area is determined from direct measurement of the residual hardness impression. This difference is due to the fact that in some materials with large elastic recovery the area of the residual impression may be less than the one measured at peak load. Finite element simulation has shown that this is only significant in materials with extremely small values of E/H (Bolshakov and Pharr, 1998). The Oliver-Pharr method has been found to be acceptable for various materials including aluminium, quartz, soda lime glass, sapphire, tungsten and fused silica (Oliver and Pharr,

1992). For glasslike material, E/H = 12.0, whereas for the aluminum-like material E/H = 117.5. Experimental data showed that E/H is rarely less than 10 or more than 150 for a wide variety of metals, ceramics, and polymers. Thus, the glass-like material is on the low end of the E/H spectrum while aluminum-like material is near the high end (Bolshakov and Pharr, 1998).

2.13 Limitations of the Oliver-Pharr Method: Pile-up and sink-in

2.13.1 Pile-up

A significant problem with the Oliver-Pharr method is that it is based on elastic contact relationships, and does not account for pile-up of material around the contact impression, as is observed in many elastic-plastic materials. When pile-up occurs (Figure 2.15) the contact area is greater than that predicted by the method and both the hardness and modulus can be overestimated by up to 50 % (Oliver and Pharr, 2004).

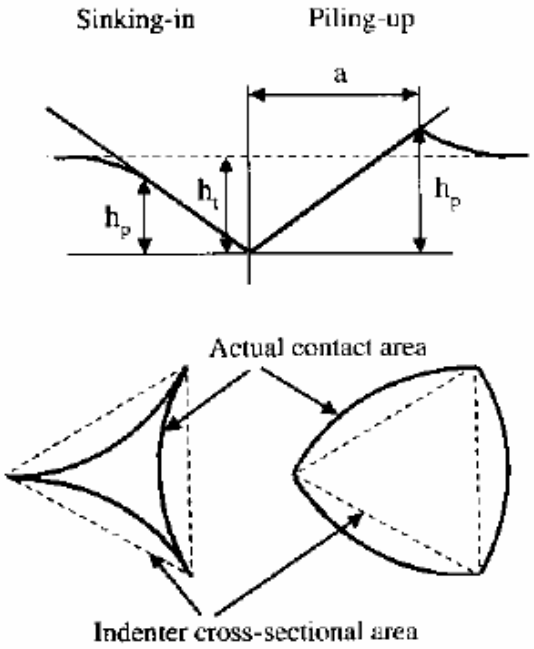

Figure 2.15 Effect of piling-up and sinking-in on contact area for penetrations of depth, h_t where h_p = contact depth (Fischer-Cripps, 2002).

The most important material properties affecting pile-up are the ratio of the effective modulus to yield stress, E_{eff}/σ_y, and the work-hardening behaviour of the material. In general, pile-up is greatest in materials with a large E_{eff}/σ_y and in materials which undergo little or no work hardening (i.e., "soft" metals that have been cold-worked prior to indentation). The ability to work harden inhibits pile-up because as material at the surface adjacent to the indenter hardens during deformation, it constrains the upward flow of material to the surface. Therefore, due to inaccuracies in the predicted contact area, the Oliver-Pharr method works best for materials such as hard ceramics where mainly small sink-in occurs (Fischer-Cripps, 2002; Oliver and Pharr, 2004).

2.13.2 Sink-in

Since nanoindentation can assess the mechanical properties of very small regions, it is a suitable means for measuring the mechanical properties of small particles or thin films. However, there are some inherent problems in using nanoindentation to examine the properties of thin films. In the case of a hard film on a soft substrate there is the tendency for the material around the indenter to sink-in. the greater the mismatch in hardness, the greater the likelihood of excessive sink-in. Although the Oliver-Pharr method, used in determining the contact depth and contact area from experimental data, predicts some degree of sink-in, it doesn't work well for excessive sink-in (Hay, J. C. and Pharr, 1997; Hay, J., 2009).

These situations are most likely to occur when testing hard films on soft substrates where the mismatch in hardness between the substrate and film can become very large. The result is that the Oliver-Pharr method of determining the contact depth overestimates the effective contact depth and the actual contact area. Therefore, when the contact area is overestimated, the hardness is underestimated by a factor of similar scale, and the Young's modulus is underestimated by a factor which scales as the square root of the error in contact area (Hay, J. C. and Pharr, 1997). For hard films on soft substrates, the hardness and modulus will tend to approach the film properties for shallow depths. With increasing penetration depth the measured hardness and modulus will approach the values of the substrate (Figure 2.16).

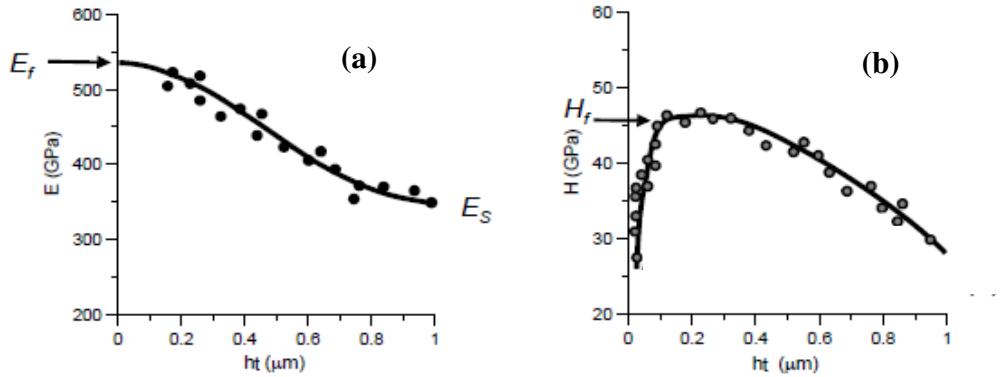

Figure 2.16 Effect of substrate indentation depth on a) the modulus and b) hardness (adapted from Fischer-Cripps, 2009) .

To determine the mechanical properties of thin films, substrate effects must be avoided. When faced with excessive sink-in, there are some limited choices (Miyake *et al.*, 2004; Fischer-Cripps, 2009; Hay, J., 2009):

1. Decide that the error is acceptable

2. Measure the contact area directly using some form of microscopy, and use the ratio force/area to calculate the hardness directly without using the Oliver-Pharr model.

3. Derive the thin films properties from the composite properties of the films and substrate system using analytic or computational modelling.

4. Make a shallow indentation so that the substrate effects can be neglected. This requires knowledge of the critical penetration depth beyond which the influence of substrate becomes significant.

According to the UK National Physical Laboratory's recommendations (Peggs and Leigh, 1983), the indentation depth should not exceed a tenth of the thickness of the region of the specimen that is being tested. That is also Bückle's one-tenth rule for the critical ratio of depth to thickness, at which the contribution of the substrate is negligible (Bückle, 1973). Numerical simulations have demonstrated, however, that this 10 % "rule-of-thumb" is not

stringent enough for a hard film on a soft substrate, where the influence of the substrate starts at 7 % of the film thickness (Cai and Bangert, 1995; Li, X and Bhushan, 2003).

2.14 Measuring substrate independent modulus of thin films using analytical models

In order to calculate the film modulus from the substrate-affected modulus, several models have been proposed. The first model (Doerner and Nix, 1986) assumed a linear transition from film to substrate, and introduced a constant that had to be obtained empirically. Gao *et al*., (1992) proposed a simple approximate model with no adjustable parameters. To govern the transition in elastic properties from film to substrate they derived two functions, I_0 and I_1. Song and colleagues (Rar *et al.*, 2002; Xu, H. and Pharr, 2006) produced a simpler model that predicts the composite response better if the film is more compliant than the substrate. This model is called the "Song–Pharr model" in the literature. The Song–Pharr model is illustrated schematically in Figure 2.17. This model is based on the assumption that a column of material under the indenter, defined by the contact radius, can be separated from the surrounding material and modelled as two springs in series, with the contribution of each spring weighted according to a/t (tip radius/film thickness ratio) by the function I_0.

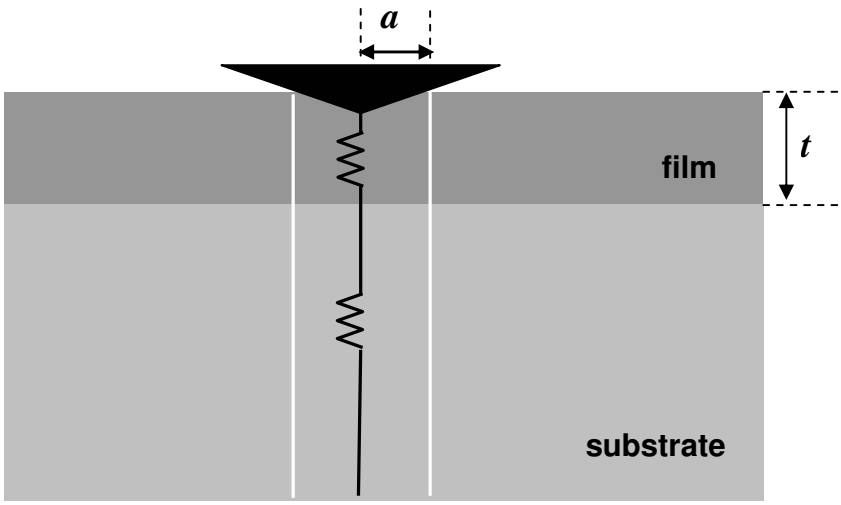

Figure 2.17 Schematic of the Song–Pharr model, which assumes that material under the indenter can be separated from the surrounding material and modeled as two springs in series (adapted from Hay and Crawford, 2010).

The measured (or apparent) shear modulus, μ_a, is related to the shear modulus of the film, μ_s, and that of the substrate, μ_f, by

$$\frac{1}{\mu_a} = \frac{(1-I_0)}{\mu_s} + \frac{I_0}{\mu_f} \tag{2.22}$$

The weighting function, I_0, provides a smooth transition from film to substrate and is expressed by (Gao *et al.*, 1992)

$$I_0 = \frac{2}{\pi}\arctan\left(\frac{t}{a}\right) + \frac{1}{2\pi(1-v_a)}\left[(1-v_a)\frac{t}{a}\ln\left(\frac{1+\left(\frac{t}{a}\right)^2}{\left(\frac{t}{a}\right)^2}\right) - \frac{\frac{t}{a}}{1+\left(\frac{t}{a}\right)^2}\right] \tag{2.23}$$

where t is the film thickness, a is the contact radius, and v_a is the apparent Poisson's ratio. The Song–Pharr approach includes a simplification, which separates the effect of transition in bulk modulus from the relatively minor effect of transition in Poisson's ratio. The simplified form of Equation 2.22 is achieved by assuming that a single apparent Poisson's ratio, v_a, can be used to represent the behaviour of the entire column of the material. The expression for this apparent value is

$$v_a = 1 - \left[\frac{(1-v_s)(1-v_f)}{1-(1-I_1)v_f - I_1 v_s}\right] \tag{2.24}$$

In this expression for v_a, the weighting function, I_1, is expressed by the equation (Gao *et al.*, 1992):

$$I_1 = \left(\frac{2}{\pi}\right)\arctan\left(\frac{t}{a}\right) + \frac{\frac{t}{a}}{\pi}\ln\left(\frac{1+\left(\frac{t}{a}\right)^2}{\left(\frac{t}{a}\right)^2}\right) \tag{2.25}$$

The Young's modulus of the film is calculated from the film shear modulus and Poisson's ratio as (Hay, J. and Crawford, 2010)

$$E_f = 2\mu_f\left(1+\nu_f\right) \tag{2.26}$$

The apparent shear modulus, μ_a, is calculated by using the equation

$$\mu_a = \frac{E_a}{2\left(1+\nu_a\right)} \tag{2.27}$$

The apparent Young's modulus, E_a, is calculated from the apparent reduced modulus, E_{ra}, as

$$E_a = \frac{\left(1-\nu_a^2\right)}{\frac{1}{E_{ra}} - \frac{\left(1-\nu_i^2\right)}{E_i}} \tag{2.28}$$

where E_i and ν_i represent the properties of the indenter material - for the case of a diamond Berkovich indenter E_i = 1140 GPa and ν_i = 0.07. The apparent reduced modulus is calculated using the equation:

$$E_{ra} = \frac{\sqrt{\pi}S}{2\sqrt{A}} \tag{2.29}$$

where A and S are the projected normal contact area and contact stiffness, respectively (Hay, J. and Crawford, 2010). The Song–Pharr model (Rar *et al.*, 2002) is based on

experiments using a Berkovich tip, assuming that the results obtained can be modelled by a conical indenter with an equivalent area function. The effective contact radius, a, is calculated from nanoindentation measurements of the contact area, A, using the equation

$$a = \sqrt{\left(\frac{A}{\pi}\right)} \tag{2.30}$$

The Song–Pharr model is supposed to work well for compliant films on stiff substrates when $E_f < E_s$ and a/t <1. Although its applicability to stiff particles/compliant substrate systems has still not been fully studied, the Song–Pharr model will be used in this work in order to obtain the substrate independent modulus of calcite-polymer composites.

2.15 Measuring substrate independent hardness by conventional methods

When the Oliver-Pharr model is unable to give satisfactory results due to excessive sink-in, the hardness can still be measured by conventional methods. The indentation hardness of a material, H, is conventionally defined as a mean pressure, i.e., the maximum normal load, P_{max}, divided by contact area, A_c, according to the equation

$$H = \frac{P_{max}}{A_c} \tag{2.31}$$

Equation 2.31 indicates that in order to obtain an accurate hardness it is important to precisely determine the contact area. In the case of conventional indentation, the contact area is determined by direct measurement of the area of the residual impression left by the Berkovich pyramidal tip (Figure 2.18).

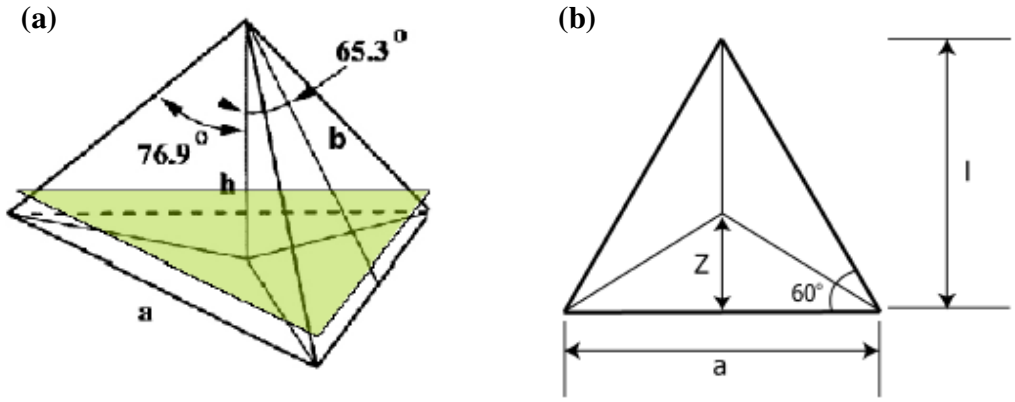

Figure 2.18 Schematic of a three sided Berkovich tip a) three-dimensional view and b) plan view (Fischer-Cripps, 2002; Kim, D. K., 2011).

For an indentation with a Berkovich tip, the contact area, A_c, is given by (Miyake *et al.*, 2004):

$$A_c = \frac{l^2}{\sqrt{3}\sin\alpha} \qquad (2.32)$$

where α is the apical angle (the angle between a face and the central axis, see Figure 2.18) of a Berkovich tip (65.3º), and l is the height of the triangular residual impression (Figure 2.15). The indentation hardness, H, is then calculated by:

$$H = \frac{P_{\max}\sqrt{3}\sin\alpha}{l^2} \qquad (2.33)$$

It should be noted that equation 2.33 assumes that the size of the observed residual indentation impression is the same as that of the projected area under maximum load. Obviously the size of the indentation at full load can be larger than the residual impression when the load is removed due to elastic recovery of the material tested. By AFM direct measurements of the indent residual impression Miyake *et al.*, (2004) found that the hardness of the glass BK7, fused silica and silicon could be accurately calculated by using Equation 2.30. The authors used however a indenter tip with an apical angle of 21.6º which

is much sharper than the usual Berkovich tip (65º) and used materials with an elastic modulus > 72 GPa.

2.16 Indentation size effects in hardness testing

The hardness of a material is not a unique property but is a measure of the reaction of the material to the type of the disturbing force imposed. Hardness is therefore a function of the test method and on the measuring process, which can impose a different pattern of stress on the sample for different load ranges (McColm, 1990). The indentation size effect (ISE), whereby the hardness of a material usually decreases with increasing applied load, i.e., with increasing indentation size, has been observed in a variety of materials. ISE has been attributed to a number of phenomena/mechanisms, including: elastic resistance, dislocation band spacing, indentation edges acting as a plastic hinge, dislocations for nanoindentations on metallic materials, work hardening during indentation, load to initiate plastic deformation or the effect of machining-induced residual stresses on the surface of a hardness measurement (Ren *et al.*, 2003). Several other mechanisms have been proposed; these include the influence of harder surface layers, a dependence of flow strength on gradients of plastic flow or the formation of micro-cracks under the indenter (Poole *et al.*, 1996). Investigations have also shown a dependence of hardness on grain size when grains are very large compared with indent size according to the equation

$$H = \frac{K}{\sqrt{d}} \qquad (2.34)$$

where K is a constant and d is the grain diameter. It should be noted that equation 2.34 has been observed to work for metallic systems (McColm, 1990). In a ceramic such as MgO, when indents are made at approximately the same size as the grain size, the material hardens as the grain size increases. This different mechanical behaviour can be explained by the contrast between ionic bond strength and grain-boundary cohesive forces compared to the similarity between weak metallic bonds and metal grain-boundary forces. Other models such as the Meyer's model (Tabor, 1951), the Hays-Kendall model (Hays and Kendall, 1973), the elastic recovery model (Tarkanian *et al.*, 1973), the proportional

specimen resistance model (Li, H. and Bradt, 1993), etc., have been proposed for describing the indentation size effect. Peng *et al*., (2004) assessed the applicability of some of these models in analyzing the ISE in the nanoindentation region. By using a Berkovich tip, in the peak load range between 7.5 and 500 mN on soda-lime glass, polycrystalline tetragonal ZrO_2 and a hot-pressed Si_3N_4, these authors concluded that Meyer's law was the only model that provided a satisfactory description for the experimental data for each tested material. In these experiments, the Hay–Kendall approach, the proportional specimen resistance (PSR) model and the elastic recovery model, yielded meaningless values of the parameters included in the corresponding equations, invalidating the applicability of these models in analyzing the ISE in the nanoindentation region (Peng *et al.*, 2004). It should be noted that although Meyer's law could provide a satisfactory description for the experimental data for each material, it cannot provide any knowledge of the real origin of ISE.

In ceramic single crystals, cracks and dislocations are energy absorption mechanisms that emerge in order to accommodate the strain imposed by the indenter. If the indentation load is too low the hardness can be dominated by the ease with which dislocations can move in the near surface region. Hence the nature of the surface will appear to be dominant in setting a hardness value for the material. A load too large in order to overcome or minimize the sample surface factors can produce cracks around the indenter. The presence of cracks associated with an indent can result in a lower hardness value for the material as indentation pressure is deflected into crack nucleation and propagation mechanisms (McColm, 1990).

2.17 Micro-compressive testing

The determination of mechanical properties of small volumes is most frequently carried out using nanoindentation. Uniaxial micro-compression testing has also become a frequently used technique to determine the mechanical response of various materials at the small scale. Using flat punch compression, Ahuja (1977) developed a single-particle crush-test system, and measured the strength of polystyrene and polycarbonate particles between 7.5 μm and 15 μm in diameter. The diametrical compression, a technique in which a single particle is

crushed between two parallel surfaces while the load required to cause fracture is measured, was the basis of the micromanipulation technique. This technique has been used to measure the mechanical properties of single biological and non-biological particulate materials, including animal cells (Zhang, Z. *et al.*, 1992), plant cells (Thomas *et al.*, 2000), alumina powder granules 50 μm in diameter (Saito *et al.*, 2002), pharmaceutical excipients (Yap *et al.*, 2006; Yap *et al.*, 2008) polymer particles (Müller *et al.*, 2005; Ok Kim and Hee Jin, 2007) and microcapsules (Zhang, Z. *et al.*, 1999; Zhang, G. and Sun, 2001; Sun, G. and Zhang, 2002).

2.18 Mechanical properties in compression

In a compression test (Figure 2.19), an engineering stress-strain curve is constructed from load, *P*, versus displacement measurements.

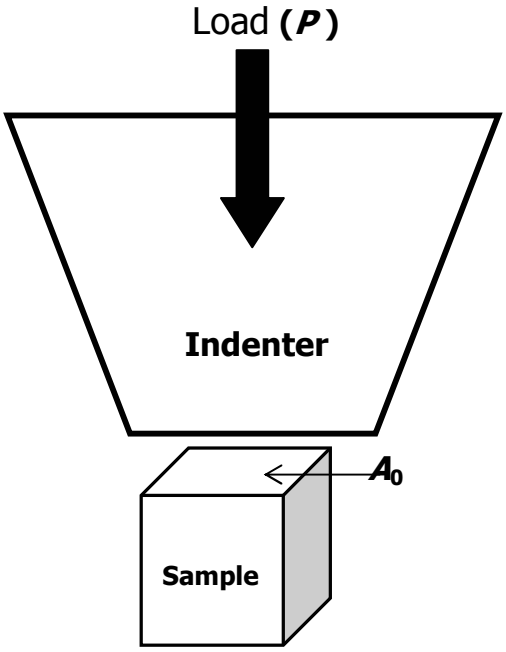

Figure 2.19 Simplified compression test.

To eliminate sample geometry effects, the load is divided by the original cross sectional area, A_0, of the sample to obtain the compressive engineering stress (σ_c)(Kuhn and Medlin, 2000; Mitchell, 2004) using the equation

$$\sigma_c = \frac{P}{A_0} \tag{2.35}$$

The compressive strain, ε_c, used for the engineering stress-strain curve is obtained by dividing the gauge length of the specimen, δ, by its original length, L_0, according to the equation

$$\varepsilon_c = \frac{\delta}{L_0} = \frac{\Delta L}{L_0} = \frac{(L - L_0)}{L_0} \tag{2.36}$$

Since both the stress and the strain are obtained by dividing the load and displacement by constant factors, the load-displacement curve has the same shape as the engineering stress-strain curve. Figure 2.20 shows the stress–strain curve for a typical compression test. Once the stress–strain curve has been generated, important mechanical properties such as the modulus of elasticity or compressive strength of a material can be obtained.

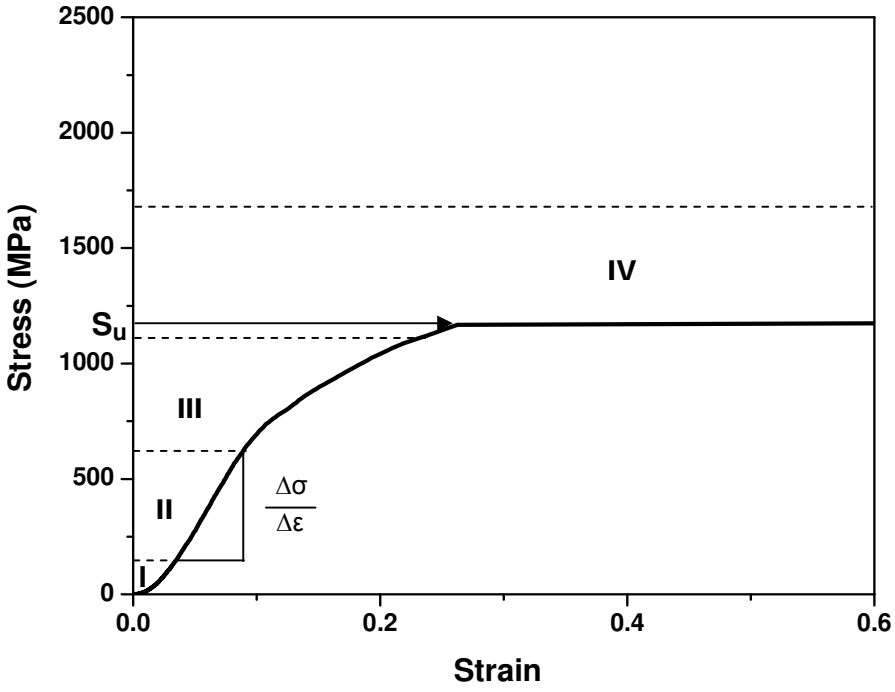

Figure 2.20 A typical stress-strain curve for a pure calcite crystal deformed in compression.

The compressive modulus of elasticity, E_c, represents the stress-strain ratio in the elastic region of Figure 2.20, and can be determined as the slope of the stress–strain curve within the linear region (Kiser *et al.*, 1999; ASTM-C1358, 2000; Ziskind *et al.*, 2010) using the equation

$$E_c = \frac{\sigma_c}{\varepsilon_c} \tag{2.37}$$

Material creep or deflection of the test machine also contribute to give inaccurate values of the modulus (Ashby *et al*., 2007). In a uniaxial compression test, the strength is referred as the uniaxial compressive strength (UCS), S_u, and is defined as the maximum compressive stress a material can sustain before final fracture. Fracture in this context can be defined as the failure process by which a structure (e.g. a specimen) disintegrates into two or more pieces (Bieniawski, 1967). The UCS is measured by dividing the maximum load, $P_{\max}$, before fracture by the original cross-sectional area of the specimen (ASTM-C1358, 2000; Zhang, H. *et al.*, 2006; Ziskind *et al.*, 2010) according to the equation

$$S_u = \frac{P_{\max}}{A_0} \tag{2.38}$$

For some engineering applications, where weight minimization is an important factor, materials are often designed on the basis of a given strength or modulus per unit weight of material. Thus materials are often compared according to the specific strength, S_u/ρ, or specific modulus, E/ρ, where ρ is the density of the material. Another important parameter for materials under compression is energy absorption. The maximum energy per volume absorbed by the material under compression is an indication of the amount of work per unit volume that can be done on the material without causing it to fracture. This energy, W, is the area under the stress-strain curve up to the point of fracture, and can be written as

$$W = \int_0^{\varepsilon} \sigma \, \mathrm{d}\varepsilon \qquad (2.39)$$

where W is the energy absorption capacity (work of fracture), ε the compressive strain, and σ the compressive stress. The energy absorption capacity or work of fracture is both a measure of a material's strength and ability to deform plastically (Motz *et al.*, 2002; Mitchell, 2004; Liu *et al.*, 2010).

2.19 Compression of calcite

The stress-strain curve of rocks such as granite or calcite marble under compression can be divided into four stages (Figure 2.20) (Brace *et al.*, 1966). The first part of a plot of stress (ordinate) against strain (abscissa) for a crystalline rock curves so as to increase the slope with increasing stress (Stage I). The initial upward curvature of the stress-strain curve in Stage I, which implies a hardening of the rock with increasing stress, is attributed to the compaction of loose grain boundaries and the closing of pre-existing cracks and pores by the applied compressive stress (Brace, 1965; Mogi, 1973; Paterson and Wong, 2005). This initial increase in the slope of the stress-strain curve can also be caused by settling down effects in the testing machine (Paterson and Wong, 2005).

The initial stress-strain curvature at low stress gradually ceases and a linear proportionality between stress and strain is gradually reached (Stage II). Since the pores in most rocks are small and the cracks flat, they are closed by a small stress. Above this stress, no change in stiffness due to crack and pore closure occurs, and the stress-strain curve is linear. This linear relation is attributed to the elastic deformation of the grains after pore and crack closure has reached a limit (Walsh, 1965). After this linear proportionality between stress and strain has been reached, the slope of the stress-strain curve starts to decrease (Stage III). This effect is associated with plastic deformation and microfracturing (Mogi, 1973). The formation and propagation of large numbers of microcracks distributed uniformly throughout the rock have their origin at microdefects and microheterogeneities such as cavities, grain boundaries or inclusions (Nemat-Nasser *et al.*, 2001). This microcrack

proliferation progressively destroys the load-bearing capacity of the rock permitting irreversible strain to occur (Hawkes and Mellor, 1970).

The propagation of microcracks in this stage is a stable process in which the cracks only extend by limited amounts in response to an increasing stress and do not develop a macroscopic fracture. The load-bearing capacity of a rock depends thus not on the largest, least-oriented, highest-stressed defect, but on the entire defect population (Paterson and Wong, 2005). In compression of a brittle or low-ductility material, the test ends when the slope of the curve approaches zero (leading to a plateau in the stress-strain curve), which indicates the structural collapse of the specimen. The fracture can occur catastrophically by shear failure along one large shear plane, leading to the complete separation of the specimen or by the progressive development of internal cracking, leading to crushing of the material (Hawkes and Mellor, 1970).

2.20 Problems with compression Testing

When testing materials it is important that the test method should give precise, reproducible and accurate results. The compression test appears easy to conduct, however it is very difficult to accurately measure compressive mechanical properties such as compressive strength. In a compression test the mechanical properties depend not only in the internal intrinsic composition and structure of the tested material but also upon the testing parameters used in the testing process. The most relevant intrinsic factors in calcite rocks includes porosity, cracks, the properties of the individual crystals (grains), the way in which the crystals are assembled, including their amounts, sizes, shapes, distributions and orientations.

The properties of a single crystal depend on its chemical composition (bond strength), lattice structure (which determines glide systems), and by lattice defects such as vacancies and dislocations. The testing parameters include specimen size and geometry, degree of isotropy, temperature, water content, contact problems, radial constraints and strain rate (Newman and Sigvaldason, 1965; Hawkes and Mellor, 1970; Donath and Fruth, 1971). Since different testing parameters can lead to different results, the testing physical

conditions must be completely specified before the material characteristics can be determined, as outlined in Sections 2.20.1-2.20.5.

2.20.1. Size-scale effects

Athough all materials have specific inherent materials properties, these can only be considered unique when they are independent of a specimen size and shape (Yi *et al.*, 2006). A mechanical size-scale effect can be defined as a change in a material's mechanical properties due to a change in either the physical dimensions of a sample or the dimensions of an internal structure. The dependence of fracture stress on size is very important because of the large difference in scale between laboratory test specimens and the materials involved in engineering practice. It is therefore necessary to consider size effects in order to compare tests on samples of different sizes.

Size dependence in ceramics has been connected to a statistical distribution in the defect magnitude at which fracture is initiated, and is also related to the scatter in strength between specimens in identical tests. Several types of size dependencies have been predicted by various weakest link theories. Some of these theories predict a fracture stress proportional to $V^{-1/\beta}$ (Weibull, 1939, 1951) or to $(\log V)^{-1/\alpha}$ (Epstein, 1948), where V is the volume (the number of defects is assumed to be proportional to the volume) and α or β are constant. The weakest link theories treat the formation of the first crack, and not the structural failure of a test specimen. Although size dependency expressions may give an indication of volume effects for direct tensile and compression tests on fine-grained and glassy materials, they apply only indirectly to final collapse of most compression specimens, in which multiple internal cracking precedes collapse (Paterson and Wong, 2005).

Brady (1969) has suggested that weakest link theories cannot be applied to fracture of rock and proposed instead a statistical theory based on the proliferation of microcracking. This author assumed that failure in rocks occurs when the volumetric strain due to microcracking reach a critical value. Studies made on plaster suggest that the fracture stress depends on the available elastic strain energy in the specimen and hence on its dimensions (Glucklich and Cohen, 1967; Einstein *et al.*, 1970). The experimental observations of size dependence in brittle rocks have been made primarily in uniaxial compression or in

Brazilian tests. In general, they show a decrease in fracture stress as the dimensions of the specimen is increased (Bieniawski, 1968; Herget and Unrug, 1976; Heuze, 1980; Dey and Halleck, 1981). Hoek and Brown (1980) gave an approximate rule that the uniaxial compressive strength varies inversely as $d^{0.18}$ in the range 10 to 100 mm diameter, while Bazant and Kazemi (1990) suggest an inverse proportionality to $(d_0 - d)^{½}$ where d is the diameter and d_0 is a constant. Size effects are also observed at the micron-scale. Micro-compression studies on crystalline metallic single crystals pillars ranging from 0.5 to 40 μm in diameter and with an aspect ratio ranging from 2:1 to 4:1 showed a large increase in the yield stress as the diameters of the test pillars decreased (Uchic *et al.*, 2004) (Figure 2.21 and 2.22).

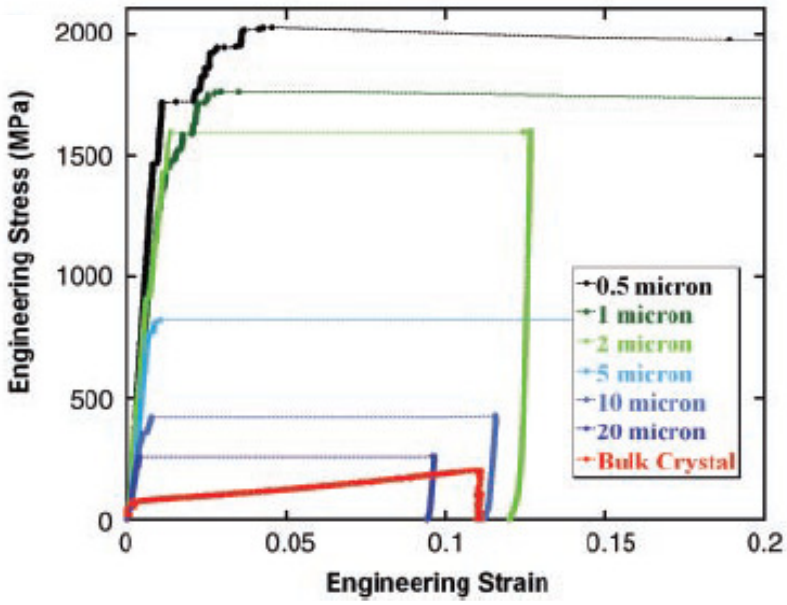

Figure 2.21 Stress-strain curve for Ni_3Al-Ta microsamples ranging in size from 20 to 0.5 μm in diameter, as well as the stress-strain curve for a bulk single crystal having approximate dimensions 2.5 × 2.5 × 7.5 mm (Uchic *et al.*, 2004).

For a Ni_3Al-1% Ta alloy (Figure 2.21), these authors observed an increase in the flow stress from 250 MPa for a 20 μm diameter sample to 2 GPa for a 0.5 μm diameter sample. The observed flow stresses were much higher than those found for bulk crystals, which themselves exhibit a flow stress of only 81 MPa. Tests performed by the same authors on 5 μm diameter samples of pure Ni (Figure 2.23.2) also showed an increase in the yield stresses of these samples when compared with 20 μm diameter samples. A large variation

of 70 MPa was also observed among the tested 5 μm diameter samples yield stresses. This increased scatter for reduced sample dimensions was also observed in other micro-compression experiments (Kiener *et al.*, 2009).

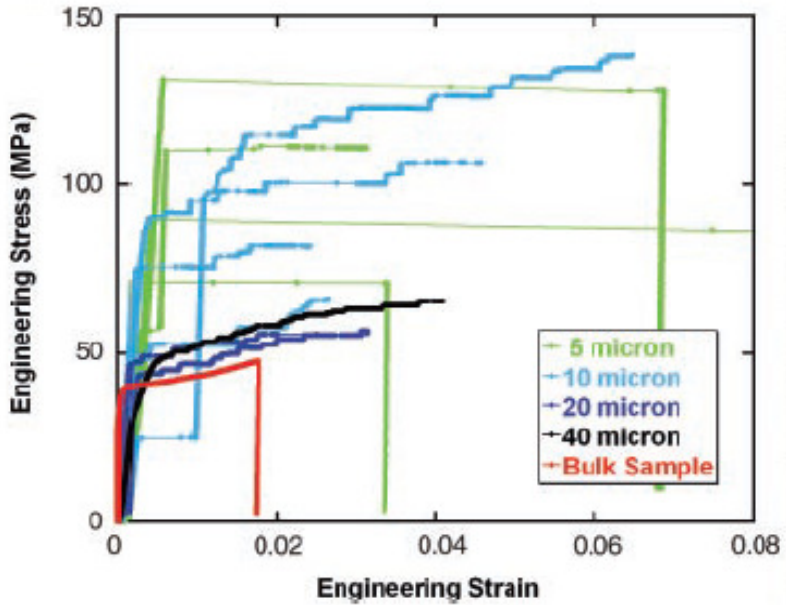

Figure 2.22 Stress-strain curve for pure Ni microsamples ranging in size from 40 to 5 μm in diameter, as well as the stress-strain curve for a bulk single crystal having approximate dimensions 2.6 × 2.6 × 7.4 mm (Uchic *et al.*, 2004).

Other experiments performed on gold pillars confirmed this significant flow stress increase (Greer and Nix, 2005; Nix *et al.*, 2007). These authors proposed that due to the small dimensions of the specimens the dislocations that are present at the onset of plastic deformation would leave these specimens before dislocations can multiply resulting in a state of dislocation starvation. If this state is reached, very high stresses would be required to nucleate new dislocations, either at the sample surface or in the bulk of the crystal, leading to the observed near-theoretical strengths. Compression studies on size effects at the microscale in materials other than metals have to the author's knowledge not yet been conducted.

2.20.2. Shape factor

Shape can also have a large influence on fracture strength. One of the parameters which affects the uniaxial compressive strength (UCS) of materials is the length to diameter or aspect ratio (*L/D*). It has been observed in materials testing that in uniaxial compression the UCS decreases as the aspect ratio increases. The main reason for the aspect ratio dependence results from the perturbation of the homogeneous stress field by boundary effects at the contact with the platens, where frictional constraint is an important factor (Paterson and Wong, 2005).

For compression of fibre reinforced ceramic composites, ASTM C1358 (2000) recommends straight-sided specimens with minimum gage length of 25 mm and a length of at least 50 mm of the gripped sections at each end of the specimen. The recommendation is therefore to use a minimum aspect ratio (*L/D*) of 2:1. Compression studies on limestone measuring 2 inches in diameter (*D*) showed a increase in the UCS from 69.2 MPa to 75.2 MPa for a decrease in aspect ratio from 2.5:1 to 2:1, and an increase from 75.2 MPa to 77.1 MPa for a decrease in aspect ratio from 2:1 to 1:1 (Tuncay and Hasancebi, 2009). This shows that differences between UCS measured on specimens using other aspect ratios than the ASTM C1358 recommended ratio of 2:1 can exist.

Several formulas have been used to convert the UCS values of specimens with aspect ratios less than 2 to a standard ratio which is accepted as 2. Experiments on breccia rocks (made by recrystalized limestone) on 101.3 mm diameter cores, for example, were used to obtain a formula to convert UCS values of tests specimens having an aspect ratio less than 2:1 to that of a specimen with an aspect ratio of 2:1 (Kahraman and Alber, 2006), according to the equation

$$UCS_2 = \frac{8UCS}{7 + \frac{2D}{L}} \qquad (2.40)$$

where UCS_2 is the corrected value for an aspect ratio of 2:1, while the UCS is the measured value on cores with a aspect ratio less than 2:1. UCS can also differ according to whether the test specimen has a cubic or cylindrical geometry. For normal-strength concrete a factor of 1.2 is generally used to convert cylinder strength to cube strength. For high-strength concrete however, the influence of specimen shape is decreased and the factor 1.2 is reduced to 1.12 (Yi *et al.*, 2006).

2.20.3 Contact problems

In a perfect uniaxial compression test there should be at all points in the specimen, one principal stress, directed parallel to the loading and sample axes, and equal in magnitude to the applied load divided by the cross-sectional area of the test sample (Newman and Sigvaldason, 1965). Material specimens are generally not loaded uniformly due to their basic non-homogeneity or to small misalignments. Internal cracking of the specimen may not be symmetrical with respect to the specimen axis, and therefore the stress applied on the specimen may not remain uniform during the test (Kuhn and Medlin, 2000).

Loading platens and end surfaces of test samples are generally assumed to be perfectly in-plane and parallel, so that full contact occurs when they are brought together in parallel alignment. This is seldom the case because it is very difficult to induce intimate contact between the sample and the loading platens. Departures from flatness, lack of parallelism, foreign particles or asperities in the surfaces can induce non-uniform pressure distribution at the contact zone. A non-uniform stress field can cause cracking in the contact zone, and cause premature fracture of the specimen. The lack of parallelism can be caused by a misalignment of the platen drive system, a tilted sample surface, or a rotation of the platen in an insufficiently stiff machine when the test specimen has not been correctly centred (Hawkes and Mellor, 1970).

An investigation (Hoskins and Horino, 1968) on the effects of surface roughness and lack of parallelism on the compressive strength of granite, sandstone, marble, and limestone specimens showed that surface roughness up to 0.05 mm had no great effect on strength or mode of failure. The same investigation showed that for a non-adjustable loading head, i.e.

one lacking a spherical swivel, a departure from parallelism of up to 0.13° could be tolerated without any noticeable effect on the measured strength. Compression experiments on misfit Ni_3Al parallelepipeds also showed a decrease in the modulus between 3 and 10 times the real material modulus as the top surface of the sample plastically deforms to accommodate this misalignment (Shi *et al.*, 1996). Micro-compression investigations on nano-crystalline nickel via finite-element simulations (with the commercial finite element program ABAQUS) also showed that the modulus of elasticity was reduced by a factor of four with a 4° misalignment (Zhang, H. *et al.*, 2006).

2.20.4 Radial constraints

In a uniaxial compression test, friction between the sample and the compression platens can produces radial constraint at the end planes of the specimen. Since the modulus of the steel platens is usually higher than that of any rock, a mis-match of lateral strain between the specimen and the platen will cause a perturbation in the desired uniform stress field. Various attempts have been made to decrease the frictional restraint in the compression test:

1. Matching the radial strain of the test specimen by using another piece of the same rock (Brace, 1964; Paulding, 1966). A disadvantage of this technique is the preparation of the samples, which is still too expensive and time-consuming.

2. Using epoxy cement (Mogi, 1966) or a layer of a low friction material like PTFE/Teflon between the platen and rock (Hsu, 1967).

3. Use of interfacial lubricants. Uniaxial compression experiments, for example, showed that the use of lubricant Castrol™ LMX grease had the effect of decreasing the yield strength (2200 MPa to 1700 MPa) of 3.5 mm diameter cylindrical aluminium specimens (L/D = 0.4) (Li *et al.*, 2009).

4. Using hydrostatic loading. In this test, cylindrical specimens surrounded by a fluid are subjected to simple compression in the presence of a superposed hydrostatic pressure (Paterson and Wong, 2005).

5. Increasing the length to diameter ratio (*L/D*) (see Section 2.20.2).

Since radial constraint can compensates to some extent for imperfections in end surface preparation, its total elimination may not be desirable (Hawkes and Mellor, 1970).

2.20.5 Strain rate, temperature, water content and anisotropy

In general, ceramic materials are less sensitive to changes in strain rate or temperature compared with other materials such as polymers or metals. The maximum stress carried by the test specimen may however vary considerably with the loading rate and the duration of the test. Uniaxial compression tests on Carrara marble showed for example an increase in the UCS from 135 MPa to 170 MPa when the strain rate was increased from 10^{-7} s^{-1} to 10^{-2} s^{-1} (Sano *et al.*, 1981). In sandstone the UCS increase was from 73 MPa to 81 MPa as the strain rate was increased from 2.5 10^{-5} s^{-1} to 2.5 10^{-3} s^{-1}. The same increase in UCS was found as the loading time to failure was reduced from 5 min to 3 s. For rocks, ASTM-D420 (2000) recommends a loading rate which will produce failure of the specimen between 2 and 15 min. Uniaxial compression tests on limestone and marble showed that there was no significant difference between loading rates which produced a failure in 2–3 min and loading rates that produced failure in 8–10 min (Tuncay and Hasancebi, 2009).

The strength and deformability of rocks can also be affected by temperature. Uniaxial compression experiments on calcite single crystal cylinder specimens, under a confined pressure of 0.5 GPa showed that by increasing the temperature from 20° to 300° the yield strength decreases from 245 MPa to 43 MPa in a direction parallel to the *c*-axis (Turner *et al.*, 1954). Uniaxial compression tests performed on parallelepipedic samples (7 x 7 x 22 mm^3) of fine-grain limestones (micrites) showed however a much lower temperature influence on the UCS. For micrite the UCS was found to be 400 MPa at 20° , 375 MPa at 180° and 300 MPa for temperatures above 300° (Doukhan *et al.*, 1976).

Moisture content can also have an influence on the measured strength of calcite rocks depending on the type of rock. In the case of Carrara Marble the uniaxial strength of the wet rock is about 2 % less than that of the dry rock. For Solnhofen limestone, the reduction in the uniaxial strength due to wetting is 30 % (Rutter, 1972). Rutter (1972) gives a cause for this effect; the action of water at grain boundaries. This weakening effect of water through action at grain boundaries is therefore likely to be greatest in rocks of high porosity and small grain-size in which a large surface area will be exposed to the pore fluid. Anisotropy can also influence the measured mechanical properties. Uniaxial compression experiments (under a confined pressure of 500 MPa) on calcite single crystal cylinder specimens, showed that by changing the crystallographic orientation of the specimen the yield strength increases by a factor of 2. The lowest yield strength of 245 MPa was measured if the compressive force was applied parallel to the *c*-axis and 478 MPa if applied at 30° from *c* (Turner *et al.*, 1954).

2.21 Focused ion beam (FIB)

Focused ion beam, also known as FIB, is a technique used for deposition, and ablation of materials. The first FIB instruments evolved from advances in field ion microscopes, and through the development of high resolution liquid metal ion sources (LMISs). In the 1980s, FIB instruments were utilised by the semiconductor industry as mask or circuit repair equipment. In the 1990s FIB instruments began to be used in research laboratories, and today they are becoming a powerful tool for TEM sample preparation, microstructural analysis, and nanomachining (Volkert and Minor, 2007).

The emergence of commercial focused ion beam instruments allowed the production of micron-sized specimens that are much smaller than traditional machining techniques. Uchic *et al*. (2004) were the first to use the FIB to fabricate micro-compression specimens, 0.5 to 40 μm in diameter, into the surface of bulk materials. Once the specimens were prepared, they were tested with a conventional nanoindentation device fitted with a flat-punch tip. In this modification, the sharp Berkovich tip was replaced by a flat-ended tip, converting the indentation system into a compression system. This technique, commonly called micro-

compression, has been utilised in conjunction with FIB to investigate specimen geometry and size effects on the mechanical properties of single crystals of metals and alloys (Uchic *et al.*, 2004; Greer and Nix, 2005; Uchic and Dimiduk, 2005; Choi *et al.*, 2007; Kiener *et al.*, 2009; Yang *et al.*, 2009). Uniaxial micro-compression testing using a nanoindenter equipped with a flat tip has also been used to characterize the strength and fracture of wood cell walls (Xinan *et al.*, 2010), glass (Koopman *et al.*, 2004) and biomaterials (Ziskind *et al.*, 2010).

2.21.1 Focused ion beam (FIB) working principle

The FIB instrument is similar to a scanning electron microscope, except that the beam that is rastered over the sample is an ion beam rather than an electron beam. FIB systems typically use a finely focused beam of gallium ions (Ga^+) that can be operated at low beam currents for imaging or high beam currents for site specific sputtering or milling (Stevie *et al.*, 2005). The basic FIB instrument (Figure 2.23) consists of a vacuum system and chamber, a liquid metal ion source, an ion column, a sample stage, detectors, gas delivery system and a computer to run the complete instrument.

The ion source type used in all commercial systems and in the majority of research systems designed with micromachining applications is the liquid metal ion source (LMIS). There are several metallic elements or alloy sources that can be used in a LMIS. Gallium (Ga^+) is currently the most commonly used LMIS for commercial FIB instruments for several reasons:

1- Its low melting point (T = 29.8 °C) minimizes any reaction or interdiffusion between the liquid and the tungsten needle.
2- Its low volatility at the melting point conserves the supply of metal and yields a long source life.
3- Its low vapor pressure allows Ga^+ to be used in its pure form instead of in the form of an alloy source and yields a long lifetime since the liquid will not evaporate.
4- It has excellent mechanical, electrical, and vacuum properties.

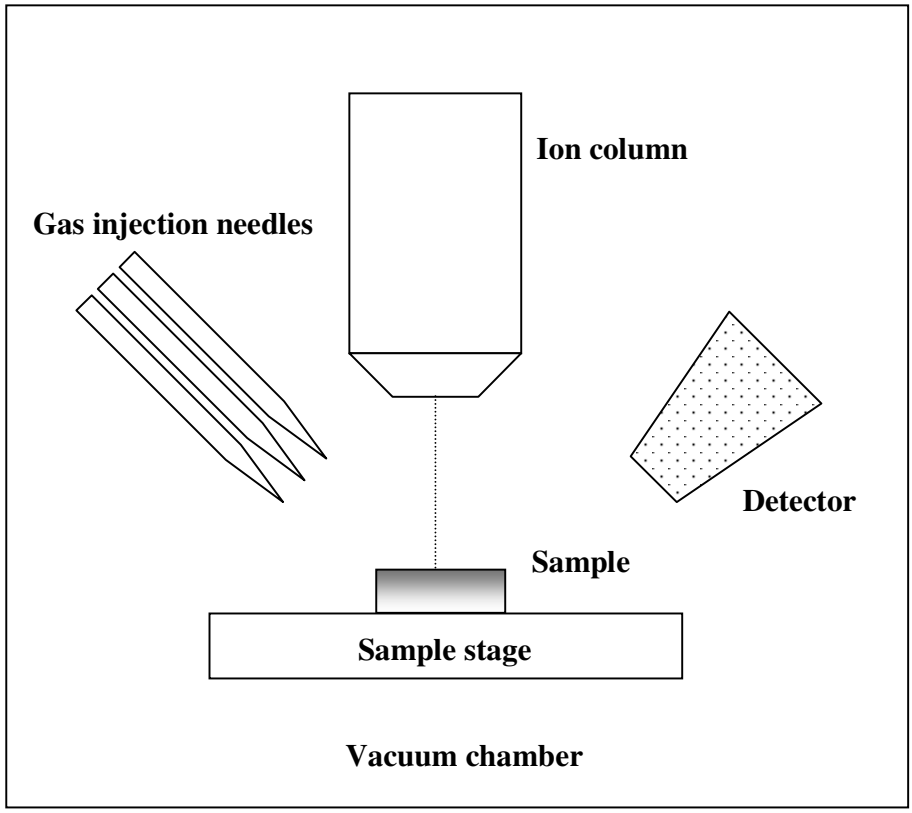

Figure 2.23 A schematic diagram of a basic FIB system (reproduced from Stevie *et al*., 2005).

The basic operation of a FIB instrument starts with heated Ga^+ ions flowing from a reservoir to the needle tip (with an end radius of about 2-10 μm). The Ga^+ ions are then extracted by a large negative potential (10^{10} V m^{-1}) between the needle and an extraction electrode. The current density of Ga^+ ions that may be extracted by the electric field is on the order of $1x10^8$ A cm^{-2}. The Ga^+ ions are then directed through an ion beam column, which consists of two lenses (a condenser and objective lens), that define and then focus the beam on the sample (Stevie *et al.*, 2005). The size and shape of the beam intensity profile on the sample determines the basic imaging resolution and micromachining precision. The sample is mounted on a stage with three-axis translation, rotation, and tilt capabilities. Once the 5-30 keV Ga^+ ion beam collides with a target atom in the sample surface, the translational energy transferred to the atom can exceed a critical value called the displacement energy (typically on the order of 20 eV). If this happens the atom will be

knocked out of its original site leading to sputtering. The sputtering process allows precision milling of the specimen down to sub micrometre or even to nano scale. FIB is therefore suited in its ability to fabricate 3D structures, while maintaining sub-micron precision in a variety of metallic and non-metallic systems.

Depending on the application, the various emitted particles or radiation from the collision can be detected with appropriate detectors in the sample chamber. Secondary electrons generated by the interaction of the ion beam with the sample surface can be used to obtain high-spatial-resolution images. The ions sputtered from the sample can also be detected using a variety of detectors such as charge electron multipliers. FIB can also be incorporated in a system with both electron and ion beam columns, allowing the same feature to be investigated using either of the beams. Secondary electrons generated by the incident ion beam can crack hydrocarbon precursor conducting materials (W, Pt, or C) or insulating material (SiO_2). The local deposition of material also enables sophisticated micromanipulation within the FIB chamber. The result is a system that can cut (sputter), paste (deposit material), and watch (image), all with very high spatial resolution and controlled through one software program (Volkert and Minor, 2007).

2.22 Principles of Scanning Electron Microscopy

Scanning electron microscopy (SEM) is a method for high-resolution imaging of surfaces and uses electrons rather than light to obtain an image. The advantages of SEM over light microscopy include greater magnification (up to 100,000×), greater resolution (1-5 nm) and a much greater depth of field which allows focusing a large amount of a sample at any one time (Goldstein, 2003). The basic functioning of the SEM starts with the production of an electron beam by a filament, located in the electron gun, at the top of the microscope (Figure 2.24). A voltage is applied to the filament, causing it to heat up. This filament, which is a loop commonly made of tungsten, functions as the cathode. After being generated the electron beam is first attracted through the anode (Figure 2.24), which is maintained at a positive voltage (ranging from 5 to 30 kV) relative to the filament. This causes electrons to accelerate towards and through the anode, following a vertical path through the microscope, which is held within a vacuum.

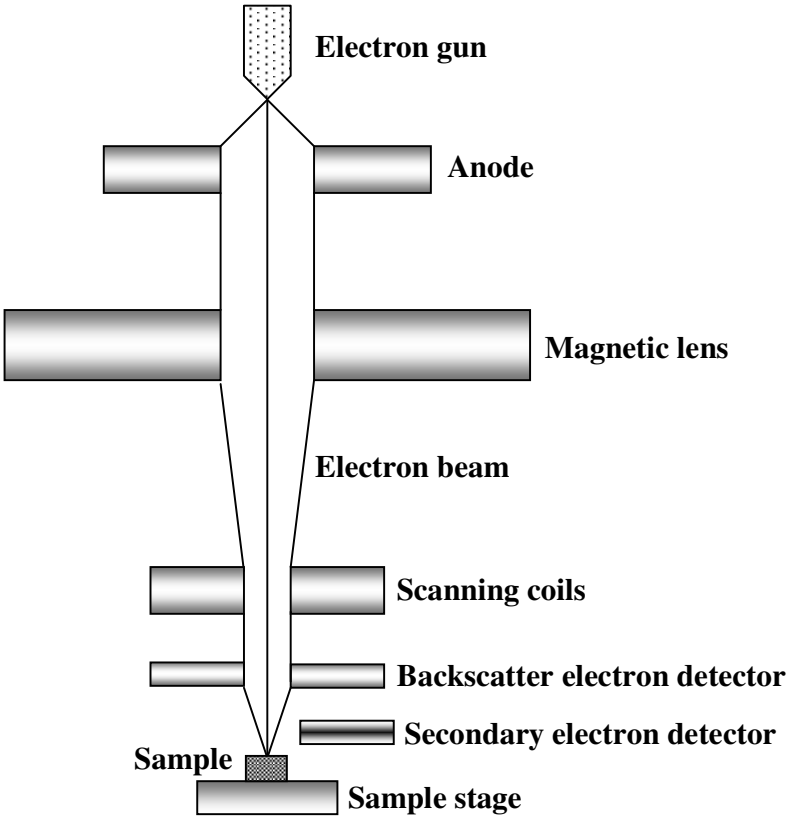

Figure 2.24 Basic components of the scanning electron microscope (Adapted from Purdue, 2011).

After being attracted through the anode, the electron beam is focused as a fine point on the sample by magnetic lenses. The focal length is adjusted by varying the current through the coils of the magnetic lenses. After passing the lenses, the beam is passed through scanning coils which deflect it along both the *x* and *y*-axes over a rectangular area of the sample, in a raster fashion. Once the beam strikes the surface of the sample, the incident electrons, called primary electrons, can interact with the sample in one of two ways, which are described as being either elastic or inelastic. The elastic interaction involves the collision of primary (beam) electrons with the nuclei of the atoms of the sample, without any significant kinetic energy loss. In this case the trajectory of the primary beam electrons can be altered, with about 30% of the primary electrons re-emerging from the sample, giving rise to the backscattered electron signal (BE or BSE).

The detection of the backscattered electrons forms the basis of a useful imaging technique, with contrast based on atomic number (Goldstein, 2003). The inelastic interaction also involves the collision of primary electrons with the nuclei of the atoms of the sample, but with a loss in kinetic energy of the primary electrons. This lost kinetic energy is transferred to the atoms of the sample which causes the ejection of loosely bound electrons from the outer electron shells. These low-energy ejected electrons are known as secondary electrons (SE), and it is the detection of these electrons that provides the usual choice for imaging, as they give the best possible resolution. All SEM instruments have SE detectors, whilst BSE detectors are normally available as optional add-on extras. In addition, the process of inelastic scattering that leads to the production of secondary electrons is also associated with the generation of characteristic X-rays and Auger electrons, both of which can be detected and processed, and then used as the basis for separate spectroscopic analysis (i.e. energy dispersive X-ray analysis (EDX) and Auger Electron Spectrometry (AES).

2.23 Principles of Atomic Force Microscopy (AFM)

An Atomic Force Microscope (AFM) derives from the Scanning Probe Microscopy (SPM) family of instruments, which are based on the development of the scanning tunnelling microscope (STM) (Binnig *et al.*, 1982). In 1985, Binnig *et al*., developed an AFM to measure ultra small forces (less than 1μN) between the AFM tip and a conductive or insulating sample surface. Since then the AFM has become a popular surface profiler for topographic and normal force measurements from the micro- to the nanoscale. An AFM can be used either in the static or the dynamic mode. In the static mode, also referred to as the repulsive or contact mode, a sharp tip at the end of a flexible cantilever is brought into contact with the surface of the sample. One disadvantage of this mode, however, is that the tip can damage the surface or drag particles along with it that are not securely attached to the sample. In the dynamic mode, also referred as noncontact mode, the tip is oscillated and brought into close proximity to, but not in contact with, the sample. To minimize the effects of friction and other lateral forces on topography measurements in the contact mode, and to measure the topographies of soft surfaces, AFMs can also be operated in the tapping mode. In this mode the cantilever is oscillated in a noncontact mode, but at a closer distance from

the sample. Since the tip is not dragged along the surface for both tapping and noncontact modes, they are less sensitive but also slower than the contact mode. In contact mode, during initial contact, the atoms at the end of the tip experience a very weak repulsive force due to electronic orbital overlap with the atoms in the surface of the sample. The force acting on the tip causes the cantilever to deflect, which is measured by using a laser beam deflection technique (Figure 2.25). In this technique a laser beam from a diode laser is directed by a prism onto the back of a cantilever near its free end.

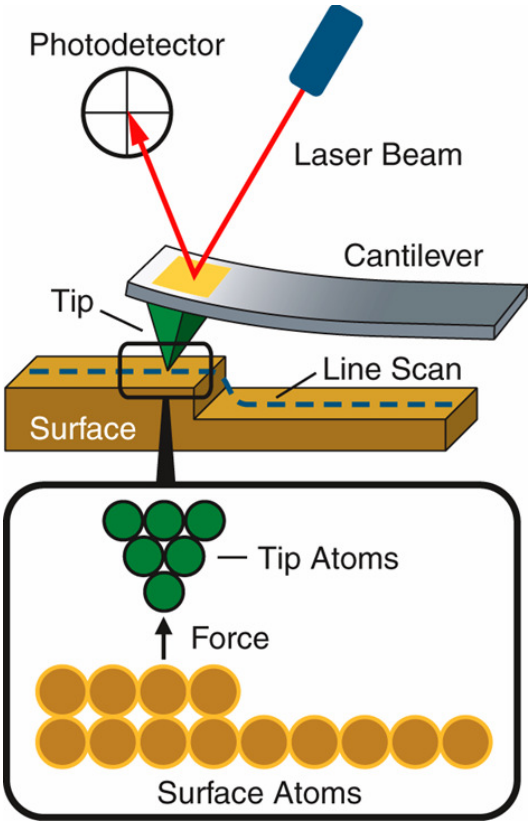

Figure 2.25 Principle of operation of the AFM. The sample is scanned using a small tip and the cantilever deflection is measured using a laser deflection technique (Agilent, 2011).

Topographic features of the sample cause the tip to deflect in the vertical direction as the sample is scanned under the tip. This tip deflection will change the direction of the reflected

laser beam, which is directed through a mirror onto photodetectors. The differential signal from the top and bottom photodetectors provides the AFM signal, which is a sensitive measure of the cantilever vertical deflection. The deflection can be measured to within 0.02 nm, so a force as low as 0.2 nN (corresponding to a normal pressure of ≈ 200 MPa for a Si_3N_4 tip with a radius of about 50 nm against single-crystal silicon) can be detected for a typical cantilever spring constant of 10 Nm^{-1}.

Using an AFM operated in the contact mode, topographic images with a vertical resolution of less than 0.1 nm (as low as 0.01 nm) and a lateral resolution of about 0.2 nm can be obtained (Bhushan and Marti, 2007). The resolution of the AFM is dependent on several parameters. An important parameter that effects the resolution is the type of tip used. Sharper tips can enter into cavities on the surface without the wider part of the tip touching the border of the cavity. Another important parameter is the set-up of the piezoelectric actuators that control the motion of the tip in the *x*, *y* and *z* directions. The force with which the tip interacts with the sample is controlled by the actuators which are in turn controlled by the system's software. The software also controls the gain that controls the sensitivity of the tip and the speed with which the tip scans the surface. These three software controlled parameters affect the resolution of the image since scanning the surface too fast can reduce the capacity of the tip to produce a perfect contour of the surface topography.

2.24 References

Addadi, L., Aizenberg, J., Albeck, S., Berman, A., Leiserowitz, L. and Weiner, S., 1994, *Controlled occlusion of proteins: A tool for modulating the properties of skeletal elements*, Mol. Cryst. Liquid Cryst. Sci. Technol., 248, 185-198.

Agilent, 2011, Atomic Force Microscopy Resource Library, from: http://www.jpk.com/atomic-force-microscopy.

Ahuja, S. K., 1977, *The critical stresses of brittle and ductile polymeric particles*, Powder Technology, 16, 1, 17-22.

Aizenberg, J., 2006, *Nanomechanics of biological single crystals*: *The Role of Intracrystalline Proteins*, Nanomechanics of Materials and Structures, Springer, Dordrecht, Netherlands, 99-108.

Aizenberg, J., Hanson, J., Koetzle, T. F. and Weiner, S., 1997, *Control of macromolecule distribution within synthetic and biogenic single calcite crystals*, J. Am. Chem. Soc., 119, 881–886.

Ashby, M. Hugh, S. and Cebon, D., 1994, Materials: Engineering, Science, Processing and Design, Butterworth-Heinemann, 55.

ASM, 2003, *Characterization and failure analysis of plastics*, The materials information society, 359-382.

ASTM-C1358, 2000, *Standard test method for monotonic compressive strength testing of continuous fiber-reinforced advanced ceramics with solid rectangular cross-section speciments at ambient temperatures*, ASTM American Society for Testing and Materials, Philadeplhia, vol 15.01.

ASTM-D420, 2000, *Soil and Rock*, ASTM American Society for Testing and Materials, Philadeplhia, 04.08.

Auskern, A. and Horn, W., 1971, *Some Properties of Polymer-Impregnated Cements and Concretes*, Journal of the American Ceramic Society, 54, 6, 282-285.

Bangs, 2010, *Bangs laboratories, Inc.*

Barry, C. and Norton, G., *Ceramic Materials- Science and Engineering*, Springer Science and Business Media, LLC.

Barthelat, F., 2007, *Biomimetics for next generation materials*, Phil. Trans. R. Soc., 365, 2907–2919.

Bažant, Z. P.and Kazemi, M. T., 1990, *Size Effect in Fracture of Ceramics and Its Use To Determine Fracture Energy and Effective Process Zone Length*, Journal of the American Ceramic Society, 73, 7, 1841-1853.

Beegan, D., Chowdhury, S. and Laugier, M. T., 2005, *Work of indentation methods for determining copper film hardness*, Surface and Coatings Technology, 192, 1, 57-63.

Berman, A., Addadi, L., Kvick, A., Leiserowitz, L., Nelson, M. and Weiner, S., 1990, *Intercalation of sea urchin proteins in calcite: study of a crystalline composite material*, Science, 2, 250, 4981, 664-667.

Bhimasenachar, J., 1945, *Elastic constants of calcite and sodium nitrate*, Proc. Indian Acad. Sci. Sect. A 22, 199-208.

Bhushan, B. and Marti, O., 2007, *Scanning Probe Microscopy – Principle of Operation, Instrumentation, and Probes*, Springer Handbook of Nanotechnology, Springer Berlin, 573-617.

Bieniawski, Z. T., 1967, *Mechanism of brittle fracture of rock: Part I--theory of the fracture process*, International Journal of Rock Mechanics and Mining Sciences & Geomechanics, 4, 4, 395-406.

Bieniawski, Z. T., 1968, *The effect of specimen size on compressive strength of coal*, International Journal of Rock Mechanics and Mining Sciences & Geomechanics Abstracts, 5, 4, 325-335.

Binnig, G., Quate, C. F. and Gerber, C., 1986, *Atomic force microscope*, Phys. Rev. Lett., 56, 930-933.

Binnig, G., Rohrer, H., Gerber, C. and Weibel, E., 1982, *Surface studies by scanning tunneling microscopy*, Phys. Rev. Lett. , 49, 57-61.

Bolshakov, A. and Pharr, G. M., 1998, *Influences of pileup on the measurement of mechanical properties by load and depth sensing indentation techniques*, Journal of Materials Research, 13, 1049-1058.

Brace, W. F., 1964, *Brittle fracture of rocks*, *In State of Stress in the Earth's Crust*, (ed Judd), American Elsevier Publishing, 111-180.

Brace, W. F., 1965, *Some New Measurements of Linear Compressibility of Rocks*, Journal of Geophysical Research, 70, 2, 391-398.

Brace, W. F., Paulding, B. W. and Scholz, C., 1966, *Dilatancy in Fracture of Crystalline Rocks*, Journal of Geophysical Research, 71, 16, 3939.

Brady, B., 1969, *A statistical theory of brittle fracture for rock materials. Part I. Brittle failure under homogeneous axisymmetric states of stress*, Int. J. Rock. Mech. Min., 6, 21-42.

Briscoe, B. J., 1998, *Nano-indentation of polymeric surfaces*, Journal of Physics and Applied Physics, 31, 19, 2395.

Bruet, B. J. F., Qia, H. J., Boyce, M. C., Panas, R., Tai, K., Frick, L. and Ortizb, C., 2005, *Nanoscale morphology and indentation of individual nacre tablets from the gastropod mollusc Trochus niloticus*, J. Mater. Res., 20, 9, 2400-2419.

Bryant, W. and Wiebking, H., 2002, *Effect of calcium carbonate size and loading level on the impact performance of rigid PVC compounds containing varying amounts of acrylic impact modifier,* Society of Plastics Engineers ANTEC Conference Proceedings, vol 3.

Bückle, H., 1973, *The Science of Hardness Testing and Its Research Applications*, ASM Metals Park, Ohio, 453.

Cai, X. and Bangert, H., 1995, *Hardness measurements of thin films-determining the critical ratio of depth to thickness using FEM*, Thin Solid Films, 264, 1, 59-71.

Carter, B. and Norton, G., 2007, *Ceramic Materials, Science and Engineering*, Springer, 37, 675-689.

Carter, G. M., Henshall, J. L. and Wakeman, R. J., 1993, *Knoop hardness and fracture anisotropy of calcite*, Journal of Materials Science Letters, 12, 6, 407-410.

Chawla, K. K., 2003, *Matrix Composites*, Kluwer Academic Publishers, Pages.

Chen, J. and Bull, S. J., 2009, *The investigation of creep of electroplated Sn and Ni-Sn coating on copper at room temperature by nanoindentation*, Surface and Coatings Technology, 203, 12, 1609-1617.

Choi, Y. S., Uchic, M. D., Parthasarathy, T. A. and Dimiduk, D. M., 2007, *Numerical study on microcompression tests of anisotropic single crystals*, Scripta Materialia, 57, 9, 849-852.

Chudoba, T. and Richter, F., 2001, *Investigation of creep behaviour under load during indentation experiments and its influence on hardness and modulus results*, Surface and Coatings Technology, 148, 2-3, 191-198.

Defoe, O. K., Compton and Arthur, H., 1925, *The Density of Rock Salt and Calcite*, Physical Review, 25, 5, 618-620.

Devore, L. J., 2011, *Probability and Statistics for Engineering and the Sciences*, 8th, Duxbury Press.

Dey, T. and Halleck, P., 1981, *Some aspects of size effect in rock failure*, Geophys. Res. Lett., 8, 7, 691-694.

Doerner, M. F. and Nix, W. D., 1986, *A method for interpreting the data from depth-sensing indentation instruments*, J. Mater. Res., 1, 601-609.

Donath, F. A. and Fruth, L. S., 1971, *Dependence of Strain-Rate Effects on Deformation Mechanism and Rock Type*, The Journal of Geology, 79, 3, 347-371.

Doukhan, J. C., Henry, J. P. and Paquet, J., 1976, *Microstructure and brittle behaviour of fine grain calcite (micrite)*, Journal of Materials Science, 11, 10, 1884-1892.

Downs, R. T., 2006, *The RRUFF Project: an integrated study of the chemistry, crystallography, Raman and infrared spectroscopy of minerals.* Paper presented at the Program and Abstracts of the 19th General Meeting of the International Mineralogical Association in Kobe, Japan, 3-13.

Einstein, H., Baecher, G. and Hirschfeld, R., 1970, *The effect of size on the strength of a brittle rock*, International Society of Rock Mechanics, Proceedings, 1, 1-19.

Eldin, N. N. and Senouci, A. B., 1993, *Rubber-Tire Particles as Concrete Aggregate*, Journal of Materials in Civil Engineering 5, 4, 478-496.

Emlet, R., 1982, *Echinoderm calcite: a mechanical analysis from larval spicules*, Biol. Bul., 163, 264-275.

Epstein, B., 1948, *Statistical Aspects of Fracture Problems*, Journal of Applied Physics, 19, 2, 140-147.

Field, J. S. and Swain, M. V., 1993, *A Simple Predictive Model for Spherical Indentation* Journal of Materials Research 8(2), 297–306.

Fischer-Cripps, A. C., 2002, *Nanoindentation*, Springer-Verlag, Berlin Germany.

Fischer-Cripps, A. C., 2009, *The IBIS Handbook of Nanoindentation*, Fischer-Cripps Laboratories Pty Ltd.

Fröhlich, F. and Grau, P., *Anordnung einer registrierenden Härteprüfung unter Last*, DDR Patent 121 386.

Gao, H., Chiu, C. H. and Lee, J., 1992, *Elastic contact versus indentation modeling of multi-layered materials*, Int. J. Solids Struct., 29, 20, 2471-2492.

Glucklich, J. and Cohen, L., 1967, *Size as a factor in the brittle-ductile transition and the strength of some materials*, Int. J. Fract. Mech., 3, 278–289.

Goldstein, J., 2003, *Scanning electron microscopy and x-ray microanalysis*, Springer.

Greer, J. R. and Nix, W. D., 2005, *Size dependence in mechanical properties of gold at the micron scale in the absence of strain gradients*, Applied Physics and Materials Science & Processing, 90, 1, 203-203.

Grodzinski, P., 1952, *Elastic and Plastic Hardness of Hard Materials*, Nature, 169, 925-26.

Hanim, H., Zarina, R., Ahmad, M. Y., Ishak, M. Z. A. and Hassan, A., 2008, *The Effect of Calcium Carbonate Nanofiller on the Mechanical Properties and Crystallisation Behaviour of Polypropylene*, Malaysian Polymer Journal, 3, 12, 38-49.

Hartman, P. and Perdok, W. G., 1955, *On the relations between structure and morphology of crystals*, Acta Cryst., 8, 521-529.

Hawkes, I. and Mellor, M., 1970, *Uniaxial testing in rock mechanics laboratories*, Engineering Geology, 4, 3, 179-285.

Hay, J., 2009, *Introduction to instrumented indentation testing*, Experimental Techniques, 33, 6, 66-72.

Hay, J. and Crawford, B., 2010, *Measuring substrate-independent modulus of thin films*, Journal of Materials Research, 26, 06, 727-738.

Hay, J. C. and Pharr, G. M., 1997, *Critical issues in measuring the mechanical properties of hard films on soft substrates by nanoindentation techniques*, Conference: 1997 fall meeting of the Materials Research Society, Boston, MA (United States), 1-5 Dec 1997.

Hays, C. and Kendall, E. G., 1973, *An analysis of Knoop microhardness,* Metall., 6, 275-282.

Herget, G. and Unrug, K., 1976, *In situ rock strength from triaxial testing*, International Journal of Rock Mechanics and Mining Sciences & Geomechanics Abstracts, 13, 11, 299-302.

Heuze, F., 1980, *Scale effects in the determination of rock mass strength and deformability*, Rock Mechanics and Rock Engineering, 12, 3, 167-192.

Hoek, E. and Brown, E., 1980, *Underground excavation engineering*, Institution of Mining and Metallurgy, Elsevier Applied Science.

Hoskins, J. R. and Horino, F. G., 1968, *Effect of end conditions on determining compressive strength of rock samples*, U.S. Bur. Mines Dept, 7171.

Hsu, T. C., 1967, *A study of the compression test for ductile materials*, Am. Soc. Mech. Engrs., 67, 11, 16.

Kahraman, S. and Alber, M., 2006, *Estimating unconfined compressive strength and elastic modulus of a fault breccia mixture of weak blocks and strong matrix*, International Journal of Rock Mechanics and Mining Sciences, 43, 8, 1277-1287.

Kelly, A. and Zweben, C., 2000, *Comprehensive Composite Materials*, Copyright 2000 Elsevier Ltd.

Kermouche, G., Loubet, J. L. and Bergheau, J. M., 2008, *Extraction of stress-strain curves of elastic-viscoplastic solids using conical/pyramidal indentation testing with application to polymers*, Mechanics of Materials, 40, 4-5, 271-283.

Khaloo, A. R., Dehestani, M. and Rahmatabadi, P., 2008, *Mechanical properties of concrete containing a high volume of tire rubber particles*, Waste Management, 28, 12, 2472-2482.

Kiener, D., Motz, C. and Dehm, G., 2009, *Micro-compression testing: A critical discussion of experimental constraints*, Materials Science and Engineering, 505, 1-2, 79-87.

Kiener, D., Motz, C., Rester, M., Jenko, M. and Dehm, G., 2007, *FIB damage of Cu and possible consequences for miniaturized mechanical tests*, Materials Science and Engineering, 25, 262-272.

Kim, D. K., 2011, *Nanoindentation*, Lecture 1- Basic Principle, Department of Material Science and Engineering KAIST, from http://www.slideshare.net/viet4777/nano-indentation-lecture1

Kim, Y.-Y., Ganesan, K., Yang, P., Kulak, A. N., Borukhin, S., Pechook, S., Ribeiro, L., Kroger, R., Eichhorn, S. J., Armes, S. P., Pokroy, B. and Meldrum, F. C., 2011, *An artificial biomineral formed by incorporation of copolymer micelles in calcite crystals*, Nat. Mater., 10, 890-896.

Kim, Y.-Y., Ribeiro, L., Maillot, F., Ward, O., Eichhorn, S. J. and Meldrum, F. C., 2010, *Bio-Inspired Synthesis and Mechanical Properties of Calcite–Polymer Particle Composites*, Advanced Materials, 22, 18, 2082-2086.

Kinosita, K., 1972, *Recent Developments in the Study of Mechanical Properties of Thin Films*, Thin Solid Films, 12, 17-28.

Kiser, M., He, M. Y. and Zok, F. W., 1999, *The mechanical response of ceramic microballoon reinforced aluminum matrix composites under compressive loading*, Acta Materialia, 47, 9, 2685-2694.

Koch, T., Kogler, F. R., Schubert, U. and Seidler, S., 2007, *Mechanical Properties of Organic-Inorganic Hybrid Materials Determined by Indentation Techniques*, Monats hefte für Chemie, Chemical Monthly, 138, 4, 293-299.

Koopman, M., Gouadec, G., Carlisle, K., Chawla, K. K. and Gladysz, G., 2004, *Compression testing of hollow microspheres (microballoons) to obtain mechanical properties*, Scripta Materialia, 50, 5, 593-596.

Kuhn, H. and Medlin, D., 2000, *ASM metal handbook: Mechanical Testing and Evaluation*, ASM International, 8.

Larson, R. A. and Palazotto, A. N., 2009, *Property estimation in FGM plates subject to low-velocity impact loading*, Journal of mechanics of materials and structures, 4, 7-8.

Lawn, B. R., 1993, *Fracture of Brittle Solids*, Cambridge University Press.

Li, H. and Bradt, R. C., 1993, *The microhardness indentation load/size effect in rutile and cassiterite single crystals*, J. Mater. Sci., 28, 917-926.

Li, M., Carter, C. B., Hillmyer, M. A. and Gerberich, W., 2001, *Adhesion of polymer-inorganic interfaces by nanoindentation*, J. Mater. Res., 16, 3378-3388.

Li, X. and Bhushan, B., 2003, *Nanomechanical characterisation of solid surfaces and thin films*, International materials reviews, 48, 3, 125-164.

Li, X. and Bhushan, B., 2002, *A review of nanoindentation continuous stiffness measurement technique and its applications*, Materials Characterization, 48, 1, 11-36.

Li, X., Chang, W. C., Chao, Y. J., Wang, R. and Chang, M., 2004, *Nanoscale Structural and Mechanical Characterization of a Natural Nanocomposite Material: The Shell of Red Abalone*, Nano Letters, 4, 4, 613-617.

Li, X. and Nardi, P., 2004, *Micro/nanomechanical characterization of a natural nanocomposite material: the shell of Pectinidae*, Nanotechnology, 15, 211-217.

Lin, Y. C., Weng, Y. J., Pen, D. J. and Li, H. C., 2009, *Deformation model of brittle and ductile materials under nano-indentation*, Materials & design, 30, 5, 1643-1649.

Ling, T. C., 2011, *Prediction of density and compressive strength for rubberized concrete blocks*, Construction and Building Materials, 25, 11, 4303-4306.

Lippmann, F., 1973, *Sedimentary carbonate minerals.* Springer-Verlag, Berlin.

Liu, J. A., Yu, S. R., Hu, Z. Q., Liu, Y. H. and Zhu, X. Y., 2010, *Deformation and energy absorption characteristic of Al2O3f/Zn-Al composite foams during compression*, Journal of Alloys and Compounds, 506, 2, 620-625.

Lu, D., Sun, F. and Li, L., 2007, *Study on vibrational modes by group theory and infrared spectra by DFT for calcite crystal*, Chinese optics letters, 5, 6, 370-372.

Lucca, D. A., Herrmann, K. and Klopfstein, M. J., 2010, *Nanoindentation: Measuring methods and applications*, CIRP Annals - Manufacturing Technology, 59, 2, 803-819.

Lucas, B. and Oliver, W., 1999, *Indentation power-law creep of high-purity indium*, Metallurgical and Materials Transactions, 30, 3, 601-610.

Lucas, B. N., Oliver, W. C. and Swindeman, J. E., 1998, *The dynamics of frequency-specfic, depth-sensing indentation testing*, MRS proceedings, 522.

Ma, Y., Cohen, S. R., Addadi, L. and Weiner, S., 2008, *Sea Urchin Tooth Design: An "All-Calcite" Polycrystalline Reinforced Fiber Composite for Grinding Rocks*, Advanced Materials, 20, 8, 1555-1559.

Mann, A. B., 2005, *Nanotribology and Nanomechanics: An Introduction*, Nanomechanical Properties of Solid Surfaces and Thin Films, 12.

Martens, A., 1898, Handbuch der Materialienkunde fur den Maschinenbau, Springer, Berlin.

McCaffrey, J. P., Phaneuf, M. W. and Madsen, L. D., 2001, *Surface damage formation during ion-beam thinning of samples for transmission electron microscopy*, Ultramicroscopy, 87, 3, 97-104.

McColm, I. J., 1990, *Ceramic hardness*, Plenum Press, New York.

McDonald, J. H., 2009, *Handbook of Biological Statistics*, Sparky House Publishing.

McElhaney, K. W., Vlasssak, J. J. and Nix, W. D., 1998, *Determination of indenter tip geometry and indentation contact area for depth-sensing indentation experiments*, J. Mater. Res., 13, 1300-1306.

MetPrep, 2010, *MetPrep price list*, from: http://www.uki.net/php/files/metprepcms.uki.net/pricelist_2011.pdf

Mitchell, B. S., 2004, *An introduction to materials engineering and science*, A John Wiley & Sons, Inc. Publications.

Miyake, K., Fujisawa, S., Korenaga, A., Ishida, T. and Sasaky, S., 2004, *The Effect of Pile-Up and Contact Area on Hardness Test by Nanoindentation*, Japanese Journal of Applied Physics, 43, 7B, 4602–4605.

Miyake, K., Satomi, N. and Sasaki, S., 2006, *Elastic modulus of polystyrene film from near surface to bulk measured by nanoindentation using atomic force microscopy*, Applied Physics Letters, 89, 3, 1925-1.

Miyata, N. and Jinno, H., 1982, *Micromechanics Approach to the Indentation Hardness of Glass Matrix Particulate Composites*, J. Mat. Sci., 17, 547-557.

Mogi, K., 1966, *Some precise measurements of fracture strength of rocks under uniform compressive stress*, Rock Mech. Eng. Geol., 4, 1, 41-55.

Mogi, K., 1973, *Rock Fracture*, Annual Review of Earth and Planetary Sciences, 1, 63-84.

Moh'd, B. K., 2009, *Compressive Strength of Vuggy Oolitic Limestones as a Function of Their Porosity and Sound Propagation*, Jordan Journal of Earth and Environmental Sciences, 2, 1, 18-25.

Mori, T. and Tanaka, K., 1973, *Average stress in matrix and average elastic energy of materials with misfitting inclusions*, Acta Metallurgica, 21, 5, 571-574.

Motz, C., Pippan, R. and Kriszt, B., 2002, *Handbook of cellular metals: Production, Processing, Applications*, Wiley-VCH Verlag GmbH & Co. KGaA.

Moureaux, C., Perez-Huerta, A., Compere, P., Zhu, W., Leloup, T., Cusack, M. and Dubois, P., 2010, *Structure, composition and mechanical relations to function in sea urchin spine*, Journal of Structural Biology, 170, 1, 41-49.

MTS, S. C., 2002, *XP user's guide*, Systems Corporation MTS.

Müller, E., Chung, J. T., Zhang, Z. and Sprauer, A., 2005, *Characterization of the mechanical properties of polymeric chromatographic particles by micromanipulation*, Journal of Chromatography A, 1097, 1-2, 116-123.

Nemat-Nasser, S., Buschow, K. H. J., Robert, W. C., Merton, C. F., Bernard, I., Edward, J. K., Subhash, M. and Patrick, V., 2001, *Brittle Materials: Compressive Strength*, Encyclopedia of Materials: Science and Technology, Oxford: Elsevier, 806-811.

Newman, K. and Sigvaldason, T., 1965, *Testing machine and specimen characteristics and their effect on the mode of deformation, failure, and strength of materials*, Proceedings of the Institution of Mechanical Engineers, Conference Proceedings, 180, 1964-1970.

Nix, W. D., Greer, J. R., Feng, G. and Lilleodden, E. T., 2007, *Deformation at the nanometer and micrometer length scales: Effects of strain gradients and dislocation starvation*, Thin Solid Films, 515, 6, 3152-3157.

Ok Kim, D. and Hee Jin, J., 2007, *Mechanical property investigation of single polymer particles with the variation of molecular structure of crosslinking monomer*, Journal of Applied Polymer Science, 105, 2, 783-789.

Oliver, W. C. and Pharr, G. M., 1992, *An improved technique for determining hardness and elastic modulus*, J. Mater. Res., 7, 6, 1564-1583.

Oliver, W. C. and Pharr, G. M., 2004, *Measurement of hardness and elastic modulus by instrumented indentation: Advances in understanding and refinements to methodology*, J. Mater. Res., 19, 1, 3-20.

Park, J. B. and Lakes, R. S., 1992, *Biomaterials*: *An Introduction***,** Plenum press.

Paterson, M. S. and Wong, T. f., 2005, *Experimental Rock Deformation – The Brittle Field*, Springer-Verlag Berlin Heidelberg.

Paulding, B. W., 1966, *Testing Techniques for Rock Mechanics*, Am. Soc. Testing Mater, Spec. Tech. Pub, 402, 73-84.

Peggs, G. N. and Leigh, I. C., 1983, *Report MOM62*, UK National Physical Laboratory, England.

Peng, Z., Gong, J. and Miao, H., 2004, *On the description of indentation size effect in hardness testing for ceramics: Analysis of the nanoindentation data*, Journal of the European Ceramic Society, 24, 8, 2193-2201.

Pethica, J. B. and Oliver, W. C., 1987, *Tip surface interactions in STM and AFM*, Physica Scripta, T19A, 61-66.

Pharr, G. M. and Bolshakov, A., 2002, *Understanding nanoindentation unloading curves*, J. Mater. Res.,17, 2660-2671.

Pine, D., 2007, Department of Physics, New York University, Washington, USA, from http://physics.nyu.edu/pine/research/nanocopoly.html

Podrazky, V. and Sedmerova, V., 1966, *Densities of collagen dehydrated by some organic solvents*, Cellular and Molecular Life Sciences, 22, 12, 792-792.

Pokroy, B., Fitch, A. and Zolotoyabko, E., 2006, *The Microstructure of Biogenic Calcite: A View by High-Resolution Synchrotron Powder Diffraction*, Advanced Materials, 18, 18, 2363-2368.

Poole, W. J., Ashby, M. F. and Fleck, N. A., 1996, *Micro-hardness of annealed and work-hardened copper polycrystals*, Scripta Materialia, 34, 4, 559-564.

Presser, V., Schultheiß, S., Berthold, C. and Nickel, K. G., 2009, *Sea Urchin Spines as a Model-System for Permeable, Light-Weight Ceramics with Graceful Failure Behavior. Part II.*
Mechanical Behavior of Sea Urchin Spine Inspired Porous Aluminum Oxide Ceramics under Compression, Journal of Bionic Engineering, 6, 3, 203-213.

Purdue, 2011, *Scanning Electron Microscope*, Purdue University, from http://www.purdue.edu/rem/rs/sem.htm.

Rachlin, A. L., Henderson, G. S. and Cynthia, M., 1992, *An atomic force microscope study of the calcite cleavage plane: Image averaging in Fourier space*, American Mineralogist, 77, 904-910.

Ramakrishna, S. and Hamada, H., 1998, *Energy Absorption Characteristics of Crash Worthy Structural Composite Materials*, Key Engineering Materials, 141-143, 585-622.

Rao, P., 2003, *Biomimetics*, Sadhana, 28, Parts 3 & 4, 657–676.

Rar, A., Song, H. and Pharr, G. M., 2002, *Assessment of new relation for the elastic compliance of a film–substrate system, in Thin Films: Stresses and Mechanical Properties* Mater. Res. Soc. Symp. Proc., 695, 431.

Ren, X. J., Hooper, R. M., Griffiths, C. and Henshall, J. L., 2003, *Indentation size effect in ceramics: Correlation with H/E*, Journal of Materials Science Letters, 22, 15, 1105-1106.

Rho, J. Y., Tsui, T. Y. and Pharr, G. M., 1997, *Elastic properties of human cortical and trabecular lamellar bone measured by nanoindentation*, Biomaterials, 18, 20, 1325-1330.

Rice, R. W., 2000, *Mechanical properties of ceramics and composites*, CRC Press, 245-294.

Robach, J. S., Stock, S. R. and Veis, A., 2005, *Transmission electron microscopy characterization of macromolecular domain cavities and microstructure of single-crystal calcite tooth plates of the sea urchin Lytechinus variegatus*, Journal of Structural Biology, 151, 1, 18-29.

Roskill, 2012, *Ground and Precipitated Calcium Carbonate: Global industry markets & outlook*, Roskill Consulting Group, from http://www.roskill.com/reports/industrial-minerals/ground-and-precipitated-calcium-carbonate-1.

Rösler, J., Harders, H. and Bäker, M., 2007, *Mechanical Behaviour of Engineering Materials*, Springer-Verlag Berlin Heidelberg.

Rutter, E. H., 1972, *The influence of interstitial water on the rheological behaviour of calcite rocks*, Tectonophysics, 14, 1, 13-33.

Saint-Gobain, C., 2012, *The materials of choice for today's armor protection systems*, from http://www.hexoloy.com/product-applications/armor/armor.

Saito, Y., Nyumura, J., Zhang, Y., Tanaka, S., Uchida, N. and Uematsu, K., 2002, *Kinetics of property change associated with atmospheric humidity changes in alumina powder granules with PVA binder*, Journal of the European Ceramic Society, 22, 16, 2835-2840.

Sano, O., Ito, I. and Terada, M., 1981, *Influence of strain rate on dilatancy and strength of Oshima granite under uniaxial compression*, J. Geophys. Res., 86, 9299–9311.

Sarikaya, M., 1994, *An Introduction to Biomimetics: A Structural Viewpoint*, Microscopy research and technique, 27, 360-375.

Seto, J., Ma, Y., Davis, S. A., Meldrum, F., Gourrier, A., Kim, Y., Schilde, U., Sztucki, M., Burghammer, M., Maltsev, S., Jager, C. and Colfen, H., 2012, *Structure-property relationships of a biological mesocrystal in the adult sea urchin spine*, Proc. Nat. Acad. Sci., 109, 10, 3699-3704.

Sheng, Y. S., Zhao, J., Zhou, B., Ding, X. and Wang, Z., 2006, *In situ preparation of CaCO3/polystyrene composite nanoparticles*, Materials Letters, 60, 3248–3250.

Shi, X., Saada, G. and Veyssiere, P., 1996, *The effect of prestraining temperature on the mechanical behaviour of Ni3(Al, Hf) single crystals*, Philosophical Magazine A, 73, 5, 1419-1438.

Specialty-Minerals, 2012, *Calcium Carbonate in Plastics*, from http://www.specialtyminerals.com/specialty-applications/specialty-markets-for-minerals/plastics/gcc-in-plastics/.

Stevie, F. A., Giannuzzi, L. A. and Prenitzer, B. I., 2005, *Introduction to Focused Ion Beams: Instrumentation, Theory, Techniques and practice*, Springer Inc.

Stillwell, N. A. and Tabor, D., 1961, *Elastic Recovery of Conical Indentations*, Proc. Phys. Soc. London 78, 169-178.

Stryjak, A. J. and McMillan, P. W., 1978, *Microstructure and Properties of Transparent Glass-Ceramics*, J. Mat. Sci., 13, 1794–1804.

Sun, G. and Zhang, Z., 2002, *Mechanical strength of microcapsules made of different wall materials*, International Journal of Pharmaceutics, 242, 1-2, 307-311.

Sun, L., Gibson, R. F., Gordaninejad, F. and Suhr, J., 2009, *Energy absorption capability of nanocomposites: A review*, Composites Science and Technology, 69, 14, 2392-2409.

Tabor, D., 1948, *theory of static and dynamic hardness*, Engineering, 165, 289-292.

Tabor, D., 1951, *The Hardness of Metals*, Oxford University Press, Oxford, UK.

Tarkanian, M. L., Neumann, J. P. and Raymond, L., 1973, *Determination of the temperature dependence of {100} and {112} slip in tungsten from Knoop hardness measurements*, American Society for Metals, Metal Park, OH, 187–198.

Tegethoff, F. W., 2002, *Calcium Carbonate: From the Cretaceous Period into the 21st Century*, Birkhauser Verlag.

Ternovskij, A. P., Alechin, V. P., Shorshorov, M. C., Khrushchov, M. M. and Skvorcov, V. N., *O Mikromechaniceskich Ispytanijach Materialov Putjom Vdavlivanija*, Micromechanical Material Tests by Indentation, Zavodskaja Laboratorija, 39,1242–1247.

Thomas, C. R., Zhang, Z. and Cowen, C., 2000, *Micromanipulation measurements of biological materials*, Biotechnology Letters, 22, 7, 531-537.

Tuncay, E. and Hasancebi, N., 2009, *The effect of length to diameter ratio of test specimens on the uniaxial compressive strength of rock*, Bulletin of Engineering Geology and the Environment, 68, 4, 491-497.

Turner, F. J., Griggs, D. T. and Heard, H., 1954, *Experimental deformation of calcite crystals* Geological Society of America Bulletin, 65, 9, 883-934.

Uchic, M. D. and Dimiduk, D. M., 2005, *A methodology to investigate size scale effects in crystalline plasticity using uniaxial compression testing*, Materials Science and Engineering A, 400-401, 268-278.

Uchic, M. D., Dimiduk, D. M., Florando, J. N. and Nix, W. D., 2004, *Sample dimensions influence strength and crystal plasticity*, Science, 305, 5686, 986-989.

Underwood, E. E., 1970, *Quantitative Stereology*, Addison-Wesley Pub. Co.

VanLandingham, M., 2003, *Review of Instrumented Indentation*, J. Res. Natl. Inst. Stand. Technol., 108, 249-265.

Vincent, J., Bogatyreva, O., Bogatyrev, N., Bowyer, A. and Pahl, A., P., 2006, *Biomimetics: its practice and theory*, J. R. Soc. Interface, 3, 471–482.

Volkert, C. A. and Minor, A. M., 2007, *Focused Ion Beam Microscopy and Micromachining*, MRS Bulletin, 32, 389-399.

Wainwright, S. A., Biggs, J. D., Currey, W. D. and Gosline, J. D., 1976, *Mechanical Design in Organisms*, London, Edward Arnold.

Walsh, J. B., 1965, *Effect of Cracks on Uniaxial Elastic Compression of Rocks*, Journal of Geophysical Research, 70, 2, 399-411.

Warren, R., 1992, *Ceramic-Matrix composites*, Chapman and Hall.

Weber, J., Greer, R., Voight, B., White, E. and Roy, R., 1969, *Unusual strength properties of echinoderm calcite related to structure*, Journal of Ultrastructure Research, 26, 5-6, 355-366.

Weibull, W., 1939, *A statistical theory of the strength of materials*, Ing. Vet. Akad., Stockholm, Handlinger, 151.

Weibull, W., 1951, *A statistical distribution function of wide applicability*, J. Appl. Mech., 18, 293–297.

Weiner, S. and Addadi, L., 1997, *Design strategies in mineralized biological materials*, J. Mater. Chem.**,** 7**,** 689-702.

Weiner, S., Addadi, L. Wagner, H. D., 2000, *Materials design in biology*, Materials Science and Engineering, 11, 1-8.

Wiebking, H., 1998, *Fillers in PVC: A review of the basics*, Specialty Minerals Inc., from http://www.specialtyminerals.com/fileadmin/user_upload/mti/DataSheets/S-PM-AT-177%20pvc%20fillers%20bro.pdf.

Wiebking, H., 2005, Increasing the flexural modulus of rigid PVC at elevated temperature Journal of Vinyl and Additive Technology, 12, 1, 37-40.

Xinan, Z., Qiuhong, Z., Siqun, W., Rosa, T., Edgar, L. C. and Guanben, D., 2010, *Characterizing strength and fracture of wood cell wall through uniaxial micro-compression test*, Composites Part A: Applied Science and Manufacturing, 41, 5, 632-638.

Xu, H. and Pharr, G. M., 2006, *An improved relation for the effective elastic compliance of a film/substrate system during indentation by a flat cylindrical punch*, Scr. Mater., 55, 4, 315-318.

Xu, Z.-H. and Rowcliffe, D., 2004, *Finite element analysis of substrate effects on indentation behaviour of thin films*, Thin Solid Films, 447-448, 399-405.

Xu, Z. H. and Li, X. D., 2006, *Sample size effect on nanoindentation of micro-/nanostructures*, Acta Materialia, 54, 6, 1699-1703.

Yang, Y., Ye, J. C., Lu, J., Liu, F. X. and Liaw, P. K., 2009, *Effects of specimen geometry and base material on the mechanical behavior of focused-ion-beam-fabricated metallic-glass micropillars*, Acta Materialia, 57, 5, 1613-1623.

Yap, S. F., Adams, M., Seville, J. and Zhang, Z., 2006, *Understanding the mechanical properties of single micro-particles and their compaction behaviour*, China Particuology, 4, 1, 35-40.

Yap, S. F., Adams, M. J., Seville, J. P. K. and Zhang, Z., 2008, *Single and bulk compression of pharmaceutical excipients: Evaluation of mechanical properties*, Powder Technology, 185, 1, 1-10.

Yi, S.-T., Yang, E.-I. and Choi, J.-C., 2006, *Effect of specimen sizes, specimen shapes, and placement directions on compressive strength of concrete*, Nuclear Engineering and Design, 236, 2, 115-127.

Yonezu, A., Ogawa, T. and Takemoto, M., 2004, *AE Analysis on the Fracture Mechanism of Ceramics During Indentation Testing*, Paper presented at the Conference: 2004 SEM X International Congress & Exposition on Experimental & Applied Mechanics.

Zar, J. H., 2010, *Biostatistical Analysis*, 5th Edition, Prentice Hall.

Zhang, G. and Sun, Z., 2001, *Mechanical properties of melamine-formaldehyde microcapsules*, Journal of Microencapsulation, 18, 5, 593-602.

Zhang, H., Schuster, B. E., Wei, Q. and Ramesh, K. T., 2006, *The design of accurate micro-compression experiments*, Scripta Materialia, 54, 2, 181-186.

Zhang, Z., Ferenczi, M. A. and Thomas, C. R., 1992, *A micromanipulation technique with a theoretical cell model for determining mechanical properties of single mammalian cells*, Chemical Engineering Science, 47, 6, 1347-1354.

Zhang, Z., Saunders, R. and Thomas, C. R., 1999, *Mechanical strength of single microcapsules determined by a novel micromanipulation technique*, Journal of Microencapsulation, 16, 1, 117-124.

Zheng, L., Huo, X. S. and Yuan, Y., 2008, *Strength, Modulus of Elasticity, and Brittleness Index of Rubberized Concrete*, Journal of Materials in Civil Engineering, 20, 11, 692-699.

Ziskind, D., Fleischer, S., Zhang, K., Cohen, S. R. and Daniel Wagner, H., 2010, *A novel experimental method for the local mechanical testing of human coronal dentin*, Dental Materials, 26, 2, 179-184.

Zügner, S., 2002, *Untersuchungen zum elastisch-plastischen Verhalten von Kristalloberflächen mittels Kraft-Eindringtiefen-Verfahren*, Thesis from the Bayerischen Julius Maximilians Universität Würzburg.

Zügner, S., Marquardt, K. and Zimmermann, I., 2006, *Influence of nanomechanical crystal properties on the comminution process of particulate solids in spiral jet mills*, European Journal of Pharmaceutics and Biopharmaceutics, 62, 2, 194-201.

Zysset, P. K., Edward Guo, X., Edward Hoffler, C., Moore, K. E. and Goldstein, S. A., 1999, *Elastic modulus and hardness of cortical and trabecular bone lamellae measured by nanoindentation in the human femur*, Journal of Biomechanics, 32, 10, 1005-1012.

3. EXPERIMENTAL METHODOLOGY

3.1 Introduction

This chapter details the preparation and testing methods carried out in this work. Owing to the sample dimensions (10-50 μm) the experimental methods were chosen for their suitability to investigate the mechanical properties of micron-scale samples. Sample morphology and surface were characterised using SEM and AFM. Mechanical testing was performed by nanoindentation and micro-compression techniques. The purpose of the nanoindentation procedure was to measure and compare the elastic modulus and hardness of all the samples used in this work. The micro-compression testing technique was used to further characterize the mechanical properties of the composite crystals and to evaluate their deformation and fracture behaviour under compression. By using the micro-compression testing technique, mechanical properties such as compressive strength, compressive modulus, strain at fracture and energy absorption capacity prior to fracture were obtained. By dividing these mechanical properties by the respective density of the crystals, specific mechanical properties were also obtained.

Seven different types of calcite single crystal were tested by nanoindentation in order to measure and compare their moduli and hardness. These crystals were biogenic calcite from a sea urchin spine, Iceland spar (a mineral form of calcite) and five synthetic crystals. One of the synthetic crystals was pure calcite, and was used as a control, the other synthetic crystals were calcite composites with different amounts of polystyrene inclusions and a calcite composite occluded with di-block co-polymer micelles. All these samples were kindly provided by Prof. Fiona Meldrum and Dr Yiyeoun Kim (Chemistry, University of Leeds), as this project formed was a collaborative EPSRC funded programme. The micro-compression studies were divided in two parts. In the first part three synthetic crystals (control and two composites (1.8 vol.% PS and 6 vol.% PS)) were tested. In the second part the same samples (control and two composites (1.8 vol.% PS and 6 vol.% PS)) were first machined by focused ion beam (FIB) into cubic shapes prior to testing. Due to the late

availability of the composite occluded with di-block co-polymer micelles, only the composites occluded with PS were tested under compression.

3.2 Production of synthetic crystals

The protocols for the production of all the samples used in this work were elaborated by the group of Prof Fiona Meldrum and Dr Yi-Yeoun Kim (Chemistry, University of Leeds). All the synthetic crystals were produced by the ammonia diffusion method. In this method a solution of calcium chloride in an open Petri dish is placed in a desiccator, together with some ammonium carbonate in another dish (Figure 3.1)

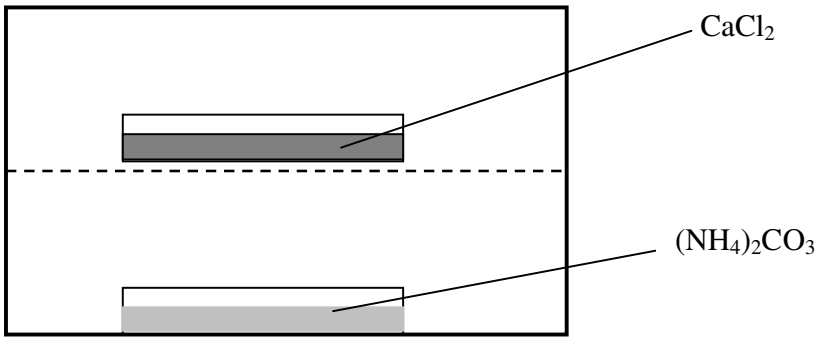

Figure 3.1 Dessicator containing the Petri dishes.

Ammonium carbonate, $(NH_4)_2CO_3$, is in the form of a solid powder, which decomposes slowly to give ammonia, water, and carbon dioxide, according to equation

$$(NH_4)_2CO_{3\,(s)} \longrightarrow NH_{3(g)} + H_2O_{(l)} + CO_{2\,(g)}$$

Ammonia and carbon dioxide then diffuse slowly into the calcium chloride solution, with the following equilibria:

$$NH_{3\,(aq)} + H_2O_{\,(l)} \longleftrightarrow NH_4^+{}_{(aq)} + OH^-{}_{(aq)}$$

$$CO_{2\,(aq)\,)} + H_2O_{\,(l)} \longleftrightarrow H_2CO_{3\,(aq)}$$

$$H_2CO_{3\,(aq)} + H_2O_{(l)} \longleftrightarrow HCO_3^-{}_{(aq)} + H_3O^+{}_{(aq)}$$

This finally allows calcium carbonate crystals to form following the equation

$$CO_3^{2-}{}_{(aq)} + Ca^{2+}{}_{(aq)} \longleftrightarrow CaCO_{3(s)}$$

Solutions (1.25 mM) containing 10 ml of calcium chloride ($CaCl_2.2H_2O$) were placed in 3.5 cm Petri dishes, and polystyrene particles (PS), functionalized with acrylic acid groups (PS/15%AA), were added at different concentrations (Table 3.1):

Table 3.1 Synthetic crystals produced with different PS amounts and sizes.

n	Samples (PS initial concentration)	Particle size filler (nm)	Final volume fraction of occluded PS
1	Pure calcite (control)	-	0 vol.% PS
2	0.005 % wt PS	200	1.8 vol.% PS
3	0.02 % wt PS	200	6 vol.% PS
5	0.1 % wt PS	200	23 vol.% PS

The concentration of 0.005 % was the minimum PS concentration added to the initial solution that allowed the occlusion of 1.8 vol.% PS throughout the entire crystal. Concentrations lower than 0.005 % resulted in occlusion of PS only at the crystals' surface. The concentration of 0.02 % in the initial solution allowed the production of rhombohedral crystals. This permitted a comparison between different samples (1.8 vol.% PS, 6 vol.% PS and control) under the same shape in the compression experiments. Concentrations of 0.1 % PS in the initial solution produced crystals with a rugby ball shape and resulted in the maximum amount of PS occlusion (23 vol.%). A calcite-polymer composite, occluded with 29 vol.% di-block co-polymer micelles functionalised with anionic carboxylated chain groups, was also produced by the group of Prof. Fiona Meldrum and Dr Yiyeoun Kim (Kim, Y.-Y. *et al.*, 2011). The volume fraction of this composite was determined by Dr Yiyeoun Kim using thermogravimetric analysis. The 20 nm co-polymer micelles were

added to a 10 ml calcium chloride solution (1.5 mM) at a concentration of 70 mg L^{-1}. This concentration allowed an efficient occlusion of the polymer throughout the entire crystal. Glass cover slips which had been prior-cleaned with Piranha solution were placed at the base of the dishes, which were then transferred to a sealed desiccator containing a vial of solid ammonium carbonate. Crystallisation was then allowed to proceed for up to 5 days, after which time the glass slides were removed from solution, and were washed with water before being allowed to air dry (Kim, Y.-Y. *et al.*, 2010; Kim, Y.-Y. *et al.*, 2011). In order to estimate the volume fraction of occluded PS in each sample the Delesse relation (Underwood, 1970) was used, *i.e*

$$V_V \approx A_A \qquad (3.2)$$

where V_V is the volume fraction and A_A is the area fraction of a component. By using the Delesse principle, the volume fraction of the 3D polymer spheres in each composite was calculated by the area fraction of the 2D PS circles at the composite surface. The area of the 2D PS particles in the crystal surface was calculated from SEM images of the FIB machined composites using image analysis software (imageJ).

3.3 Nanoindentation

3.3.1 Preparation of samples for nanoindentation

After being dried, all the synthetic crystals were embedded at room temperature in a styrene-based polyester casting resin, 'kleer set resin' (MetPrep Ltd, Curriers Close, Coventry, UK), prior to nanoindention. This procedure was necessary in order to have a resin cylinder with a flat surface with the crystals horizontal and at the same level. This procedure was a requirement of the nanoindentation system utilised; any deviation from horizontal leads to large variation in mechanical properties. A biogenic single crystal from sea urchin spine and a mineral form of calcite (Iceland spar) were also embedded at room temperature in a styrene-based polyester casting resin cylinder.

The embedded sea urchin spine and Iceland spar calcite specimens were first ground with silicon carbide paper of increasing grades of fineness, and were then polished on soft cloths embedded with 1 μm 0.5 μm and 0.25 μm diamond slurry prior to nanoindention. Synthetic crystals of pure calcite (control) were also embedded in two other mounting compounds resins. One of the resins, 'Di-hard' (MetPrep Ltd), was a styrene-based polyester resin filled with a silica quartz (SiO_2) mineral powder and was prepared at ambient temperature. The other resin, 'ProbeMet' (Buehler, WMG International Manufacturing Centre, Coventry, UK), was a thermosetting epoxy resin filled with copper (Cu) and silica quartz. The ProbeMet resin, which contained the previously added samples, was prepared at 150 ºC under a pressure of 200 bar.

3.3.2 Nanoindentation of samples

The mechanical properties of all the samples were studied using a nanoindenter XP (MTS, Nano Instruments Innovation Center, Oak Ridge, USA) (Figure 3.2), equipped with a Berkovich pyramidal tip and a × 40 microscope objective.

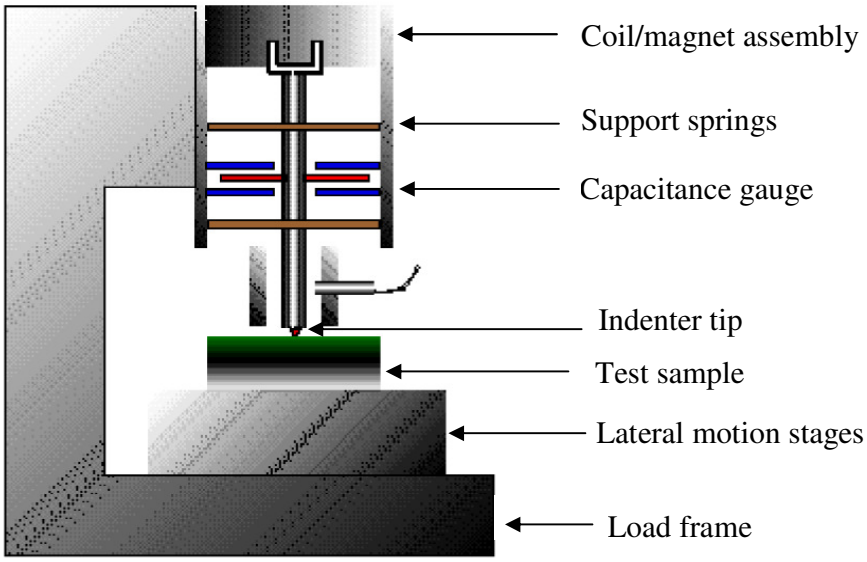

Figure 3.2 Schematic of a nanoindenter XP (MTS, 2002).

The nanoindenter XP uses the operating system software Testworks 4. This software uses the Oliver-Pharr data analysis method to obtain mechanical properties. The software procedure employed was the XP basic hardness, modulus, tip calibration, with constant stiffness measurement (CSM). This procedure allows the hardness and modulus measurements as a function of depth. Tip shape calibration (or area-function calibration) was performed on a fused silica (SiO_2) calibration standard provided with the system. The objective of this calibration is to measure the cross-sectional area, A, of the indentation tip as a function of the distance, *d*, from the apex, also called the contact depth. The area-function calibration is the process of determining the best-fit coefficients according to equation

$$A(d) = a_0 d^2 + a_1 d + a_2 d^{1/2} + a_3 d^{1/4} \ldots \qquad (3.1)$$

where a_0, a_1,…, a_i are the coefficients calculated by the Testworks 4 software method "XP Basic Tip Calibration" procedure (MTS, 2002). The theoretical modulus for fused silica is 73 GPa and the hardness is 9 GPa (MTS, 2002). Since fused silica is homogeneous, the hardness and modulus should not vary with depth. In addition, fused silica is non-reactive, so surface effects will be negligible if the surface is free of debris and moisture. Tests on fused silica were also performed regularly in order to check if excessive tip rounding, contamination of the tip or other possible sources of error had occurred. Typical hardness and modulus data obtained for fused silica are reported in Figures 3.3 and 3.4. The allowable drift rate was 0.05 nm s^{-1} and the approach velocity was 50 nm s^{-1}. The surface approach distance and surface approach distance were 1000 nm with a surface approach sensitivity of 25 % and strain rate of 0.05 s^{-1}. A holding period at the maximum load of 10 s was also used in order to allow creep displacement to become negligible.

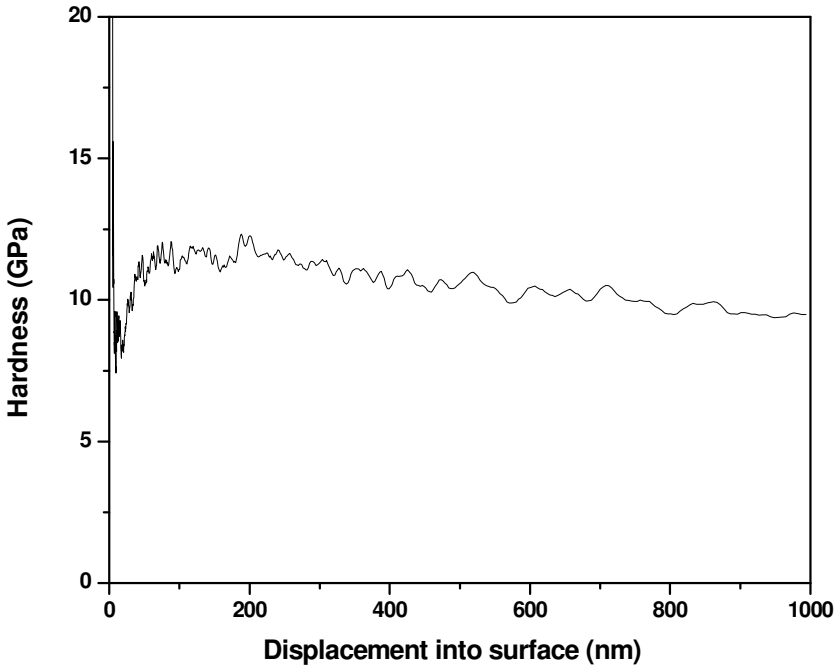

Figure 3.3 Typical hardness data plotted as a function of depth for fused silica (calibration sample) using the CSM method.

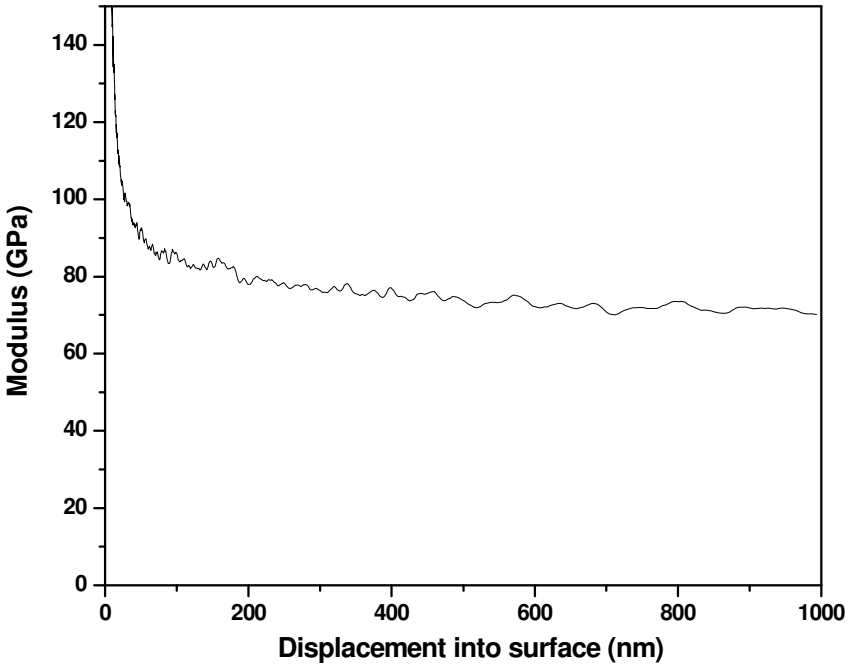

Figure 3.4 Typical elastic modulus data plotted as a function of depth for fused silica (calibration sample) using the CSM method.

Poisson's ratio of pure calcite (ν = 0.28) was used as an approximation of the composite's unknown Poisson's ratio in order to calculate the mechanical properties. Since the Poisson's ratio of polystyrene is 0.34, the composites Poisson's ratios should be somewhat larger than 0.28. In isotropic materials, errors of 10 % in the elastic modulus have been reported for variations in the Poisson's ratio from 0.25 to 0.45 (Rho *et al.*, 1997; Zysset *et al.*, 1999). Since our composites Poisson's ratios should be below 0.34 the errors associated with the elastic modulus should be well below 10 %. The mounting resin cylinders containing all the samples were then mounted on the nanoindenter sample tray which was fixed on the nanoindenter motion system (Figure 3.5). This system is responsible for moving the samples under the nanoindenter tip and objective according to software instructions.

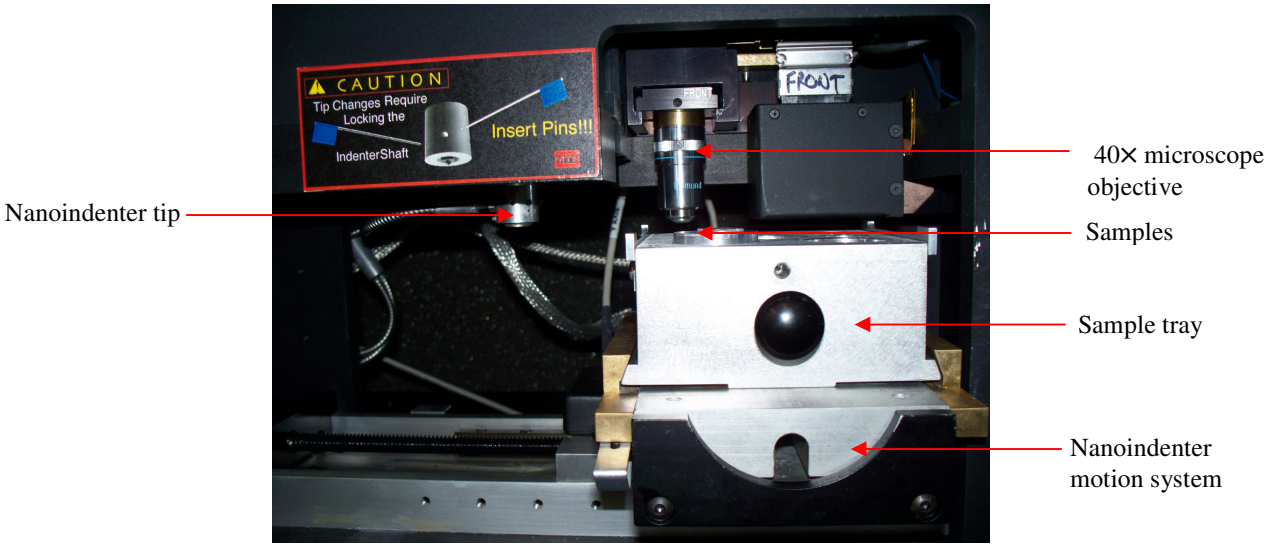

Figure 3.5 Nanoindenter motion system with sample tray containing the sample.

Due to the small sample dimensions (10-50 µm) and nanoindenter precision some alignment correction procedures were performed prior to each test. The first procedure was a "Microscope to Indenter Calibration" on an aluminum calibration standard provided with the system. The relative softness of this material, coupled with the highly polished surface,

allow for the creation of a large and visible indentation. After a sample had been selected, another microscope to indenter calibration was performed near the sample.

The indenter tip was cleaned between tests with a cotton swab soaked with isopropyl alcohol. The purpose of this cleaning process was to avoid the accumulation of microscopic debris attached to the tip which could influence the test results. Finally the mean unloading elastic modulus and hardness were obtained from ten representative properties-displacement curves for each sample, recorded at a fixed depth of 500 nm. This depth was chosen as a compromise in order to overcome tip rounding effects at depths under 200 nm, and to avoid substrate influence and crack formation at larger depths. When the sample size is comparable to the indent size, the indentation-induced plastic zone can be affected by the sample boundary.

For accurate determination of hardness within an error of 5 % it is recommended that the specimen radius should be more than 3.3 times the indent radius (Xu, Z. H. and Li, 2006). Considering an indent radius of ~ 1.5 μm for a 500 nm indentation, the specimen radius should be larger that 5 μm. Since the smallest crystal sample used in this work has a radius larger than 5 μm, the measured mechanical properties should not be affected by sample boundary effects. The polymer particle sizes (20 nm and 200 nm) used as fillers in the calcite matrix are also much smaller than the scale of deformation produced by the indentation. These tests were also used to measure the substrate independent modulus and hardness, as described in Sections 2.14 and 2.15. The specific hardness and modulus were obtained by dividing the substrate independent modulus and hardness by the density of each sample. The density of the samples was calculated by the sum of the partial density ρ_i of each component (calcite and polymer) in the composite according to the equation

$$\rho = \sum_i \rho_i \qquad (3.3)$$

The partial density ρ_i of each component was obtained by using the density of each component and their respective volume fraction in the composite according to the equation

$$\rho_i = \rho \frac{V_i}{V} \qquad (3.4)$$

where V_i/V is the volume fraction of each component. The density of calcite, co-polymer micelles, PS, and biomolecule utilised were 2.71 g cm^{-3} (Defoe *et al.*, 1925), 1.0 g cm^{-3} (Kim, Y.-Y. *et al.*, 2011), 1.06 g cm^{-3} (Bangs, 2010), and 1.35 g cm^{-3} (Podrazky and Sedmerova, 1966) respectively.

3.4 Micro-compression

3.4.1 Micro-sample fabrication using Focused Ion Beam (FIB) milling

Four crystals of each sample (control and two composites (1.8 vol. % PS and 6 vol. % PS)) were first machined using a FIB into a cubic shape prior to testing by micro-compression. The size and shape of the 10 μm^3 cubic samples were chosen, taking into consideration original crystals sizes (15-30 μm), the maximum allowed load before a risk of tip damage (500 mN) and time saving factors in the machining procedure employed. The micro-sample fabrication methodology used in this work is based on FIB milling (see Section 2.21).

The crystal samples (originally grown on a 1 cm^2 and 1 mm thick silicon wafer) to be machined were first selected according to location and size. In order to facilitate the milling of the sample by the incident beam the crystal had to be located near the border of the silicon wafer. The crystal sample also had to be at a sufficient distance from other surrounding crystals or particles. This condition was necessary in order to compress a single chosen crystal, and not others proximal to it (Figure 3.6). The size of the crystals was also an important factor to take into consideration since the choice of crystals much larger than 10 μm^3 would have required a much longer milling time. Once the crystal was selected, the milling procedure was performed using a Novolab 200 Dual Beam FIB (FEI Ltd, Philips House, Cambridge, UK) operated at voltage up to 20 kV (Ga^+ beam) with a maximum beam current of 110 pA.

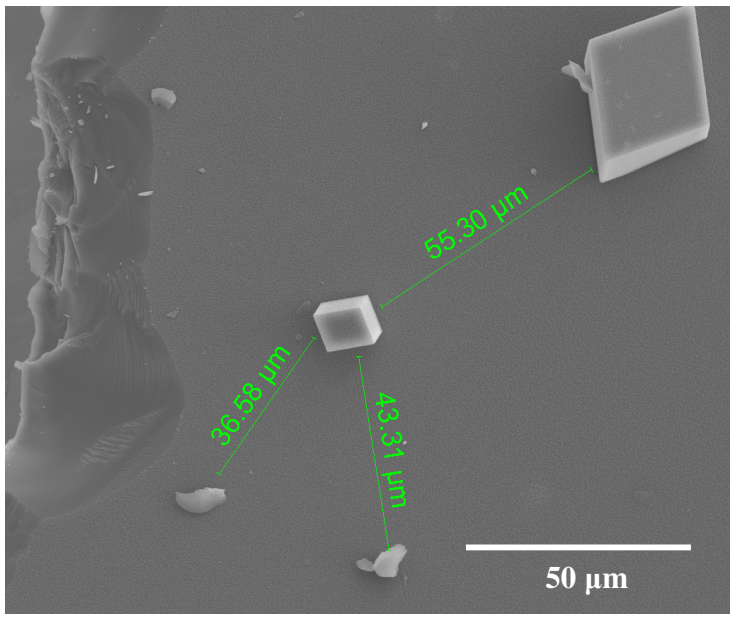

Figure 3.6 A typical SEM image of the field of view used to select an appropriate crystal sample for FIB milling.

3.4.2 Micro-compression of synthetic calcite composites

The micro-compression methodology followed in this thesis is based on that suggested by Uchic *et al*., (2004). In order to carry out micro-compression experiments the typical nanoindenter Berkovich pyramidal tip was replaced by a 100 µm diameter flat punch tip. The micro-compression experiments were divided in two parts. In the first part, three synthetic crystals (control and two composites (1.8 vol.% PS and 6 vol.% PS)) were tested. In the second part the same samples (control and two composites (1.8 vol.% PS and 6 vol.% PS)) were first machined by FIB into cubic (10 μm^3) shape prior to testing. The silicon wafers containing the samples were first fixed to a glass slide with cyanocrylate glue. The glass slide was then fixed to the nanoindenter aluminium cylinder stub with double tape. This set-up was necessary to reduce as much as possible any possible compliance of the system silicon wafer-glass slide- aluminium cylinder. Before each test, the silicon wafer was tested in compression (Figure 3.7) in order to check for system compliance or a contaminated tip.

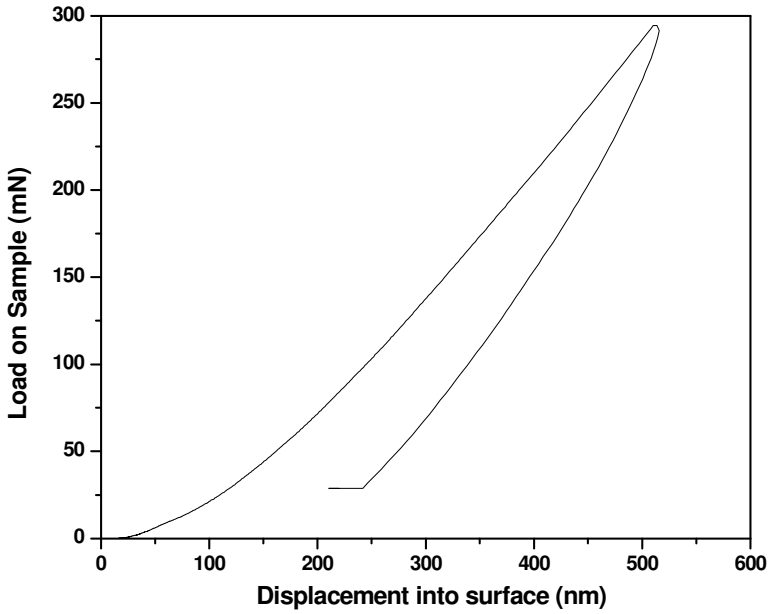

Figure 3.7 A typical load-displacement curve from a micro-compression of the silicon substrate using a clean tip.

Before each test the "Microscope to Indenter Calibration" alignment correction procedure were performed. The indenter tip was also cleaned before each test with a cotton swab soaked with isopropyl alcohol (Figure 3.8 and 3.9).

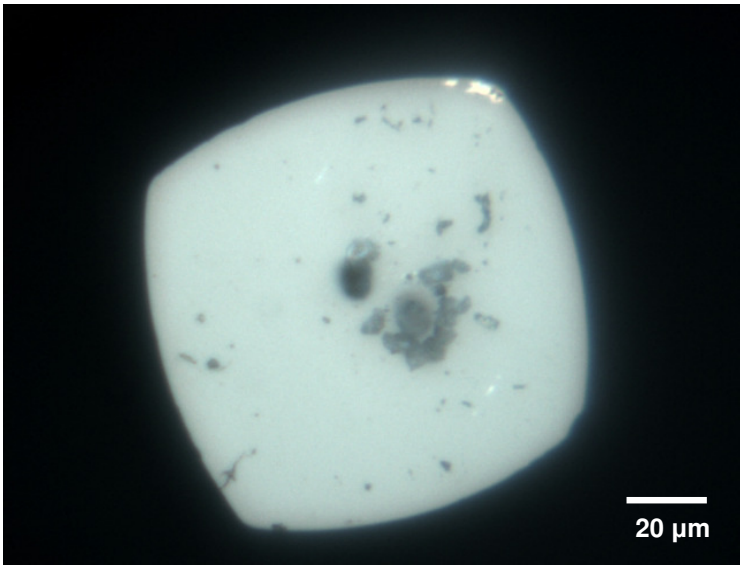

Figure 3.8 Optical microscope image of a flat tip (100 µm) for micro-compression experiments with crystal debris attached to its surface.

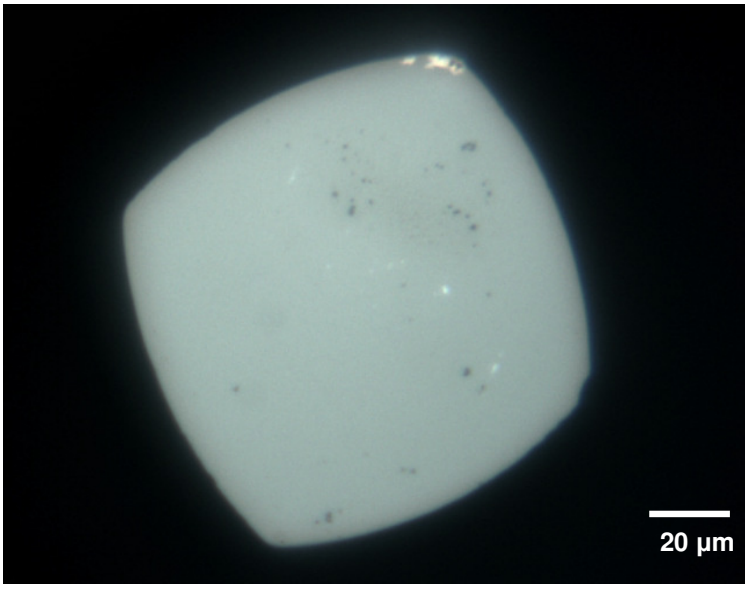

Figure 3.9 Optical microscope image of a cleaned flat tip (100 µm) for micro-compression experiments.

Ten synthetic crystals for each sample (control and two (1.8 vol.% PS and 6 vol.% PS)) were then selected and tested. The load-displacement curve of each test was converted to an engineering stress-strain curve by using the dimensions of each crystal (Tables 3.2-3.4).

Table 3.2 Synthetic pure calcite (control) crystals dimensions and maximum force at fracture.

n	Maximum Force (N) $\times 10^{-1}$	Area (μm^2)	Area (m^2) $\times 10^{-10}$	Height (µm)
1	2.8	31 × 35	11.1	30.3
2	4.0	29 × 29	8.6	29.1
3	3.7	26 × 26	6.7	25.6
4	4.4	34 × 30	10.0	29.4
5	3.6	35 × 29	11.0	29.2
6	4.3	28 × 29	8.3	27.9
7	4.4	33 × 31	9.7	30.3
8	3.4	35 × 32	11.1	31.5
9	4.3	33 × 34	11.1	32.5
10	2.3	31 × 35	11.1	30.3

Table 3.3 Synthetic calcite (1.8 vol.% PS) composite crystals dimensions and maximum force at fracture.

n	Maximum Force (N) $\times 10^{-1}$	Area (μm)	Area (m^2) $\times 10^{-10}$	Height (μm)
1	1.8	22 × 26	5.7	17.3
2	2.3	27 × 30	8.1	20.5
3	1.9	26 × 26	6.8	18.7
4	1.6	22 × 22	4.8	15.8
5	1.2	22 × 18	4.0	14.3
6	1.0	22 × 26	5.7	17.3
7	1.4	19 × 20	3.8	14.2
8	3.1	22 × 22	4.8	15.8
9	2.1	28 × 30	8.4	20.3
10	2.8	31 × 33	10.2	23.0

Table 3.4 Synthetic calcite (6 vol.% PS) composite crystals dimensions and maximum force at fracture.

n	Maximum Force (N) $\times 10^{-1}$	Area (μm^2)	Area (m^2)$\times 10^{-10}$	Height (μm)
1	1.1	18 × 21	3.7	13.5
2	1.9	24 × 28	6.6	18.1
3	2.0	29 × 29	8.6	22.6
4	1.5	24 × 29	6.9	18.1
5	1.7	24 × 24	5.5	18.1
6	1.8	24 × 24	5.5	18.1
7	2.3	35 × 35	11.3	21.4
8	2.1	35 × 29	11.0	22.6
9	2.4	38 × 39	11.5	28.9
10	1.4	29 × 29	8.6	22.3

The dimensions of the selected parallelepiped shaped crystals were measured by using a MicroXam surface mapping microscope equiped with the mapping and analysis software

MapVue (Phase Shift Technology Inc., Tucson, AZ, USA). The aspect ratio (Height/Side) of these crystals was 0.99 ± 0.13 for the control, 0.72 ± 0.1 for the 1.8 vol.% PS and 0.75 ± 0.05 for the 6 vol.% PS composites. As already discussed in point 2.20.2 the UCS is significantly decreased when the specimen aspect ratios are larger than 2.0. Studies on limestone have shown however that the UCS is not significantly affected when the aspect ratio approaches 1.0 (Tuncay and Hasancebi, 2009). The same studies found that a decrease in the aspect ratio from 1.5 to 1.0 would only increase the UCS from 76.6 ± 1.5 MPa to 77.1 ± 2.1 MPa. The maximum applied load was 450 mN, with an approach velocity of 100 nm s^{-1} and a strain rate of 0.05 s^{-1}. Composite crystals (control and two composites (1.8 vol.% PS and 6 vol.% PS) which had been previously shaped into 10 μm^3 cubes were also compressed using the same procedure, but using a maximum applied load of 300 mN instead.

The stress was calculated by dividing the recorded load by the initial area of crystal (engineering stress). This initial area corresponds to the crystal surface in contact with the flat tip indenter. The compressive modulus represents the stress-strain ratio in the elastic region and was determined as the slope of the stress–strain curve within the linear region. The compressive strength is the stress at the ultimate structural failure. The point of ultimate structural failure was taken to be the longest and last step in the stress-strain curve. This step, represented by a plateau in the curve, corresponds to a discontinuity in the indenter motion caused by a sudden advance of the flat punch at constant load. The energy absorption capacity (work of fracture) was calculated from the stress-strain curves according to Equation 2.39 (in Section 2.18). For this the trapezoid area calculation method was used.

The area under a flat (slope = 0) stress-strain curve was not taken into consideration in the total work computation since no force was exerted on the flat punch during this portion of the curve. Ten tests were selected for each sample and mean mechanical property values were obtained (compressive strength, compressive modulus, fracture strain (%) and work to fracture). In order to compare the means between samples several statistical comparison procedures were utilised (see Appendix). All these statistical calculations were performed

using the softwares IBM SPSS Statistic 17 and excel 2007. The specific compressive mechanical properties were obtained by dividing these by the density of each sample. The density of the samples was calculated according to equations 3.3 and 3.4 (see Section 3.3.2).

3.5 Scanning Electron Microscopy (SEM)

SEM was used in order to obtain pre- and post-test images of the samples. The purpose of this was to analyse the surface, morphology and dimensions of the samples prior and after testing. The scanning electron microscope used was a FEG SEM Philips XL30 (FEI Ltd, Philips House, Cambridge, UK) operated at voltage of 10 kV. An Olympus BH–2 optical microscope (Olympus Optical Co Ltd, London, UK) a JEOL JSM 6300 (JEOL Ltd, Welwyn Garden City, UK) and a Zeiss EVO-60 VP SEM system (Carl Zeiss Ltd, Cambridge, UK) were also used to locate the indented crystals prior to imaging them.

3.5.1 Preparation of samples for SEM

Because the SEM utilizes vacuum conditions and uses electrons to form an image, special preparations of the samples must take place. Since all the samples in this work were non-conducting they required coating prior to imaging them with the SEM. This was done by covering the sample with a thin layer of conductive material (gold) using an Edwards S150B sputter coater unit (Eduards, Eduards Global Headquarters, West Sussex, UK). For this the samples were first placed in a small chamber in a vacuum. The chamber is filled gradually with argon gas and an electric field (40 mA) causes electrons to be removed from the argon, making the atoms positively charged. The argon ions then become attracted to a negatively charged gold foil. The argon ions knock gold atoms from the surface of the gold foil which then fall and settle onto the surface of the sample, producing a thin gold coating.

3.6 Atomic force microscopy measurements

AFM studies were carried out to analyse and measure the dimensions of the residual indents. The residual indent area was calculated by using the measured height (L) of the residual pyramidal impression, according to Equation 2.32 (Section 2.15). AFM measurements were performed with a Digital Instruments CP-II (Veeco Instruments Ltd,

Cambridge, UK) at room temperature. Since the samples used in this work were hard and smooth enough, the images were obtained in contact mode at a gain between 0.2 and 0.5. The scan rate of the cantilever was 0.7 Hz. The UnitV 2000 and Proscan 1.9 software packages were used to process and analyse the AFM images.

3.7 References

Bangs, 2010, *Bangs laboratories, Inc.*

Defoe, O. K., Compton and Arthur, H., 1925, *The Density of Rock Salt and Calcite*, Physical Review, 25, 5, 618-620.

Kim, Y.-Y., Ribeiro, L., Maillot, F., Ward, O., Eichhorn, S. J. and Meldrum, F. C., 2010, *Bio-Inspired Synthesis and Mechanical Properties of Calcite–Polymer Particle Composites*, Advanced Materials, 22, 18, 2082-2086.

Kim, Y.-Y., Ganesan, K., Yang, P., Kulak, A. N., Borukhin, S., Pechook, S., Ribeiro, L., Kroger, R., Eichhorn, S. J., Armes, S. P., Pokroy, B. and Meldrum, F. C., 2011, *An artificial biomineral formed by incorporation of copolymer micelles in calcite crystals*, Nat. Mater., 10, 890-896.

MTS, S. C., 2002, *XP user's guide*, Systems Corporation MTS.

Podrazky, V. and Sedmerova, V., 1966, *Densities of collagen dehydrated by some organic solvents*, Cellular and Molecular Life Sciences, 22, 12, 792-792.

Rho, J. Y., Tsui, T. Y. and Pharr, G. M., 1997, *Elastic properties of human cortical and trabecular lamellar bone measured by nanoindentation*, Biomaterials, 18, 20, 1325-1330.

Tuncay, E. and Hasancebi, N., 2009, *The effect of length to diameter ratio of test specimens on the uniaxial compressive strength of rock*, Bulletin of Engineering Geology and the Environment, 68, 4, 491-497.

Uchic, M. D., Dimiduk, D. M., Florando, J. N. and Nix, W. D., 2004, *Sample dimensions influence strength and crystal plasticity*, Science, 305, 5686, 986-989.

Xu, Z. H. and Li, X. D., 2006, *Sample size effect on nanoindentation of micro-/nanostructures*, Acta Materialia, 54, 6, 1699-1703.

Zysset, P. K., Edward Guo, X., Edward Hoffler, C., Moore, K. E. and Goldstein, S. A., 1999, *Elastic modulus and hardness of cortical and trabecular bone lamellae measured by nanoindentation in the human femur*, Journal of Biomechanics, 32, 10, 1005-1012.

4. MECHANICAL PROPERTIES OF COMPOSITE CRYSTALS BY MICRO-COMPRESSION

The micro-compression experiments were divided into two parts. In the first part, three synthetic crystals (control and two composites (1.8 vol.% PS and 6 vol.% PS)) were tested under compression. In the second part of this work, the same synthetic crystals used in the first part (control and two composites (1.8 vol.% PS and 6 vol.% PS) were first machined by FIB milling into a cubic (10 μm^3) shape prior to testing. This allowed a comparison between machined and non-machined crystal samples specimens. Although a selection was performed in order to obtain non-machined crystals of the same sizes and aspect ratios, some differences still exist, not only inside a group of crystals of the same sample but also between samples. The upper sides of the non-machined crystals were also found to suffer from a lack of parallelism. The purpose of machining the sample crystals into 10 μm^3 specimens was to rule out any effect (different size, aspect ratio, lack of parallelism) that could mask the influence of different PS content between the tested specimens. Machined samples also allowed the contact area during compression to be more precisely known, giving a better estimate of compressive strengths of the materials studied.

4.1 Scanning electron microscopy

Scanning electron microscopy allowed the observation and comparison of the crystal deformation behaviour that occurs under load, as well as other crystal features. Because of limited resourses, *in situ* SEM mechanical testing was not used in this work. Figures 4.1 and 4.2 show a synthetic pure calcite crystal (control) before and after compression by flat punch testing. Figure 4.1 shows that the calcite crystal is a rhombohedral shape, as is typical for this form of calcium carbonate. Figure 4.2 shows that through compression the entire pure calcite crystal fractures into multiple small fragments. This fracture behaviour therefore confirmed the characteristic brittle behaviour of pure calcite. This behaviour is replicated for the pillar specimens, whereby a regularly shaped pillar for the pure calcite crystal (Figure 4.3) is fractured into many pieces after flat punch compression (Figure 4.4).

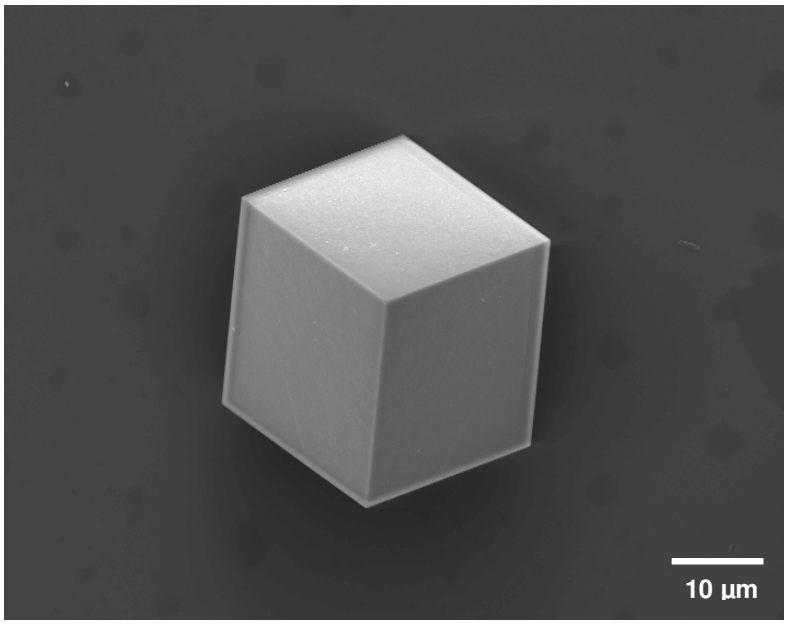

Figure 4.1 Synthetic pure calcite crystal (control).

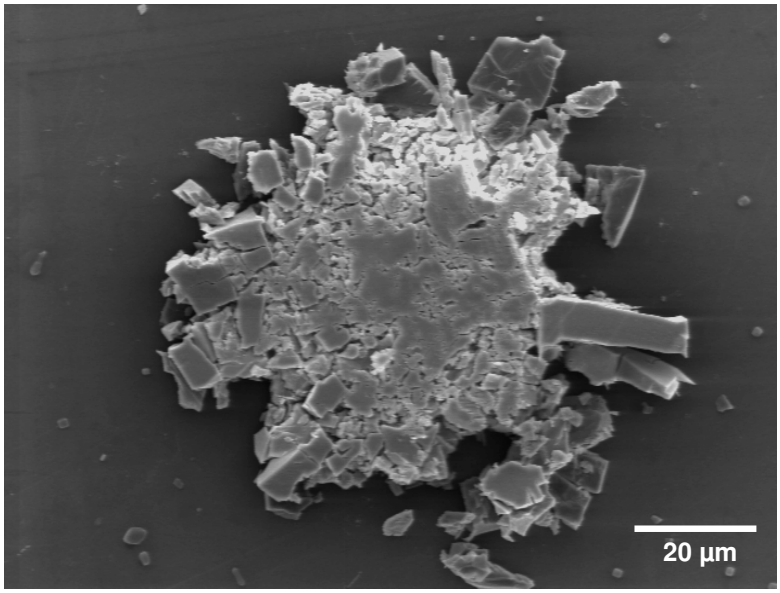

Figure 4.2 Flat punch compressed pure calcite crystal (control) (450 mN maximum load).

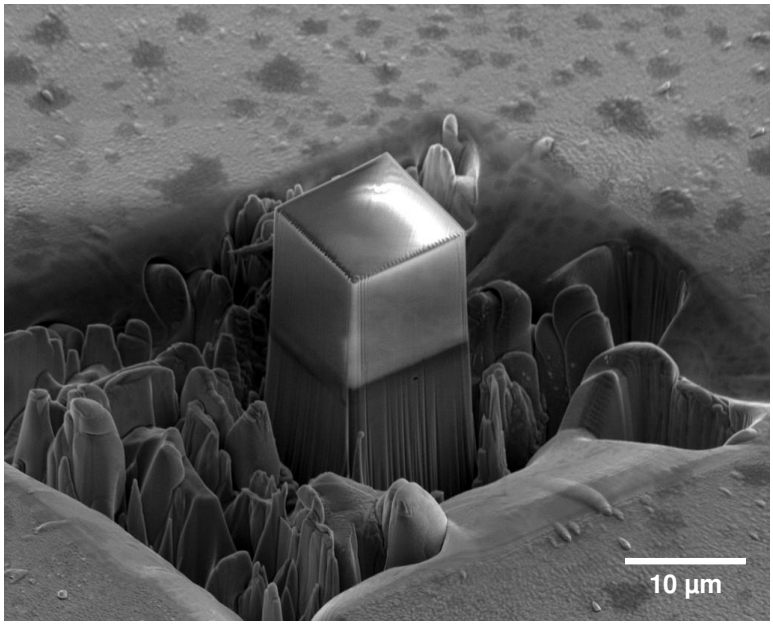

Figure 4.3 FIB machined pure calcite crystal (control).

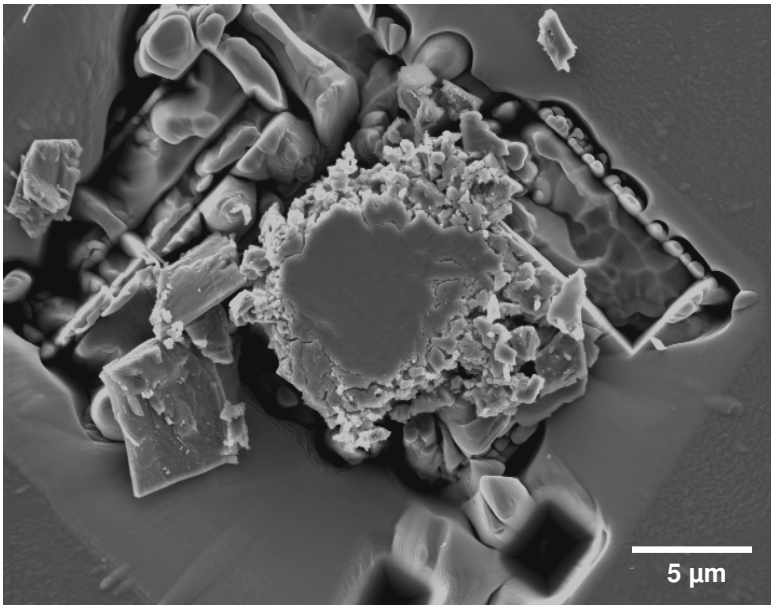

Figure 4.4 Compressed FIB machined pure calcite crystal (control) (300 mN maximum load).

Figures 4.5 and 4.6 show a synthetic composite crystal with 1.8 vol.% occluded 200 nm PS particles, before and after compressed by the flat punch respectively.

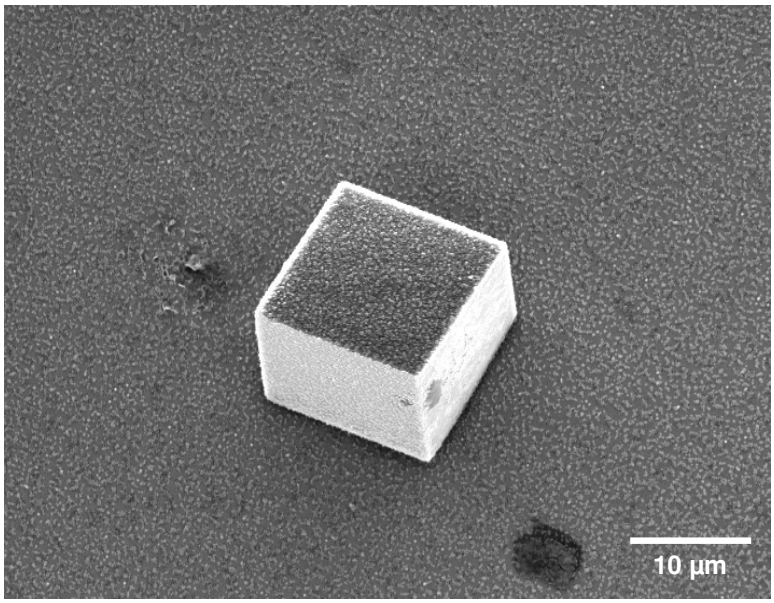

Figure 4.5 Composite crystal with 1.8 vol.% PS.

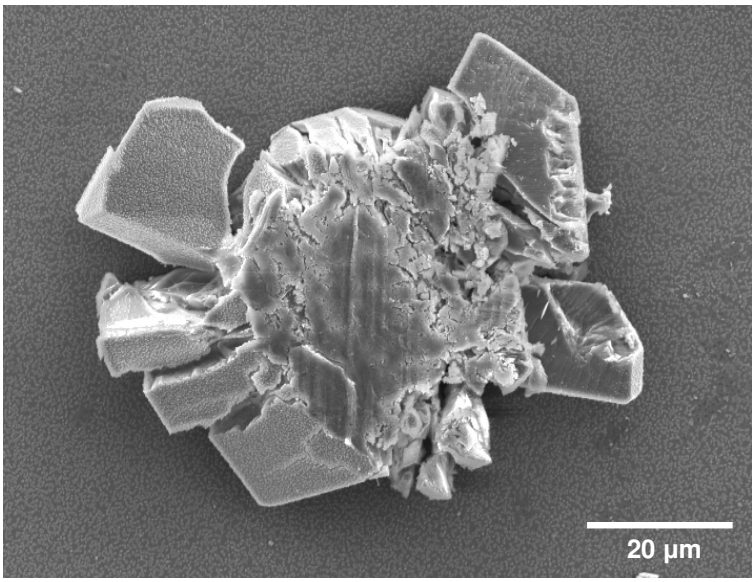

Figure 4.6 Compressed composite crystal with 1.8 vol.% PS (450 mN maximum load).

Figure 4.5 shows that the crystal maintains the same rhombohedral shape seen for synthetically produced calcite without inclusions. Figure 4.6 further shows that the compression of this composite crystal is characterised by the formation of fractures surfaces which separate the crystal into large blocks. The compression of this composite crystal did not lead therefore to the formation of small fragments, as was the case in pure calcite. This shows that the occluded PS particles appear to reduce the characteristic brittle behaviour of calcite. Figure 4.7 shows the surface of a synthetic composite crystal with 1.8 vol.% occluded 200 nm PS particles. This image shows that a large number of PS particles are visible at the composite's surface.

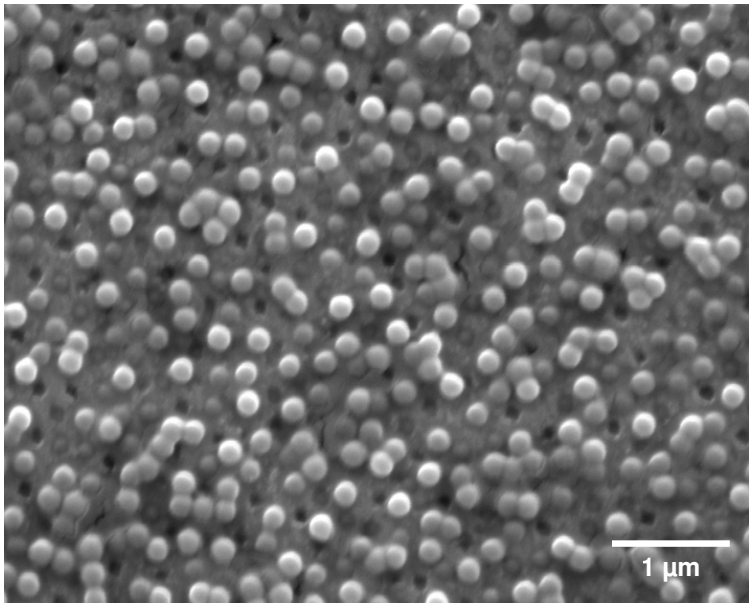

Figure 4.7 Surface of composite crystal with 1.8 vol.% PS.

Figure 4.8 shows an inner fractured surface of the same composite crystal. This image shows that the PS concentration below the surface is much lower than at the surface. It is also observed that some PS particles have been deformed by the fracture process. This deformation of the polymer is an indication of a strong calcite-PS interface. This synthetic composite crystal was also machined into a 10 μm^3 cube (Figure 4.9) and compressed with the flat punch (Figure 4.10).

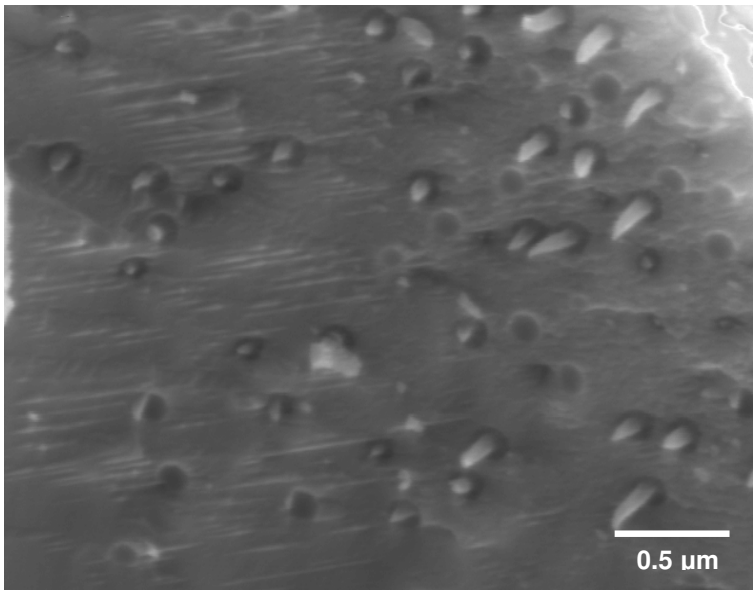

Figure 4.8 Fractured surface of a compressed composite crystal with 1.8 vol.% PS.

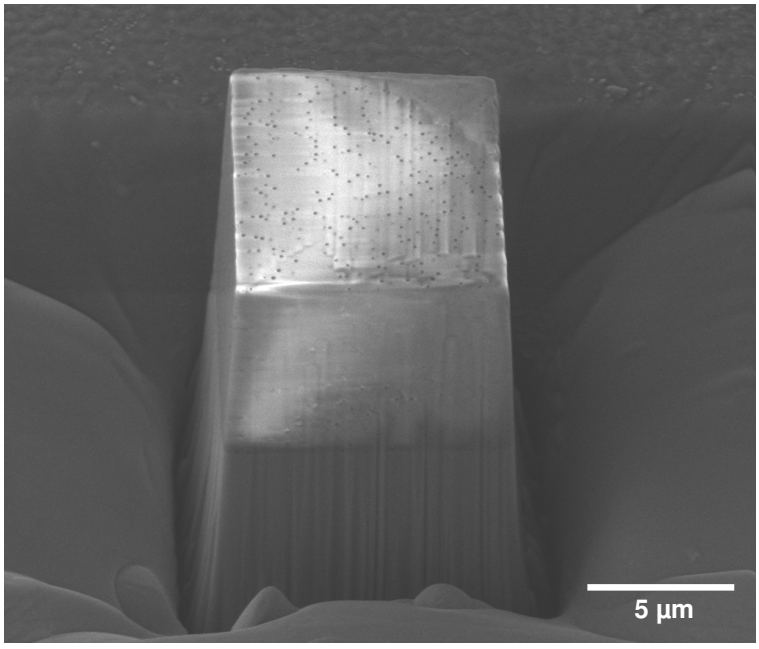

Figure 4.9 FIB machined composite crystal with 1.8 vol.% PS.

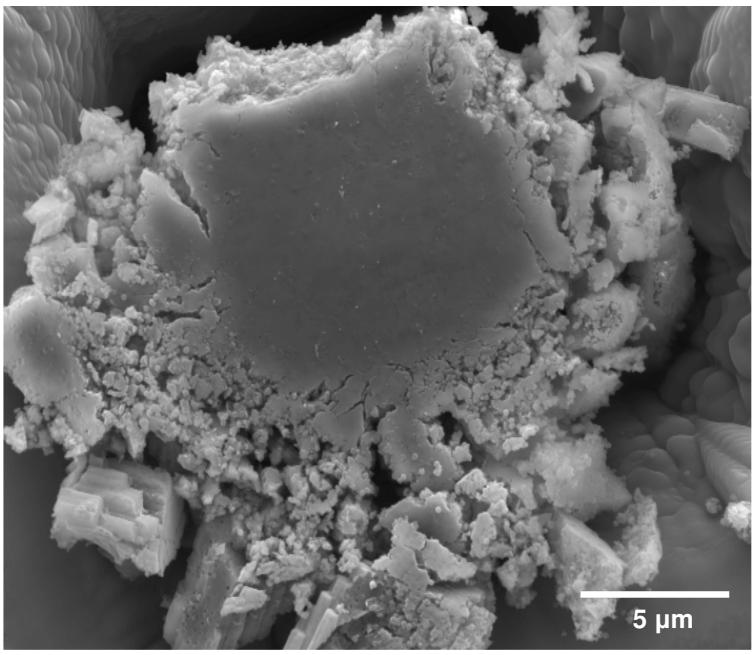

Figure 4.10 Flat punch compressed FIB machined composite crystal with 1.8 vol.% PS.

Figures 4.11 and 4.12 show a synthetic composite crystal with 6 vol.% occluded 200 nm PS particles, before and after respectively, being compressed by the flat punch.

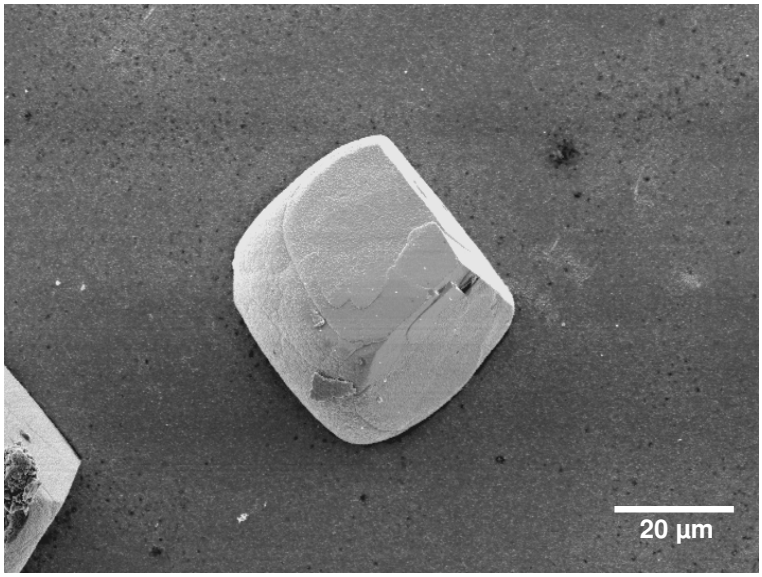

Figure 4.11 Composite crystal with 6 vol.% PS.

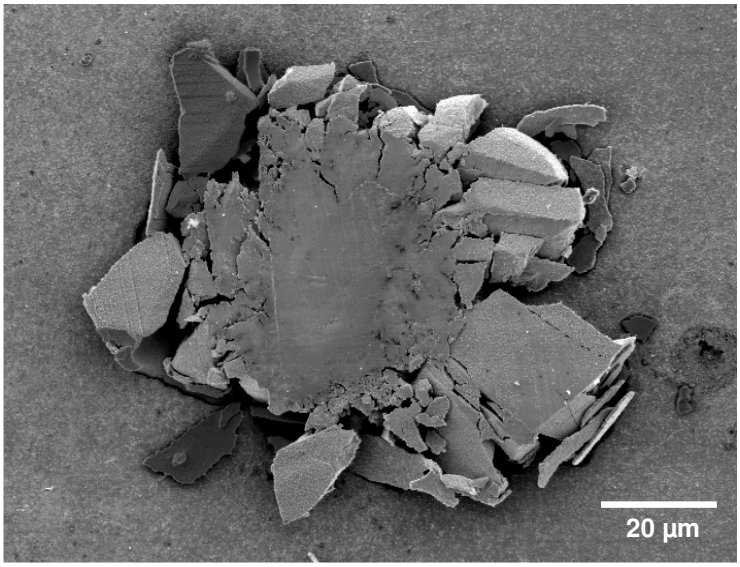

Figure 4.12 Flat punch compressed composite crystal with 6 vol.% PS (450 mN maximum load).

As was the case for the composite with 1.8 vol.% PS, the compression of this composite was also characterised by the formation of fractures which separated the crystal into much larger pieces than those observed for pure calcite crystals. No significant differences in the sizes or numbers of the formed blocks, post-fracture, were observed between the composites with 1.8 vol.% PS and 6 vol.% PS.

In Figure 4.13 it is again observed (as in Figure 4.8) that the PS particles have been deformed during fracture. The deformation of the polymer also indicates that a potential crack bridging mechanism is occurring (Section 2.8.2), whereby material remains connected to either side of the crack zone. This synthetic composite crystal was also machined into a 10 μm^3 cube (Figure 4.14) and compressed using the flat punch (Figure 4.15).

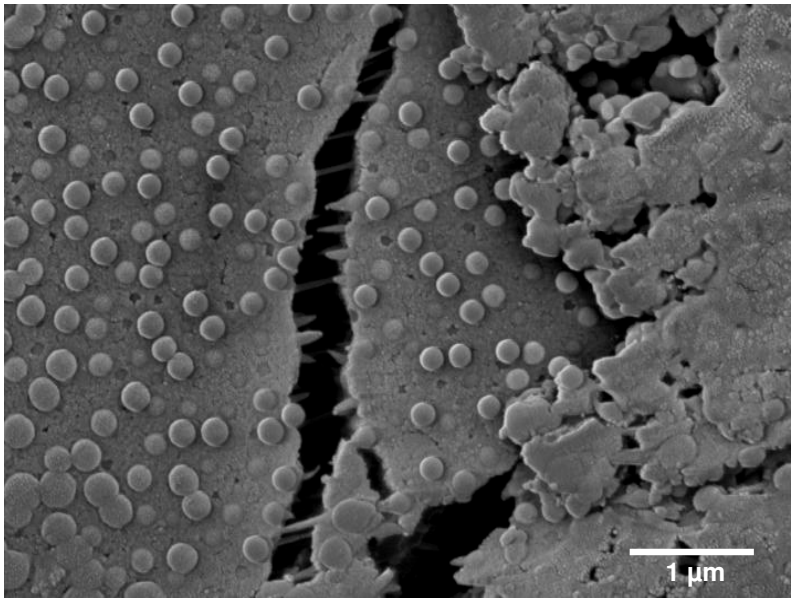

Figure 4.13 Fractured surface of compressed composite crystal with 6 vol.% PS.

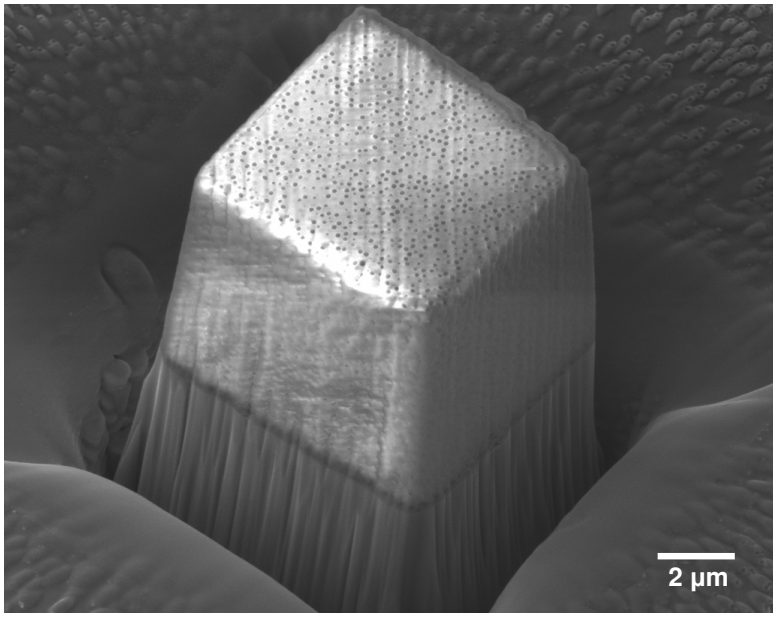

Figure 4.14 FIB machined composite crystal with 6 vol.% PS.

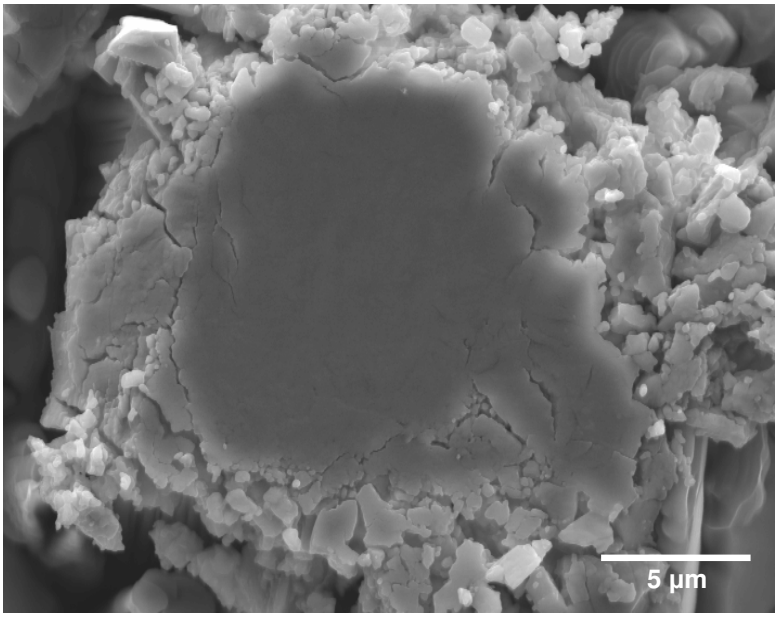

Figure 4.15 Flat punch compressed FIB machined composite crystal with 6 vol.% PS.

Figure 4.16 shows a synthetic composite crystal with 23 vol.% PS after being compressed by a Berkovich tip. This figure shows that the occlusion of 23 vol.% 200 nm PS particles changed the characteristic rhombohedral shape of the pure calcite crystal into a "rugby ball" shaped crystal.

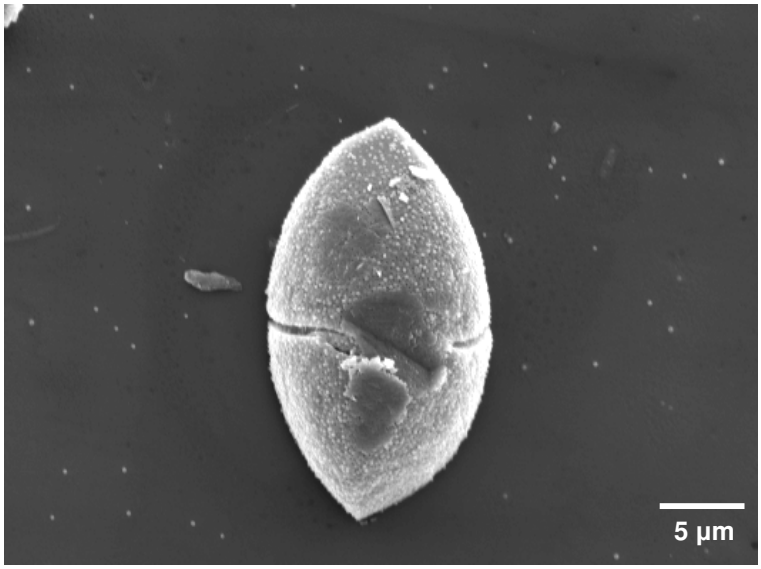

Figure 4.16 Composite crystal with 23 vol.% PS.

An indentation of this composite crystal gave rise to a large fracture, which allowed the deformation of the PS particles to be observed in greater detail (Figure 4.17).

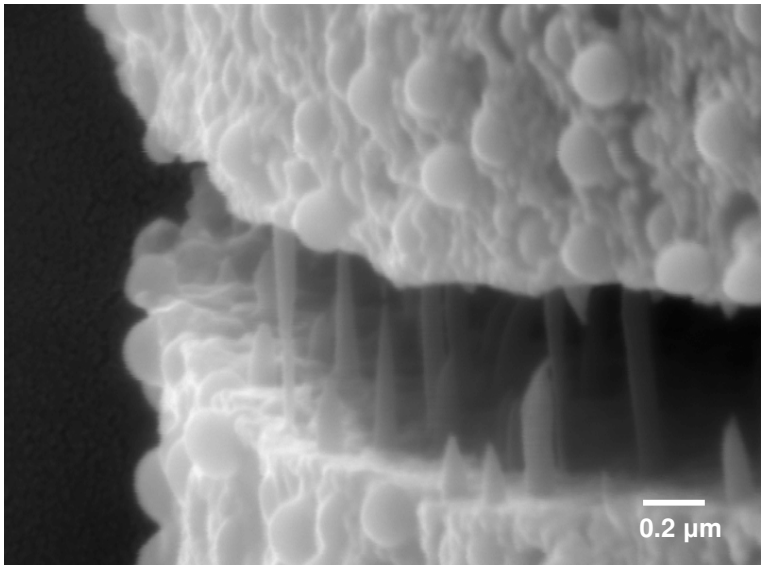

Figure 4.17 Inner details of a fracture on the composite crystal with 23 vol.% PS.

4.2 Compressive mechanical properties

Figures 4.18 show representative engineering stress-strain curves obtained by compressing the non-machined composite crystals (1.8 vol.% and 6 vol.% occluded 200 nm PS particles) and pure calcite crystals (control) with a flat punch. These curves reveal the deformation behaviour leading to the crystal fracture (ultimate structural failure). The final fracture occurs when the slope of the curve approaches zero (leading to a plateau in the stress-strain curve). The point of final fracture in the curve corresponds to the uniaxial compressive strength (UCS) (S_u) (highlighted by arrows in Figure 4.18). It is observed that the fracture of the control crystal (pure calcite) occurred at a lower strain level. Contrasting with the single step compression of the control, the stress-strain curves of the composite crystals showed that the fracture occurred at higher strain, with the formation of an intermediate step (highlighted by arrows in Figure 4.18) before final fracture. The stress increase at the end of the curves is caused by the compression of the crystals debris by the flat punch after the final fracture of the crystals.

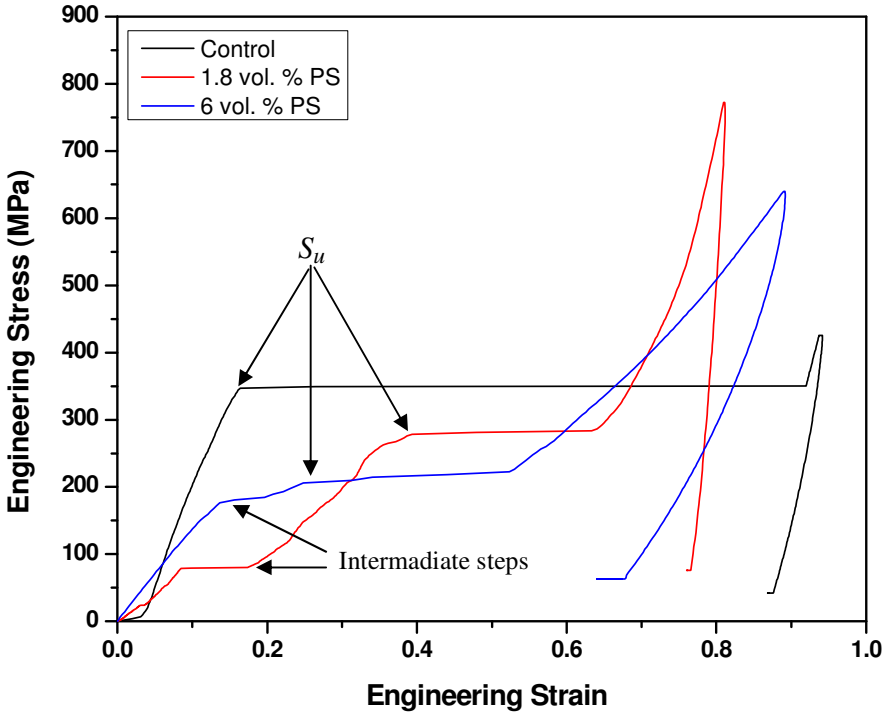

Figure 4.18 Enginnering stress-strain curves for bulk compression of non-machined synthetic pure calcite crystals (control) and synthetic calcite composites with 1.8 vol.% PS and 6 vol.% PS.

Figures 4.19 show representative engineering stress-strain curves obtained by compressing the 10 μm^3 cube machined composite crystals (1.8 vol.% PS and 6 vol.% PS) and pure calcite (control) with a flat punch tip. It is noted that the fracture of the composite crystals occurred in a single step event as was the case for the machined and non-machined pure calcite crystal (control). The intermediate steps observed for the non-machined composite crystals before fracture may reflect the lack of initial parallelism between the flat tip and the top of the crystal surface at the contact zone. This lack of parallelism could induce a non-uniform pressure distribution in the contact zone and initiate a premature cracking process. After the linear proportionality between stress and strain, the slope of the stress-strain curves of pure calcite and the composite crystals with 1.8 vol.% PS start to decrease gradually before final structural failure occurs. As discussed in Section 2.19 of the literature review this effect is associated with plastic deformation and micro-fracturing (Mogi, 1973). The fact that this behaviour is not observed in the composite with 6 vol.% PS may indicate

a reduction of the micro-fracturing process introduced by the occlusion of more polymeric material.

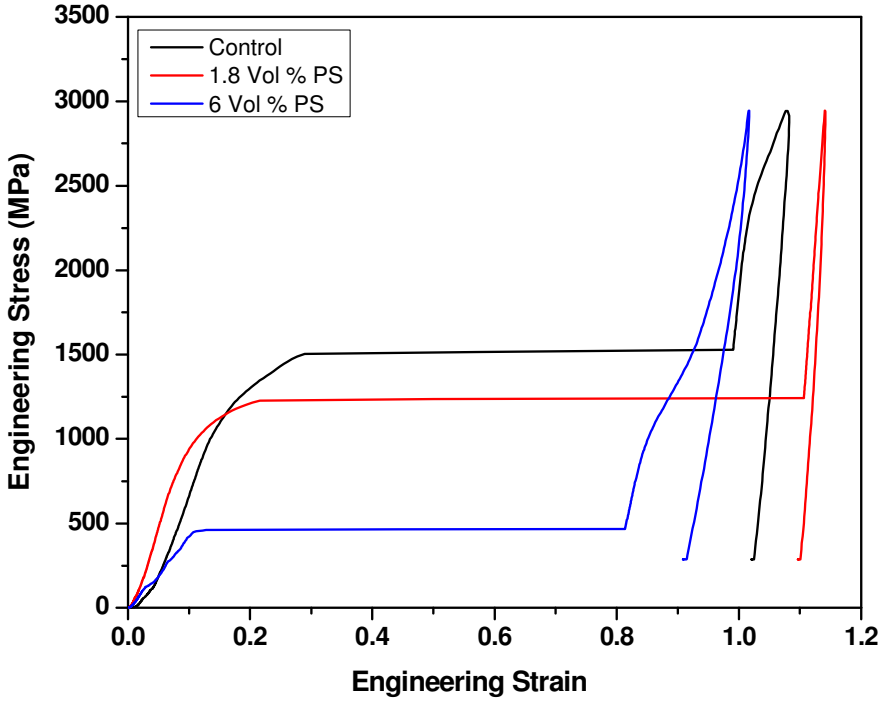

Figure 4.19 Enginnering stress-strain curves for bulk compression of 10 μm^3 cube machined synthetic pure calcite crystals (control) and synthetic calcite composites with 1.8 vol.% PS and 6 vol.% PS.

Tables 4.1 and 4.2 report the mean compressive mechanical properties obtained for the non-machined and machined crystal samples respectively.

Table 4.1 Compressive mechanical properties of non-machined specimens crystals.

Samples *	Compressive strength (UCS) (MPa)	Work of fracture (Jm^{-3}) × 10^6	fracture strain (%)	Compressive modulus (*Ec*) (MPa)
Pure calcite (control)	392 ± 112	40.3 ± 22.9	17.7 ± 5.8	2645 ± 394
Calcite with 1.8 vol. % PS	308 ± 52	39.6 ± 7.9	28.0 ± 5.2	1423 ± 670
Calcite with 6 vol. % PS	234 ± 59	32.7 ± 13.1	22.9 ± 8.3	1490 ± 403

*Means ± SD from 10 samples for each calcite crystal

Table 4.2 Compressive mechanical properties of 10 μm^3 machined specimens crystals.

Samples *	Compressive strength (UCS) (MPa)	Work of fracture (Jm^{-3}) × 10^6	fracture strain (%)	Compressive modulus (*Ec*) (MPa)
Pure calcite (control)	1143 ± 259	157 ± 69	22.1 ± 5.8	9724 ± 1054
Calcite with 1.8 vol. % PS	1052 ± 181	84.2 ± 55	12.9 ± 5.7	11057 ± 1497
Calcite with 6 vol. % PS	374 ± 74	17.6 ± 6.4	8.7 ± 2.6	4803 ± 1538

*Means ± SD from 4 samples for each calcite crystal

Figure 4.20 compares the ultimate compressive strengths (UCS) of machined and non-machined crystal specimens.

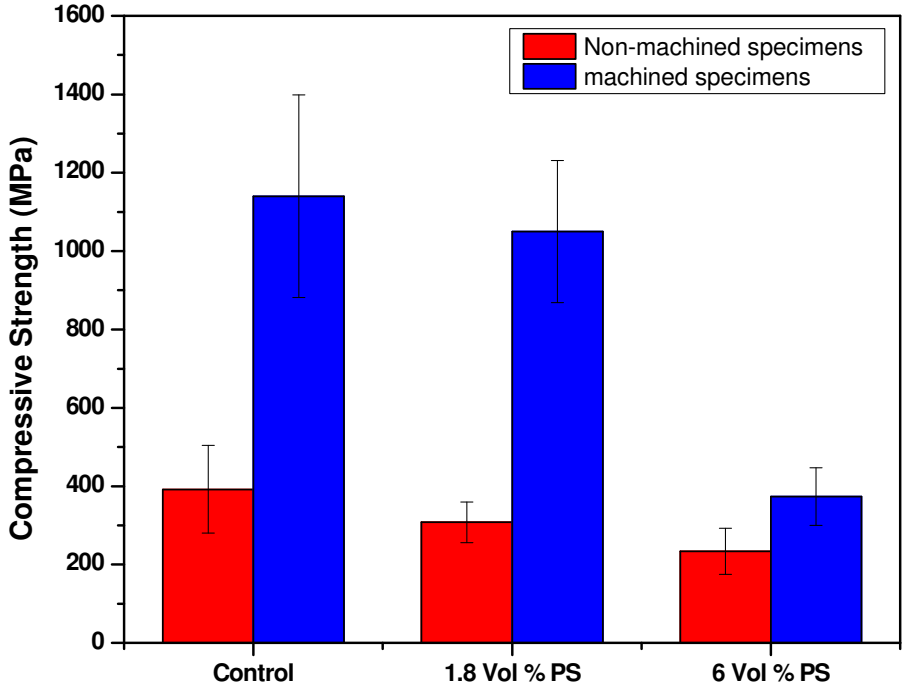

Figure 4.20 Compressive strength of non-machined and 10 μm^3 machined specimens: Synthetic pure calcite crystals (control) and synthetic calcite composites crystals with 1.8 vol. % PS and 6 vol. % PS.

Comparison of the mean values using the Games-Howell procedure at a 95 % confidence level indicated that the compressive strength of the non-machined pure calcite specimens

was reduced by the inclusion of 6 vol. % PS ($p = 0.004$, Table 7.3 in Appendix). No significant difference was found between the non-machined pure calcite specimens (control) and the non-machined composite occluded with 1.8 vol. % PS ($p = 0.129$, Table 7.3 in Appendix). A more detailed discussion of the statistical methods applied can be found in Appendix. It is observed that the machined specimens have significantly larger UCS than non-machined specimens. A larger initial contact misfit between the indenter flat tip and the top of the non-machined crystal surfaces could contribute to lower the UCS of these crystals (Section 2.20.3). The UCS obtained for both machined and non-machined pure calcite specimens (control) were also much larger than values (70-140 MPa) reported in the literature for larger specimens (Weber *et al.*, 1969). This is possibly due to the size scale effect discussed in Section 2.20.1.

A Tukey test at a 95 % confidence level showed no statistical difference between the UCS of the machined composite with 1.8 vol.% PS and the one of pure calcite (control) ($p = 0.776$, Table 7.6 in Appendix). The reduction in UCS was particularly significant for the machined composite with 6 vol.% PS ($p = 0.001$, Table 7.6 in Appendix). Experiments performed on concrete filled with rubber particles showed that the decrease in the compressive strength of the tested specimens could reach values as high as 85 %, depending to rubber content (Eldin and Senouci, 1993). The possible reasons for this strength reduction were attributed to the reduction of the quantity of the solid load-carrying material with increasing rubber content, the weak bonding between rubber and mortar and to stress concentrations at the filler-matrix boundaries (Zheng *et al.*, 2008). Eldin and Senouci (1993) found that a mathematical model that describes the effect of porosity on the strength reduction of concrete could also be applied to rubber filled concrete.

Since PS has a much lower elastic modulus than calcite, the polymer occlusions could produce a similar effect to pores in the calcite structure, and be the source of stress concentrations. This could lead to a large strength reduction in the calcite-polymer composite and explain the low UCS obtained for the 6 vol.% PS composite. By using a pore volume fraction of 6 vol.% and Equation 2.8 (Section 2.9), which expresses the reduction in compressive strength according to pore fraction, a prediction of strength

reduction as high as 40 % is found. The UCS of the pure calcite specimen was reduced by about 70 % with the occlusion of 6 vol.% PS particles. Even if the larger PS volume fraction at the top surface of the machined crystal (8.8 vol.% PS) is used in Equation 2.8 the obtained reduction (52 %) is still much lower than the one obtained. It is possible that the UCS may have been affected by the stress concentrations located at the top of the specimen, where cracks could easily initiate and propagate into the entire specimen. Some experiments have shown that the impact of highly-accelerated Ga^+ ions produced in the FIB milling process could produce defects such as amorphisation, dislocations or ion implantation over a layer that is tens of nanometers thick (Kiener *et al.*, 2007; McCaffrey *et al.*, 2001; Uchic and Dimiduk, 2005). The FIB milling can thus damage the polymer or calcite-polymer interface and could have affected significantly the mechanical properties of the 6 vol.% PS composite. SEM observations of the machined composites' surfaces however showed no evidence of such damage. The influence of the FIB milling process on the composite mechanical properties will require therefore further investigation. Figure 4.21 compares the compressive modulus of machined and non-machined crystal specimens.

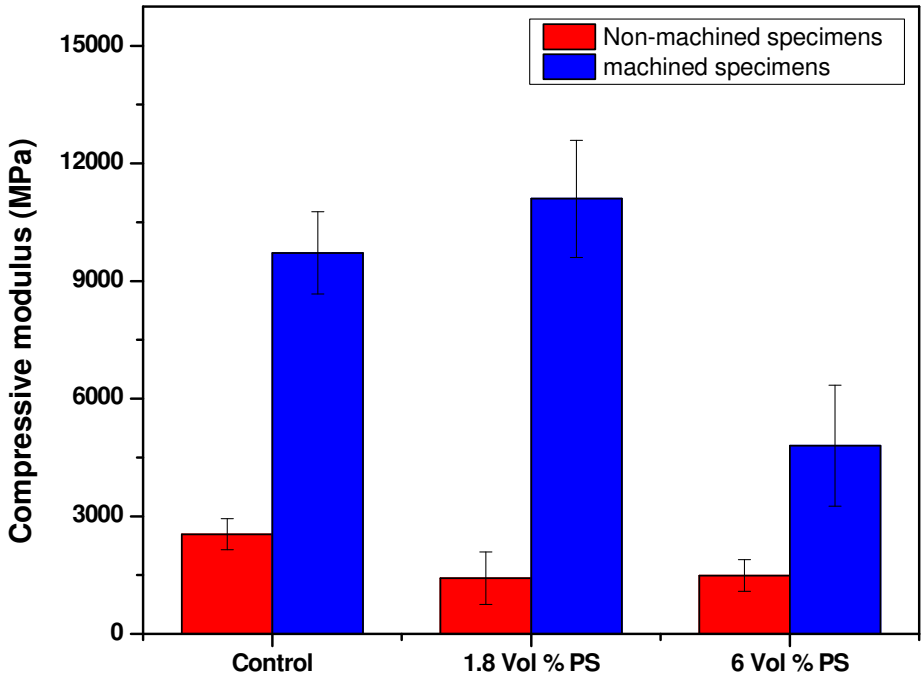

Figure 4.21 Compressive modulus of non-machined and 10 μm^3 machined specimens: Synthetic pure calcite crystals (control) and synthetic calcite composites crystals with 1.8 vol.% PS and 6 vol.% PS.

These data show that the machined specimens appear to have a higher modulus than the non-machined specimens. This could be a size scale effect, but is probably due to the larger initial contact misfit mentioned earlier in relation to the UCS. A Tukey HSD test at a 95 % confidence level showed no statistical difference between the compressive modulus of the machined composites with 1.8 vol.% 200 nm PS particles and that of pure calcite (control) ($p = 0.520$, Table 7.9 in Appendix). From Figure 4.21 it is observed that the compressive modulus of the machined pure calcite specimens was significantly reduced by the occlusion of 6 vol.% 200 nm PS particles ($p = 0.003$, Table 7.9 in Appendix). This could also be due to the quantity reduction of the solid load-carrying material and/or stress concentrations at the filler-matrix boundaries. The compressive modulus of the non-machined pure calcite specimens was also found to have been reduced by both 1.8 and 6 vol.% occluded PS ($p = 0.000$ for both, see Table 7.12 in Appendix). Figure 4.22 compares the strain at fracture (%) between machined and non-machined crystal specimens. It is noted that for the machined specimens the strain at fracture of pure calcite was significantly reduced by the inclusion of 6 vol.% PS ($p = 0.010$, Table 7.15 in Appendix).

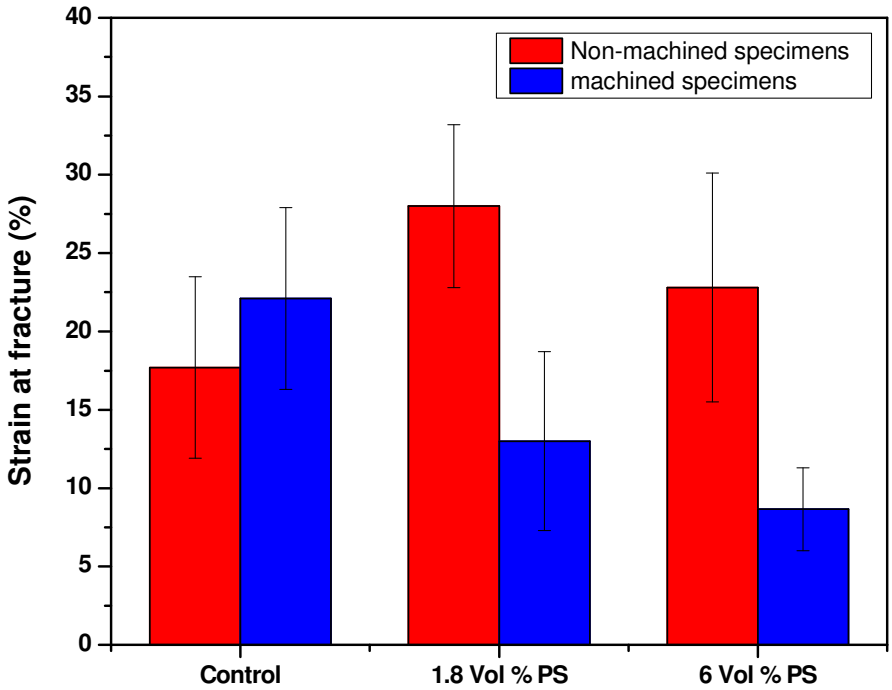

Figure 4.22 Strain at fracture for non-machined and 10 μm^3 machined specimens: Synthetic pure calcite crystals (control) and synthetic calcite composites crystals with 1.8 vol.% PS and 6 vol.% PS.

No statistical difference was found between pure calcite and the machined composite occluded with 1.8 vol.% PS ($p = 0.066$, Table 7.15 in Appendix). This trend was not observed for the non-machined specimens, which showed an increase in the strain at fracture by the inclusion of 1.8 vol.% PS ($p = 0.021$, Table 7.18 in Appendix). The larger strain at fracture for the non-machined composites compared to the non-machined pure calcite control is possibly caused again by a larger initial misfit (lack of parallelism) between the indenter flat tip and the top of these crystal surfaces. This initial misfit would cause these crystals to collapse more gradually, increasing thereby the strain at fracture. Figure 4.23 compares the work of fracture (see Section 2.18) for the machined and non-machined crystal specimens. A Games-Howell test at a 95 % confidence level showed no statistical difference between the work of fracture of the non-machined control crystal and the non-machined composites with 1.8 vol.% PS ($p = 0.996$) or 6 vol.% PS ($p = 0.666$, Table 7.21 in Appendix). No statistical difference was found between the work of fracture of the machined composites with 1.8 vol.% PS and that of pure calcite (control) ($p = 0.155$, Table 7.24 in Appendix).

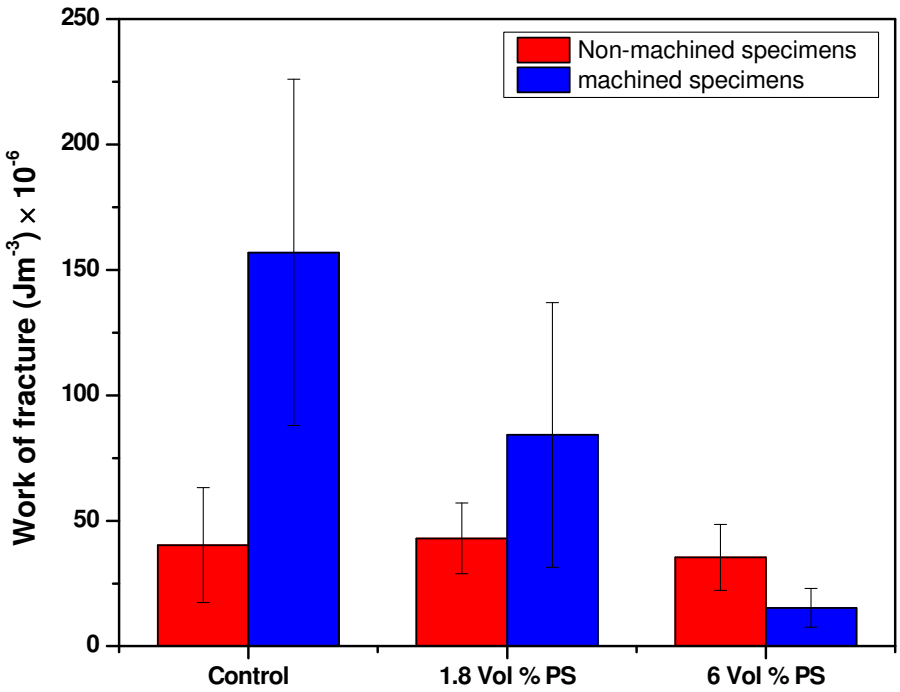

Figure 4.23 Work of fracture for non-machined and 10 μm^3 machined specimens: Synthetic pure calcite crystals (control) and synthetic calcite composites crystals with 1.8 vol.% PS and 6 vol.% PS.

From Figure 4.23 it is observed that the work of fracture of the machined pure calcite specimens was significantly reduced by the occlusion of 6 vol.% 200 nm PS particles ($p = 0.009$, Table 7.24 in Appendix). This low energy absorption capacity is an expected result since the work of fracture depends on the compressive strength and strain at fracture and both these parameters were significantly reduced by the occlusion of 6 vol.% 200 nm PS particles. The early catastrophic failure of this composite prevented therefore further energy consumption during the compression test.

Although stress concentrations originated by rubber particles, pores or voids generally lower the fracture strength of brittle materials the work of fracture may not follow the same trend. Compression studies on concrete filled with rubber particles showed an increase in the energy absorption capacity of this composite up to 25 vol.% of rubber content (Khaloo *et al.*, 2008). Beyond rubber concentrations of 25 %, Khaloo *et al*. (2008) found a decrease in the energy absorption capacity of the composite due to the gradual reduction in strength. Compression studies have also shown that although sea urchin spine has up to 60 vol.% porosity, its energy absorption capacity was found to be higher than conventional porous alumina ceramic (~ 20 vol.% porosity) (Presser *et al.*, 2009). These tests were however performed on segments of the spine which are characterised by a complex and diverse structure. Further compression tests will be necessary to study the compressive properties of sea urchin spine at the micro-scale level and compare these results to pure calcite.

4.3 Specific compressive mechanical properties

Since for some engineering applications (Section 2.7.1) weight minimization is an important factor, the specific compressive strengths (S_u/ρ), moduli and work of fracture of the machined specimens were calculated and compared (see Figures 4.24, 4.25 and 4.26).

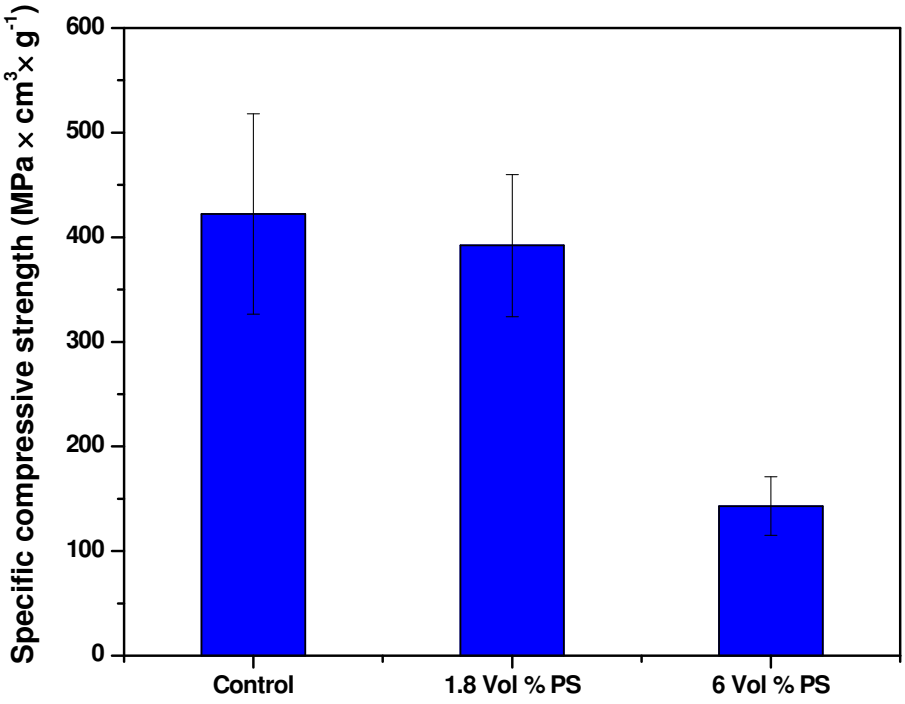

Figure 4.24 Specific compressive strength of 10 μm^3 machined specimens: Synthetic pure calcite crystals (control) and synthetic calcite composites crystals with 1.8 and 6 vol.% PS.

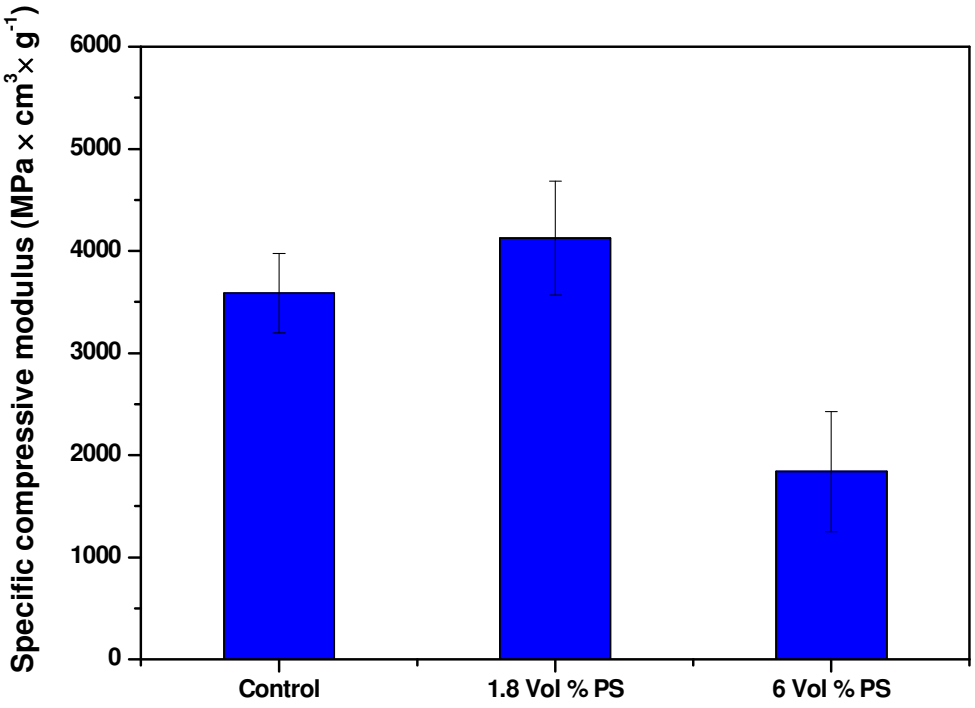

Figure 4.25 Specific compressive modulus of 10 μm^3 machined specimens: Synthetic pure calcite crystals (control) and synthetic calcite composites crystals with 1.8 and 6 vol.% PS.

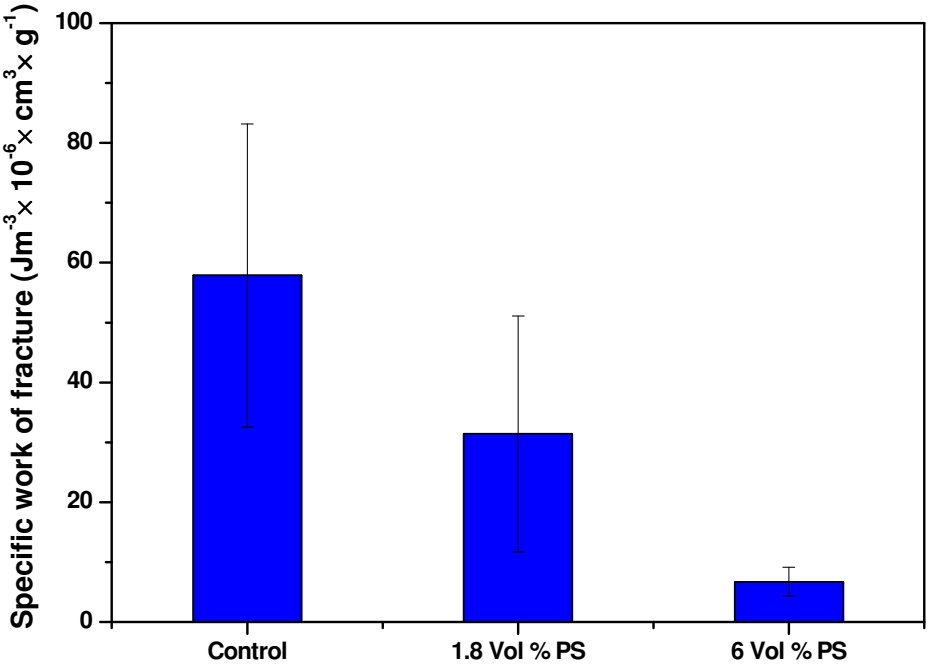

Figure 4.26 Specific work of fracture of 10 μm^3 machined specimens: Synthetic pure calcite crystals (control) and synthetic calcite composites crystals with 1.8 and 6 vol.% PS.

As was the case for the compressive properties, it is observed that none of the measured specific mechanical properties has been increased by the occlusion of both PS concentrations (see Tables 7.27, 7.30 and 7.33 in Appendix for multiple means comparison). This is due to the low amounts of occluded PS used in this experiment (only 1.8 vol.% and 6 vol.%), which do not largely reduce the density of the composite when compared with pure calcite.

4.4 Conclusions

By using a micro-compression technique, new insights into the deformation behaviour of these new calcite polymer composites were obtained. By comparing the results obtained between machined and non-machined crystal samples it was observed that the strain at fracture and work of fracture of the machined specimens was significantly decreased by the occluded polymer. This decrease was not observed in the non-machined crystal samples which showed the opposite trend. A lack of initial parallelism between the flat punch and the micro-compression specimens is thought to be the source of this difference. The SEM

images showed that the compressed pure calcite crystal (control) was fractured into small fragments, whereas the composites with occluded PS were fractured into larger blocks. From this it can be concluded that the occluded polymer reduced the characteristic brittle behaviour of pure calcite crystals. In the fracture zones it was also observed that some PS particles had been deformed during the failure of the crystals. The deformation of these PS particles shows that a potential crack bridging mechanism is occurring. Crack bridging is an energy-dissipating mechanism found in some biogenic materials, such as seashells, and is used to improve fracture toughness. The occluded PS could therefore potentially lead to an enhancement of the composites' work of fracture.

By taking into consideration the results obtained with the machined specimens it was observed however that, contrary to the qualitative toughening described above, none of the compressive properties or specific compressive mechanical properties had been increased by the occlusion of both PS concentrations. From this it can be concluded that although some energy dissipation/absorption mechanism was present, through the deformation of the occluded polymer, this effect was largely outweighed by a significant decrease in strength and strain at failure introduced by the polymer. The large decrease of these properties is thought to be caused by the reduction of the solid load-carrying material and stress concentrations at the filler-matrix boundaries. The FIB milling process may have also damaged the polymer or calcite-polymer interface and contribute to the increase of stress concentrations. Further studies will be therefore necessary to investigate the structural changes introduced by the polymers on the calcite structure and the influence of the utilised milling process on the composite's surface. This micro-compression investigation showed therefore that the occluded 200 nm PS particles were inappropriate to increase the compressive or specific UCS, work of fracture, modulus and strain at fracture of pure calcite. This composite is therefore not suited for lightweight structural crashworthiness, construction or protective armour applications where properties such as high strength or high energy absorption capacity are important requirements.

4.5 References

Eldin, N. N. and Senouci, A. B., 1993, *Rubber-Tire Particles as Concrete Aggregate*, Journal of Materials in Civil Engineering 5, 4, 478-496.

Khaloo, A. R., Dehestani, M. and Rahmatabadi, P., 2008, *Mechanical properties of concrete containing a high volume of tire rubber particles*, Waste Management, 28, 12, 2472-2482.

Kiener, D., Motz, C., Rester, M., Jenko, M. and Dehm, G., 2007, *FIB damage of Cu and possible consequences for miniaturized mechanical tests*, Materials Science and Engineering, 25, 262-272.

McCaffrey, J. P., Phaneuf, M. W. and Madsen, L. D., 2001, *Surface damage formation during ion-beam thinning of samples for transmission electron microscopy*, Ultramicroscopy, 87, 3, 97-104.

Mogi, K., 1973, *Rock Fracture*, Annual Review of Earth and Planetary Sciences, 1, 63-84.

Presser, V., Schultheiß, S., Berthold, C. and Nickel, K. G., 2009, *Sea Urchin Spines as a Model-System for Permeable, Light-Weight Ceramics with Graceful Failure Behavior. Part II. Mechanical Behavior of Sea Urchin Spine Inspired Porous Aluminum Oxide Ceramics under Compression*, Journal of Bionic Engineering, 6, 3, 203-213.

Uchic, M. D. and Dimiduk, D. M., 2005, *A methodology to investigate size scale effects in crystalline plasticity using uniaxial compression testing*, Materials Science and Engineering A, 400-401, 268-278.

Weber, J., Greer, R., Voight, B., White, E. and Roy, R., 1969, *Unusual strength properties of echinoderm calcite related to structure*, Journal of Ultrastructure Research, 26, 5-6, 355-366.

Zheng, L., Huo, X. S. and Yuan, Y., 2008, *Strength, Modulus of Elasticity, and Brittleness Index of Rubberized Concrete*, Journal of Materials in Civil Engineering, 20, 11, 692-699.

5: MECHANICAL PROPERTIES OF COMPOSITE AND BIOGENIC CRYSTALS BY NANOINDENTATION

5.1 Sea urchin spine calcite compared to Iceland spar calcite

5.1.1 Scanning electron microscopy (SEM)

SEM was used to study the residual impression marks left by the Berkovich tip. Figures 5.1 and 5.2 show representative residual indentations marks performed to a depth of 2 μm on sea urchin spine calcite and Iceland spar calcite, respectively. This particular indentation depth allowed a better observation of the materials deformation response to the indentation applied load. Figure 5.1 shows that the indentation performed on sea urchin spine gave rise to three radial cracks around the indent impression (indicated in Figure 5.1 by arrows). These cracks are the surface traces of circular median cracks formed beneath the indent surface (McColm, 1990; Lawn, 1993; Yonezu *et al.*, 2004). The delamination of material next to the indent is possibly caused by a lateral crack progression underneath the specimen surface.

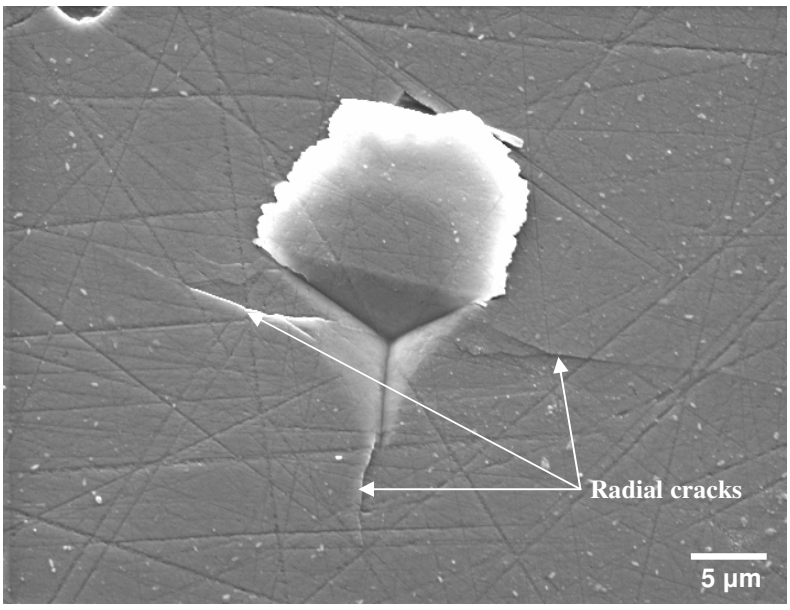

Figure 5.1 An SEM image of a residual impression made during the nanoindention of a sample of sea urchin spine calcite. Indentation was performed at a load of 183 mN. Arrows indicate radial cracks around the indent.

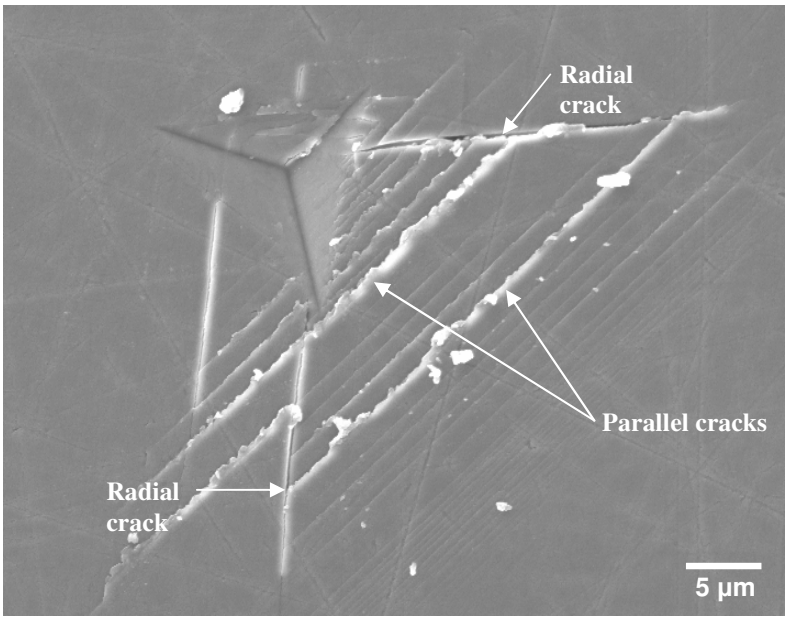

Figure 5.2 An SEM image of a residual impression made during the nanoindention of a sample of Iceland spar calcite. Indentation was performed at a load of 166 mN. Arrows indicate radial and parallel cracks formed at the indent location.

Figure 5.2 shows that the indentation performed on Iceland spar calcite gave rise to two radial cracks and a multitude of parallel cracks outside the indent impression (indicated in Figure 5.2 by arrows). Radial cracks are generally seen to emanate from the edges of the indent impression, where stress is most highly concentrated. This may specially occur if the edges of the indent are favourably oriented along trajectories of minimum energy pathways (McColm, 1990). In calcite, cracking is expected to occur preferentially in directions parallel to the {104}cleavage planes of calcite (Carter, G. M. *et al.*, 1993; Lawn, 1993). At the nanometer scale, the crystal structure of the sea urchin spine is less ordered than the one of pure calcite (Section 2.5). This less ordered structure could possibly hinder the formation of the multiple parallel cracking observed in Iceland spar calcite. This different cracking behaviour is an indication of a different deformation mechanism between sea urchin spine and Iceland spar calcite.

5.1.2 Atomic force microscopy

Atomic force microscopy (AFM) was also used to study the residual impression marks left by the Berkovich tip. Since all the composite samples were indented at a 500 nm depth, all the AFM imaging was performed on samples indented to this depth. Figures 5.3 and 5.4 show AFM images of residual indentations performed on sea urchin spine calcite. The cross-sectional profile of the residual indentation mark shows that the depth of the residual indentation is less than half the 500 nm displacement into the surface recorded by the software (Figure 5.4). This difference can be explained by the elastic recovery of the material after tip removal. Nanoindentation experiments on biogenic aragonite also showed such large elastic recovery: from ~ 65 nm (depth at peak load) to ~ 23 nm (residual impression depth) (Bruet *et al.*, 2005).

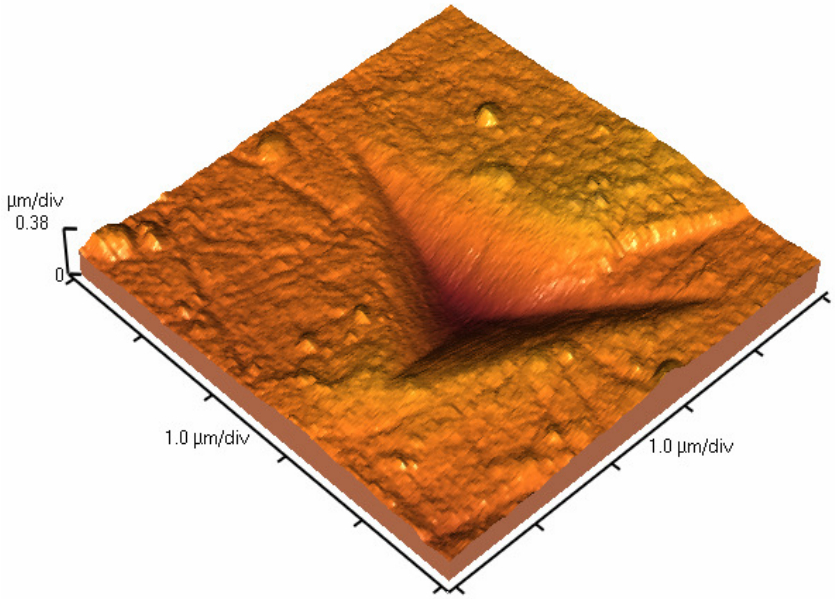

Figure 5.3 A three-dimensional AFM image of a residual nanoindentation mark left on sea urchin spine calcite (5.0 x 5.0 μm^2 scale) deformed to an initial depth of 500 nm using a load of 17 mN.

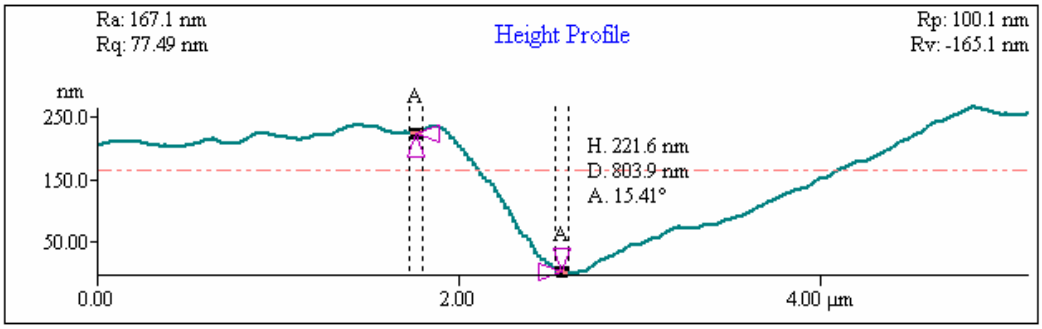

Figure 5.4 Cross-sectional view of the residual nanoindentation mark left on sea urchin spine calcite (5.0 µm scan) obtained from the AFM imaging. Sample was deformed to an original depth of 500 nm using a load of 17 mN.

The cross-sectional profile in Figure 5.4 also did not show any significant pile-up at the edges of the impression. Nanoindentation experiments on biogenic aragonite showed that some pile-up formed around the indent (Li, X. and Nardi, 2004; Bruet *et al.*, 2005). However these experiments were performed on a different crystal form of calcite, and the samples were fresh or soaked with water prior to testing. Pile-up is produced by the upward flow of material to the surface due to the indenter tip penetration, and is a form of plastic deformation. Excessive pile-up can lead to an overestimation of the measured hardness and modulus, by an underestimation of the projected area of the indent. The absence of pile-up is therefore an advantage when using the Oliver-Pharr method, which works better for materials where mainly small sink-in occurs (Fischer-Cripps, 2002; Oliver and Pharr, 2004).

Figures 5.5 and 5.6 show an AFM image and the profile of a representative residual indentation mark from an indentation performed at 500 nm depth on Iceland spar calcite. The cross-sectional investigation (Figure 5.6) of the residual nanoindentation mark revealed no pile-up around the indent impression.

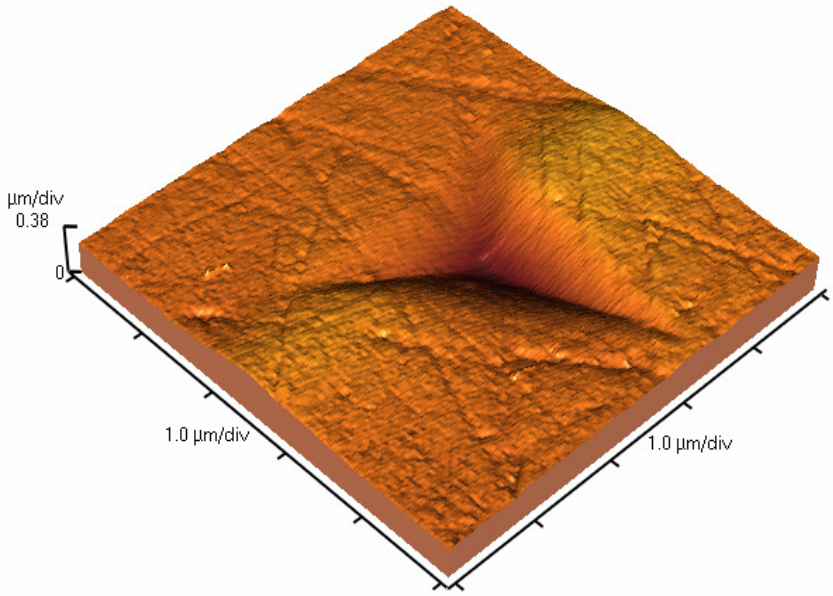

Figure 5.5 A three-dimensional AFM image of a residual nanoindentation mark left on Iceland spar calcite (5.0 x 5.0 μm^2 scale) deformed to an initial depth of 500 nm using a load of 15 mN.

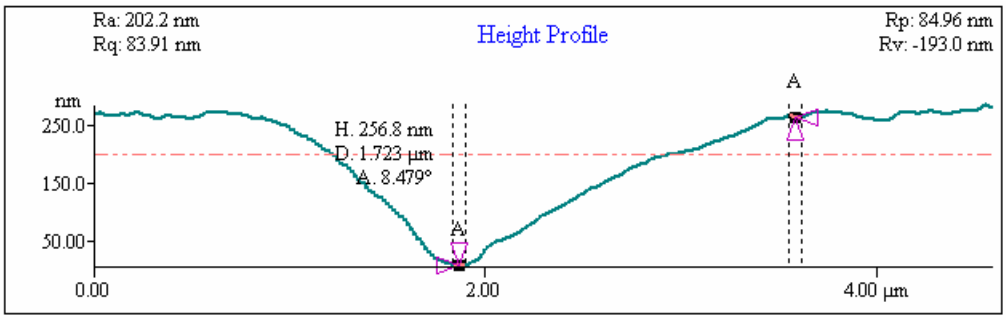

Figure 5.6 Cross-sectional view of the residual nanoindentation mark left on Iceland spar calcite (5.0 µm scan) obtained from the AFM imaging. Sample was deformed to an original depth of 500 nm using a load of 15 mN.

5.1.3 Mechanical properties

Figure 5.7 compares representative load-displacement curves of sea urchin spine calcite and Iceland spar calcite at a maximum recorded depth of 500 nm. In Figure 5.7 pop-in phenomena are observed for both loading curves. Pop-ins are small bumps in the loading curve caused by the quick displacement of the indenter due to a sudden compliance of the

tested material. In brittle materials, pop-ins are associated with the formation of cracks (Lin *et al.*, 2009) in response to high stress concentrations.

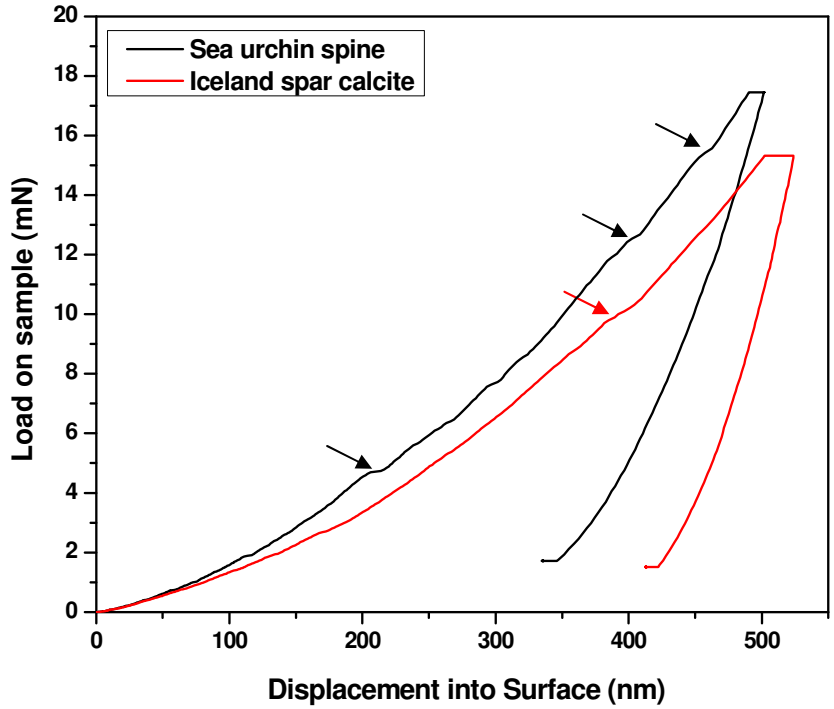

Figure 5.7 Typical load-displacement curves for sea urchin spine calcite and Iceland spar calcite. Pop-in phenomena are highlighted by arrows.

The short plateau at the top of the curves represents the displacement of the tip at constant maximum load for a period of 10 s once the final depth of 500 nm is reached. In some materials, displacements recovered during unloading may not be entirely elastic, therefore, the use of the unloading curve in the analysis of elastic properties, as is the case in the Oliver-Pharr method, can lead to inaccuracies. To minimize nonelastic effects during unloading a holding period at peak load is therefore included in the loading sequence, to allow time dependent effects to diminish (Oliver and Pharr, 1992). The observed plateaus at the top of the curves are caused by time dependent plastic deformation of the material under constant load, and are thought to be indentation creep (Lucas, B. and Oliver, 1999; Chen and Bull, 2009). Although time dependent deformation in ceramics should only occur at elevated temperatures (Li, X. and Bhushan, 2002), several experiments on ceramic

materials, including calcite, have shown that this is not the case (Chudoba and Richter, 2001; Zügner *et al.*, 2006).

In Figure 5.7 it can be observed that the plateau at the top of the sea urchin spine curve is shorter than the one for the Iceland spar curve. This indicates that even at a higher load, the displacement of the tip into the surface of the sea urchin spine calcite, during the 10 s period, was smaller than the one on Iceland spar calcite. This possibly shows that sea urchin spine calcite has a higher creep resistance than Iceland spar calcite. This behaviour was not expected since a calcite material with occluded polymer (proteins) should creep more than pure calcite. Further controlled studies will be necessary to confirm this different creep behaviour. Figures 5.8 and 5.9 compares the average modulus and hardness determined from ten independent nanoindentations performed at depths of 500 nm, 1 μm and 2 μm on sea urchin spine calcite and Iceland spar calcite.

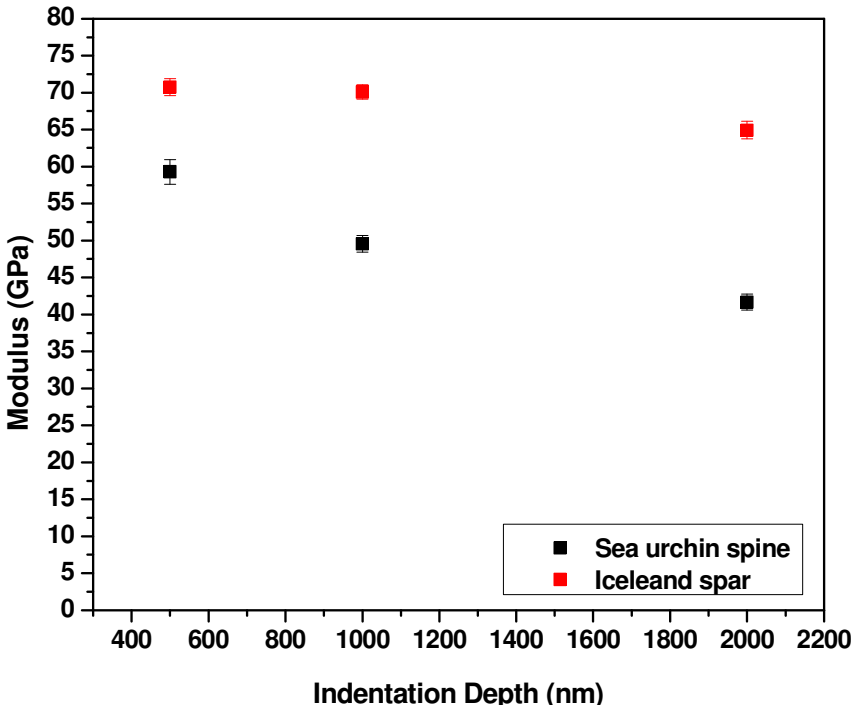

Figure 5.8 Modulus of sea urchin spine and Iceland spar calcite as a function of indentation depth. Error bars reported are standard deviations from the mean.

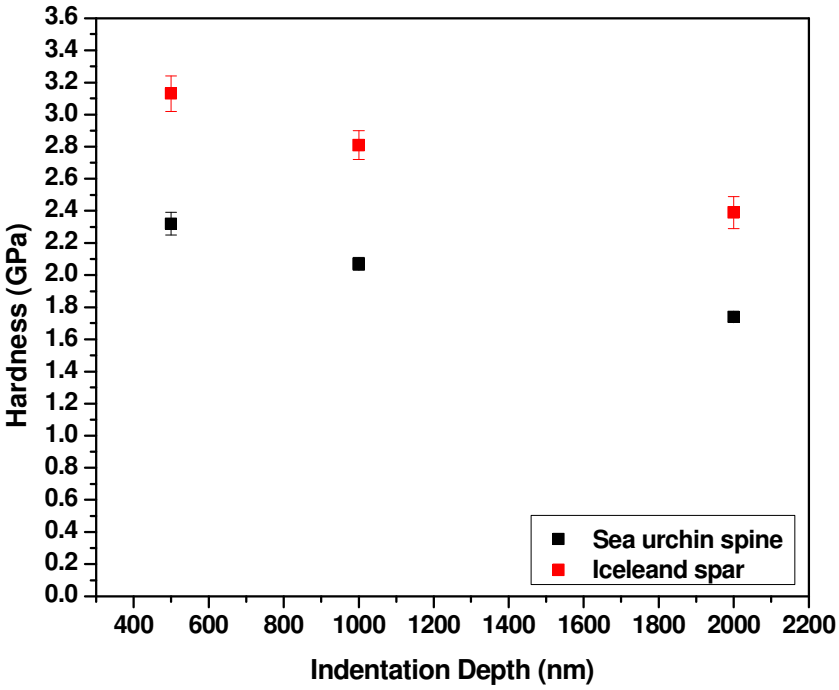

Figure 5.9 Hardness as a function of indentation depth for sea urchin spine and Iceland spar calcite as a function of indentation depth. Error bars reported are standard deviations from the mean.

From Figure 5.8 it can be observed that for all the measured depths, the sea urchin spine calcite modulus is lower than that of Iceland spar calcite. These data confirm previous results, reported in Section 2.5, showing that the modulus of biogenic calcite is lower than non-biogenic calcite. Figure 5.9 also shows that for all the measured depths, the sea urchin spine calcite hardness is higher than the one of Iceland spar calcite. This result shows the ability of organisms such as sea urchins, to generate materials with seemingly improved mechanical properties; a strategy which forms the basis of this thesis. From Figure 5.8 it can also be observed that the modulus of sea urchin spine calcite decreases significantly with depth. Experiments performed on biogenic aragonite from sea shells also showed a decrease in the modulus of this material, showing an indentation size effect (Li, X. *et al.*, 2004; Bruet *et al.*, 2005). The hardness of both samples also decreases with depth (Figure 5.9). This shows an indentation size effect (ISE), as previously reported for many materials (Section 2.16), including nonbiogenic calcite (Zügner, 2002). This indentation size effect highlights the importance of taking into consideration the indentation depth when comparing mechanical properties between materials.

5.1.4 Conclusions

Indentations performed on sea urchin spine calcite (biogenic calcite) and Iceland spar calcite (non-biogenic calcite) showed that these two materials behave differently. The response of the Iceland spar calcite was characterised by the creation of radial and multiple parallel cracks close to the indent residual impression. The multiple parallel cracking was not observed for sea urchin spine calcite even when a higher load was used. The hardness and modulus of the sea urchin spine calcite were also found to be higher and lower respectively compared to Iceland spar calcite. In order to replicate these results, employing synthetically generated materials, two approaches are used; namely the incorporation of polystyrene beads (PS) and di-block co-polymer micelles into single calcite crystals. These materials attempt to mimic sea urchin spine, and the mechanics of these materials are compared to pure synthetically generated calcite crystals.

5.2 Calcite-polymer composite crystals with different amounts of 200 nm PS particles

5.2.1 Scanning electron microscopy

Figure 5.10 shows a representative residual impression from an indentation performed at 500 nm depth on a synthetic pure calcite crystal (control). It is observed that this indentation has generated parallel cracks at the edge of the indent impression (indicated in Figure 5.12 by arrows). Figures 5.11, 5.12 and 5.13 show representative residual impressions from indentations performed at 500 nm depths on calcite-polymer composite crystals with 1.8, 6 and 23 vol.% of occluded 200 nm PS particles respectively. These images show that parallel cracks at the edge of the indent impression of the composite with 1.8 vol. % PS are also visible (indicated in Figure 5.11 by arrows). These parallel cracks are the surface expression of fractured planes beneath the indent surface. SEM observations showed that no cracks were visible at the indent impressions of the composites with 6 and 23 vol.% PS (Figures 5.12 and 5.13 respectively).

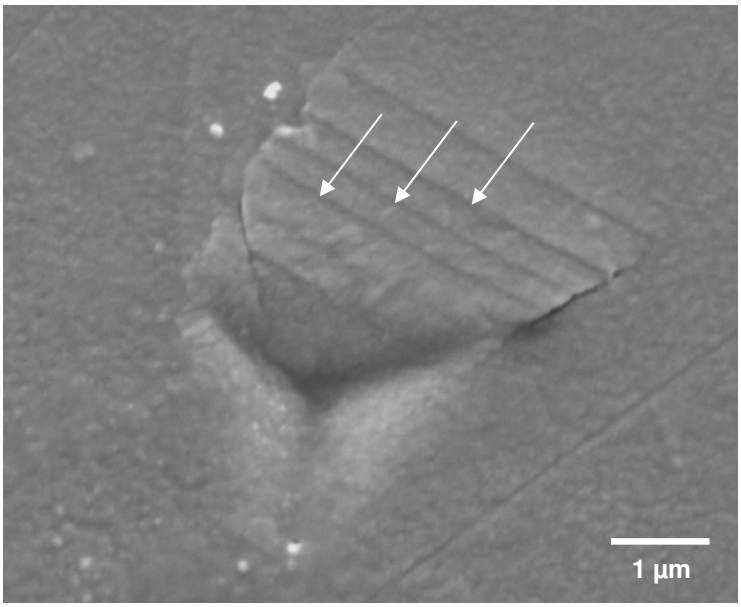

Figure 5.10 An SEM image of a residual nanoindentation impression left on a pure calcite crystal (control). Arrows indicate parallel cracks formed at the side of the indent.

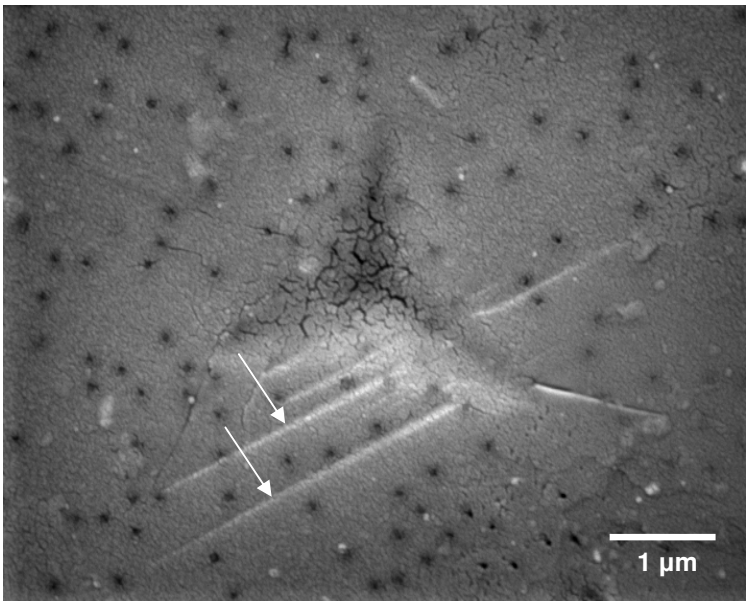

Figure 5.11 An SEM image of a residual nanoindentation impression left on a composite calcite crystal with 1.8 vol.% PS. Arrows indicate parallel cracks formed at the side of the indent.

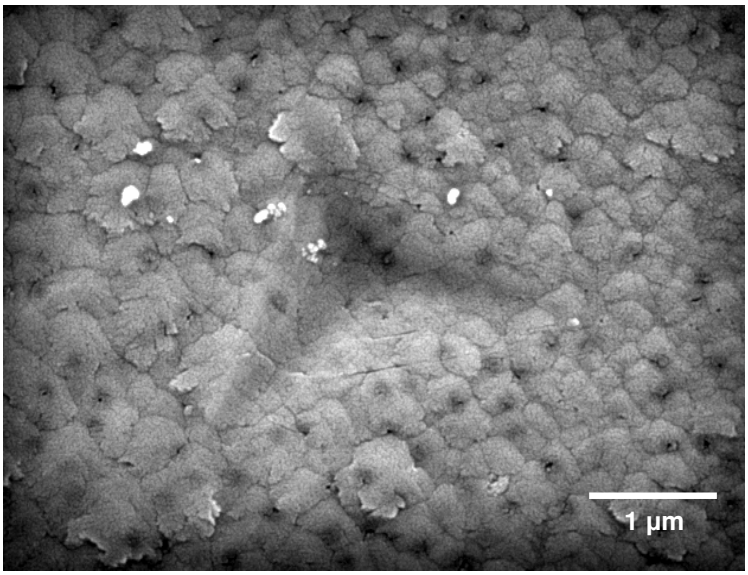

Figure 5.12 An SEM image of a residual nanoindentation impression left on a composite calcite crystal with 6 vol.% PS.

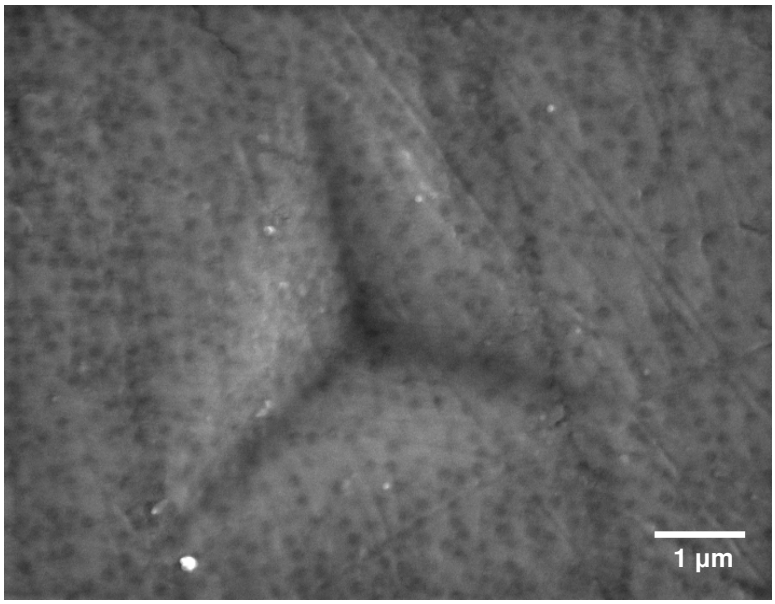

Figure 5.13 An SEM image of a residual nanoindentation impression left on a composite calcite crystal with 23 vol.% PS.

The fact that the cracks observed in the control and composite crystals with 1.8 vol.% PS are always located at one side of the indent impressions may be due to a lack of parallelism between the indenter tip and the crystal surface. This lack of parallelism would cause a non-uniform pressure as the indenter tip penetrates the crystal surface and could explain the observed cracking behaviour. The sides of the Berkovich residual impressions left on the control and especially on composite crystals with 1.8 vol.% PS also appear to have different sizes. These asymmetrical residual impressions could also be caused by the lack of parallelism between the indenter tip and the crystal surface.

The sizes of the residual impressions appear to increase as the amount of occluded polymer is also increased (Figures 5.11-5.13). Since the resin in which the samples are embedded has a very low modulus (4.84 ± 0.2 GPa), it is possible that these different sizes may be caused by a compliance of the resin (substrate) as the indenter pushes the crystal in order to perform the indentation (Section 2.13.2). Part of the 500 nm displacement of the indenter would be performed into the crystal and another part would be made by the displacement of the crystal into the resin. The displacement contribution of the indenter into the crystal would be in this case larger for the composites with larger amounts of occluded polymer. This will be further discussed in Section 5.2.3 and 5.4. The compliance of the resin could also be the cause of the lack of parallelism between the indenter tip and the crystal surface during the indentation. Since the Oliver-Pharr method utilised by the nanoindenter requires the surface of the sample to be horizontal, the absence of this condition could have a detrimental effect on the measured mechanical properties.

5.2.2 Atomic force microscopy

Figures 5.14 and 5.15 show AFM images of a representative residual impression from an indentation performed at a 500 nm depth on a synthetic pure calcite crystal (control). As was the case for Iceland spar calcite, the cross-sectional investigation of the residual indentation marks left on synthetic pure calcite (control) (Figure 5.15) didn't show any significant pile-up at the edges of the indent impression. The AFM images also confirmed the formation of parallel cracks (arrows) at the edges of the indent impression, as also observed in the SEM images.

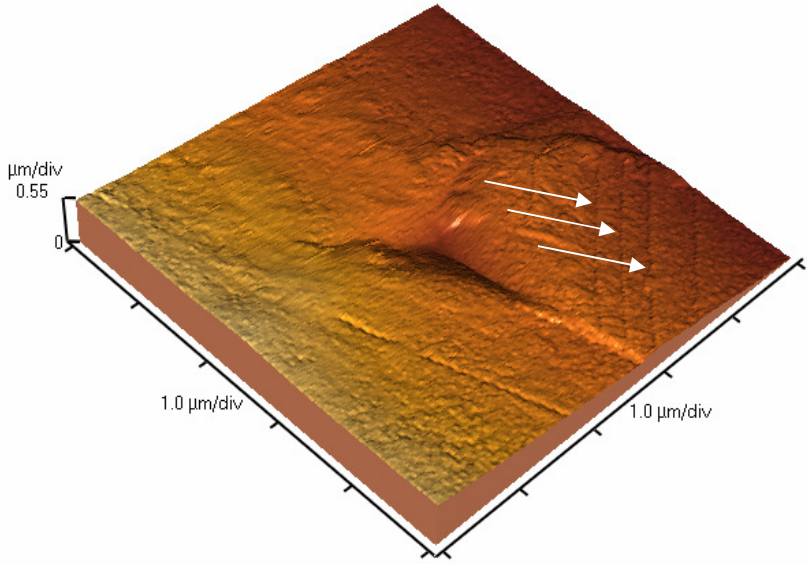

Figure 5.14 A three-dimensional AFM image of a residual nanoindentation mark left on synthetic pure calcite (control) (5.0 x 5.0 µm^2 scale) deformed to an initial depth of 500 nm using a load of 10 mN. Arrows indicate parallel cracks formed at the edge of the indent.

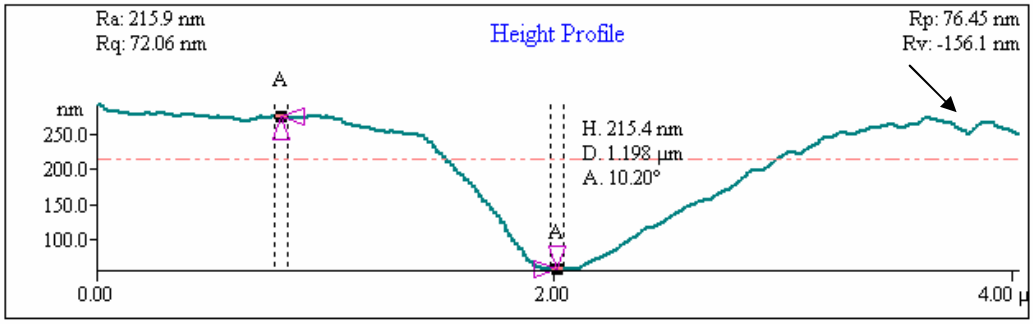

Figure 5.15 Cross-sectional view of the residual nanoindentation mark left on synthetic pure calcite (control) (5.0 µm scan), obtained from the AFM imaging. Sample was deformed to an original depth of 500 nm using a load of 10 mN. Arrow indicates one of the cracks formed at the edge of the indent.

Figures 5.16 and 5.17 show AFM images of a representative residual impression from an indentation performed at 500 nm depth on calcite-polymer composite crystals with 1.8 vol.% PS.

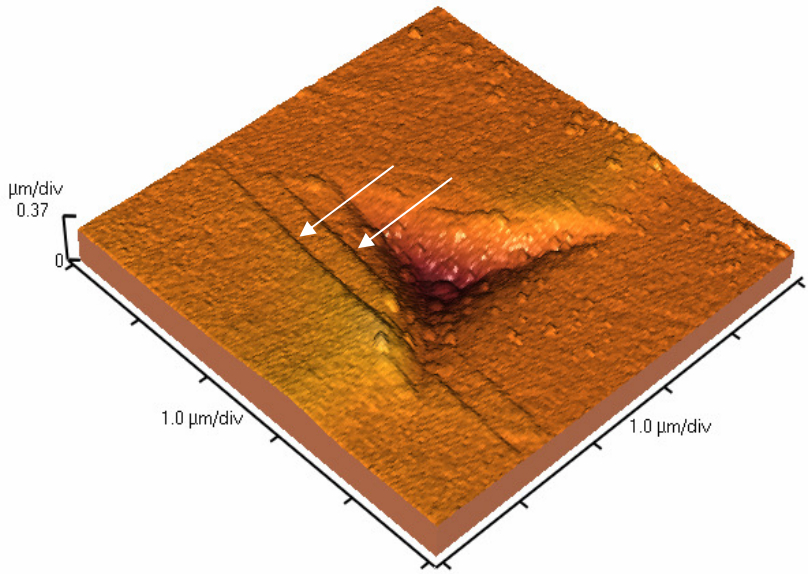

Figure 5.16 A three-dimensional AFM image of a residual nanoindentation mark left on a composite calcite crystal with 1.8 vol.% PS (5.0 x 5.0 µm^2 scale) deformed to an initial depth of 500 nm using a load of 12 mN. Arrows indicate parallel cracks formed at the edge of the indent.

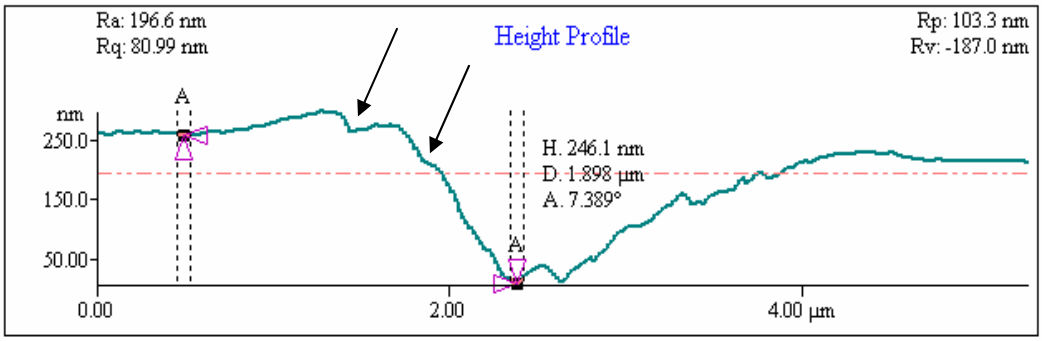

Figure 5.17 Cross-sectional view of the residual nanoindentation mark left on a composite calcite crystal with 1.8 vol.% PS (5.0 µm scan), obtained from the AFM imaging. Sample was deformed to an original depth of 500 nm using a load of 12 mN. Arrows indicate parallel cracks formed at the edge of the indent.

The profile of these images did not indicate any significant pile-up at the edges of the indent. Since excessive pile-up can lead to an overestimation of the measured hardness and modulus, these results are evidence that this does not occur. This study also confirmed the presence of parallel cracks (indicated in Figures 5.16 and 5.17 by arrows) already observed

in the SEM investigation. As discussed in Section 2.16 of the literature review the presence of cracks associated with an indent could result in a lower hardness value for the material and reduce therefore the reliability of the performed hardness measurements.

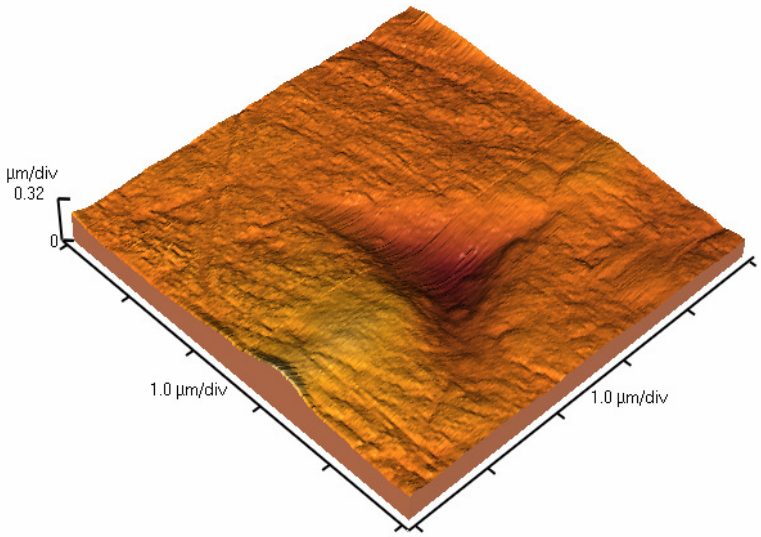

Figure 5.18 A three-dimensional AFM image of a residual nanoindentation mark left on a composite calcite crystal with 6 vol.% PS (5.0 x 5.0 µm^2 scale), deformed to an initial depth of 500 nm using a load of 7.5 mN.

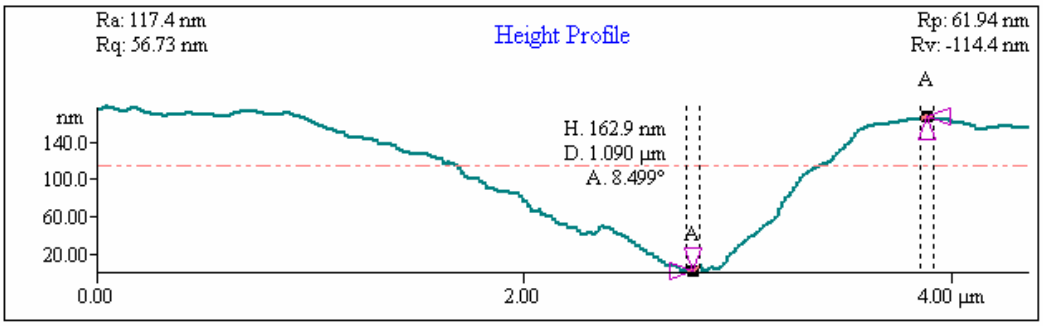

Figure 5.19 Cross-sectional view of the residual nanoindentation mark left on a composite calcite crystal with 6 vol.% PS (5.0 µm scan), obtained from the AFM imaging. Sample was deformed to an original depth of 500 nm using a load of 7.5 mN.

Figures 5.18 and 5.19 show AFM images of a representative residual impression left on the surface of a calcite-polymer crystal with 6 vol.% PS. The profile of this indent did not indicate any significant pile-up or visible cracks at the indent impression. Figures 5.20 and

5.21 show AFM images of a representative residual impression left on the surface of a calcite-polymer composite crystal with 23 vol.% PS. The profile of this indent did not show any significant pile-up at the edges of the impression. No cracks were observed at the residual indent impression.

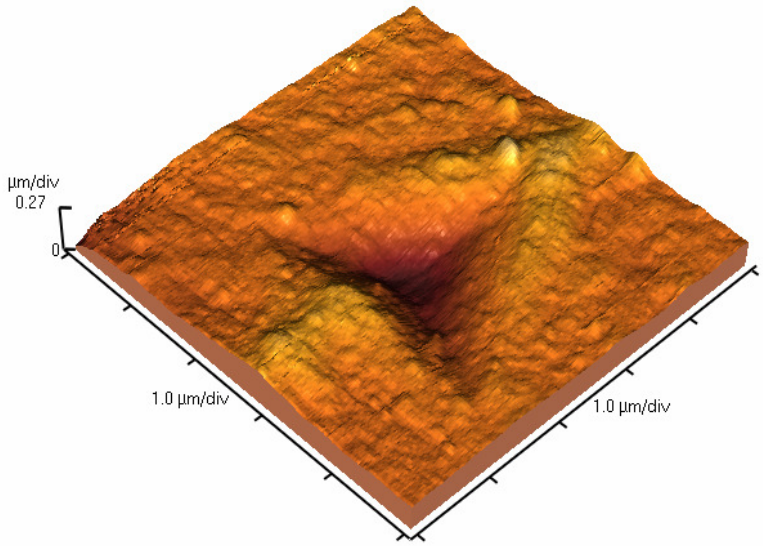

Figure 5.20 A three-dimensional AFM image of a residual nanoindentation mark left on a composite calcite crystal with 23 vol.% PS (5.0 x 5.0 µm^2 scale), deformed to an initial depth of 500 nm using a load of 7 mN.

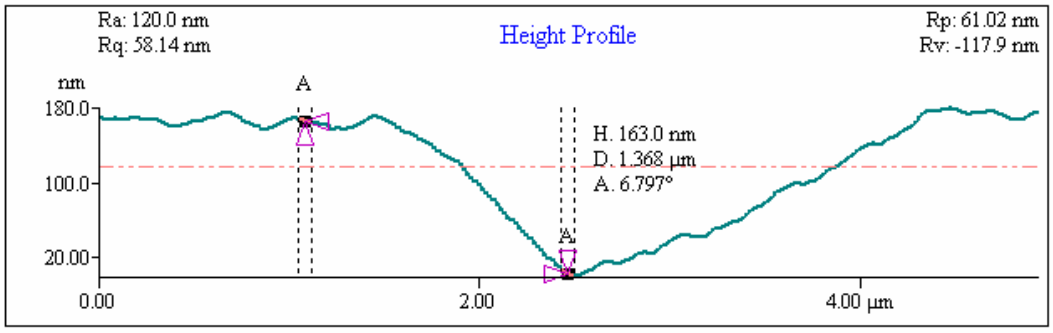

Figure 5.21 Cross-sectional view of the residual nanoindentation mark left on a composite calcite crystal with 23 vol.% PS (5.0 µm scan), obtained from the AFM imaging. Sample was deformed to an original depth of 500 nm using a load of 7 mN.

The cross-sectional profile investigation of the residual impressions left on the calcite-polymer composites with 6 vol.% PS (Figure 5.19) and 23 vol.% PS (Figure 5.21) after indentation showed that their residual depth was shallower than the ones obtained for pure

calcite and the calcite-polymer composites with 1.8 vol.% PS (Figures 5.15 and 5.17 respectively). This indicates possibly a larger elastic recovery of these composite materials after tip removal. The AFM investigation also confirmed the asymmetry of the residual impressions observed in the SEM images.

5.2.3 Mechanical properties

Figure 5.22 compares representative load-displacement curves of sea urchin spine calcite, Iceland spar calcite, synthetic pure calcite (control) and synthetic calcite with 1.8, 6 and 23 vol.% of 200 nm PS particles. In this figure it is noted that the load required to produce an indentation of 500 nm on sea urchin spine calcite and Iceland spar calcite is larger than the loads required to produce the same indentation on all the synthetic crystals. The loading curves of synthetic calcite with 23 vol.% PS appear smoother than all the other curves, with no steps observed in the data. This may be due to the fact that the polymer addition may reduce the crack behaviour responsible for the pop-in phenomenon seen for the other samples.

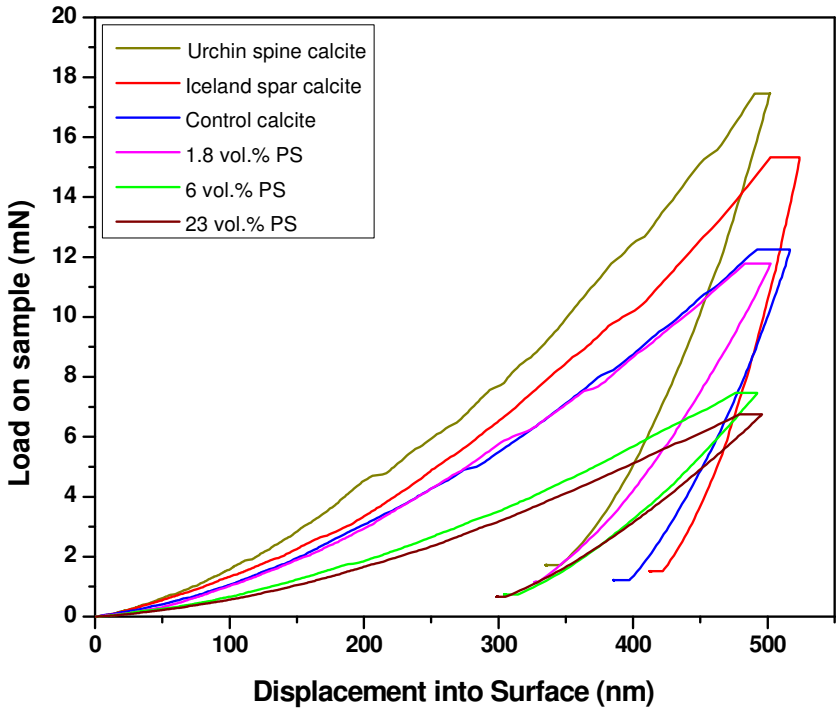

Figure 5.22 Typical load-displacement curves for sea urchin spine calcite, Iceland spar calcite, synthetic pure calcite (control) and synthetic calcite with 1.8, 6 and 23 vol.% PS occlusions.

Figures 5.23 and 5.24 show representative hardness and moduli, respectively, as a function of displacement into surface, for each sample. The measurement of mechanical properties as a function of depth allows the anisotropy of the composite crystals to be investigated at the nanoscale. In Figure 5.23 it is observed that the hardness of all the samples is very large at the beginning of the displacement and decreases rapidly to a minimum, before starting to increase again until a plateau is reached. Several indentation size effects (ISE) can contribute to this behaviour (Section 2.16). One of the most common ISE is related with the blunting of the Berkovich tip due to manufacturing limitations and wear (Fischer-Cripps, 2002). Since the area calculation method assumes a perfectly sharp indenter, at shallow depths, this assumption will produce a large difference between the actual area of contact and that calculated upon the basis of a perfect geometry. ISE effects decrease significantly after ~ 100 nm, where the measured hardness starts to be independent of depth. Figure 5.23 did not show any evidence of significant hardness anisotropy in the interval 200-500 nm where hardness was observed to reach a constant value.

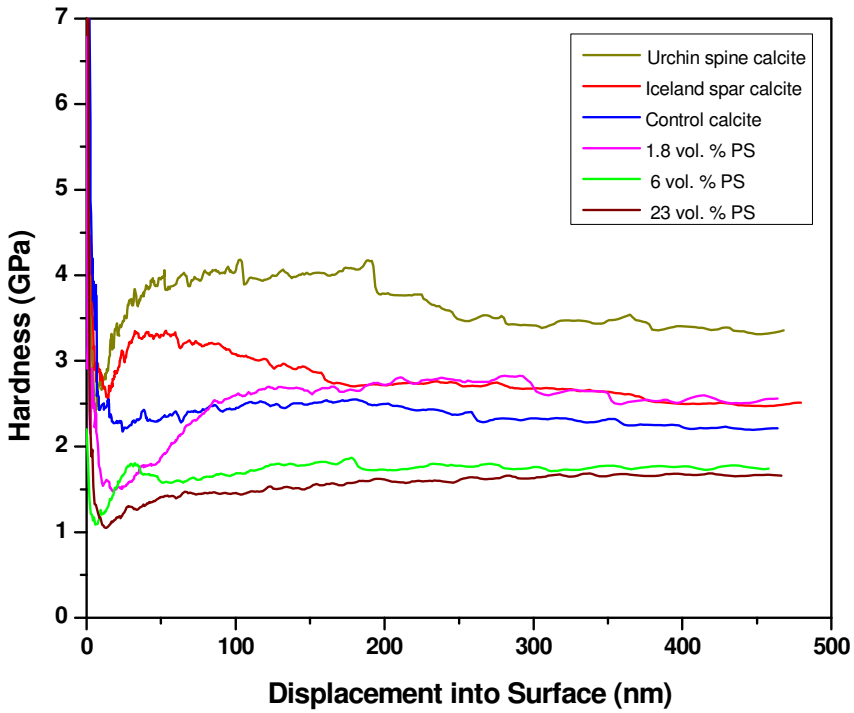

Figure 5.23 Hardness as a function of displacement into the surface of sea urchin spine calcite, Iceland spar calcite, synthetic pure calcite (control) and synthetic calcite with 1.8, 6 and 23 vol.% PS inclusions.

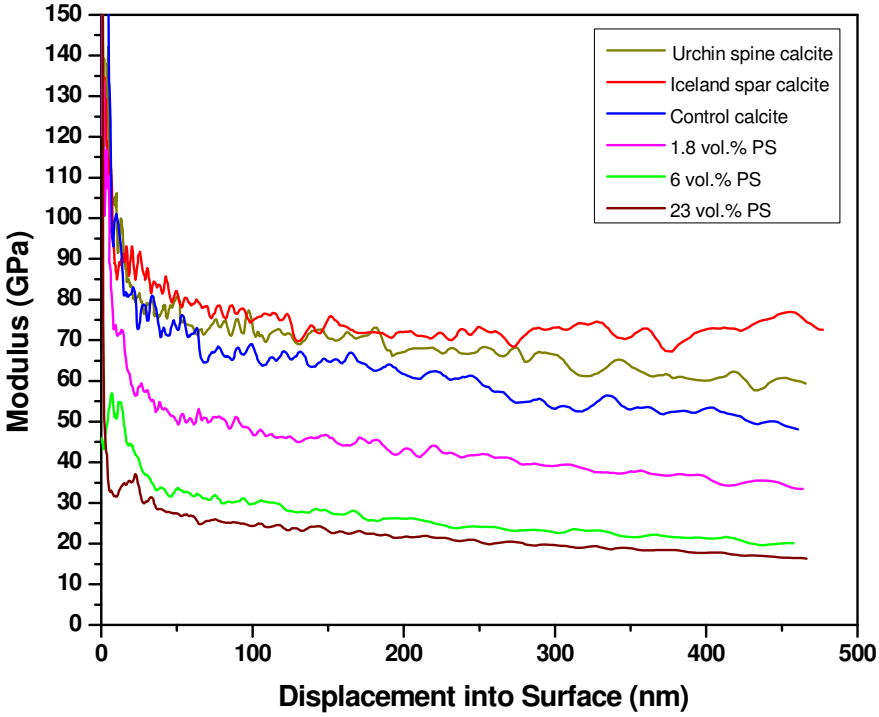

Figure 5.24 Elastic modulus as a function of displacement into the surface of sea urchin spine calcite, Iceland spar calcite, synthetic pure calcite (control) and synthetic calcite with 1.8, 6 and 23 vol.% PS inclusions.

In Figure 5.24 it can be observed that due to ISE the moduli of all the samples are very high at very shallows depths. As was the case for hardness, ISE effects start to decrease significantly after ~ 100 nm. The slight decrease in the modulus of pure calcite after 100 nm is not expected, since Zügner *et al*., (2002) found that it increased between 100 nm and 300 nm (Section 2.5). For hard films on soft substrates, the measured modulus may tend to approach the values of the substrate with increasing penetration depth (Figure 2.16). The decrease in the modulus of pure calcite (control) is however not evidence of substrate compliance since fused silica shows the same behaviour for shallow depths (Figure 3.4). Figure 5.25 compares the average hardness of ten independent nanoindentations, performed at a depth of 500 nm on ten different crystals of each sample.

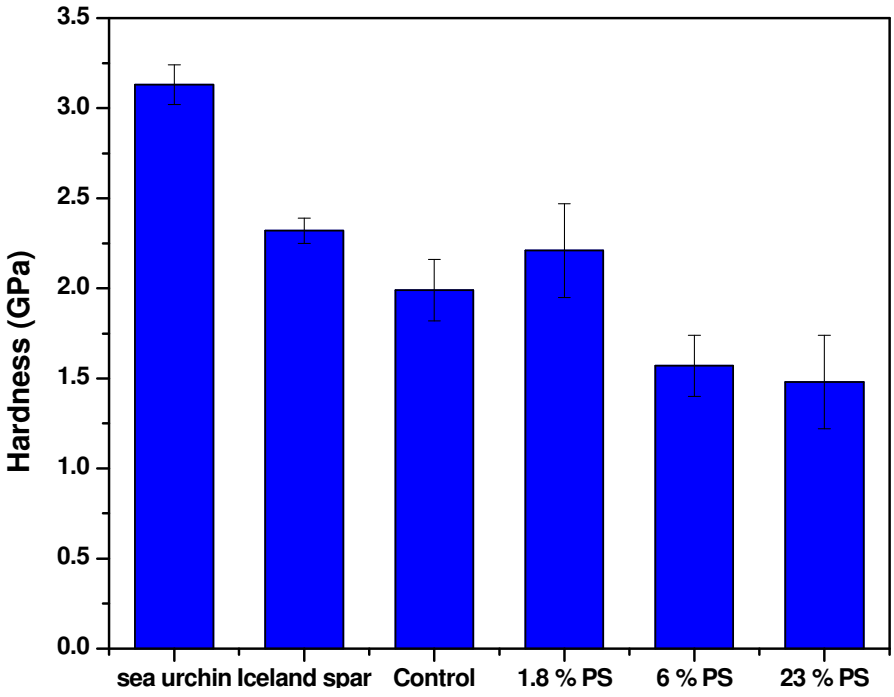

Figure 5.25 Average hardness from ten independent indentations performed at a depth of 500 nm for sea urchin spine calcite, Iceland spar calcite, synthetic pure calcite (control) and synthetic calcite with 1.8, 6 and 23 vol.% PS inclusions.

These data show that there is not a large difference in hardness between the control and Iceland spar calcite. It should be noted that the hardness of the Iceland spar calcite (2.32 ± 0.1 GPa) is slightly lower than typical values reported in the literature for pure calcite (2.8-3.4 GPa) by Zügner *et al.* (2002, 2006). This may be due to an indentation and/or sample size effects since the values obtained by Zügner *et al.* (2002, 2006) were measured at a maximum depth of 300 nm on 500 μm samples (Section 2.5). Figure 5.26 compares the average moduli of ten independent nanoindentations, performed at a depth of 500 nm on ten different crystals of each sample.

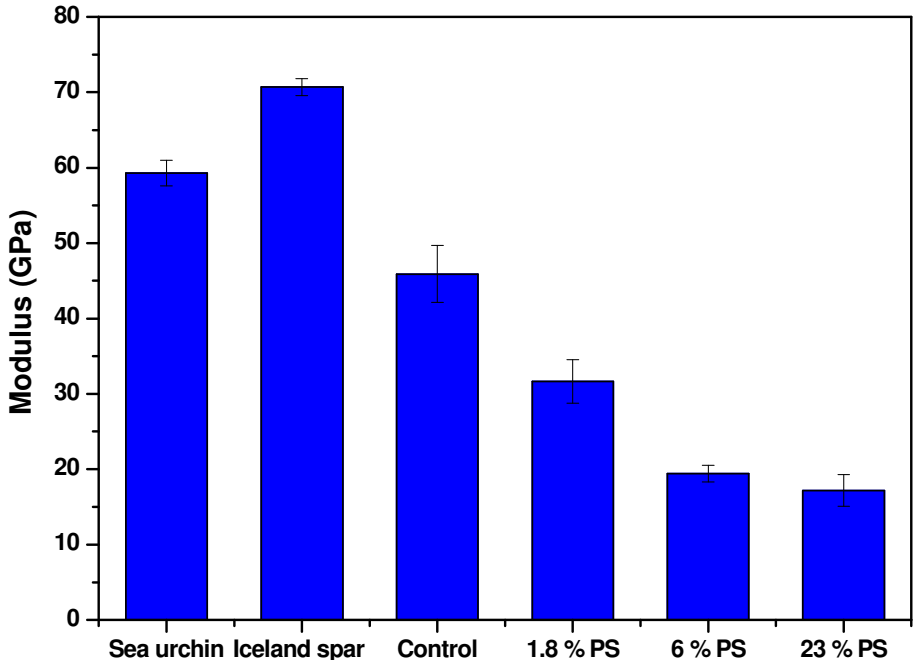

Figure 5.26 Average moduli from ten independent indentations performed at a depth of 500 nm for sea urchin spine calcite, Iceland spar calcite, synthetic pure calcite (control) and synthetic calcite with 1.8, 6 and 23 vol.% PS inclusions.

These data show that the moduli of all the synthetic composites are much lower than the moduli of sea urchin spine calcite (59.3 ± 1.7 GPa) and Iceland spar calcite (70.7 ± 1.1 GPa). The modulus of synthetic pure calcite (45.9 ± 3.8 GPa), used as a control, is also seemingly lower than the moduli of both sea urchin spine calcite and Iceland spar calcite, and much lower than the reported values of pure calcite (in the range 83-88 GPa) (Zügner *et al.*, 2006). As already mentioned, since the resin in which the samples are embedded has a very low modulus (4.84 ± 0.2 GPa), it is possible that the low modulus of pure calcite control may have been caused by a substrate effect (Section 2.13.2). This substrate effect could be caused by a compliance of the resin (substrate) as the indenter pushes into the crystal in order to perform the indentation. The measured total elastic recovery would be in this case due to the contributions of both the sample and the system substrate-sample. This substrate compliance would also explain the different sizes of the residual indents impressions left on the composites (Section 5.2.1).

5.2.4 Conclusions

The AFM and SEM investigations of the residual impressions left after indentation showed the presence of parallel cracks at the indent impressions of pure calcite and calcite-polymer composite crystals with 1.8 vol.% PS. These cracks were not visible on the calcite-polymer composites with 6 and 23 vol.% PS. The cracks in these composites have therefore been suppressed by the presence of occluded polymer. Since these cracks are produced by the fracture of planes beneath the indenter, it can be concluded that the occlusion into calcite of 6 and 23 vol.% 200 nm PS particles modified the mechanical properties of calcite by increasing its resistance to brittle fracture. Since the modulus of the synthetic pure calcite crystal (control) was much lower than the expected value of pure calcite it is possible that the measured mechanical properties may have been affected by the resin (substrate) compliance. This substrate compliance could also explain some differences found in the crystals residual impressions symmetry and sizes. Further studies will be necessary to elucidate this substrate effect (see Section 5.4).

5.3 Calcite-polymer composites with 20 nm co-polymer micelles

5.3.1 Scanning electron microscopy

Figure 5.27 shows a synthetic calcite crystal with 29 vol.% occluded 20 nm di-block co-polymer micelles (Kim, Y.-Y. *et al.*, 2011). Figure 5.28 shows a representative residual impression from an indentation performed at 500 nm depth on this synthetic calcite crystal. This SEM image of the indented surface shows no cracks around the impression. This image also confirmed the indent impression asymmetry already observed on other samples (Section 5.2.1).

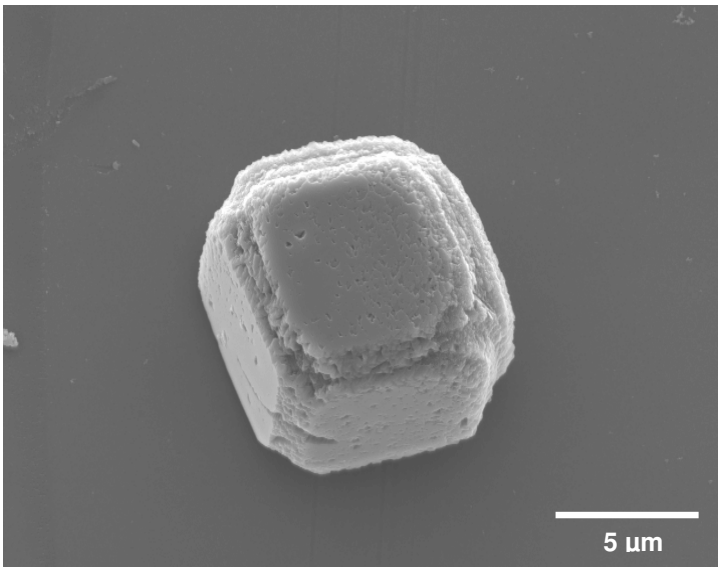

Figure 5.27 Synthetic calcite crystal with 29 vol.% occluded 20 nm di-block co-polymer micelles.

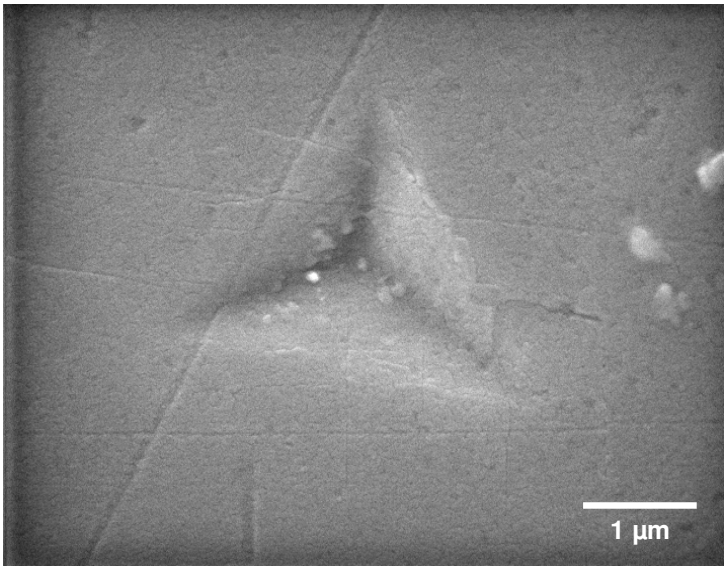

Figure 5.28 An SEM image of a typical residual nanoindentation impression left on synthetic calcite crystal with 29 vol.% occluded 20 nm di-block co-polymer micelles.

5.3.2 Atomic force microscopy

Figures 5.29 and 5.30 show AFM images of a representative residual impression from an indentation performed at 500 nm depth on a synthetic calcite crystal with 29 vol.% occluded 20 nm di-block co-polymer micelles. The cross-sectional investigation of the residual indentation marks revealed a slight pile-up at the indent impressions (Figure 5.30). The AFM investigation also confirmed the absence of cracks at the indent impressions.

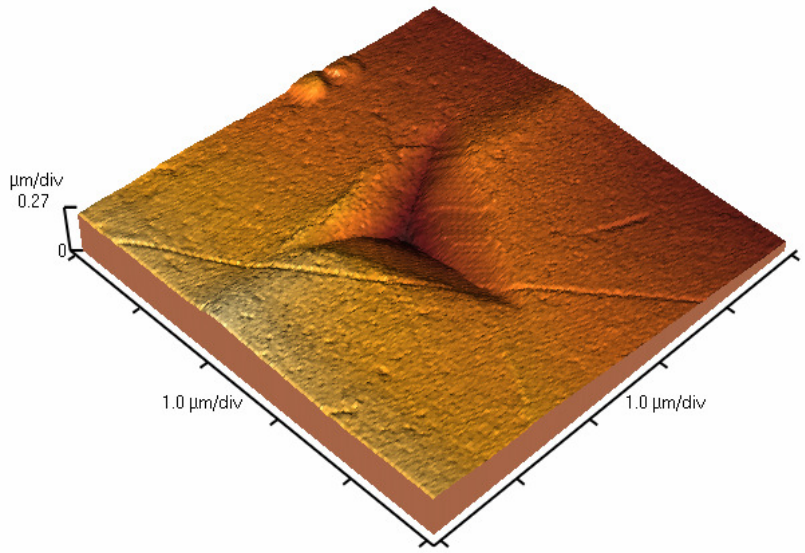

Figure 5.29 A three-dimensional AFM image of a residual nanoindentation mark left on a synthetic calcite crystal with 29 vol.% occluded 20 nm co-polymer micelles (5.0 x 5.0 µm^2 scale), deformed to an initial depth of 500 nm using a load of 9.7 mN.

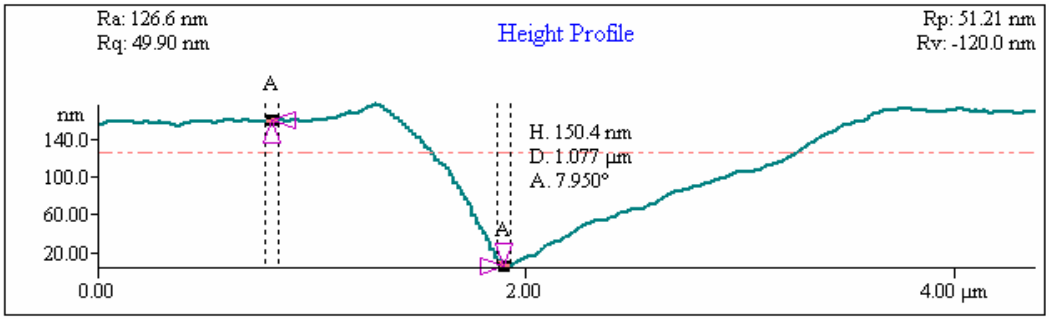

Figure 5.30 Cross-sectional view of the residual nanoindentation mark left on a synthetic calcite crystal with 29 vol.% occluded 20 nm co-polymer micelles (5.0 µm scan), obtained from the AFM imaging. Sample was deformed to an original depth of 500 nm using a load of 9.7 mN.

5.3.3 Mechanical properties

Figure 5.31 compares representative load-displacement curves of synthetic pure calcite (control) and synthetic calcite with 29 vol.% occluded 20 nm di-block co-polymer micelles.

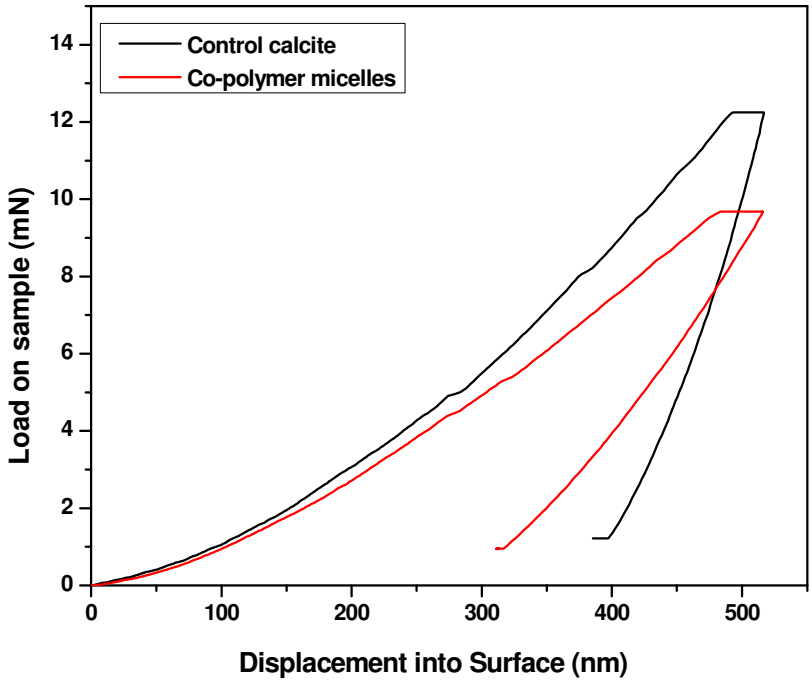

Figure 5.31 Typical load-displacement curves for synthetic pure calcite (control) and synthetic calcite with 29 vol.% occluded 20 nm co-polymer micelles.

The investigation of the loading curves showed that the composite crystal occluded with the micelles also had a smoother loading curve than the pure calcite crystal (control). Figures 5.32 and 5.33 compare the moduli and hardness averages, respectively, of ten nanoindentations performed on ten crystals of synthetic pure calcite (control) and synthetic calcite with 29 vol.% occluded 20 nm di-block co-polymer micelles, at a depth of 500 nm. Figure 5.32 shows that the modulus of the synthetic composite is much lower than the modulus of synthetic pure calcite (control). A two sample t-test at a 95 % confidence level confirmed that the hardness of this composite was larger than that of pure calcite ($p = 0.002$, Table 7.36 in Appendix).

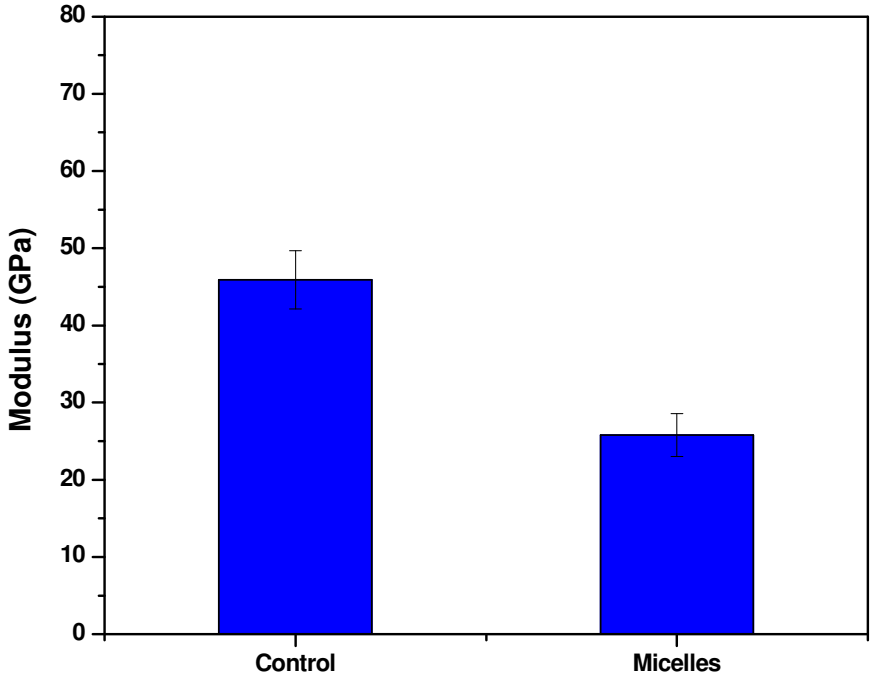

Figure 5.32 Average moduli from ten independent indentations performed at a depth of 500 nm for synthetic pure calcite (control) and synthetic calcite with 29 vol.% occluded 20 nm co-polymer micelles.

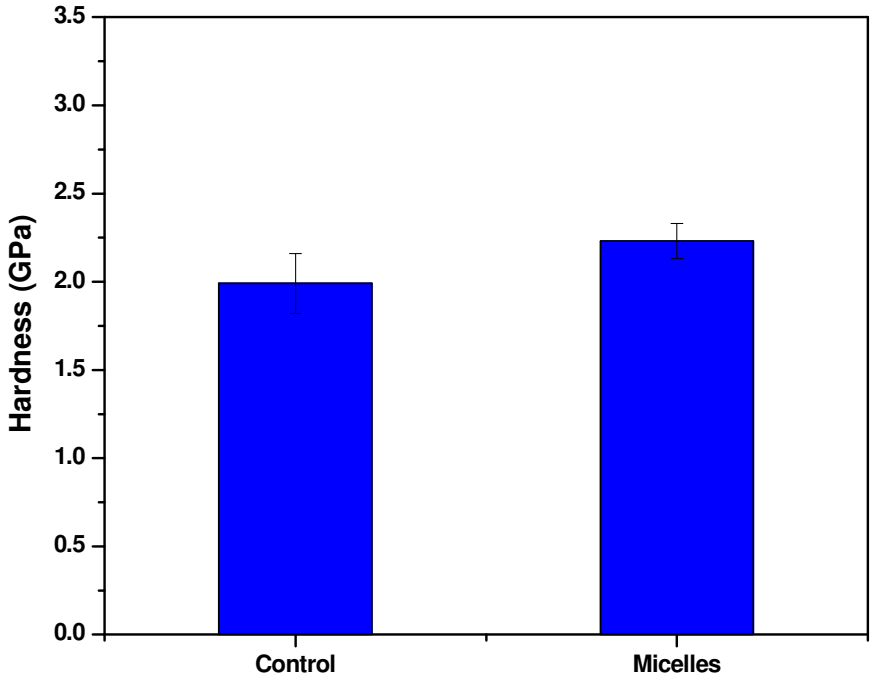

Figure 5.33 Average hardness from ten independent indentations performed at a depth of 500 nm for synthetic pure calcite (control) and synthetic calcite with 29 vol.% occluded 20 nm co-polymer micelles.

5.3.4 Conclusions

The SEM and AFM investigations of the composites' residual indent impressions did not show the presence of the characteristic brittle fracture observed in synthetic pure calcite (control). The modulus of the composite with 29 vol.% occluded 20 nm di-block co-polymer micelles was also found to be largely reduced by the occluded polymer while its hardness was increased. Since the measured mechanical properties of the tested samples may also have been affected by the resin (substrate) compliance, a study was undertaken to elucidate this possible substrate effect.

5.4 Substrate compliance

5.4.1 Substrate influence on the modulus and hardness

The results obtained in Section 5.2 showed that the modulus of synthetic pure calcite used as a control (45.9 ± 3.8 GPa) was much lower than the modulus of Iceland spar calcite (70.7 ± 1.1 GPa) and reported and generally accepted values for pure calcite (83-88 GPa) (Zügner *et al.*, 2006). As explained in the methodology chapter, the crystals were embedded in a styrene-based polyester casting resin in order to test a flat horizontal surface, enabling reliable and reproducible nanoindentation measurements. This resin functions as a substrate beneath the samples and should not be compliant during the tests. Since it was suspected that the low modulus of the control could be caused by the compliance of the resin, a series of tests were performed in order to understand the effect of the substrate on the obtained mechanical properties.

The first test consisted of measuring the mechanical properties of crystals of different sizes. Several pure calcite crystals (control) of different sizes were produced and embedded in Kleer-set resin. Once embedded in the resin, the crystals were selected according to four different sizes:12.5, 18.5, 35 and 60 μm. Ten crystals for each specific size were then nanoindented to a depth of 500 nm. Figures 5.34 and 5.35 show the results obtained for the hardness and modulus respectively, as a function of the crystal size. Figure 5.34 showed that the hardness of all the tested crystal sizes did not exceeded 2 GPa.

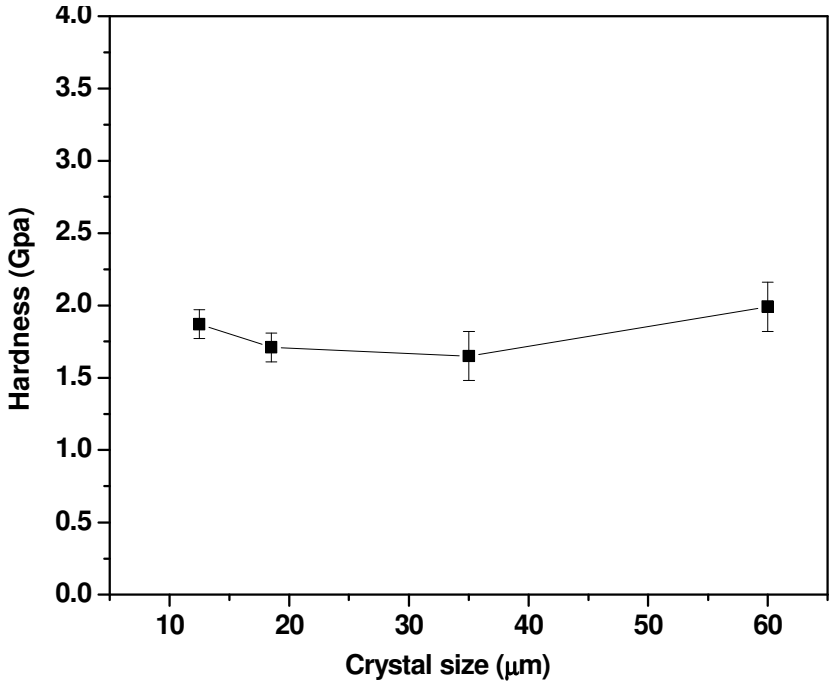

Figure 5.34 Hardness as a function of crystal size for synthetic pure calcite (control) embedded in Kleer-set resin.

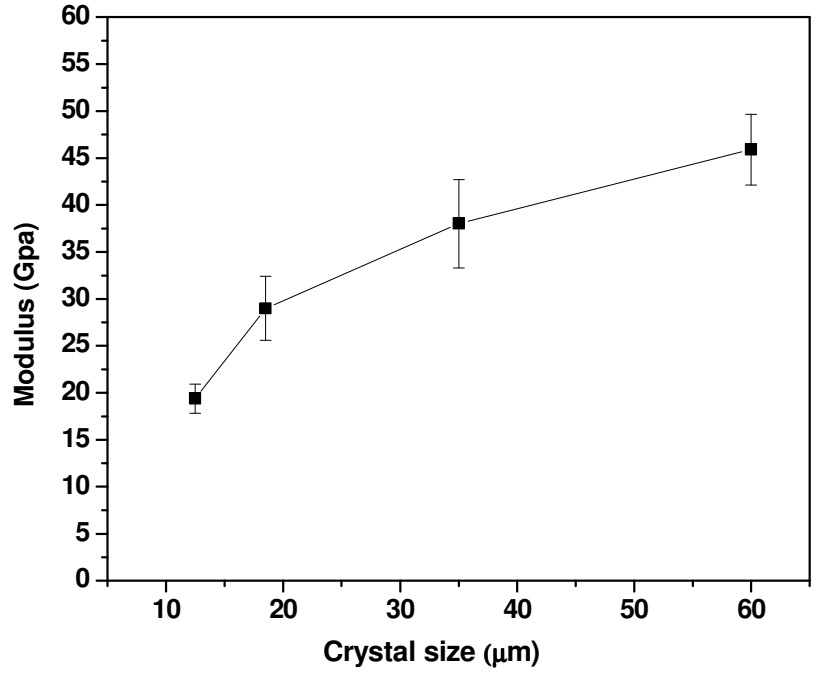

Figure 5.35 Modulus as a function of crystal size for synthetic pure calcite (control) embedded in Kleer-set resin.

Figure 5.35 shows that the modulus decreases significantly as the crystal size becomes smaller. This large modulus dependence according to crystal size possibly confirms the

presence of a significant substrate compliance. Since small crystals are pushed further down into the resin than larger crystals, a larger portion of the elastic displacement during unloading is performed by the substrate. This substrate compliance could explains the low modulus (45.9 ± 3.8 GPa) obtained for the 60 μm pure calcite control crystal which is much lower than values found in the literature (83-88 GPa) (Zügner *et al.*, 2006); although this will be discussed further in Section 5.5.

5.4.2 Mechanical properties of different resins

Since it was unclear if Kleer-set resin was inappropriate for this testing procedure, two other resins available in the market were used for comparison purposes. One of the resins (Di-hard) was a styrene-based polyester resin filled with a silica quartz (SiO2) mineral powder and was prepared at ambient temperature. This resin is reported to qualitatively have "a very high hardness" by the manufacturer, although no specific hardness value was given (MetPrep, 2010). The final resin used (ProbeMet) was a thermosetting epoxy resin filled with copper (Cu) and silica quartz powders. The ProbeMet resin, containing calcite crystals, was prepared at 150 °C under a pressure of 200 bar. This resin has an advertised hardness of 97 Shore D (~ 0.4 GPa). Figure 5.36 shows the average modulus of the resins from a set of ten nanoindentations tests. These data show that the Kleer-set and Di-hard resins have similar moduli and the ProbeMet resin the highest.

Figure 5.37 shows the average hardness values obtained for the resins from ten nanoindentation tests. A Games-Howell test at a 95 % confidence level showed that the hardness of the ProbeMet resin was significantly higher than that of the Kleer-set ($p = 0.009$) and Di-hard resins ($p = 0.001$, Table 7.39 in Appendix). No significant difference was found between the Kleer-set and Di-hard resins hardness ($p = 0.109$, Table 7.39 in Appendix). It should be noted that the standard deviations of both the Di-hard and ProbeMet resins are much larger than the one of Kleer-set resin. Observation of the nanoindented surfaces of these resins showed that at the micron-scale the silica quartz and copper fillers are not uniformly distributed throughout the polymer matrix. This could create local variance of mechanical properties and explain the larger standard deviations found on the measurements performed on these resins.

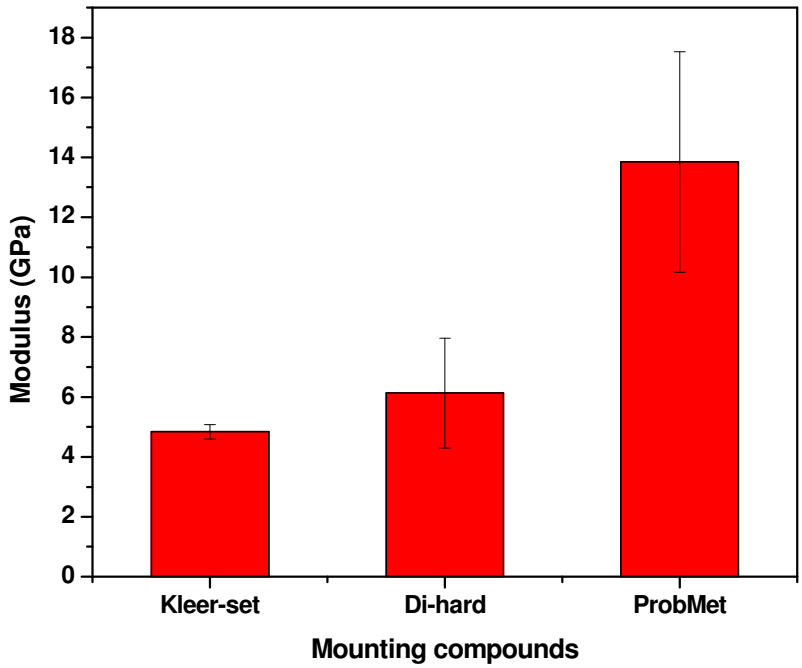

Figure 5.36 Modulus of the three tested resins used for mechanical measurements of pure calcite crystals. Values were obtained by nanoindentation to a depth of 500 nm.

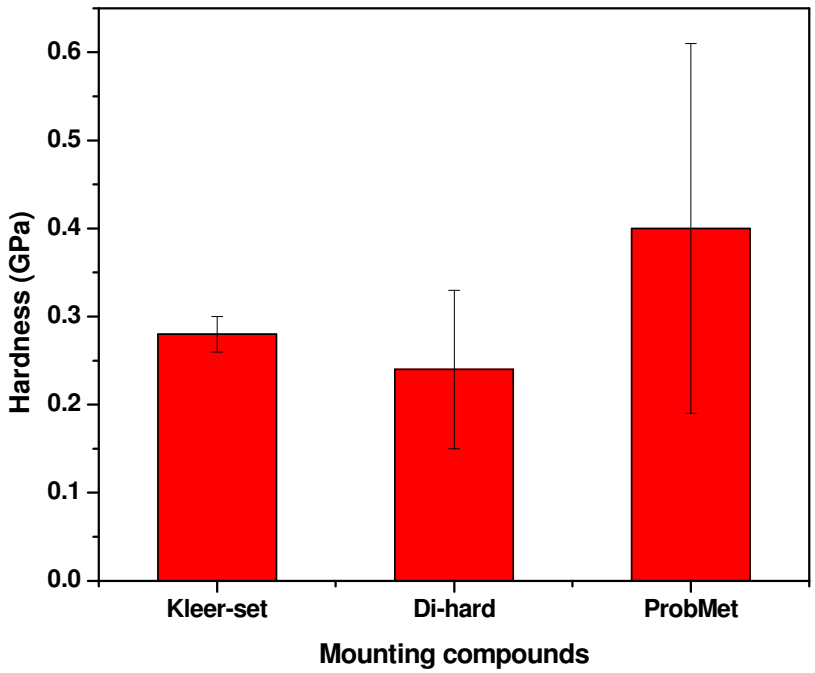

Figure 5.37 Hardness of the three tested resins used for mechanical measurements of pure calcite crystals. Values were obtained by nanoindentation to a depth of 500 nm.

5.4.3 Compliance magnitude of different resins

In order to compare the compliance magnitude of the three resins, several pure calcite crystals (control) were embedded in Di-hard and ProbeMet resins. Ten pure calcite crystals (control) imbedded in the ProbeMet resin for each specific size (12.5, 18.5, 35 and 60 µm) were then selected and tested at a depth of 500 nm. Due to poor visibility conditions only control crystals of 60 µm were tested on the Di-hard resin. Given that the moduli (and therefore the compliances) of Kleer-set and Di-hard resins are similar, comparisons are only necessary between Kleer-set and ProbeMet resins. Figure 5.38 shows the results obtained for the modulus as a function of the crystal size for all the tested resins.

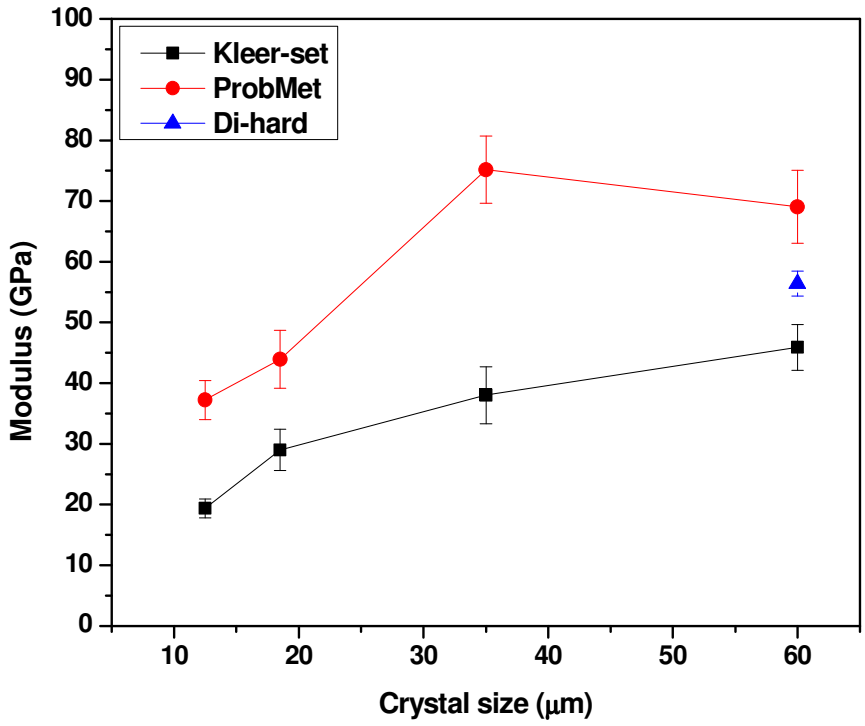

Figure 5.38 Modulus as a function of crystal size for synthetic pure calcite (control) embedded in Kleer-set, ProbeMet and Di-hard resins. Moduli are determined from nanoindentation of the crystals to a depth of 500 nm.

These data show that the moduli of crystals embedded in the ProbeMet resin are larger than the ones for the other two resins. The measured moduli for the 35 µm and 60 µm control crystals imbedded in the ProbeMet resin were 75.18 ± 5.54 GPa and 69.03 ± 6.00 GPa respectively. These moduli have therefore the same order of magnitude as values obtained for Iceland spar calcite (70.7 ± 1.1 GPa) and literature values (83-88 GPa) (Zügner *et al.*,

2006). The modulus of the 60 µm control crystals embedded in the Di-hard resin was 56.39 ± 2.08 GPa, still lower than for ProbeMet. Figure 5.39 shows the results obtained for the hardness as a function of the crystal size for all the tested resins. These data show that the hardness of crystals embedded in the ProbeMet resin are larger than obtained from the samples embedded in the other two resins. The measured hardness values for the 12.5 µm, 18.5 µm, 35 µm and 60 µm control crystals embedded in the ProbeMet resin were 2.59 ± 0.10 GPa, 3.43 ± 0.28 GPa, 3.94 ± 0.27 GPa and 2.78 ± 0.16 GPa respectively. These values have the same order of magnitude as the hardness of Iceland spar calcite (2.32 ± 0.1 GPa), obtained from indentation in Kleer-set resin, and reported values for pure calcite (2.8- 3.4 GPa) (Zügner *et al.*, 2006).

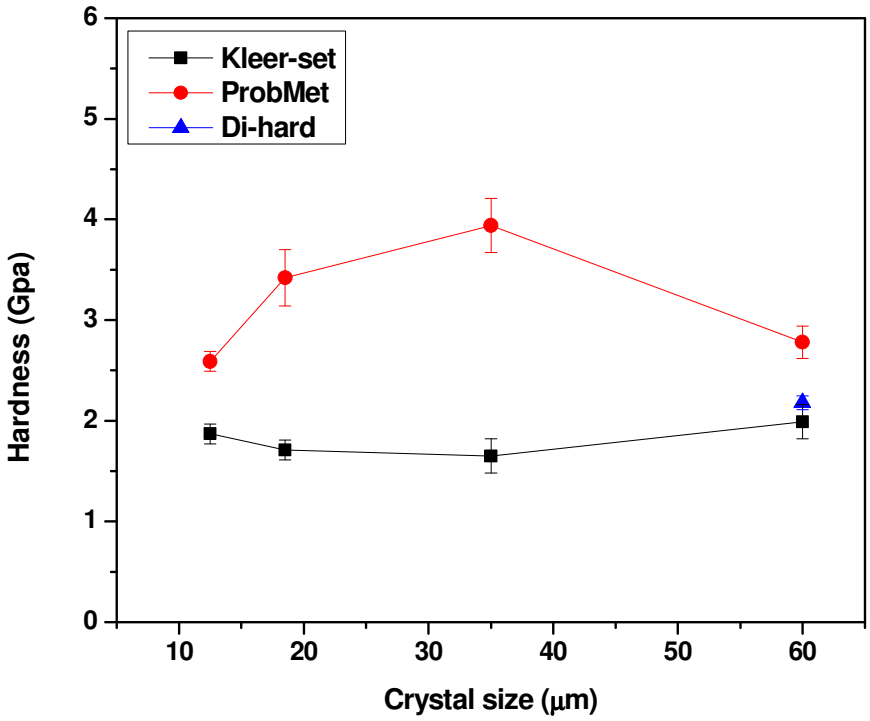

Figure 5.39 Hardness as a function of crystal size for synthetic pure calcite (control) imbedded in Kleer-set, ProbeMet and Di-hard resins. Data were obtained by nanoindentation to a depth of 500 nm.

5.4.4 Conclusions

As already mentioned, although the Oliver-Pharr method predicts some degree of compliance (sink-in phenomenon), it does not work well for excessive sink-in situations (Hay, J. C. and Pharr, 1997; Hay, J., 2009). Since the composite crystals used in this work

are smaller than 60 μm, it can be concluded that the Kleer-set resin, used in these experiments as a substrate, is inappropriate for this testing procedure. It is believed that small crystals will, when indented, subject the resin underneath the crystal to a high stress, leading to a deformation of the resin. This deformation will depend on the compliance of the resin, and so a less compliant resin is thought to be less affected by this. These tests also confirmed the inadequacy of the UK National Physical Laboratory's recommendations and the Buckle's one-tenth rule, in which the indentation depth should not exceed a tenth of the thickness of the region of the specimen that is being tested (Section 2.13.2). From the data obtained (Figures 5.38 and 5.39) it can be concluded that the ProbeMet resin could possibly be an appropriate resin to obtain the effective modulus and hardness values of crystals equal or larger than 35 μm. As already mentioned in the experimental methodology the ProbeMet resin with the included samples is however prepared at 150 °C under a pressure of 200 bar. Since at the micro-scale this resin does not offer homogenous mechanical properties and the preparation conditions could degrade the polymers occluded in the crystals, this resin was not used in further experiments.

5.5 Substrate independent mechanical properties

5.5.1 Substrate independent modulus

Given that the Kleer set resin had to be used for the measurement of the mechanical properties, and since the moduli of the synthetic crystals obtained by the Oliver-Pharr method are affected by the mechanical properties of the resin, an estimate of the elastic moduli of the samples was obtained by using the Song-Pharr model (Rar *et al.*, 2002). This model takes into account the substrate compliance (Section 2.14) when testing a material with a higher stiffness placed above it. Figure 5.40 compares the average moduli obtained from ten tests. Data are obtained using the Oliver-Pharr method and the Song-Pharr model performed on each sample: Synthetic pure calcite (control) and synthetic calcite composite crystals with 1.8, 6 and 23 vol.% occluded 200 nm PS particles. These data show that for all the samples the moduli estimated by the Song-Pharr model are higher than those obtained by the Oliver-Pharr method. These differences are particularly significant for

synthetic pure calcite (control) and synthetic calcite with 1.8 vol.% occluded 200 nm PS particles.

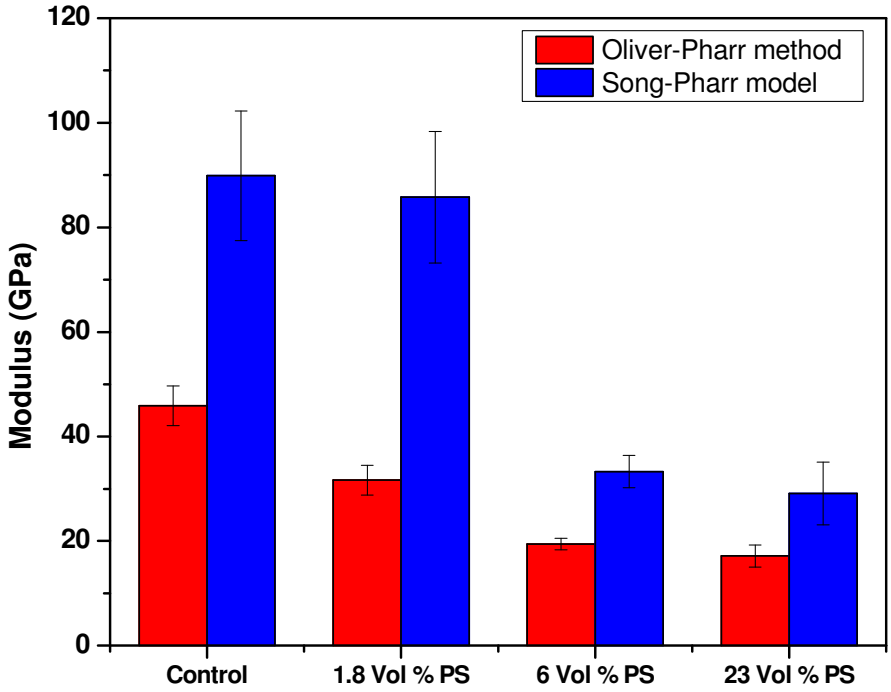

Figure 5.40 Average moduli obtained from ten nanoindentations. Data determined by the Oliver-Pharr method and the Song-Pharr model for each sample: Synthetic pure calcite (control) and synthetic calcite with 1.8, 6 and 23 vol.% occluded 200 nm PS particles.

The modulus of synthetic pure calcite control estimated by the Song-Pharr model (89.9 ± 12.4 GPa) is similar to another value reported for this mineral (83-88 GPa) (Zügner *et al.*, 2006). A Games-Howell test at a 95 % confidence level showed no statistical difference between the estimated modulus values of the control and the synthetic calcite with 1.8 vol.% PS (85.8 ± 12.6 GPa) ($p = 0.898$, Table 7.42 in Appendix). The modulus of synthetic pure calcite (control), estimated by the Song-Pharr model, was found to decrease to 33.3 ± 3.1 GPa and 29.1 ± 6.0 GPa by the occlusion of 6 vol.% and 23 vol.% PS particles respectively. No significant difference was found between the estimated moduli of the 6 vol.% and 23 vol.% PS composites ($p = 0.262$, Table 7.42 in Appendix). Figure 5.41 compares the moduli averages of ten tests obtained by the Oliver-Pharr method and the Song-Pharr model performed on synthetic pure calcite (control) and synthetic calcite with

29 vol.% occluded 20 nm di-block co-polymer micelles. The Song-Pharr estimated modulus mean of synthetic calcite occluded with the micelles (75.1 ± 15.6 GPa) was found to be lower than the value of pure calcite (p = 0.017, Table 7.45 in Appendix). This result shows therefore that although this composite has a large amount of occluded polymer (29 vol.%), it has a higher modulus than the composites occluded with 6 and 23 vol.% 200 nm PS particles.

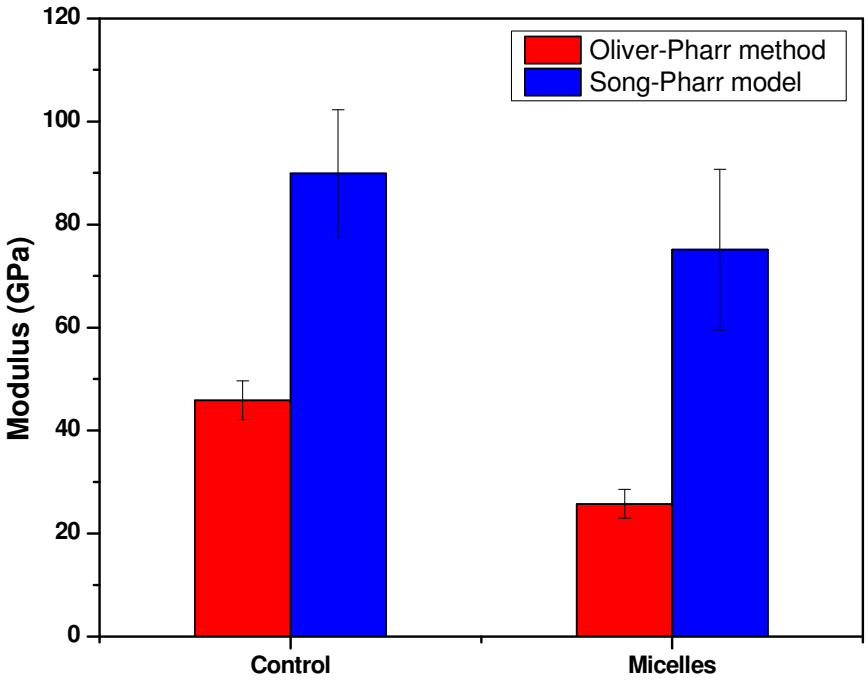

Figure 5.41 Average moduli obtained from ten nanoindentations. Data determined by the Oliver-Pharr method and the Song-Pharr model for each sample: Synthetic pure calcite (control) and synthetic calcite with 29 vol. % occluded 20 nm di-block co-polymer micelles.

5.5.2 Substrate independent hardness

As explained in Section 2.13.2, since the Oliver-Pharr method does not work well when excessive sink-in occurs, the hardness of the synthetic crystals were obtained by the conventional method (see Section 2.15) using equation 2.33. The areas of the residual impressions left by the Berkovich pyramidal tip were calculated according to Equation 2.33. The heights of the triangular residual impressions (L) were measured by AFM. Figure 5.42 compares the hardness averages of ten tests obtained with the Oliver-Pharr and the conventional method performed on each sample: sea urchin spine calcite, Iceland spar

calcite, synthetic pure calcite (control) and synthetic calcite with 1.8, 6 and 23 vol.% occluded 200 nm PS particles.

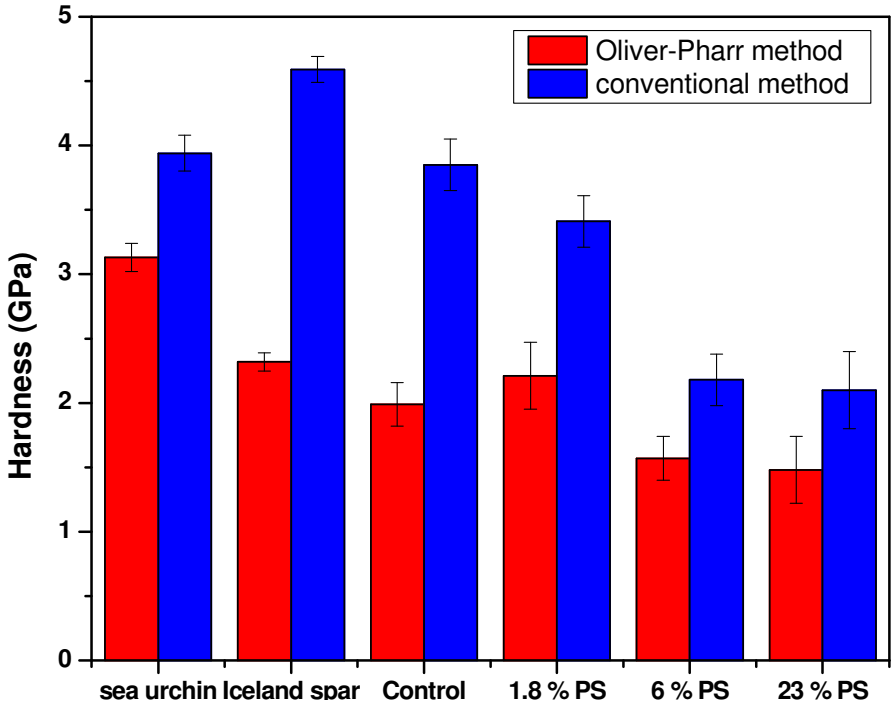

Figure 5.42 Average hardness obtained from ten nanoindentations. Data determined by the Oliver-Pharr and conventional methods for each sample: Synthetic pure calcite (control) and synthetic calcite with 1.8, 6 and 23 vol.% occluded 200 nm PS particles.

These data show that the hardness of sea urchin spine calcite and Iceland spar calcite obtained by the conventional method (3.63 ± 0.1 GPa and 2.81 ± 0.1 GPa respectively) are larger than the values obtained by the Oliver-Pharr method (3.13 ± 0.1 GPa and 2.32 ± 0.1 GPa respectively). This is possibly due to some elastic recovery of the indented area. This elastic recovery would lead to an underestimation of the area under maximum load and consequently to an overestimation of the hardness (Section 2.15). The hardness of synthetic pure calcite (control) obtained by the conventional method (3.85 ± 0.2 GPa) is slightly larger than reported values for pure calcite (2.8-3.4 GPa) (Zügner, 2002; Zügner *et al.*, 2006). This is possibly due to the already mentioned elastic recovery of the indented area which would lead to an overestimation of the measured hardness or to a size-scale effect. Zügner *et al.,* (2002) reported a 8.3 % hardness increase, from 2.89 ± 0.34 GPa to

3.13 ± 0.38 GPa as the crystal size was reduced from 500 μm to 100 μm. Since the tested pure calcite control crystals have a size of approximately 20 μm, the slightly larger than expected obtained hardness value of the control could also be caused by a size scale effect. The hardness values of synthetic calcite crystals with 1.8, 6 and 23 vol.% occluded 200 nm PS particles, obtained by the conventional method, were found to be 3.41 ± 0.2 GPa, 2.18 ± 0.2 GPa and 2.06 ± 0.3 GPa respectively (see Table 7.48 in Appendix for statistical multiple means comparison). Although larger amounts of occluded PS suppressed the typical cracking behaviour of pure calcite, this crack suppression was not associated with a hardness increase. The large decrease in hardness when the amount of polymer is increased from 1.8 to 6 vol.% was also observed in relation to compressive strength (Section 4.2). As for the strength, the significant decrease in hardness may also be caused by the reduction of the solid load-carrying material and stress concentrations at the PS particles-matrix boundaries. Figure 5.43 compares the hardness averages of ten tests obtained by the Oliver-Pharr and conventional methods performed on synthetic pure calcite (control) and synthetic calcite with 29 vol.% occluded 20 nm di-block co-polymer micelles.

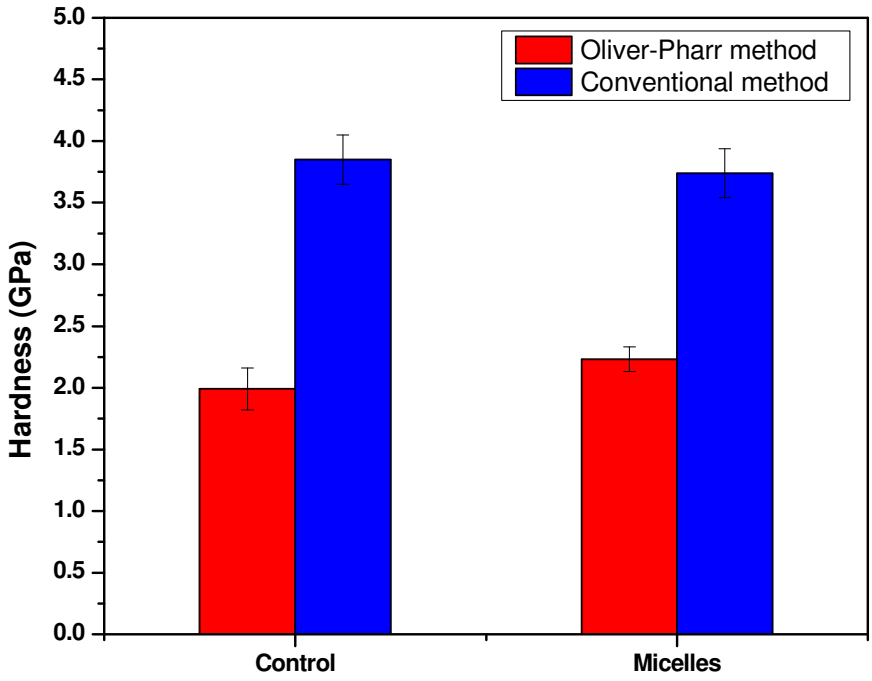

Figure 5.43 Average hardness obtained from ten nanoindentations. Data determined by the Oliver-Pharr and conventional methods for each sample: Synthetic pure calcite (control) and synthetic calcite with 29 vol.% occluded 20 nm di-block co-polymer micelles.

The hardness value of synthetic calcite occluded with the micelles, obtained by the conventional method, was found to be 3.74 ± 0.2 GPa. A two sample t-test, assuming equal variances and a confidence level of 95 %, did not find any statistical difference between this value and the hardness of pure calcite (control) ($p = 0.379$, Table 7.51 in Appendix). These data show therefore that although the composite occluded with the 29 vol.% co-polymer micelles has a lower modulus than pure calcite it has the same hardness. The decrease in the modulus while maintaining a high hardness makes this composite approximate the mechanical behaviour observed in sea urchin spine calcite.

TEM studies performed by Kim Y-Y. *et al.*, (2011) showed the presence of the di-block co-polymer micelles within the calcite lattice. Contrasting with the bulky PS polymers, the smaller size of the co-polymers micelles would allow these to be better accommodated within the calcite lattice and induce a different mechanical behaviour. By using synchrotron high-resolution powder XRD and infrared spectroscopy the same authors also found the presence of high compressive strains at the micelles-calcite interface associated with a level of atomic disorder comparable to that of biogenic calcite. As already mentioned in Sections 2.6, 2.8 and 2.9, the presence of biomolecules and/or structural disorder associated with it, could interfere with the propagation of fractures along the cleavage planes of calcite and modify its mechanical properties.

The higher hardness of the composite occluded with the co-polymer micelles may be connected with the better accommodation of the co-polymer micelles within the calcite lattice than the larger PS particles. This particular accommodation would be the source of a certain beneficial degree of structural disorder and compressive strain at the micelles-calcite interface. This would allow a reduction of the brittleness and modulus of calcite without affecting significantly its hardness. The higher hardness of the sea urchin spine calcite when compared with mineral calcite are thought to be connected with several parameters: smaller domain sizes, higher structural disorder (lower crystallinity), 2 nm layer of amorphous calcium carbonate containing biomolecules surrounding each domain and the presence of 10-100 nm cavities filled with biomolecules (Moureaux *et al.*, 2010; Seto *et al.*, 2012).

Although the co-polymer micelles occlusion have introduced some degree of structural disorder, this occlusion has possibly not reproduced all the necessary parameters involved in the superior mechanical properties of the sea urchin spine calcite. The reasons for this are still not clear but they are probably connected with some differences between the co-polymer micelles and the biogenic molecules: size, shape, surface group characteristics or other unknown parameters. Since a layer as thin as 2 nm of amorphous calcium carbonate containing biomolecules are thought to surround each domain (Seto *et al.*, 2012) it is unlikely that the 20 nm micelles can be accommodated in such a layer.

The acidic carbonate groups of the biomolecule could also possibly better replace those of the calcium carbonate than the more rigid co-polymer micelles (Pokroy *et al.*, 2006) and contribute to a different accommodation of the biomolecules in the calcite lattice. Further studies will be necessary to study the effect of different amounts/kinds of polymers on the composite's structure and mechanical properties. These studies could also elucidate the connection between structural changes such as domain size, structural disorder or lattice strain introduced by the polymers and the composites' mechanical properties.

5.5.3 Material models

Figure 5.44 and 5.45 compares the moduli and hardness predicted by the Mori-Tanaka and Miyata and Jinno models (Mori and Tanaka, 1973; Miyata and Jinno, 1982) respectively with those obtained with the Song-Pharr model and Oliver-Pharr method (in the case of sea urchin spine), for each tested sample: Urchin spine calcite, synthetic calcite with 1.8 vol.%, 6 vol.% and 23 vol.% occluded 200 nm PS particles and synthetic calcite with 29 vol.% occluded 20 nm di-block co-polymer micelles. The volume fractions of the samples under study were therefore used in these models in order to predict the moduli and hardness of hypothetical composites with the same volume fractions.

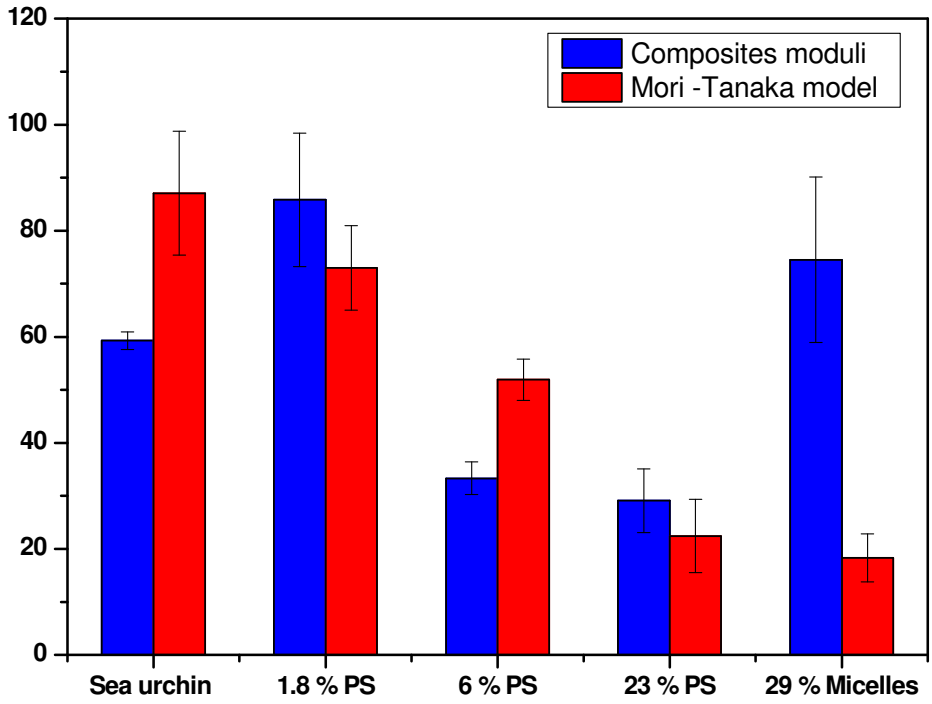

Figure 5.44 Comparison between the moduli predicted by the Mori-Tanaka model and the ones obtained by the Song-Pharr model and Oliver-Pharr method, for each tested sample: Urchin spine calcite, synthetic calcite with 1.8, 6 and 23 vol.% occluded 200 nm PS particles and synthetic calcite with 29 vol.% occluded 20 nm co-polymer micelles.

Figure 5.44 shows that although sea urchin spine calcite has a very low organic content (0.1 vol.% occluded 10 nm biomolecules) its modulus is lower than that predicted by the Mori-Tanaka model. The hardness of sea urchin spine calcite (Figure 5.45) was found to be of the same order of magnitude than the one predicted by the Miyata and Jinno model. The lower than expected modulus of the sea urchin spine calcite shows the capacity of organisms in creating biomaterials with specific mechanical properties (Ma *et al.*, 2008).

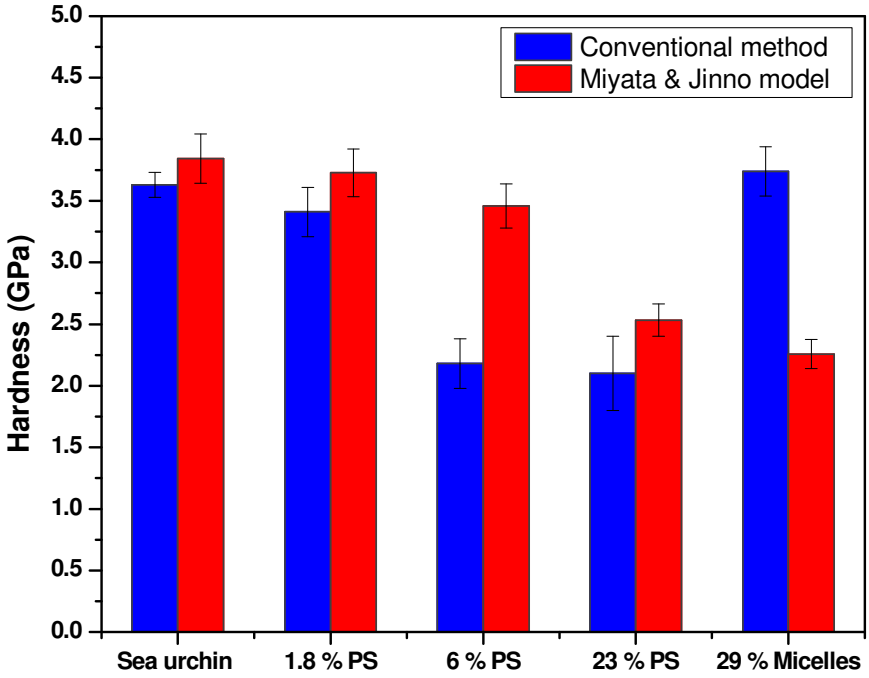

Figure 5.45 Comparison between the hardness predicted by the Miyata and Jinno model and the one obtained by the conventional method, for each tested sample: Urchin spine calcite, synthetic calcite with 1.8, 6 and 23 vol.% occluded 200 nm PS particles and synthetic calcite with 29 vol.% occluded 20 nm micelles.

Figures 5.44 and 5.45 also shows that the composite with 29 vol.% occluded 20 nm di-block co-polymer micelles has a much higher modulus and hardness than the ones predicted by the models. Although the utilised models do not take into consideration all the parameters effects (filler size, matrix-filler interface etc.), they showed that the calcite crystals occluded with the co-polymer micelles is the composite sample which deviates the most from expected values.

5.5.4 Specific modulus and specific hardness

Since for some engineering applications weight minimization is an important factor (see Section 2.7.1), the specific modulus (E/ρ) and specific hardness (H/ρ) were calculated for each tested sample (Figure 5.46 and 5.47). These data showed that the specific modulus of pure calcite was significantly reduced by the occlusion of 6 vol.% and 23 vol.% 200 nm PS particles. A multiple mean comparison test (Games-Howell procedure) at a 95 % confidence level indicated no statistical difference between the means of pure calcite and

the composite occluded with 1.8 vol.% PS (p = 0.993, Table 7.54 in Appendix). No statistical difference was detected between the means of the composites occluded with 6 vol.% and 23 vol.% PS (p = 0.999, Table 7.54 in Appendix). The specific modulus of synthetic calcite with 29 vol.% occluded 20 nm co-polymer micelles was also not found to be significantly different than that of pure calcite (p = 1.000, Table 7.54 in Appendix).

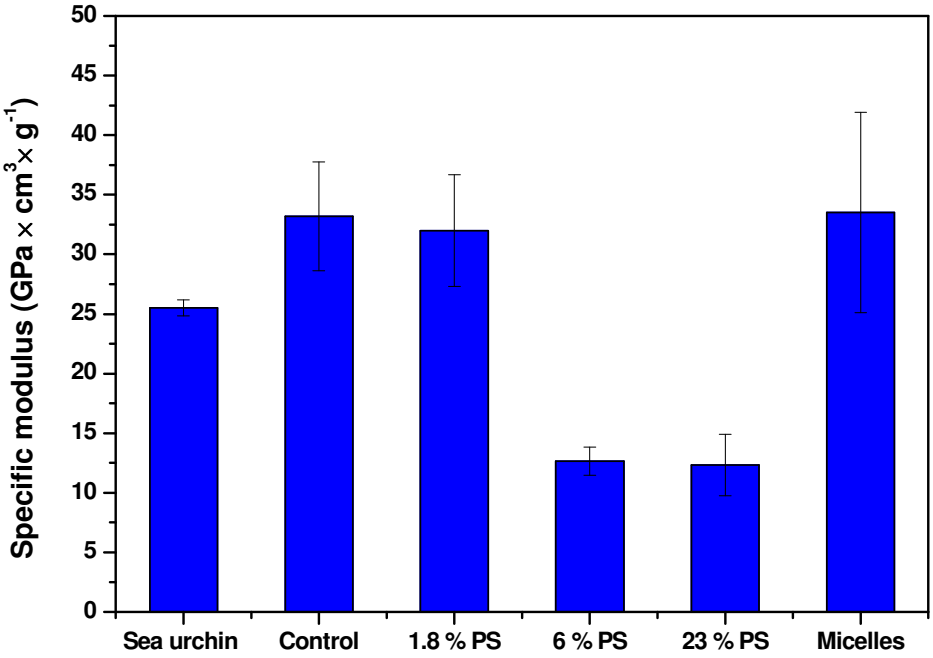

Figure 5.46 Average specific moduli obtained from ten nanoindentations for each sample: Urchin spine calcite, synthetic pure calcite (control), synthetic calcite with 1.8, 6 and 23 vol.% occluded 200 nm PS particles and synthetic calcite with 29 vol.% occluded 20 nm di-block co-polymer micelles.

Figure 5.47 shows the specific hardness (H/ρ) for each tested sample. The analysis of the obtained data showed that the specific hardness of pure calcite was also significantly reduced by the occlusion of 6 vol.% and 23 vol.% of 200 nm PS particles (See Table 7.57 in Appendix for statistical multiple means comparison). The specific hardness mean of pure calcite was found to be increased by 18 % by the occlusion of 29 vol.% 20 nm co-polymer micelles (p = 0.000, Table 7.57 in Appendix). This calcite-polymer composite was therefore the only composite which showed a specific hardness larger than that of pure calcite. Since calcium carbonate is used as a filler in plastics, rubbers and other

construction/industrial materials (see Section 2.7.1), this new composite could potentially be used as a lighter calcium carbonate replacement in some of these industries. This is especially important in the automobile or aerospace industries where weight reduction is an important factor

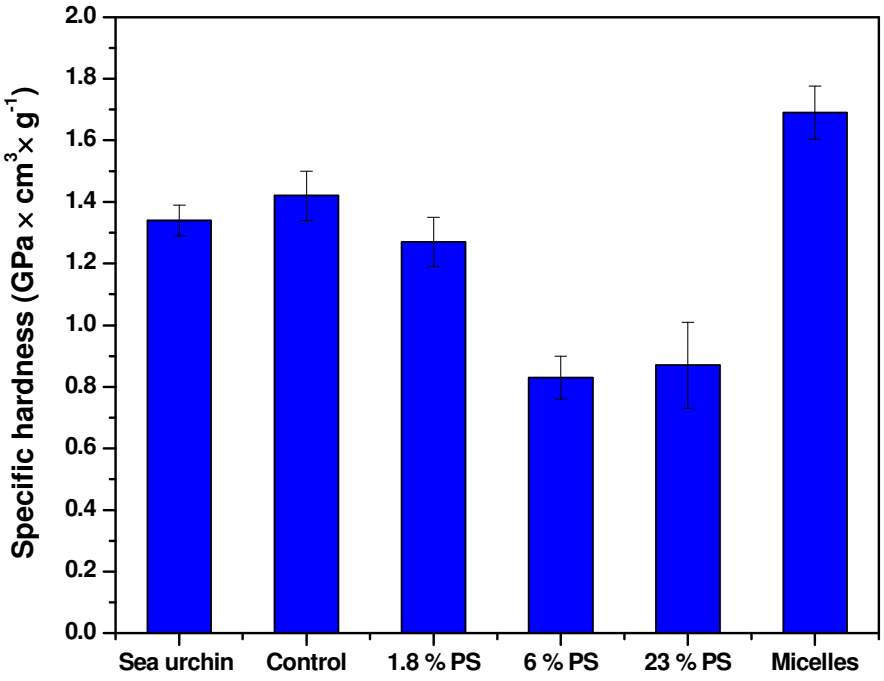

Figure 5.47 Average specific hardness obtained from ten nanoindentations for each sample: Urchin spine calcite, synthetic pure calcite (control), synthetic calcite with 1.8, 6 and 23 vol.% occluded 200 nm PS particles and synthetic calcite with 29 vol.% occluded 20 nm di-block co-polymer micelles.

5.5.5 Conclusions

By using the Song-Pharr model new moduli values were estimated for all the crystal samples affected by the resin compliance. By using this model the modulus of synthetic pure calcite control was found to be 89.9 ± 12.4 GPa. Since this value has the same magnitude as an accepted value reported for pure calcite (83-88 GPa) (Zügner *et al.*, 2006) found in the literature, it can be concluded that the Song-Pharr model also works well for hard particles on soft substrates. By direct AFM measurements of the residual indentation impressions (contact area) new substrate independent hardness values were also recalculated. The obtained results showed that although no statistical difference was found between the estimated modulus values of the control and the synthetic calcite with 1.8

vol.% 200 nm PS, the hardness of this composite was slightly reduced by the occluded polymer. The modulus and hardness of synthetic pure calcite (control) were also found to have been significantly reduced by the occlusion of 6 vol.% and 23 vol.% 200 nm PS particles. Although the modulus of synthetic calcite occluded with 29 vol.% 20 nm co-polymer micelles was slightly reduced by the polymer, its hardness was found to be the same as pure calcite. This was not expected since a decrease in the modulus is often accompanied by a lower hardness.

None of the tested composites showed a higher specific modulus than pure calcite. However the composite occluded with 29 vol. % 20 nm micelles was found to have a higher specific hardness than pure calcite. This shows that although the employed biomimetic approach was unable to create a material such as the sea urchin spine, which occluded with a soft polymer, displays a higher hardness and lower modulus than pure calcite, the approach was successful in decreasing the weight of calcite without decreasing its hardness. Although none of the tested composites would be suited for applications where a high hardness is an important requirement (polishing ceramic abrasives, cutting tools etc), the composite occluded with the co-polymer micelles could potentially be used as a lighter calcium carbonate replacement in the automobile or aerospace industries where weight reduction is an important factor.

5.6 References

Bruet, B. J. F., Qia, H. J., Boyce, M. C., Panas, R., Tai, K., Frick, L. and Ortizb, C., 2005, *Nanoscale morphology and indentation of individual nacre tablets from the gastropod mollusc Trochus niloticus*, J. Mater. Res., 20, 9, 2400-2419.

Carter, G. M., Henshall, J. L. and Wakeman, R. J., 1993, *Knoop hardness and fracture anisotropy of calcite*, Journal of Materials Science Letters, 12, 6, 407-410.

Chen, J. and Bull, S. J., 2009, *The investigation of creep of electroplated Sn and Ni-Sn coating on copper at room temperature by nanoindentation*, Surface and Coatings Technology, 203, 12, 1609-1617.

Chudoba, T. and Richter, F., 2001, *Investigation of creep behaviour under load during indentation experiments and its influence on hardness and modulus results*, Surface and Coatings Technology, 148, 2-3, 191-198.

Fischer-Cripps, A. C., 2002, *Nanoindentation*, Springer-Verlag, Berlin Germany.

Hay, J. C. and Pharr, G. M., 1997, *Critical issues in measuring the mechanical properties of hard films on soft substrates by nanoindentation techniques*, Conference: 1997 fall meeting of the Materials Research Society, Boston, MA (United States), 1-5 Dec 1997.

Hay, J., 2009, *Introduction to instrumented indentation testing*, Experimental Techniques, 33, 6, 66-72.

Kim, Y.-Y., Ganesan, K., Yang, P., Kulak, A. N., Borukhin, S., Pechook, S., Ribeiro, L., Kroger, R., Eichhorn, S. J., Armes, S. P., Pokroy, B. and Meldrum, F. C., 2011, *An artificial biomineral formed by incorporation of copolymer micelles in calcite crystals*, Nat. Mater., 10, 890-896.

Lawn, B. R., 1993, *Fracture of Brittle Solids*, Cambridge University Press.

Li, X. and Bhushan, B., 2002, *A review of nanoindentation continuous stiffness measurement technique and its applications*, Materials Characterization, 48, 1, 11-36.

Li, X., Chang, W. C., Chao, Y. J., Wang, R. and Chang, M., 2004, *Nanoscale Structural and Mechanical Characterization of a Natural Nanocomposite Material: The Shell of Red Abalone*, Nano Letters, 4, 4, 613-617.

Li, X. and Nardi, P., 2004, *Micro/nanomechanical characterization of a natural nanocomposite material: the shell of Pectinidae*, Nanotechnology, 15, 211-217.

Lin, Y. C., Weng, Y. J., Pen, D. J. and Li, H. C., 2009, *Deformation model of brittle and ductile materials under nano-indentation*, Materials & design, 30, 5, 1643-1649.

Lucas, B. and Oliver, W., 1999, *Indentation power-law creep of high-purity indium*, Metallurgical and Materials Transactions, 30, 3, 601-610.

Ma, Y., Cohen, S. R., Addadi, L. and Weiner, S., 2008, *Sea Urchin Tooth Design: An "All-Calcite" Polycrystalline Reinforced Fiber Composite for Grinding Rocks*, Advanced Materials, 20, 8, 1555-1559.

McColm, I. J., 1990, *Ceramic hardness*, Plenum Press, New York.

Miyata, N. and Jinno, H., 1982, *Micromechanics Approach to the Indentation Hardness of Glass Matrix Particulate Composites*, J. Mat. Sci., 17, 547-557.

MetPrep, 2010, *MetPrep price list*, from:
http://www.uki.net/php/files/metprepcms.uki.net/pricelist_2011.pdf

Mori, T. and Tanaka, K., 1973, *Average stress in matrix and average elastic energy of materials with misfitting inclusions*, Acta Metallurgica, 21, 5, 571-574.

Moureaux, C., Perez-Huerta, A., Compere, P., Zhu, W., Leloup, T., Cusack, M. and Dubois, P., 2010, *Structure, composition and mechanical relations to function in sea urchin spine*, Journal of Structural Biology, 170, 1, 41-49.

Oliver, W. C. and Pharr, G. M., 1992, *An improved technique for determining hardness and elastic modulus*, J. Mater. Res., 7, 6, 1564-1583.

Oliver, W. C. and Pharr, G. M., 2004, *Measurement of hardness and elastic modulus by instrumented indentation: Advances in understanding and refinements to methodology*, J. Mater. Res., 19, 1, 3-20.

Pokroy, B., Fitch, A. and Zolotoyabko, E., 2006, *The Microstructure of Biogenic Calcite: A View by High-Resolution Synchrotron Powder Diffraction*, Advanced Materials, 18, 18, 2363-2368.

Rar, A., Song, H. and Pharr, G. M., 2002, *Assessment of new relation for the elastic compliance of a film–substrate system, in Thin Films: Stresses and Mechanical Properties* Mater. Res. Soc. Symp. Proc., 695, 431.

Seto, J., Ma, Y., Davis, S. A., Meldrum, F., Gourrier, A., Kim, Y., Schilde, U., Sztucki, M., Burghammer, M., Maltsev, S., Jager, C. and Colfen, H., 2012, *Structure-property relationships of a biological mesocrystal in the adult sea urchin spine*, Proc. Nat. Acad. Sci., 109, 10, 3699-3704.

Yonezu, A., Ogawa, T. and Takemoto, M., 2004, *AE Analysis on the Fracture Mechanism of Ceramics During Indentation Testing*, Paper presented at the Conference: 2004 SEM X International Congress & Exposition on Experimental & Applied Mechanics.

Zügner, S., 2002, *Untersuchungen zum elastisch-plastischen Verhalten von Kristalloberflächen mittels Kraft-Eindringtiefen-Verfahren*, Thesis from the Bayerischen Julius Maximilians Universität Würzburg.

Zügner, S., Marquardt, K. and Zimmermann, I., 2006, *Influence of nanomechanical crystal properties on the comminution process of particulate solids in spiral jet mills*, European Journal of Pharmaceutics and Biopharmaceutics, 62, 2, 194-201.

6. CONCLUSIONS AND SUGGESTIONS FOR FUTURE WORK

6.1 Conclusions

In this study the suitability of particular polymer inclusions for improving specific mechanical properties of calcite has been investigated. Nanoindentation and micro-compression were chosen to investigate the surface and bulk deformation behaviour of micron-size calcite-polymer composite crystals. In order to carry out the nanoindentation testing it was necessary to embed the crystals in a resin material to produce a flat surface. This flat surface was required so that reliable indentation of the samples could take place. A low value of the modulus of pure calcite crystals, used as a control, was found to be caused by a compliance of the resin substrate into which the crystal samples were embedded. A study of some of the hardest resins available on the market showed that these were however inappropriate to be used as a substrate. The Oliver-Pharr method utilised in the nanoindentation procedure was therefore found to be inadequate to measure the hardness and modulus of the crystal samples.

Since the moduli of the synthetic crystals obtained by the nanoindenter based Oliver-Pharr method were affected by the mechanical properties of the resin, a corrected value of the elastic moduli of the samples was obtained by using the Song-Pharr model. This model takes into consideration the substrate compliance in order to obtain the substrate independent modulus. Although this model was supposed to work well for compliant films on stiff substrates its applicability to stiff particles/compliant substrate systems had still not been fully studied. By using this model the modulus of the synthetic pure calcite control was found to be 89.9 ± 12.4 GPa. Since this value has the same magnitude as values for pure calcite found in the literature, it is concluded that the Song-Pharr model appears to work well for hard particles on soft substrate. Since the resin compliance is also thought to have an effect on the hardness, this parameter was recalculated by conventional methods.

By analyzing the obtained substrate independent data it was found that the modulus of synthetic calcite occluded with 29 vol.% 20 nm co-polymer micelles was reduced by the

polymer, while its hardness remained unchanged. The hardness and modulus of pure calcite were also found to be significantly reduced by the occlusion of different amounts of 200 nm PS particles. These polymers are therefore not suited to improving the hardness of pure calcite. Block co-polymer micelles were however shown to increase the specific hardness of calcite: an effect not observed for PS. Taking into consideration that this composite has the same specific modulus as pure calcite, it is thought that this material may have potential for applications where weight minimization is an important factor.

The use of the FIB allowed the crystal samples to be machined into specimens with the same dimensions allowing reliable mechanical data to be obtained. Previous flat punch compression data suggested that the contact area was not readily obtained using non-conventional crystal geometries. FIB milling permitted a better assessment of the polymer inclusions influence on the composites' compressive properties. This investigation showed qualitatively that the characteristic brittle behaviour of pure calcite is reduced by the occluded polystyrene. Images of cracks, post-fracture of the specimens, indicated deformation of the polymer. This is evidence of the occurence of a crack bridging mechanism. It was thought that this could lead to an enhancement of the strain at fracture and work of fracture of these composites when compared with pure calcite.

The micro-compression data showed however that both strain at fracture and work of fracture of synthetic pure calcite were reduced by the occluded polymer particles. Due to the low density reduction introduced by the 1.8 and 6 vol.% 200 nm PS particles, these polymers were also unable to increase the specific compressive mechanical properties (work of fracture, strength, strain and modulus) of pure calcite. These biomimetic composites are therefore not suited for applications where properties such as high strength or high energy absorption capacity are important requirements.

6.2 Suggestions for future works

Since on a weight basis the 20 nm co-polymer micelles proved to be the only polymer inclusions that increased the specific hardness of calcite, further studies utilising this polymer should be continued. Since the toughening capacity of particles having an aspect ratio close to 1 is predicted to be somewhat less than for fibers (Warren, 1992), longer polymer chain inclusions should also be tried. Since smaller and larger biomolecules than the micelles co-polymer were found to be located between and within domains of the sea urchin spine calcite (Seto *et al.*, 2012), different polymer sizes (1-100 nm) should also be used. Micro-compression in conjunction with the FIB technique would allow the bulk deformation behaviour and the compressive mechanical properties of these composites to be compared with pure calcite. Performing the micro-compression test in a SEM, using an adjustable sample holder adapted with a goniometer would minimize any contact misfit between the flat punch and the top surface of the micro-compression sample (Uchic and Dimiduk, 2005; Zhang, H. *et al.*, 2006; Kiener *et al.*, 2009). Nanoindentation can also be a very useful technique in order to investigate the surface deformation behaviour and mechanical properties of these composites. In order to avoid the Oliver-Pharr method limitations when using a compliant substrate, the composite crystals should be nanoindented directly on the silicon substrate in which they were initially grown.

Since the crystals do not have the horizontal top surface required for nanoindentation, the test should be performed in an instrument with adjustable sample holder capacity. AFM based technology equipped with a Triboscope Hysitron force transducer was already proven to be successful in probing the mechanical properties of micron size calcite crystals (Zügner, 2002; Zügner *et al.*, 2006). This type of instrument allows the sample orientation to be adjusted in order to obtain a horizontal top surface. Moreover, this instrument offers the additional advantage of imaging the area to be studied before and after indenting. These tests will assess the degree of reliability of the Song-Pharr model and conventional methods utilised in this work. Nanoindentation could also be used to study the time dependent plastic deformation behaviour of the calcite composites under constant load (indentation creep) (Chudoba and Richter, 2001; Li, X. and Bhushan, 2002; Chen and Bull, 2009). This

information is especially relevant in applications where relaxation processes dictate performance, as excessive creep can cause an unexpected increase in friction due to changes in contact area. The temperature influence on the mechanical properties of the composites should also be assessed. This will determine the suitability of the new composites in applications where temperature resistant mechanical properties are an important requirement.

6.3 References

Chen, J. and Bull, S. J., 2009, *The investigation of creep of electroplated Sn and Ni-Sn coating on copper at room temperature by nanoindentation*, Surface and Coatings Technology, 203, 12, 1609-1617.

Chudoba, T. and Richter, F., 2001, *Investigation of creep behaviour under load during indentation experiments and its influence on hardness and modulus results*, Surface and Coatings Technology, 148, 2-3, 191-198.

Kiener, D., Motz, C. and Dehm, G., 2009, *Micro-compression testing: A critical discussion of experimental constraints*, Materials Science and Engineering, 505, 1-2, 79-87.

Li, X. and Bhushan, B., 2002, *A review of nanoindentation continuous stiffness measurement technique and its applications*, Materials Characterization, 48, 1, 11-36.

Seto, J., Ma, Y., Davis, S. A., Meldrum, F., Gourrier, A., Kim, Y., Schilde, U., Sztucki, M., Burghammer, M., Maltsev, S., Jager, C. and Colfen, H., 2012, *Structure-property relationships of a biological mesocrystal in the adult sea urchin spine*, Proc. Nat. Acad. Sci., 109, 10, 3699-3704.

Uchic, M. D. and Dimiduk, D. M., 2005, *A methodology to investigate size scale effects in crystalline plasticity using uniaxial compression testing*, Materials Science and Engineering A, 400-401, 268-278.

Warren, R., 1992, *Ceramic-Matrix composites*, Chapman and Hall.

Zhang, H., Schuster, B. E., Wei, Q. and Ramesh, K. T., 2006, *The design of accurate micro-compression experiments*, Scripta Materialia, 54, 2, 181-186.

Zügner, S., 2002, *Untersuchungen zum elastisch-plastischen Verhalten von Kristalloberflächen mittels Kraft-Eindringtiefen-Verfahren*, Thesis from the Bayerischen Julius Maximilians Universität Würzburg.

Zügner, S., Marquardt, K. and Zimmermann, I., 2006, *Influence of nanomechanical crystal properties on the comminution process of particulate solids in spiral jet mills*, European Journal of Pharmaceutics and Biopharmaceutics, 62, 2, 194-201.

APPENDIX 7: Statistical methodology

7.1 Introduction

The statistical calculations were performed using IBM SPSS Statistic 17 software and Excel 2007. In cases where only two population means had to be compared, a two-sample t-test at a 95 % confidence level was employed. The two sample t-test was used to confirm whether one population mean, μ_1, was statistically larger than the other μ_2. This test tested therefore the hypotheses Ho: $\mu_1 = \mu_2$ versus Ha: $\mu_1 > \mu_2$, where Ho and Ha represent the null hypothesis and the alternative hypothesis respectively. In each t-test a *p*-value is obtained and compared with the accepted significance level ($\alpha = 0.05$). If the *p*-value is less than 0.05 the null hypothesis is rejected and therefore one of the compared means is considered larger than the other (the *p*-value is also a measure of the strength against Ho) (Zar, 2010, chapter 8; Devore, 2011, chapter 8). The use of a two-sample t-test in order to compare more than two means would be incorrect since the probability of incorrectly rejecting at least one of the Ho (type I error) increases with the number of possible pairs of samples. For a significance level (α) of 0.05, using a t-test to compare 10 sample means would give a type I error probability of $1- (1- \alpha)^{45} = 0.90$, where 45 is the number of possible different pairwise combinations of 10 samples (Zar, 2010, chapter 10).

In order to test for differences between all possible pairs of means the multiple-comparison Tukey test was used (Zar, 2010, chapter 11.1; Devore, 2011, chapter 10.2). Since this parametric test maintains the probability of type I error at or below the stated significance level, it is more appropriate than the t-test when a multiple-comparison involving more than two means is necessary. In a Tukey test each possible pair of means are compared with each other and a *p*-value for each comparison is obtained. If the *p*-value is less than the specified α (0.05) the null hypothesis is rejected and the means are considered to be significantly different from each other. More details on the Tukey test can be found in standard statistical literature (Zar, 2010, chapter 11.1; Devore, 2011, chapter 10.2).

7.2 Analysis of the Tukey and t-test assumptions

The t-test assumes that the observations within each group are normally distributed and the variances are equal in the two groups. If the data are very nonnormal, the Mann-Whitney U-test can be used. If the data from the two populations do not have the same variance the t-test can be replaced by the Welch's t-test. This test has been shown to perform well with respect to Type I error, and is one of the easiest and reliable available procedures (Zar, 2010, chapter 8c; McDonald, 2009). Since the validity of the Tukey test also depends upon the assumptions that the samples must come from normal populations and have the same variance, a preliminary investigation of the data distribution will be performed. For nonnormal distributed data the nonparametric Rank-Sum test or data transformations procedures can be utilised (Devore, 2011, chapter 15; Zar, 2010, chapter 11.5).

If the data is normally distributed but violate the assumption of variances homogeneity, the Games-Howell multiple comparison test can be used. This test has a good power and maintains the probability of type I error around α (Zar, 2010, chapter 11.1b). As for the Tukey test if the *p*-value obtained by the Games-Howell procedure is less than 0.05 the null hypothesis will be rejected and the means will be considered significantly different from each other. In order to investigate which multiple-comparison test is suitable for the obtained data, the Levene's test is employed to check the homogeneity of the variance of all populations (Zar, 2010, chapter 8.5b). To check if the populations are normally distributed, the Shapiro-Wilk test is used (Zar, 2010, chapter 6.6d). The assumption that the data have homogenous variances or are normally distributed is fulfilled for a probability of $p>0.05$. The following Tables show the results obtained by the employed statistical procedures.

7.3 Statistical tables

Table 7.1 Results for the Shapiro-Wilk test at a 95 % confidence level - Compressive strength of non-machined crystals.

Samples (non-machined crystals)		Shapiro-Wilk		
		Statistic	df	Sig.
	Control	.964	10	.833
	1.8 % PS	.859	10	.117
	6 % PS	.937	10	.523

As can be seen in Table 7.1, since the *p*-value of all tested populations are greater than 0.05, the hypothesis that the data is normally distributed can not be rejected at the 95 % confidence level. It is therefore possible to use parametric tests in the statistical analysis.

Table 7.2 Results for the Levene's homogeneity of variances test - Compressive strength of non-machined crystals.

Levene Statistic	df1	df2	Sig.
5.068	2	27	.021

The result for the Levene's test in Table 7.2 shows that the obtained *p*-value (p = 0.021) is lower than 0.05. This shows that the assumption that all the populations have the same variance is violated at the 95 % confidence level and therefore the Games-Howell test should be used.

Table 7.3 Results for the Games-Howell multiple means comparisons procedure at a 95 % confidence level - Compressive strength of non-machined crystals.

(I) samples (crystals)	(J) samples (crystals)	Mean Difference (I-J)	Std. Error	Sig.	95% Confidence Interval	
					Lower Bound	Upper Bound
Control	1.8 % PS	83.450	39.871	.129	-21.61	188.51
	6 % PS	158.000*	40.047	.004	52.86	263.14
1.8 % PS	Control	-83.450	39.871	.129	-188.51	21.61
	6 % PS	74.550*	26.105	.029	7.12	141.98
6 % PS	Control	-158.000*	40.047	.004	-263.14	-52.86
	1.8 % PS	-74.550*	26.105	.029	-141.98	-7.12

* The mean difference is significant at the 0.05 level.

Table 7.4 Results for the Shapiro-Wilk test at a 95 % confidence level - Compressive strength of cube-machined crystals.

Samples (machined crystals)		Shapiro-Wilk		
		Statistic	df	Sig.
	Control	.859	4	.257
	1.8 % PS	.908	4	.471
	6 % PS	.859	4	.257

As can be seen in Table 7.4, since the *p*-value of all tested populations are greater than 0.05, the hypothesis that the data is normally distributed can not be rejected at the 95 % confidence level. It is therefore possible to use parametric tests in the statistical analysis.

Table 7.5 Results for the Levene's homogeneity of variances test - Compressive strength of cube-machined crystals.

Levene Statistic	df1	df2	Sig.
1.702	2	9	.236

The result for the Levene's test in Table 7.5 shows that the obtained *p*-value (p = 0.236) is greater than 0.05 and therefore, the assumption of homogeneity of variance is met. Since the data have homogenous variances the Tukey test will be used for conducting the multiple means comparison.

Table 7.6 Results for the Tukey multiple means comparisons procedure at a 95 % confidence level - Compressive strength of cube-machined crystals.

(I) samples (crystals)	(J) samples (crystals)	Mean Difference (I-J)	Std. Error	Sig.	95% Confidence Interval	
					Lower Bound	Upper Bound
Control	1.8 % PS	91.250	132.726	.776	-279.32	461.82
	6 % PS	769.000*	132.726	.001	398.43	1139.57
1.8 % PS	Control	-91.250	132.726	.776	-461.82	279.32
	6 % PS	677.750*	132.726	.002	307.18	1048.32
6 % PS	Control	-769.000*	132.726	.001	-1139.57	-398.43
	1.8 % PS	-677.750*	132.726	.002	-1048.32	-307.18

* The mean difference is significant at the 0.05 level.

Table 7.7 Results for the Shapiro-Wilk test at a 95 % confidence level - Compressive modulus of cube-machined crystals.

Samples (machined crystals)		Shapiro-Wilk		
		Statistic	df	Sig.
	Control	.940	4	.655
	1.8 % PS	.981	4	.908
	6 % PS	.988	4	.945

As can be seen in Table 7.7, since the *p*-value of all tested populations are greater than 0.05, the hypothesis that the data is normally distributed can not be rejected at the 95 % confidence level. It is therefore possible to use parametric tests in the statistical analysis.

Table 7.8 Results for the Levene's homogeneity of variances test - Compressive modulus of cube-machined crystals.

Levene Statistic	df1	df2	Sig.
.360	2	9	.707

The result for the Levene's test in Table 7.8 shows that the obtained *p*-value (p = 0.707) is greater than 0.05 and therefore, the assumption of homogeneity of variance is met at the 95 % confidence level. Since the data have homogenous variances the Tukey test will be used for conducting the multiple means comparison.

Table 7.9 Results for the Tukey HSD multiple means comparisons procedure at a 95 % confidence level - Compressive modulus of cube-machined crystals.

(I) samples (crystals)	(J) samples (crystals)	Mean Difference (I-J)	Std. Error	Sig.	95% Confidence Interval	
					Lower Bound	Upper Bound
Control	1.8 % PS	-1333.500	1165.438	.520	-4765.78	2098.78
	6 % PS	4921.000*	951.576	.003	2118.55	7723.45
1.8 % PS	Control	1333.500	1165.438	.520	-2098.78	4765.78
	6 % PS	6254.500*	1165.438	.003	2822.22	9686.78
6 % PS	Control	-4921.000*	951.576	.003	-7723.45	-2118.55
	1.8 % PS	-6254.500*	1165.438	.003	-9686.78	-2822.22

* The mean difference is significant at the 0.05 level.

Table 7.10 Results for the Shapiro-Wilk test at a 95 % confidence level - Compressive modulus of non-machined crystals.

Samples (non-machined crystals)		Shapiro-Wilk		
		Statistic	df	Sig.
	Control	.965	10	.836
	1.8 % PS	.845	10	.111
	6 % PS	.942	10	.578

As can be seen in Table 7.10, since the *p*-value of all tested populations are greater than 0.05, the hypothesis that the data is normally distributed can not be rejected at the 95 % confidence level. It is therefore possible to use parametric tests in the statistical analysis.

Table 7.11 Results for the Levene's homogeneity of variances test - Compressive modulus of non-machined crystals.

Levene Statistic	df1	df2	Sig.
.064	2	24	.938

The result for the Levene's test in Table 7.11 shows that the obtained *p*-value (p = 0.938) is greater than 0.05 and therefore, the assumption of homogeneity of variance is met at the 95 % confidence level. Since the data have homogenous variances the Tukey test will be used for conducting the multiple means comparison.

Table 7.12 Results for the Tukey HSD multiple means comparisons procedure at a 95 % confidence level - Compressive modulus of non-machined crystals.

(I) samples (crystals)	(J) samples (crystals)	Mean Difference (I-J)	Std. Error	Sig.	95% Confidence Interval	
					Lower Bound	Upper Bound
Control	1.8 % PS	1394.071*	207.484	.000	875.93	1912.22
	6 % PS	1125.800*	188.288	.000	655.59	1596.01
1.8 % PS	Control	-1394.071*	207.484	.000	-1912.22	-875.93
	6 % PS	-268.271	207.484	.413	-786.42	249.87
6 % PS	Control	-1125.800*	188.288	.000	-1596.01	-655.59
	1.8 % PS	268.271	207.484	.413	-249.87	786.42

* The mean difference is significant at the 0.05 level.

Table 7.13 Results for the Shapiro-Wilk test at a 95 % confidence level - Strain at fracture of cube-machined crystals.

Samples (machined crystals)		Shapiro-Wilk		
		Statistic	df	Sig.
	Control	.887	4	.367
	1.8 % PS	.914	4	.502
	6 % PS	.877	4	.324

As can be seen in Table 7.13, since the *p*-value of all tested populations are greater than 0.05, the hypothesis that the data is normally distributed can not be rejected at the 95 % confidence level. It is therefore possible to use parametric tests in the statistical analysis.

Table 7.14 Results for the Levene's homogeneity of variances test - Strain at fracture of cube-machined crystals.

Levene Statistic	df1	df2	Sig.
3.242	2	9	.087

The result for the Levene's test in Table 7.14 shows that the obtained *p*-value (p = 0.087) is greater than 0.05 and therefore, the assumption of homogeneity of variance is met at the 95 % confidence level. Since the data have homogenous variances the Tukey test will be used for conducting the multiple means comparison.

Table 7.15 Results for the Tukey HSD multiple means comparisons procedure at a 95 % confidence level – Strain at fracture of cube-machined crystals.

(I) samples (crystals)	(J) samples (crystals)	Mean Difference (I-J)	Std. Error	Sig.	95% Confidence Interval	
					Lower Bound	Upper Bound
Control	1.8 % PS	9.145	3.493	.066	-.61	18.90
	6 % PS	13.465*	3.493	.010	3.71	23.22
1.8 % PS	Control	-9.145	3.493	.066	-18.90	.61
	6 % PS	4.320	3.493	.463	-5.43	14.07
6 % PS	Control	-13.465*	3.493	.010	-23.22	-3.71
	1.8 % PS	-4.320	3.493	.463	-14.07	5.43

* The mean difference is significant at the 0.05 level.

Table 7.16 Results for the Shapiro-Wilk test at a 95 % confidence level – Strain at fracture of non-machined crystals.

Samples (non-machined crystals)		Shapiro-Wilk		
		Statistic	df	Sig.
	Control	.964	10	.825
	1.8 % PS	.940	10	.643
	6 % PS	.911	10	.290

As can be seen in Table 7.16, since the *p*-value of all tested populations are greater than 0.05, the hypothesis that the data is normally distributed can not be rejected at the 95 % confidence level. It is therefore possible to use parametric tests in the statistical analysis.

Table 7.17 Results for the Levene's homogeneity of variances test - Strain at fracture of non-machined crystals.

Levene Statistic	df1	df2	Sig.
1.676	2	24	.208

The result for the Levene's test in Table 7.17 shows that the obtained *p*-value (p = 0.208) is greater than 0.05 and therefore, the assumption of homogeneity of variance is met at the 95

% confidence level. Since the data have homogenous variances the Tukey test will be used for conducting the multiple means comparison

Table 7.18 Results for the Tukey HSD multiple means comparisons procedure at a 95 % confidence level - Strain at fracture of non-machined crystals.

(I) samples (crystals)	(J) samples (crystals)	Mean Difference (I-J)	Std. Error	Sig.	95% Confidence Interval	
					Lower Bound	Upper Bound
Control	1.8 % PS	-10.923*	3.786	.021	-20.38	-1.47
	6 % PS	-4.249	3.436	.444	-12.83	4.33
1.8 % PS	Control	10.923*	3.786	.021	1.47	20.38
	6 % PS	6.674	3.786	.203	-2.78	16.13
6 % PS	Control	4.249	3.436	.444	-4.33	12.83
	1.8 % PS	-6.674	3.786	.203	-16.13	2.78

* The mean difference is significant at the 0.05 level.

Table 7.19 Results for the Shapiro-Wilk test at a 95 % confidence level - Work of fracture of non-machined crystals.

Samples (non-machined crystals)		Shapiro-Wilk		
		Statistic	df	Sig.
	Control	.957	10	.754
	1.8 % PS	.799	10	.079
	6 % PS	.954	10	.722

As can be seen in Table 7.19, since the *p*-value of all tested populations are greater than 0.05, the hypothesis that the data is normally distributed can not be rejected at the 95 % confidence level. It is therefore possible to use parametric tests in the statistical analysis.

Table 7.20 Results for the Levene's homogeneity of variances test - Work of fracture of non-machined crystals.

Levene Statistic	df1	df2	Sig.
3.891	2	22	.036

The result for the Levene's test in Table 7.20 shows that the obtained *p*-value (p = 0.036) is lower than 0.05. This shows that the assumption that all the populations have the same variance is violated at the 95 % confidence level and therefore the Games-Howell test should be used.

Table 7.21 Results for the Games-Howell multiple means comparisons procedure at a 95 % confidence level - Work of fracture of non-machined crystals.

(I) samples (crystals)	(J) samples (crystals)	Mean Difference (I-J)	Std. Error	Sig.	95% Confidence Interval	
					Lower Bound	Upper Bound
Control	1.8 % PS	.647	8.053	.996	-20.78	22.08
	6 % PS	7.532	8.652	.666	-14.86	29.93
1.8 % PS	Control	-.647	8.053	.996	-22.08	20.78
	6 % PS	6.885	5.902	.493	-8.72	22.49
6 % PS	Control	-7.532	8.652	.666	-29.93	14.86
	1.8 % PS	-6.885	5.902	.493	-22.49	8.72

* The mean difference is significant at the 0.05 level.

Table 7.22 Results for the Shapiro-Wilk test at a 95 % confidence level - Work of fracture of cube-machined crystals.

Samples (machined crystals)		Shapiro-Wilk		
		Statistic	df	Sig.
	Control	.936	4	.633
	1.8 % PS	.792	4	.089
	6 % PS	.962	4	.794

As can be seen in Table 7.22, since the *p*-value of all tested populations are greater than 0.05, the hypothesis that the data is normally distributed can not be rejected at the 95 % confidence level. It is therefore possible to use parametric tests in the statistical analysis.

Table 7.23 Results for the Levene's homogeneity of variances test - Work of fracture of cube-machined crystals.

Levene Statistic	df1	df2	Sig.
6.513	2	9	.018

The result for the Levene's test in Table 7.23 shows that the obtained *p*-value (p = 0.018) is lower than 0.05. This shows that the assumption that all the populations have the same variance is violated at the 95 % confidence level and therefore the Games-Howell test should be used.

Table 7.24 Results for the Games-Howell multiple means comparisons procedure at a 95 % confidence level - Work of fracture of cube-machined crystals.

(I) samples (crystals)	(J) samples (crystals)	Mean Difference (I-J)	Std. Error	Sig.	95% Confidence Interval	
					Lower Bound	Upper Bound
Control	1.8 % PS	72.760	35.443	.155	-26.20	171.72
	6 % PS	139.335*	35.443	.009	40.38	238.29
1.8 % PS	Control	-72.760	35.443	.155	-171.72	26.20
	6 % PS	66.575	35.443	.200	-32.38	165.53
6 % PS	Control	-139.335*	35.443	.009	-238.29	-40.38
	1.8 % PS	-66.575	35.443	.200	-165.53	32.38

* The mean difference is significant at the 0.05 level.

Table 7.25 Results for the Shapiro-Wilk test at a 95 % confidence level – Specific compressive strength of cube-machined crystals.

Samples (machined crystals)		Shapiro-Wilk		
		Statistic	df	Sig.
	Control	.857	4	.249
	1.8 % PS	.901	4	.438
	6 % PS	.856	4	.246

As can be seen in Table 7.25, since the *p*-value of all tested populations are greater than 0.05, the hypothesis that the data is normally distributed can not be rejected at the 95 % confidence level. It is therefore possible to use parametric tests in the statistical analysis.

Table 7.26 Results for the Levene's homogeneity of variances test - Specific compressive strength of cube-machined crystals.

Levene Statistic	df1	df2	Sig.
1.324	2	9	.313

The result for the Levene's test in Table 7.26 shows that the obtained *p*-value (p = 0.313) is greater than 0.05 and therefore, the assumption of homogeneity of variance is met. Since the data have homogenous variances the Tukey test will be used for conducting the multiple means comparison.

Table 7.27 Results for the Tukey multiple means comparisons procedure at a 95 % confidence level - Specific compressive strength of cube-machined crystals.

(I) samples (crystals)	(J) samples (crystals)	Mean Difference (I-J)	Std. Error	Sig.	95% Confidence Interval	
					Lower Bound	Upper Bound
Control	1.8 % PS	-16.000	45.864	.936	-144.05	112.05
	6 % PS	233.250*	45.864	.002	105.20	361.30
1.8 % PS	Control	16.000	45.864	.936	-112.05	144.05
	6 % PS	249.250*	45.864	.001	121.20	377.30
6 % PS	Control	-233.250*	45.864	.002	-361.30	-105.20
	1.8 % PS	-249.250*	45.864	.001	-377.30	-121.20

* The mean difference is significant at the 0.05 level.

Table 7.28 Results for the Shapiro-Wilk test at a 95 % confidence level – Specific compressive modulus of cube-machined crystals.

Samples (machined crystals)		Shapiro-Wilk		
		Statistic	df	Sig.
	Control	.940	4	.655
	1.8 % PS	.981	4	.908
	6 % PS	.988	4	.945

As can be seen in Table 7.28, since the *p*-value of all tested populations are greater than 0.05, the hypothesis that the data is normally distributed can not be rejected at the 95 % confidence level. It is therefore possible to use parametric tests in the statistical analysis.

Table 7.29 Results for the Levene's homogeneity of variances test - Specific compressive modulus of cube-machined crystals.

Levene Statistic	df1	df2	Sig.
.434	2	9	.661

The result for the Levene's test in Table 7.29 shows that the obtained *p*-value (p = 0.661) is greater than 0.05 and therefore, the assumption of homogeneity of variance is met at the 95 % confidence level. Since the data have homogenous variances the Tukey test will be used for conducting the multiple means comparison.

Table 7.30 Results for the Tukey HSD multiple means comparisons procedure at a 95 % confidence level - Specific compressive modulus of cube-machined crystals.

(I) samples (crystals)	(J) samples (crystals)	Mean Difference (I-J)	Std. Error	Sig.	95% Confidence Interval	
					Lower Bound	Upper Bound
Control	1.8 % PS	-269.676	356.485	.737	-1264.98	725.63
	6 % PS	1748.674*	356.485	.002	753.37	2743.98
1.8 % PS	Control	269.676	356.485	.737	-725.63	1264.98
	6 % PS	2018.350*	356.485	.001	1023.04	3013.66
6 % PS	Control	-1748.674*	356.485	.002	-2743.98	-753.37
	1.8 % PS	-2018.350*	356.485	.001	-3013.66	-1023.04

* The mean difference is significant at the 0.05 level.

Table 7.31 Results for the Shapiro-Wilk test at a 95 % confidence level – Specific work of fracture of cube-machined crystals.

Samples (machined crystals)		Shapiro-Wilk		
		Statistic	df	Sig.
	Control	.936	4	.633
	1.8 % PS	.792	4	.089
	6 % PS	.962	4	.794

As can be seen in Table 7.31, since the *p*-value of all tested populations are greater than 0.05, the hypothesis that the data is normally distributed can not be rejected at the 95 % confidence level. It is therefore possible to use parametric tests in the statistical analysis.

Table 7.32 Results for the Levene's homogeneity of variances test - Specific work of fracture of cube-machined crystals.

Levene Statistic	df1	df2	Sig.
6.405	2	9	.019

The result for the Levene's test in Table 7.32 shows that the obtained *p*-value (p = 0.019) is lower than 0.05. This shows that the assumption that all the populations have the same variance is violated at the 95 % confidence level and therefore the Games-Howell test should be used.

Table 7.33 Results for the Games-Howell multiple means comparisons procedure at a 95 % confidence level - Specific work of fracture of cube-machined crystals.

(I) samples (crystals)	(J) samples (crystals)	Mean Difference (I-J)	Std. Error	Sig.	95% Confidence Interval	
					Lower Bound	Upper Bound
Control	1.8 % PS	26.505	16.041	.301	-23.59	76.60
	6 % PS	51.169	12.722	.054	-1.36	103.70
1.8 % PS	Control	-26.505	16.041	.301	-76.60	23.59
	6 % PS	24.665	9.922	.166	-16.00	65.33
6 % PS	Control	-51.169	12.722	.054	-103.70	1.36
	1.8 % PS	-24.665	9.922	.166	-65.33	16.00

* The mean difference is significant at the 0.05 level.

Table 7.34 Results for the Shapiro-Wilk test at a 95 % confidence level - Hardness mean of pure calcite compared with mean of composite occluded with 20 nm co-polymer micelles.

Samples		Shapiro-Wilk		
		Statistic	df	Sig.
	Control	.919	10	.308
	Micelles	.941	10	.567

As can be seen in Table 7.34, since the *p*-value of all tested populations are greater than 0.05, the hypothesis that the data is normally distributed can not be rejected at the 95 % confidence level. It is therefore possible to use parametric tests in the statistical analysis.

Table 7.35 Results for the Levene's homogeneity of variances test - Hardness mean of pure calcite compared with mean of composite occluded with 20 nm co-polymer micelles.

Levene Statistic	df1	df2	Sig.
6.898	1	19	.017

The result for the Levene's test shows that the obtained *p*-value (p = 0.017) is lower than 0.05. This shows that at the 95 % confidence level the populations do not have the same variance and therefore a Welch t-test assuming unequal variances should be used to compare the two population means.

Table 7.36 Results for the Welch t-test means comparison at a 95 % confidence level - Hardness mean of pure calcite compared with mean of composite occluded with 20 nm co-polymer micelles.

		Micelles	Control
Mean		2.2233	1.991818
Variance		0.010193	0.030576
Observations		10	10
df		18	
t Stat		3.755623	
Sig.		.002	
Mean Difference		.23148	
Std. Error Difference		.06164	
95% Confidence Interval of the Difference	Lower	.10098	
	Upper	.36198	

Since the obtained *p*-value (0.002) in Table 7.36 is lower than 0.05, the null hypothesis is rejected and, at a confidence level of 95 %, the micelles hardness mean is considered significantly larger than that of the control.

Table 7.37 Results for the Shapiro-Wilk test at a 95 % confidence level - Hardness of different resins.

Resins		Shapiro-Wilk		
		Statistic	df	Sig.
	Kleer set resin	.932	10	.472
	Di-hard resin	.848	10	.054
	Probmet resin	.941	10	.227

As can be seen in Table 7.37, since the *p*-value of all tested populations are greater than 0.05, the hypothesis that the data is normally distributed can not be rejected at the 95 % confidence level. It is therefore possible to use parametric tests in the statistical analysis.

Table 7.38 Results for the Levene's homogeneity of variances test - Hardness of different resins.

Levene Statistic	df1	df2	Sig.
4.383	2	38	.019

The result for the Levene's test in Table 7.38 shows that the obtained *p*-value (p = 0.019) is lower than 0.05. This shows that the assumption that all the populations have the same variance is violated at the 95 % confidence level and therefore the Games-Howell test should be used.

Table 7.39 Results for the Games-Howell multiple means comparisons procedure at a 95 % confidence level - Hardness of different resins.

(I) samples (crystals)	(J) samples (crystals)	Mean Difference (I-J)	Std. Error	Sig.	95% Confidence Interval	
					Lower Bound	Upper Bound
Kleer set resin	Di-hard resin	.06530	.02888	.109	-.0140	.1446
	Probmet resin	-.09096*	.02773	.009	-.1606	-.0213
Di-hard resin	Kleer set resin	-.06530	.02888	.109	-.1446	.0140
	Probmet resin	-.15626*	.03905	.001	-.2538	-.0587
Probmet resin	Kleer set resin	.09096*	.02773	.009	.0213	.1606
	Di-hard resin	.15626*	.03905	.001	.0587	.2538

* The mean difference is significant at the 0.05 level.

Table 7.40 Results for the Shapiro-Wilk test at a 95 % confidence level - Song-Pharr estimated modulus.

	samples	Shapiro-Wilk		
		Statistic	df	Sig.
	Control	.975	10	.934
	1.8 % PS	.913	10	.299
	6 % PS	.952	10	.693
	23 % PS	.968	10	.871

As can be seen in Table 7.40, since the *p*-value of all tested populations are greater than 0.05, the hypothesis that the data is normally distributed can not be rejected at the 95 % confidence level. It is therefore possible to use parametric tests in the statistical analysis.

Table 7.41 Results for the Levene's homogeneity of variances test - Song-Pharr estimated modulus.

Levene Statistic	df1	df2	Sig.
6.746	3	36	.001

The result for the Levene's test in Table 7.41 shows that the obtained *p*-value (p = 0.001) is lower than 0.05. This shows that the assumption that all the populations have the same variance is violated at the 95 % confidence level and therefore the Games-Howell test should be used.

Table 7.42 Results for the Games-Howell multiple means comparisons procedure at a 95 % confidence level - Song-Pharr estimated modulus.

(I) samples	(J) samples	Mean Difference (I-J)	Std. Error	Sig.	95% Confidence Interval	
					Lower Bound	Upper Bound
Control	1.8 % PS	4.10250	5.91310	.898	-12.9042	21.1092
	6 % PS	56.66250*	4.47963	.000	42.1986	71.1264
	23 % PS	60.81250*	4.76755	.000	46.1324	75.4926
1.8 % PS	Control	-4.10250	5.91310	.898	-21.1092	12.9042
	6 % PS	52.56000*	4.10674	.000	40.0209	65.0991
	23 % PS	56.71000*	4.41903	.000	43.7295	69.6905
6 % PS	Control	-56.66250*	4.47963	.000	-71.1264	-42.1986
	1.8 % PS	-52.56000*	4.10674	.000	-65.0991	-40.0209
	23 % PS	4.15000	2.15178	.262	-2.1321	10.4321
23 % PS	Control	-60.81250*	4.76755	.000	-75.4926	-46.1324
	1.8 % PS	-56.71000*	4.41903	.000	-69.6905	-43.7295
	6 % PS	-4.15000	2.15178	.262	-10.4321	2.1321

* The mean difference is significant at the 0.05 level.

Table 7.43 Results for the Shapiro-Wilk test at a 95 % confidence level - Song-Pharr estimated modulus mean of pure calcite compared with mean of composite occluded with 20 nm co-polymer micelles.

Samples		Shapiro-Wilk		
		Statistic	df	Sig.
	Control	.985	10	.987
	Micelles	.926	10	.407

As can be seen in Table 7.43, since the *p*-value of all tested populations are greater than 0.05, the hypothesis that the data is normally distributed can not be rejected at the 95 % confidence level. It is therefore possible to use parametric tests in the statistical analysis.

Table 7.44 Results for the Levene's homogeneity of variances test - Song-Pharr estimated modulus mean of pure calcite compared with mean of composite occluded with 20 nm co-polymer micelles.

Levene Statistic	df1	df2	Sig.
.303	1	18	.589

The result for the Levene's test in Table 7.44 shows that the obtained *p*-value (p = 0.589) is greater than 0.05 and therefore, the two populations variances are homogenous. Since the data have homogenous variances at a 95 % confidence level a t-test assuming equal variances will be used for conducting the means comparison.

Table 7.45 Results for the t-test two-Sample means comparison, assuming equal variances at a 95 % confidence level - Song-Pharr estimated modulus mean of pure calcite compared with mean of composite occluded with 20 nm co-polymer micelles.

		Control	Micelles
Mean		89.9225	75.1375
Variance		119.2718	189.361
Observations		10	10
df		18	
t Stat		2.633	
Sig.		.017	
Mean Difference		14.62800	
Std. Error Difference		5.55547	
95% Confidence Interval of the Difference	Lower	2.95638	
	Upper	26.29962	

As can be seen in Table 7.45, since the obtained *p*-value (0.017) is lower than 0.05, the null hypothesis is rejected and the control estimated modulus mean is considered significantly larger, at a confidence level of 95 %, than that of the micelles composite.

Table 7.46 Results for the Shapiro-Wilk test at a 95 % confidence level - Hardness measured by conventional methods.

	samples	Shapiro-Wilk		
		Statistic	df	Sig.
	Control	.955	10	.730
	1.8 % PS	.919	10	.383
	6 % PS	.906	10	.290
	23 % PS	.898	10	.239
	Iceland spar	.925	10	.402
	Sea urchin spine	.924	10	.394

As can be seen in Table 7.46, since the *p*-value of all tested populations are greater than 0.05, the hypothesis that the data is normally distributed can not be rejected at the 95 % confidence level. It is therefore possible to use parametric tests in the statistical analysis.

Table 7.47 Results for the Levene's homogeneity of variances test - Hardness measured by conventional methods.

Levene Statistic	df1	df2	Sig.
5.682	5	54	.000

The result for the Levene's test in Table 7.47 shows that the obtained *p*-value (p = 0.000) is much lower than 0.05. This shows that the assumption that all the populations have the same variance is violated at the 95 % confidence level and therefore the Games-Howell test should be used.

Table 7.48 Results for the Games-Howell multiple means comparisons procedure at a 95 % confidence level - Hardness measured by conventional methods.

(I) samples	(J) samples	Mean Difference (I-J)	Std. Error	Sig.	95% Confidence Interval	
					Lower Bound	Upper Bound
Control	1.8 % PS	.41891*	.10451	.010	.0845	.7533
	6 % PS	1.64336*	.09857	.000	1.3268	1.9599
	23 % PS	1.76891*	.13518	.000	1.3284	2.2094
	Iceland spar	1.01891*	.07987	.000	.7416	1.2962
	Sea urchin spine	.20091	.08724	.258	-.0871	.4889
1.8 % PS	Control	-.41891*	.10451	.010	-.7533	-.0845
	6 % PS	1.22444*	.09257	.000	.9254	1.5235
	23 % PS	1.35000*	.13087	.000	.9185	1.7815
	Iceland spar	.60000*	.07234	.000	.3438	.8562
	Sea urchin spine	-.21800	.08041	.140	-.4853	.0493
6 % PS	Control	-1.64336*	.09857	.000	-1.9599	-1.3268
	1.8 % PS	-1.22444*	.09257	.000	-1.5235	-.9254
	23 % PS	.12556	.12617	.911	-.2959	.5470
	Iceland spar	-.62444*	.06345	.000	-.8472	-.4017
	Sea urchin spine	-1.44244*	.07251	.000	-1.6802	-1.2047
23 % PS	Control	-1.76891*	.13518	.000	-2.2094	-1.3284
	1.8 % PS	-1.35000*	.13087	.000	-1.7815	-.9185
	6 % PS	-.12556	.12617	.911	-.5470	.2959
	Iceland spar	-.75000*	.11218	.001	-1.1543	-.3457
	Sea urchin spine	-1.56800*	.11754	.000	-1.9759	-1.1601
Iceland spar	Control	-1.01891*	.07987	.000	-1.2962	-.7416
	1.8 % PS	-.60000*	.07234	.000	-.8562	-.3438
	6 % PS	.62444*	.06345	.000	.4017	.8472
	23 % PS	.75000*	.11218	.001	.3457	1.1543
	Sea urchin spine	-.81800*	.04384	.000	-.9638	-.6722

* The mean difference is significant at the 0.05 level.

Table 7.49 Results for the Shapiro-Wilk test at a 95 % confidence level - Hardness obtained by conventional methods: mean of pure calcite compared with mean of composite occluded with 20 nm co-polymer micelles.

Samples		Shapiro-Wilk		
		Statistic	df	Sig.
	Control	.955	10	.730
	Micelles	.907	10	.263

As can be seen in Table 7.49, since the *p*-value of all tested populations are greater than 0.05, the hypothesis that the data is normally distributed can not be rejected at the 95 % confidence level. It is therefore possible to use parametric tests in the statistical analysis.

Table 7.50 Results for the Levene's homogeneity of variances test - Hardness obtained by conventional methods: mean of pure calcite compared with mean of composite occluded with 20 nm co-polymer micelles.

Levene Statistic	df1	df2	Sig.
.261	1	18	.615

The result for the Levene's test in Table 7.50 shows that the obtained *p*-value (p = 0.615) is much larger than 0.05, and therefore, the two populations variances are homogenous at the 95 % confidence level. Since the data have homogenous variances a t-test assuming equal variances will be used for conducting the means comparison.

Table 7.51 Results for the t-test assuming equal variances at a 95 % confidence level - Hardness obtained by conventional methods: mean of pure calcite compared with mean of composite occluded with 20 nm co-polymer micelles.

		Control	Micelles
Mean		3.854397	3.747072
Variance		0.04821	0.04082
Observations		10	10
df		18	
t Stat		.901	
Sig.		.379	
Mean Difference		.08891	
Std. Error Difference		.09863	
95% Confidence Interval of the Difference	Lower	-.11830	
	Upper	.29612	

Since the obtained *p*-value (0.379) in Table 7.51 is greater than 0.05, the null hypothesis is not rejected and the control hardness mean is not considered significantly different, at a confidence level of 95 %, than that of the micelles composite.

Table 7.52 Results for the Shapiro-Wilk test at a 95 % confidence level - Specific modulus.

	samples	Shapiro-Wilk		
		Statistic	df	Sig.
	Control	.974	10	.927
	1.8 % PS	.912	10	.295
	6 % PS	.951	10	.684
	23 % PS	.968	10	.873
	Micelles	.912	10	.367
	Sea urchin spine	.958	10	.766

As can be seen in Table 7.52, since the *p*-value of all tested populations are greater than 0.05, the hypothesis that the data is normally distributed can not be rejected at the 95 % confidence level. It is therefore possible to use parametric tests in the statistical analysis.

Table 7.53 Results for the Levene's homogeneity of variances test - Specific modulus.

Levene Statistic	df1	df2	Sig.
8.665	5	50	.000

The result for the Levene's test in Table 7.53 shows that the obtained *p*-value (p = 0.000) is much lower than 0.05. This shows that the assumption that all the populations have the same variance is violated at the 95 % confidence level and therefore the Games-Howell test should be used.

Table 7.54 Results for the Games-Howell multiple means comparisons procedure at a 95 % confidence level - Specific modulus.

(I) samples	(J) samples	Mean Difference (I-J)	Std. Error	Sig.	95% Confidence Interval	
					Lower Bound	Upper Bound
Control	1.8 % PS	1.19500	2.18820	.993	-5.8946	8.2846
	6 % PS	20.52500*	1.65539	.000	14.4345	26.6155
	23 % PS	20.85600*	1.80213	.000	14.6507	27.0613
	Micelles	-.51250	2.95328	1.000	-10.4285	9.4035
	Sea urchin spine	7.69500*	1.62371	.016	1.5977	13.7923
1.8 % PS	Control	-1.19500	2.18820	.993	-8.2846	5.8946
	6 % PS	19.33000*	1.52927	.000	14.0381	24.6219
	23 % PS	19.66100*	1.68702	.000	14.1232	25.1988
	Micelles	-1.70750	2.88448	.990	-11.4323	8.0173
	Sea urchin spine	6.50000*	1.49492	.015	1.2331	11.7669
6 % PS	Control	-20.52500*	1.65539	.000	-26.6155	-14.4345
	1.8 % PS	-19.33000*	1.52927	.000	-24.6219	-14.0381
	23 % PS	.33100	.89339	.999	-2.6380	3.3000
	Micelles	-21.03750*	2.50446	.000	-30.4028	-11.6722
	Sea urchin spine	-12.83000*	.43232	.000	-14.2516	-11.4084
23 % PS	Control	-20.85600*	1.80213	.000	-27.0613	-14.6507
	1.8 % PS	-19.66100*	1.68702	.000	-25.1988	-14.1232
	6 % PS	-.33100	.89339	.999	-3.3000	2.6380
	Micelles	-21.36850*	2.60379	.000	-30.7420	-11.9950
	Sea urchin spine	-13.16100*	.83323	.000	-16.0470	-10.2750
Micelles	Control	.51250	2.95328	1.000	-9.4035	10.4285
	1.8 % PS	1.70750	2.88448	.990	-8.0173	11.4323
	6 % PS	21.03750*	2.50446	.000	11.6722	30.4028
	23 % PS	21.36850*	2.60379	.000	11.9950	30.7420
	Sea urchin spine	8.20750	2.48364	.089	-1.1673	17.5823

* The mean difference is significant at the 0.05 level.

Table 7.55 Results for the Shapiro-Wilk test at a 95 % confidence level - Specific hardness.

	samples	Shapiro-Wilk		
		Statistic	df	Sig.
	Control	.940	10	.551
	1.8 % PS	.934	10	.516
	6 % PS	.908	10	.303
	23 % PS	.771	10	.387
	Iceland spar	.915	10	.315
	Sea urchin spine	.940	10	.558

As can be seen in Table 7.55, since the *p*-value of all tested populations are greater than 0.05, the hypothesis that the data is normally distributed can not be rejected at the 95 % confidence level. It is therefore possible to use parametric tests in the statistical analysis.

Table 7.56 Results for the Levene's homogeneity of variances test - Specific hardness.

Levene Statistic	df1	df2	Sig.
3.075	5	54	.017

The result for the Levene's test in Table 7.56 shows that the obtained *p*-value (p = 0.017) is lower than 0.05. This shows that the assumption that all the populations have the same variance is violated at the 95 % confidence level and therefore the Games-Howell test should be used.

Table 7.57 Results for the Games-Howell multiple means comparisons procedure at a 95 % confidence level - Specific hardness.

(I) samples	(J) samples	Mean Difference (I-J)	Std. Error	Sig.	95% Confidence Interval	
					Lower Bound	Upper Bound
Control	1.8 % PS	.15089*	.03646	.008	.0342	.2676
	6 % PS	.59056*	.03447	.000	.4803	.7008
	23 % PS	.63570*	.10036	.001	.2888	.9826
	Micelles	-.25500*	.03750	.000	-.3742	-.1358
	Sea urchin spine	.08300	.02964	.113	-.0137	.1797
1.8 % PS	Control	-.15089*	.03646	.008	-.2676	-.0342
	6 % PS	.43967*	.03481	.000	.3273	.5520
	23 % PS	.48481*	.10048	.006	.1377	.8319
	Micelles	-.40589*	.03781	.000	-.5268	-.2849
	Sea urchin spine	-.06789	.03003	.276	-.1675	.0318
6 % PS	Control	-.59056*	.03447	.000	-.7008	-.4803
	1.8 % PS	-.43967*	.03481	.000	-.5520	-.3273
	23 % PS	.04514	.09978	.997	-.3013	.3916
	Micelles	-.84556*	.03590	.000	-.9606	-.7306
	Sea urchin spine	-.50756*	.02758	.000	-.5981	-.4170
23 % PS	Control	-.63570*	.10036	.001	-.9826	-.2888
	1.8 % PS	-.48481*	.10048	.006	-.8319	-.1377
	6 % PS	-.04514	.09978	.997	-.3916	.3013
	Micelles	-.89070*	.10086	.000	-1.2381	-.5433
	Sea urchin spine	-.55270*	.09821	.003	-.8980	-.2074
Micelles	Control	.25500*	.03750	.000	.1358	.3742
	1.8 % PS	.40589*	.03781	.000	.2849	.5268
	6 % PS	.84556*	.03590	.000	.7306	.9606
	23 % PS	.89070*	.10086	.000	.5433	1.2381
	Sea urchin spine	.33800*	.03129	.000	.2353	.4407

* The mean difference is significant at the 0.05 level.

7.4 References

Devore, L. J., 2011, *Probability and Statistics for Engineering and the Sciences*, 8th, Duxbury Press.

McDonald, J. H., 2009, *Handbook of Biological Statistics*, Sparky House Publishing.

Zar, J. H., 2010, *Biostatistical Analysis*, 5th Edition, Prentice Hall.